MULTISCALE MODELLING OF INDUSTRIAL FLIGHTED ROTARY DRYERS

Thesis submitted by

Olukayode Oludamilola AJAYI, B.Tech(Hons), M.Sc (Eng) UCT

in December 2011

For the degree of Doctor of Philosophy

in the School of Engineering

James Cook University

STATEMENT OF ACCESS

I, the undersigned, author of this work, understand that James Cook University will make this thesis available for use within the University Library and, via the Australian Digital Theses network, for use elsewhere.

I understand that, as an unpublished work, a thesis has significant protection under the copyright Act and;

I do not wish to place any further restriction on access to this work.

31st December 2011

Olukayode Ajayi

DECLARATION

I declare that this thesis is my own work and has not been submitted in any form for another degree or diploma at any university or other institution of tertiary education. Information derived from the published or unpublished work of others has been acknowledged in the text and a list of references is given.

_____ 31st December 2011

Olukayode Ajayi

STATEMENT ON THE CONTRIBUTION OF OTHERS

The research project was funded by MMG Century mine, Australia. Tuition fee scholarship and stipend support was received from the School of Engineering and Physical Sciences. Graduate research scholarship awards were used to purchase high performance workstation and licenses for gProms and CFX softwares.

Inductively coupled plasma mass spectrometry (ICP-MS) and X-ray diffraction analysis was undertaken at James Cook University Advanced Analytical Center. Wendy Smith provided assistance with the editing of the final thesis.

ACKNOWLEDGEMENTS

I express my unreserved gratitude to God for His love, faithfulness and wisdom throughout the research. This piece of work is dedicated to Him.

I am deeply indebted to my supervisor Dr Madoc Sheehan for his unwavering support and guidance throughout the research. Thanks to MMG operation team leaders Scott Findlay and Clyde Goody for their support during the industrial experiments.

Many thanks to my fellow graduate students, Shaun, Reza, Om, Manish, Sepideh, Dhanya, Rhys, Raymond Kazum and Hassan for their stimulating discussions during the course of study. I am grateful to my friends Danielle, Lolade, Oyebola, Adams, Kofi and Abena for their constant encouragement.

Special thanks to my siblings Omotuyole, Busayo and Femi for their love and support. Thanks to my wife's mum for her moral support and inspiring words. I express my sincere gratitude to my parents for their continuous support, prayers and for believing in my dreams and career path.

My deepest expression of appreciation goes to my wife and son, Olubunmi Asake and David for their understanding, love, support and prayers. Thanks for your encouragement during the tough times of this research and for bearing my long working hours.

Thanks to everyone who has contributed to the success of this research one-way or the other.

TABLE OF CONTENT

LIST OF FIGURES

LIST OF TABLES

NOMENCLATURE

A	area (m^2)
A_a	slope of the line after break point (Figure E1)
A_b	slope of the line before break point (Figure E1)
$A_{\bar{N}}$	$X^{1.37} Fr^{0.41} S/d_p^3$ (m^{-1})
A_{SF}	percentage covered by scale accumulation (%)
C	concentration (ppm)
C_a	intercept of the line after break point (Figure E1)
C_b	intercept of the line before break point (Figure E1)
C_D	drag coefficient (-)
$C_{\varepsilon 1}, C_{\varepsilon 2}, C_\mu$	coefficients in turbulence model
C_F	forward step coefficient (m)
C_p	specific heat capacity (J/ (kg.K)),
CV	Controlled variable
D	diameter (m)
D_{avg}	average forward step (m)
d_p	particle diameter(m)
D_{out}	outside diameter(m)
E_{Aa}	error in slope after break point (Equation E7)
E_{Ab}	error in slope before point (Equation E7)
E_{ca}	error in intercept of the line before break point (Equation E6)
E_{cb}	error in intercept of the line after break point (Equation E6)

$E(t)$	exit-age distribution function (minutes^{-1})
e_s	particle restitution coefficient
F	mass flow rate ($kg_{wet\ solid}$/s)
ff_c	flow index
Fr	Froude number
$\bar{g}$	acceleration of gravity (m/s^2)
g_0	radial distribution function
Gu	Gukhman number
h	height of curtain (m)
h_c	convective heat transfer (J/(m^2.s.K))
h_m	mass transfer coefficient (kg/(m^2.s.Pa))
H	holdup ($kg_{wet\ solid}$)
$\bar{H}$	enthalpy energy (J/kg)
$H_{v,}$	latent heat of vaporization (KJ/kg)
h_{in}	internal convective heat transfer coefficient
h_{out}	external convective heat transfer coefficient
$h_{rad_{in}}$	internal radiation heat transfer coefficient
$h_{rad_{out}}$	external radiation heat transfer coefficient
j_H	heat transfer factor
j_m	mass transfer factor
k_2, k_3, k_4	transport coefficients (s^{-1})
k	turbulence kinetic energy (m^2/s^2)
k_g	thermal conductivity of gas (W/m ^{o}C)

$k_{g_{out}}$	thermal conductivity of gas based on shell temperature(W/m ^{o}C)
K_h	correction factor for convective heat transfer coefficient
K_p	steady state process gain
$\bar{I}$	unit stress tensor
L	length of the dryer (m)
L_s	length of flighted section (m)
M	molar flow rate (kmol/hr)
m	mass (kg)
m_s	mass per length (kg/m)
maft	mass averaged fall time (s)
mafh	mass averaged fall height (m)
$m_{p_{design}}$	Passive mass at design loading condition (kg)
M_{design}^{TOT}	total holdup (kg)
MW	Molecular weight (kg/kmol)
n	number of moles (mol)
N_c	number of cells (-)
N_f	number of flight (-)
P	pressure (kg/m s^2)
Pr	Prandtl number
$\overline{PV}$	pressure and volume in ideal gas equation
Q	heat (J/s)
r_{in}	inside radius(m)

R	ideal gas constant (J/(mol·K))
Ra	Rayleigh number
R_j	resistance
R_o	outside radius (m)
Re	Reynolds number
R_F	flight tip radius (m)
R_w	drying rate (kg/s)
S	cross sectional area of dryer (m^2) (Equation 6.40)
Sc	Schmidt number
Sh	Sherwood number
St	Stanton number
s_1	flight base length(m)
s_2	flight tip length (m)
SE_G	standard error of G in equation D4
SE_H	standard error of H in equation D4
S_F	scale accumulation factor
T	temperature (^oC)
t	time (s)
$\bar{t}_a$	active cycle time (s)
$\bar{t}_p$	passive cycle time (s)
U	velocity vector (m/s)
u	velocity fluctuations (m/s)
u_s	solid velocity (m/s)

$\bar{U}$	Internal energy (J/kg)
$\bar{u_i}, \bar{u_j}$	mean velocity components (m/s)
v_g	gas velocity (m/s)
X	holdup, % of dryer volume (%) (Equation 6.40)
X_{CO_2}	mole fraction of carbon dioxide in hot gas (kmol/kmol)
X_{DO}	mole fraction of oxygen in air (kmol/kmol)
X_{DN}	mole fraction of nitrogen in air (kmol/kmol)
X_{cw}	mole fraction of water in air (kmol/kmol)
X_{FC}	mole fraction of carbon in fuel oil(kmol/kmol)
X_{FH}	mole fraction of hydrogen in fuel oil(kmol/kmol)
X_{Fs}	mole fraction of sulphur in fuel oil(kmol/kmol)
X_{Fw}	moisture content in fuel oil (kg/kg)
X_{H_2O}	moisture content in hot gas (kg/kg)
X_N	mole fraction of nitrogen in hot gas (kmol/kmol)
X_{SO_2}	mole fraction of sulphur dioxide in hot gas (kmol/kmol)
x_i , x_j	direction coordinates *(in Equations 4.14 and 4.15)*
x_w	moisture content (kg/kg$_{\text{wet solid}}$)
x_t	tracer concentration (kg/kg)
y_w	gas humidity (kg/kg)
$\bar{Y}_{ij}$	*k*th measured value of variable *j* in experiment *i (Equation 5.22)*
Y_{ij}	*j*th predicted value of variable *j* in experiment *i (Equation 5.22)*
$\acute{y}_w$	gas humidity (mol/mol)

z	direction coordinate
Δz	length (m)

Greek letters

$\wp$	axial dispersion coefficient (m^2/s)
$\wp_{AB}$	mass diffusivity ($m^2.s^{-1}$)
α_1	flight base angle (^{o})
α_2	flight tip angle (^{o})
α	volume fraction (-)
β	interphase transfer coefficient (kg/m^3 s)
ϑ, α and β_i,	set of model parameters to be estimated (Equation 5.22)
ε_v	voidage (-)
ε_r	emissivity
ε	dissipation rate of turbulent kinetic energy(m^2/s^3)
τ	mean residence time (Equations 2.1 and 3.5) (minutes)
τ	stress tensor (Equations 4.3 and 4.4)
θ	slope of the drum (radians)
θ_{AL}	area correction factor for the unflighted sections
θ_a	area correction factor for the flighted sections
θ_D	mass averaged discharge location (degrees)
θ_k	kilning angle (radians)
θ_{loss}	heat loss turning factor
θ_s	granular temperature (m^2/s^2)

λ_s	bulk viscosity (kg/m s)
μ	dynamic viscosity (kg/m s)
μ_s	shear viscosity (kg/m s)
μ_t	turbulence viscosity (kg/m s)
ρ	density (kg/m^3)
σ_{ij}^2	variance of the *jth* measurement of variable *j* in experiment *i* (Equation 5.22)
σ^2	second moment of RTD (minutes^{-2})
$\sigma_k, \sigma_\varepsilon$	effective turbulent Prandtl numbers for the transport of ε and k.
σ_r	Stefan-Boltzmann constant
ϕ	dynamic angle of repose (^{o})
$\mathcal{R}$	mass ratio of airbone to flight-borne solids
ω	drum rotational speed (rad/s)
Ψ	mass averaged properties

Subscripts

a	active phase
AL	active layer
amb	ambient
b	bulk
c	combustion air
ct	curtain
conv	convection
D	dilution air

F	Fuel oil
f	first unloading flight
g	gas phase
i, j	directional coordinates
loss	heat loss
p	passive
pt	particle
n	last flight to discharge solid material
rad	radiation
s	solid
Tot	total holdup in the dryer
v	vapour
w	water

A**BSTRACT**

Rotary dryers are commonly used in the food and mineral processing industries for drying granular or particulate solids due to their simplicity, low cost and versatility compared to other dryers. The co-current industrial rotary dryer (MMG, Karumba) examined in this study is used in drying zinc and lead concentrate. The dryer is 22.2 metres long with a diameter of 3.9 metres. The slope and the typical rotational speed of the dryer are 4 degrees and 3 rpm respectively. The dryer has both unflighted and flighted sections with different flight configurations. Operational issues associated with the dryer that lead to the requirement for a dynamic model of the dryer include issues such as high fuel consumption and the build-up of scale on the internal surfaces.

In order to operate an optimum dryer, it is necessary to understand the mechanisms occurring within the dryer. The important transport mechanisms that govern the performance of rotary dryers are: solids transportation, heat, and mass transfer. Studies have shown that the knowledge of the solid transport is important to solve the heat and mass transfer differential equations that describe completely the temperature and moisture content profiles along the dryer for both solid and gas phases. Solid transport within the dryer can be characterised through the solid residence time distribution, which is the distribution of times taken for the solids to travel through the dryer. Solid residence time distribution can be determined experimentally. The most common experimental approach is to introduce tracer at the inlet and monitor tracer concentration at the outlet as a function time. Several modelling approaches have been taken to determine the residence time and the residence time distribution and these approaches have varied from empirical correlations to compartment modelling. In many of these approaches, loading state, residence time and operational feed rates are strongly linked. The loading state also influences

the effectiveness of particle to gas heat and mass transfer as well as the residence time distribution of solids through the dryer.

There are three potential degrees of loading in a rotary dryer namely under-loaded, design loaded and overloaded. However, most industrial rotary dryers are operated at under-loaded or overloaded, which results into poor efficiency of the dryer and the optimal economics of the dryer will not be achieved. As such, accurate estimation of the design load is critical to the optimal performance of flighted rotary dryers and is an important characteristic of flighted rotary dryer models.

To experimentally characterise MMG rotary dryer, industrial and laboratory experiments were undertaken. The industrial experiments included residence time distributions (RTD), shell temperature measurements, spatial sampling of the solids along the length of dryer, moisture content analysis and Process Information (PI) data collection. Residence time distribution experiments were carried out by injecting lithium chloride as tracer at the inlet of the dryer while sampling outlet solids over a period of time. Zinc concentrate properties such as dynamic angle of repose, bulk density and particle size were also determined. A series of different experiments were undertaken to examine the effect of speed and loading.

Flight loading experiments were carried out at pilot scale to determine the effect of moisture content and rotational speed on dryer design loadings and to facilitate accurate determination of model parameters. The flight holdup experiments involved taking photographs of the cross-sectional area of the dryer. An image analysis technique was developed to estimate the amount of material within the flights and in the airborne phase. The analysis involved developing a combined ImageJ thresholding process and in-house MATLAB code to estimate the cross-

sectional area of material within the flight. The suitability of the developed methodology was established. In addition, saturation of both the airborne and upper drum flight-borne solids was observed.

To select an appropriate geometrically derived design load model, comparison of existing design load models from the literature was undertaken. The proportion of airborne to flight-borne solids within the drum was characterised through a combination of photographic analysis coupled with Computational Fluid Dynamics (CFD) simulation. In particular, solid volume fractions of the airborne solids were characterised using a CFD technique based on the Eulerian-Eulerian approach. The suitability of using geometric models of flight unloading to predict these proportions in a design loaded dryer were discussed and a modified version of Baker's (1988) design load model was proposed.

A multiscale dynamic mass and energy process model was developed and validated for the dryer in order to characterise the performance of MMG rotary dryer. The mass and energy balance equations involved ordinary differential equations for describing the flighted sections and partial differential equations for modelling the unflighted sections. Solids in unflighted sections were modelled as the axially-dispersed plug flow system. In the flighted sections, the solids were modelled using a compartment modelling approach involving well-mixed tanks (Sheehan et al., 2005). The gas phase was modelled as a plug flow system. Simulations were undertaken using gPROMS (process modelling software). As much as possible, model coefficients were determined using geometric modelling based on material properties and dryer operational conditions. The use of this approach is termed a pseudo-physical compartment model. The solid transport model was validated using full scale residence time distribution at different experimental conditions. The model results predicted well the effect of rotational speed, internal

diameter and solid feed rate. Estimated parameters included the kilning velocity, axial dispersed coefficient and area correction factors. The validation of the energy balances was based on Process Information (PI), experimental residence time distribution and moisture content data of the studied dryer. Model parameters involving the surface area in contact with the incoming gas data were manipulated to fit experimental moisture content. The gas and solid temperature profiles were also predicted, which provide a firm basis upon which additional studies may be undertaken.

Gas inlet temperature was identified as the most suitable manipulated variable for the dryer with clean internal condition. However, to achieve desired product quality within a scaled dryer, the study suggested the solid feed rate should be reduced so as to achieve optimum gas-solid interaction. To address the high fuel consumption associated with the dryer, the study proposed externally lagging of the dryer and reduction in the gas inlet temperature to meet the desired product quality.

CHAPTER ONE

1. INTRODUCTION

Flighted rotary dryers are commonly used in the food and mineral processing industries for drying granular or particulate solids. The rotary dryer consists of a cylindrical shell slightly inclined towards the outlet as shown in Figure 1.1 and is fitted internally with an array of flights. The arrangement and type of flights vary with the nature of the granular solids. As the dryer rotates, solids are picked up by flights, lifted for a certain distance around the drum and fall through the gas stream in a cascading curtain (see Figure 1.2). Gas used as drying medium is introduced as either co-current or counter-current to the solid flow. The movement of solids through the dryer is influenced by the following mechanisms: lifting by the flights, cascading from the flights through the air stream and bouncing, rolling and sliding of the particles on impact with the bottom of the dryer (Yliniemi, 1999).

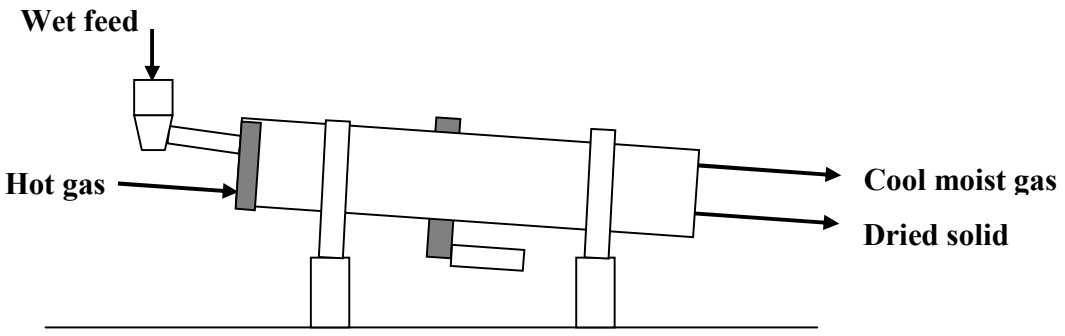

Figure 1.1: Typical example of a co-current rotary dryer

Figure 1.2: Cross-section of typical flighted rotary dryer showing the solids cascading

1.1 Motivation

The co-current industrial rotary dryer examined in this current study is used in drying zinc and lead concentrates (MMG, Karumba, 2008–2010 seasons). The dryer has both unflighted and flighted sections. Each flighted section has different flight configuration, although all flights are standard two-stage designs. Operational issues associated with the dryer include high fuel consumption and it is a challenge to operate the dryer effectively when there is hard scale build-up on the internal surfaces.

Previous studies (Alvarez & Shene, 1994; Kelly, 1995; Cao & Langrish, 2000) have also identified some other factors that affect the design and performance of a rotary dryer which include the following: physical properties of the solids, geometrical configuration of the dryer and flight geometry, gas-solid interactions and operating conditions such as solid feed rate, solid inlet temperature, gas inlet flow rate, gas inlet temperature and rotational speed of the dryer.

For better understanding of the dryer's performance, modelling can be undertaken at different scales such as unit operation scale, flight scale, curtain and particle scale. The unit operation scale models the overall process. Flight scale represents the flight loading capacity as it facilitates the gas-solids interaction. The curtain and particle scale characterises the solid properties such as dynamic angle of repose, bulk density and particle size.

The performance of rotary dryer is dictated by three important transport mechanisms, namely: solids transportation, heat and mass transfer (Prutton et al., 1942; Matchett & Baker, 1987; Renaud et al., 2000). However, studies have established that the solid distribution in the dryer affects the movement of solids within the dryer, and as well as the amount of contact surface between the gas and the solid (Duchesne et al., 1996; Sheehan et al., 2002). In rotary dryers, there are three loading states: under-loaded, design loaded and overloaded. The loading capacity of the dryer has been a key requirement to the prediction of the solid transport within the drum. It is important to operate the dryer at design loading capacity to achieve optimum gas-solids interaction. Design load models in literature have under-estimated or over-estimated the solid distribution within the dryer (Lee, 2008), which greatly affects the quantity of solids undergoing drying.

Solid transport in a rotary dryer is characterised through the interpretation of the solid residence time distribution (RTD). This solid residence time is referred to as the time required for the solid to travel the length of the dryer and it can be determined through experiment or modelling. The experimental approach involves introducing a tracer at the inlet of the dryer and the tracer concentration is monitored at the outlet as a function of time.

Modelling approaches of unflighted and flighted rotary dryers are different. To the best of the author's knowledge, there is no literature that combines the modelling of both unflighted and flighted sections within a dryer. Previous studies have modelled the solid transport in an unflighted rotary dryer using empirical correlations (Sullivan et al., 1927; Perron & Bui, 1990) and plug flow models (Sai et al.; 1990; Ortiz et al., 2003; Ortiz et al., 2005). There have also been substantial studies on the modelling of the flighted rotary dryer, which includes empirical correlations, mechanistic models and compartment models. The empirical correlation and mechanistic models do not account for the loading capacity and the effect of the flight configuration and solid properties. The compartment modelling approaches were developed to provide a more predictive means to estimate the residence time distribution. In recent examples of compartment modelling by Sheehan et al. (2005) and Britton et al. (2006), they considered the dryer geometry, solid flow properties and also the drag effect of the air stream on the solids. The model parameters were estimated based on physical descriptions (described in Britton et al. (2006)) and on geometric modelling of flight unloading (described in Britton et al. (2006) and validated experimentally in Lee and Sheehan (2010)). The accurate estimation of the design load and loading state of the dryer directly influenced determination of model parameters and the mass distribution between the compartments representing the airborne and flight-borne solids.

Although there are several published works that deal with steady-state modelling of a rotary dryer (Cao & Langrish, 2000; Shahhosseni et al., 2001; Iguaz et al., 2003; among others), there are few examples of dynamic models of rotary dryers (Duchesne et al., 1997). Models are used to predict the moisture content and temperature profiles of both phases (gas and solids) inside the dryer. These models differ in describing the drying rate, the effect of operating conditions, the solid residence time and the heat transfer. Drying occurs at different scales and it is important

that the different scale processes are taken into consideration. A multiscale model is necessary to address the complex nature of gas-solids flow in the dryer.

1.2 Objectives and aim

The aim of this study is to develop a dynamic multiscale model, which will enable and improve design and control of rotary dryers. Important information such as residence times, process input and output parameters, and energy usage can be gained from industrial dryer experimentation. However, laboratory-based and computer-based studies are required to understand and model the internal particle and flight scale phenomena that occurs. The objectives of the study are as follows:

- To develop a dynamic multiscale model to describe the MMG rotary dryer.
- To validate and optimise different scales model based on the results of industrial and laboratory experimentation.
- To utilise the overall model to determine design and control strategies to optimise dryer performance.

1.3 Structure of thesis

The thesis is divided into eight chapters:

- Chapter 1 provides the background, the aims and objective of the research.
- Chapter 2 presents the literature review on hold-up and residence time of the dryer. Previous studies on modelling of unflighted and flighted rotary dryers are also discussed.
- Chapter 3 presents the methodologies and results of the industrial testing and characterisation, which include residence time distribution trials, shell temperature measurement, PI data collection and properties of zinc concentrates.

- Chapter 4 focuses on the estimation of design loading capacity in a flighted rotary dryer. The chapter covers the flight loading experiments and detailed image analysis techniques used to analyse the photographs taken during the experiments. The effect of rotational speed and moisture content on design loading is also investigated. A combination of image analysis calculations and Computational Fluid Dynamics (CFD) simulation to estimate the masses of airborne and flight-borne solid is discussed. The content of this chapter has been accepted for publication in the following journals:
    - **Ajayi**, O.O., Sheehan, M.E., 2012. Design loading of free and cohesive solids in flighted rotary dryer. *Chemical Engineering Science Journal (in press).*
    - **Ajayi**, O.O., Sheehan, M.E., 2011. Application of image analysis to determine design loading in flighted rotary*, Powder Technology Journal (in press).*
- Chapter 5 covers the development and validation of a solid transport model for the MMG industrial rotary dryer. Parameter estimation techniques and results are discussed. Verification of the model structure and parameters is also examined. The content of this chapter was published in the following conference proceeding:
    - Sheehan, M.E., **Ajayi**, O.O., Lee, A., 2008. Modelling solid transport of industrial flighted rotary dryer. In, *Proceedings of 18th European Symposium Computer Aided Process Engineering (ESCAPE),* 2008*,* June 1–4, Lyon, France.
- Chapter 6 presents the development and incorporation of the energy equations into the validated solid transport compartment model. Parameter estimation technique and model verification are discussed.

- Chapter 7 discusses the approach to identify manipulated variables for unscaled and scaled conditions within the dryer. Engineering design options to reduce fuel consumption were examined.
- Chapter 8 presents the conclusion of the research.

CHAPTER 2

2. LITERATURE REVIEW

The literature review covers previous studies on holdup and mean residence time of rotary dryers. Various models used to estimate the design loading condition in rotary dryers will be discussed. The review will also outline the modelling approaches of both flighted and unflighted rotary dryers and highlight their deficiencies.

2.1 Holdup

There are two key property characteristics in dryer performance: residence time (RT) and hold-up. The relationship between these key properties is expressed in Equation 2.1.

$$\tau = \frac{H}{F} \qquad \textbf{2.1}$$

where *H, F* and τ are the hold-up, feed rate and residence time respectively.

Holdup is defined as the amount of solids within the dryer. Holdup is further characterised into airborne solids, and flight and drum borne solids, which are the solids within the flights and the base of the drum. The degree of flight loading is affected by the operating conditions, physical properties of the solid and the geometrical configuration of the dryer (Kelly, 1992). The importance of flight loading cannot be underestimated because the proportion of airborne solids to flight-borne solids dictates the extent of gas-solids interaction. The distribution of solids also affects the residence time because of the difference in the rate of axial advance of airborne solids and flight-borne solids. In many of the flighted rotary dryer (FRD) models in the literature, this proportion has been approximated to between 10 and 15% of the total holdup and is typically considered invariant to loading state.

2.1.1 Design load

In the rotary dryer, there are three potential degrees of loading namely under-loaded, design loaded and overloaded. A dryer is defined as operating in an under-loaded condition when the flights are not full to their capacity and unloading of the flight occurs after the 9 o'clock position as shown in Figure 2.1a. A design loaded dryer is one in which the flights are at their maximum capacity and the unloading of the flight occurs precisely at the 9 o'clock position as indicated in Figure 2.1b. The design load condition is commonly assumed to represent the point of operation where there is maximum interaction between the drying gas and the airborne solids. A dryer is classified as overloaded when there are more solids present than required to fill the flights, as illustrated in Figure 2.1c. In this situation, there is unloading of flights before the 9 o'clock position and the excess solid rolls in the base of the dryer.

The fundamental assumption in flighted rotary drying is that the kilning or rolling solids do not participate in drying to the extent that airborne solids do. As a result, their thermal and physical interactions with the gas phase are often ignored in models. It can be reasonably assumed that the operation of a dryer at under-loaded or overloaded conditions results into poor efficiency of the dryer. Consequently, the design load of a dryer is an important parameter that should be determined for optimisation, design and modelling of FRD.

Figure 2.1a: Under-loaded dryer *(Arrow indicates the 9 o'clock position and demonstrates that solids are discharged late in the rotation)*

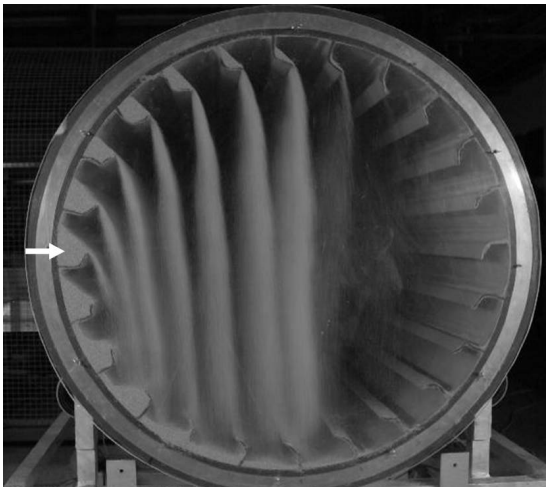

Figure 2.1b: **Intermediate loading assumed close to design load** *(Arrow shows there is discharge at precisely the 9 o'clock position)*

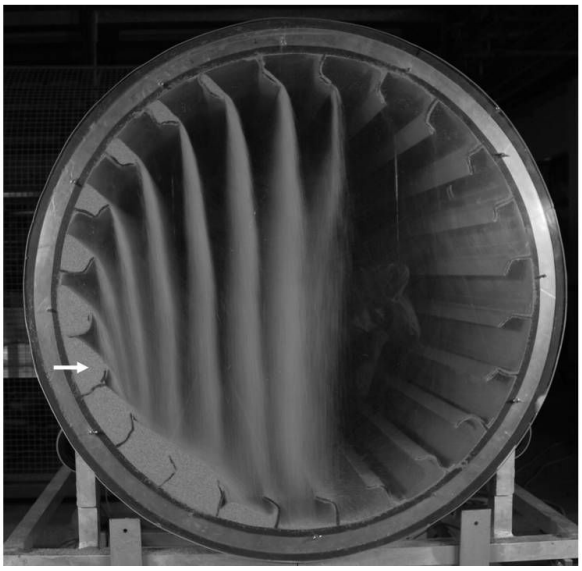

Figure 2.1c: Overloaded dryer load *(Arrow shows there is discharge before 9 o'clock position)*

Previous studies have used geometric models of flight cross sections to estimate the design load (Porter, 1963; Kelly & O'Donnell, 1977; Baker, 1988; Sherritt et al. 1993). Wang et al. (1995) developed a geometric model to determine the amount of solids contained within the two-section flight. Their geometric model was a function of flight angular position, drum rotational speed and solid properties (dynamic angle and bulk density). Revol et al. (2001) also investigated the effect of flight configuration on the volume of solids within the flights using image analysis. The authors observed that the accurate estimation of the dynamic angle of repose was a function of the flight geometry. Lee and Sheehan (2010) developed and validated a geometric unloading model. The model described the amount of solid within the flight at different angular position. Their model assumptions are: solids are free-flowing and there is a continuous unloading process. However, photographic analysis showed that the unloading process was discontinuous and the dynamic angle of repose was not constant throughout the unloading process due to an avalanching discharge pattern of solids. Despite these experimental observations, the model

results and experimental data were comparable, which indicated the model assumptions were appropriate for the unloading process.

The most commonly used design load model is Porter's assumption (Porter, 1963), described in Equation 2.2 (Sheehan et al., 2005). Porter's assumption is based on the concept that at full flight at design loading, there are sufficient solids to fill half of the total flights. In this case, a full flight is defined as the solids in the 9 o'clock flight. Kelly and O'Donnell's (1977) model presented in Equation 2.3 used a different type of flight to that of Porter (equal angular distribution flight). In all of these models, the total holdup was determined, which includes flight and airborne solids. Matchett and Sheikh (1990) invalidated Porter's assumption based on the photographic evidence that the holdup within a flight is a function of flight geometry. Their photographic evidence showed that with different flight configurations, maximum flight loading was not consistent. This indicates a lack of universality for Equation 2.2, despite its widespread use.

$$M_{Tot} = M_{FUF} \times \frac{N_f}{2} \qquad \textbf{2.2}$$

$$M_{Tot} = M_{FUF} \times \left(\frac{N_f + 1}{2}\right) \qquad \textbf{2.3}$$

M_{FUF} is the mass at the 9 o'clock position, M_{Tot} is the total hold-up of the dryer at design point including both airborne (active) solids and flight-borne (passive borne) solids and N_f is the total number of flights.

Baker (1988) proposed a model to determine only the flight-borne solids (Equation 2.4). The model was based on the assumption that the holdups of flights in the lower half of the drum are

the same as the holdups of the flights in the upper half of the drum. Baker's model involves calculating the amount of the solids in each flight above and including the 9 o'clock flight.

$$M_{design} = \left(2 \times \sum_{f}^{n} M_i \right) - M_{FUF} \qquad \textbf{2.4}$$

M_{design} is the design load based on the passive phase (TP) only and excludes airborne solids. M_i is the mass in each flight (i) with subscripts f and n referring to the 9 o'clock flight and last discharging flight respectively.

In an alternative study, Sherritt et al. (1993) developed a geometrically driven integral model of flight discharge. Their model was capable of predicting drum and more specifically airborne holdup, for under, design and overloaded dryers. Their model was predicated on knowing the initial discharge location for the first unloading flight and assumed a mirror image, with respect to loading, in the upper half and lower half flights, similar to Baker's (1988) model assumptions. However, their model was not generic with respect to flight geometry and a comparative study by Hatzilyberis and Androutsopoulos (1999) showed lower levels of predictive ability for rotating drums fitted with equal angular distribution (EAD) flights.

2.2 Residence time

Solid transport within the dryer is typically characterised through determination of the solid residence time which is the time required for an average solid particle to travel the length of the dryer. However, when the particles move through the dryer during normal operation, they do not all take the same path to exit. Dispersion is typical in an industrial flighted rotary dryer. In order to characterise the solid transport and dispersion within the dryer, residence time distributions are determined (Renaud et al., 2000; Sheehan et al., 2005). Studies have determined the solid

residence time using an experimental approach (Perron & Bui, 1990; Duchesne et al., 1996; Renaud et al., 2000; Renaud et al., 2001; Sheehan et al., 2005).

Studies have examined various parameters that affect the mean residence time of a rotary dryer (Renaud et al., 2001; Yang et al., 2003; Lisboa et al., 2007). Renaud et al. (2001) analysed the effect of a solid's feed moisture content on the mean residence time. Solid moisture content significantly affected the mean residence time and the shape of the residence time distribution (RTD). The high moisture content, the solids (in this case: sand used in cement make-up) resulted in a longer mean residence time and also altered the shape of RTD.

Yang et al. (2003) developed a dynamic experiment based on a step change of feed throughput to determine solid holdup and mean residence time in a pilot scale rotary dryer. It was observed that the rotational speed had a significant effect on the discharge solids flow rate and the average residence time. Furthermore, with increase in the feed rate throughput, there was an increase in the mean residence time. The authors noticed a linear relationship between the slope of the dryer and the mean residence time. Many of these observations confirm the general form of empirical residence time equations such as Friedman and Marshall (1949a). The authors concluded that the mean residence time is significantly affected by the changes in the flow properties of the solids which depend on moisture content. The most important of these properties is the dynamic angle of repose. This conclusion agrees with earlier findings of Renaud et al. (2001).

Matchett and Baker (1987) and Kelly (1992) concluded that flight design was a contributing factor in the accurate estimation of the mean residence time. Lisboa et al. (2007) investigated the performance of the dryer in relation to the number of flights and concluded that both residence

time and drying rate increased with number of flights. The study further established that increasing rotational speed resulted in low residence time.

2.3 Modelling approaches

Proper modelling of solid transport is important because residence time distribution and holdup significantly influence the drying process and prediction of many important process variables such as outlet moisture content and temperature. Modelling approaches for flighted dryers and unflighted dryers are different. In addition, to the best of the author's knowledge, there is no study in literature that combines the modelling of both unflighted and flighted sections within the dryer.

Models of flighted rotary dryers in the literature include empirical correlations, semi-empirical correlations, mechanistic, and compartment modelling. A comprehensive review of empirical correlations, semi-empirical correlations and mechanistic models can be found in Lee (2008). Empirical correlations and mechanistic models are simplified approaches and do not account for the effect of flight configuration and solids properties. In light of these shortcomings, the compartment modelling approach was developed. This approach utilises series-parallel formulation of well-mixed tanks commonly used in reaction engineering (Levenspiel, 1999). A recent example of a geometrically driven compartment modelling approach by Sheehan et al. (2005) and Britton et al. (2006) tested the pseudo-physical compartment model and provided a restructure for solid flow paths, which gave the actual representation of the dynamics in the rotary dryer. The model considered the dryer geometry, flight configuration, solid flow properties and also the drag effect of the air stream on the solids. It can be concluded that an appropriate solid transport model for a rotary dryer should have the following characteristics:

ability to consider the effect of flight configuration, proper distribution of solid in the dryer, solid properties should not be ignored, and ability to account for different loading state.

2.3.1 Unflighted dryer

Previous studies in unflighted dryer modelling have assumed that solids move in plug flow with (Danckwerts, 1953; Fan & Ahn, 1961, Mu & Perlmutter, 1980; Sai et al., 1990) or without (Ortiz et al., 2003; Ortiz et al., 2005) axial mixing. However, experimental RTD studies have shown that axial dispersion occurs both in unflighted and flighted dryers (Sai et al., 1990; Sheehan, 1993). In some unflighted dryer studies, empirical correlations were developed from RTD experiments (Sullivan et al., 1927; Perron & Bui, 1990). Fan and Ahn (1961) used the classic diffusion model stated in Equation 2.5 (Levenspiel, 1999) to simulate the dispersion and residence time distribution of solids in a rotating cylinder. It should be noted that Equation 2.5 only holds for no net solid flow system

$$\frac{\partial(C)}{\partial t} = \wp \frac{\partial^2(C)}{\partial z^2} \qquad \textbf{2.5}$$

where C, t, $\wp$ and z are concentration, time, dispersion coefficient and length respectively.

Sai et al. (1990) also proposed the use of an axial dispersion model with an appropriate Peclet (*Pe)* number estimated via experiments. In their study, the effects of operating conditions such as solid feed rate, rotational speed and dam height on the mean residence time were investigated. In another study, Kohav et al. (1995) used stochastic algorithms to determine the effect of segregated rolling or slumping distance on the axial dispersion in rolling and slumping beds.

2.3.2 Flighted rotary dryers

Matchett and Baker's (1987) mechanistic model was the definition work for differentiating the solids within the drum into two phases, namely: the airborne solids and flight and drum-borne solids. The airborne solids contain the particles falling from the flight acted upon by both gravity and drag due to airflow, i.e. the cascading flow. The flight and drum-borne solids are solids that remain in the flights and the drum base.

Compartment modelling approaches were developed as they provide a convenient structure to match the typical residence time distribution curves found in flighted rotary dryers. Duchesne et al. (1996) proposed a modified Cholette-Cloutier (1959) model, which accounts for the presence of dead zones. Sheehan et al. (2005) developed a pseudo-physical compartment model. Their model treated the solids as active and passive phases. The active phase consists of solid particles in contact with incoming drying gas while the passive phase does not participate in the drying process (Figure 2.2). Figure 2.3 shows their model structure, which describes the flow path into the active and passive phase.

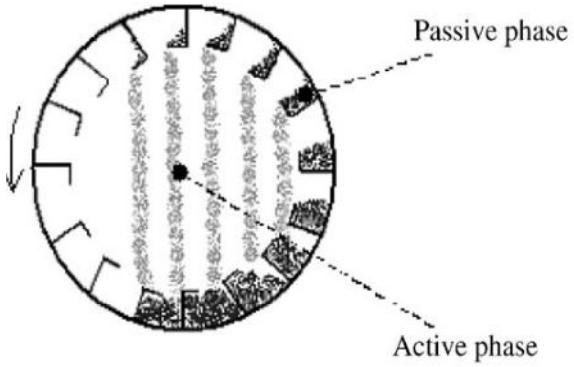

Figure 2.2: Active and passive phase (Sheehan et al., 2005)

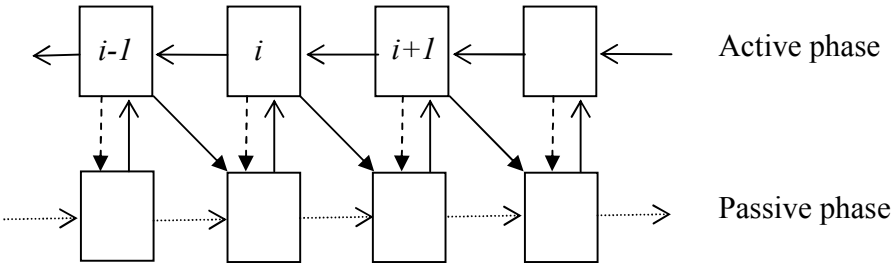

Figure 2.3: Model structure

There have been substantial rotary dryer models in the literature which have been used to predict the moisture content and temperature profile inside a dryer (Douglas et al., 1993; Cao & Langrish, 2000; Shahhosseni et al., 2001; Iguaz et al., 2003). These models differ in the way the drying rate, heat transfer and the residence time are described.

Douglas et al. (1993) developed a model based on heat and mass balance to illustrate the effect of changes in inlet conditions on the outlet conditions of sugar dryers. Both the residence time and volumetric heat coefficient were calculated using Friedman and Marshall (1949a) and Friedman and Marshall (1949b) empirical correlations respectively. The effects of flight geometry and solid distribution were not considered.

Wang et al. (1993) developed a generalised distributed parameter model for a sugar dryer. The heat transfer coefficients were calculated using three different correlations for comparison. These correlations include Freidman-Marshall (1949), Ranz-Marshall (1952), and Hironsue (1989). The gas phase was modelled as a plug flow system and the residence time was calculated via the Friedman and Marshall (1949) model. The authors concluded that a dynamic rotary dryer model should be developed to account for effect of the flight geometry and of solid distribution within the dryer.

Duchesne et al. (1997) developed a dynamic simulator of a mineral concentrate rotary dryer, which consisted of a furnace model, a solid transport model and a gas model. Their modelling approach was different from previous studies (Douglas et al., 1993; Wang et al., 1993; Perez-Correa et al., 1998) in that solid transport was modelled using the compartment model approach. The predicted and measured values of the outlet variables such as moisture and gas temperature were comparable.

Cao and Langrish (2000) also developed an overall system model for a counter-current, cascading dryer. The model used heat and mass balances around the dryer, together with the Matchett and Baker (1988) mechanistic residence time model. The heat-transfer correlation of Ranz and Marshall (1952) was used. Limitations to the Matchett and Baker (1987) mechanistic model included the requirement for an empirical holdup number determined through dryer specific experiments.

To further achieve a suitable model for rotary dryer, Shahhosseni et al. (2001) proposed an adaptive modelling strategy that combines on-line model identification with well-known conservation laws. The drying rates, the heat and mass transfer coefficients were empirically fitted based on online measured data instead of the conventional approach of using empirical correlations. The solid residence time was calculated using the modified Friedman and Marshall (1949a) correlation previously developed by the authors (Shahhosseni et al., 2000).

Didriksen (2002) presented a dynamic model for a rotary dryer, which comprises of heat and mass balances together with Kelly and O'Donnell (1968) total hold up time empirical correlation. The model showed good predictive capabilities and was used in model-based predictive controller (MPC) configuration. In another study, a model for the dehydration of

vegetable by-products in a rotary dryer was proposed (Iguaz et al., 2003). The model incorporated heat and mass balances around the dryer, the residence time model of Friedman and Marshall (1949), and the heat transfer correlation of Myklestad (1963).

Ortiz et al. (2005) proposed a dynamic simulation system for a pilot scale rotary kiln used in manufacturing activated carbon. Perry and Green's (1984) empirical model was used to predict the residence time. Their study assumed there was neither solid nor gas axial mixing and both phases were modelled as plug flow systems. Raffak et al. (2008) presented also a dynamic model for a phosphate rotary dryer. The model was based on the equations of heat and mass transfer between the gas and solids phases. The mean residence time was estimated using Alvarez and Shene's (1994) empirical model. The predicted moisture and temperature for both phases well-matched the experimental data.

Despite numerous models in literature, there remain deficiencies in the modelling of the solid transport, which give rise to doubt regarding their abilities to accurately predict the moisture and temperature profiles for both phases. Predominant deficiencies include that the loading state not taking into consideration and the mean residence times were often estimated using empirical correlations, which are invariant to solids moisture content and flight geometry, which are known to have a significant effect on the mean residence time (Renaud et al., 2000; Renaud et al., 2001; Yang et al., 2003) and residence time distribution. Thus, it is important to develop a dynamic model that will address all of these limitations.

2.4 Summary

The literature review highlighted the need to develop a dynamic model for a rotary dryer because most of the published works deal with steady-state modelling of a rotary dryer. In most of these

models, the modelling of the solid transport was based on either empirical correlations or mechanistic models. These modelling approaches do not account for the effect of loading state, flight geometry and solid properties.

To address these shortcomings, the compartment modelling approach was developed. The approach consists of series-parallel formulation of well-mixed tanks whereby the compartment numbers and model transport coefficients were derived through geometric modelling, based on dryer geometry and solids physical properties. The compartment modelling approach will be chosen for this work. In the compartment modelling approach, the loading state, residence time and solid feed rate are strongly linked. The accurate estimation of the design load and loading state of the dryer is an important characteristic of compartment modelling approach. Most design load models have not been validated experimentally.

The studied dryer has both unflighted and flighted sections. Studies have shown that the modelling approaches of the solid transport within unflighted and flighted rotary dryers are different. Therefore, the axially-dispersed plug model characterised by a kilning velocity and dispersion coefficient will be used in this study.

CHAPTER THREE

3. INDUSTRIAL SCALE TESTING

This chapter describes the laboratory and industrial experiments that provide experimental data for model validation. The geometrical configuration of the MMG co-current industrial rotary dryer was verified and used as input data for the geometric modelling. The characterisation of zinc concentrate properties (dynamic angle of repose, bulk density and particle size) was discussed. The fitted equation for moisture content profile was used in initial solid transport model fitting (Chapter 6) to account for axial variation in the dynamic angle of repose. The experimental moisture content profile was used to validate the mass and energy balances presented in Chapter 7. Heat transfer coefficient and contact surface area calculations in Chapter 7 were dependent on the assumed particle size profile.

The chapter also outlines the industrial experiments which include residence time distributions (RTD), shell temperature measurement, spatial sampling of the solid along the length of dryer, moisture content analysis and Process Information (PI) data collection. Internal temperature profiles across the dryer were not determined because of the hazards involved in carrying out the experiments within an industrial setting. The fuel and air properties were characterised through the system description. The RTD curves generated in this chapter were used in the validation of the solid transport model (Chapter 6) and in the mass and energy balance analysis (Chapter 7). The shell temperature measurement was used to estimate the heat loss profile of the dryer presented in Chapter 7. The error in PI output data was not determined.

3.1 Process description

Figure 3.1 shows the schematic diagram of the drying process. The drying process consists of the combustion chamber and the rotary dryer. The industrial rotary dryer is used to dry zinc and lead concentrate. The concentrate is fed into the dryer via a screw feeder. The typical solid inlet moisture content varies between 16% and 18% and the outlet moisture content ranges between 12% and 12.5%. The hot gas enters the dryer at 500 ^{o}C via the combustion chamber. A distributed control system (DCS) based on feed forward control is used to control the dryer. The control algorithm of the DCS calculates the amount of water to be removed using the inlet and outlet target moisture content, solid flow rate, air flow into the combustion chamber through the fan opening, and determines the quantity of fuel oil required in the combustion chamber.

The Process Information (PI) is collected using sensors and this information is referred to as PI data. Table 3.1 presents the operating variables measured via sensors and stored as PI data. The shell temperature measurements were manually collected during RTD experiments. The experiments were carried out at as steady state as possible. The averaged PI data and statistical deviations for different experiments are outlined in subsequent sections.

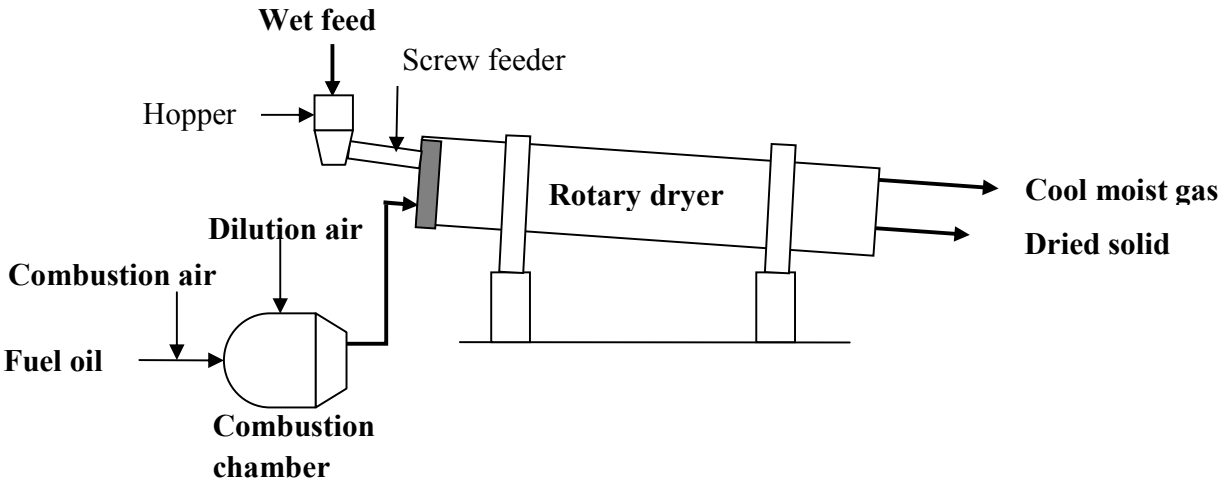

Figure 3.1: Schematic representation of the MMG combustion chamber and industrial rotary dryer

Table 3.1: List of measurements obtained via sensors

Process variable	Units
Gas inlet temperature	^{o}C
Gas outlet temperature	^{o}C
Solid feed rate	Tonnes/hour
Solid outlet temperature	^{o}C
Dilution air fan opening	%
Combustion air fan opening	%

3.2 Geometrical Configuration of the industrial dryer

The geometrical configuration of the dryer was verified during the scheduled shutdown for maintenance and internal cleaning of the dryer. The dryer is divided into five sections (Figure

3.2). Sections A and E are unflighted. Section A is fitted with chains to reduce the size of the clumped solid entering the dryer. The granulation of the zinc concentrate into spherical particles of 6–7 millimetres in size occurs at Section E. Sections B, C and D are fitted with internal flights with different configurations in each section. Flight geometry measurements are presented in Table 3.2. The dryer is 22.2 metres long with an internal diameter of 3.9 metres and inclined towards the inlet at 4 degrees. Typical rotational speed is 3 rpm.

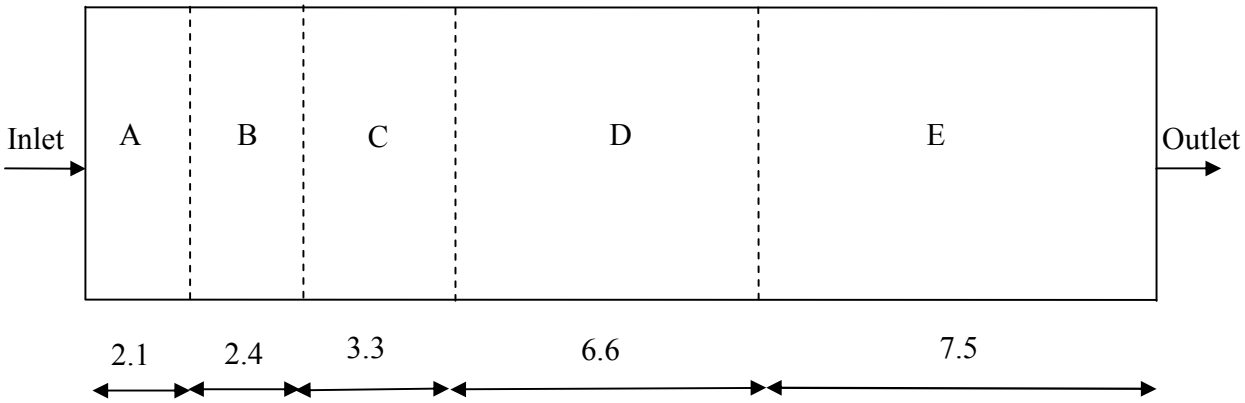

Figure 3.2: Geometrical details of the dryer ***(All length dimensions are in metres)***

Table 3.2: Geometrical configuration of the drum

Section	Length of section (m)	Flight base (m)	Flight tip (m)	Flight tip angle (^{o})	Flight base angle (^{o})	Number of flights
A	2.1	-	-	-	-	
B	2.4	0.120	0.210	135	90	30
C	3.3	0.130	0.220	150	90	30
D	6.6	0.120	0.210	130	90	30
E	7.5	-	-	-		

3.3 Characterisation of the combustion chamber

The gas flow rate into the MMG industrial rotary dryer is not directly measured. It is important to characterise the combustion chamber so as to determine its outlet gas flow rate. Air enters the combustion chamber and is heated by burning the fuel oil. The hot gas leaves the combustion chamber at an approximate temperature of 500 ^{o}C. The block flow diagram of the combustion chamber and its variables is outlined in Appendix A.

3.4 Physical properties of zinc concentrates

The study assumed the properties of zinc concentrate determined at a particular internal condition of the dryer remain constant for all test runs. Samples of zinc concentrate were taken along the length of the dryer prior to a shutdown and internal cleaning of the dryer. The dryer was full of hot zinc concentrate during this spatial sampling. Samples were taken every one metre (23 samples in total).

3.4.1 Moisture content profile

The moisture content for each sample was determined using the on-site MMG oven. A known mass of zinc sample was placed in the preheated oven at 105 ^{o}C temperature. The sample was measured after three hours and reheated for another one hour to ensure there was no moisture content within the sample. The evaporated moisture content was calculated. Figure 3.3 shows the moisture content profile along the length of the dryer. The data in Figure 3.3 was fitted using a rational polynomial function to derive Equation 3.1, relating the moisture content to the dryer length.

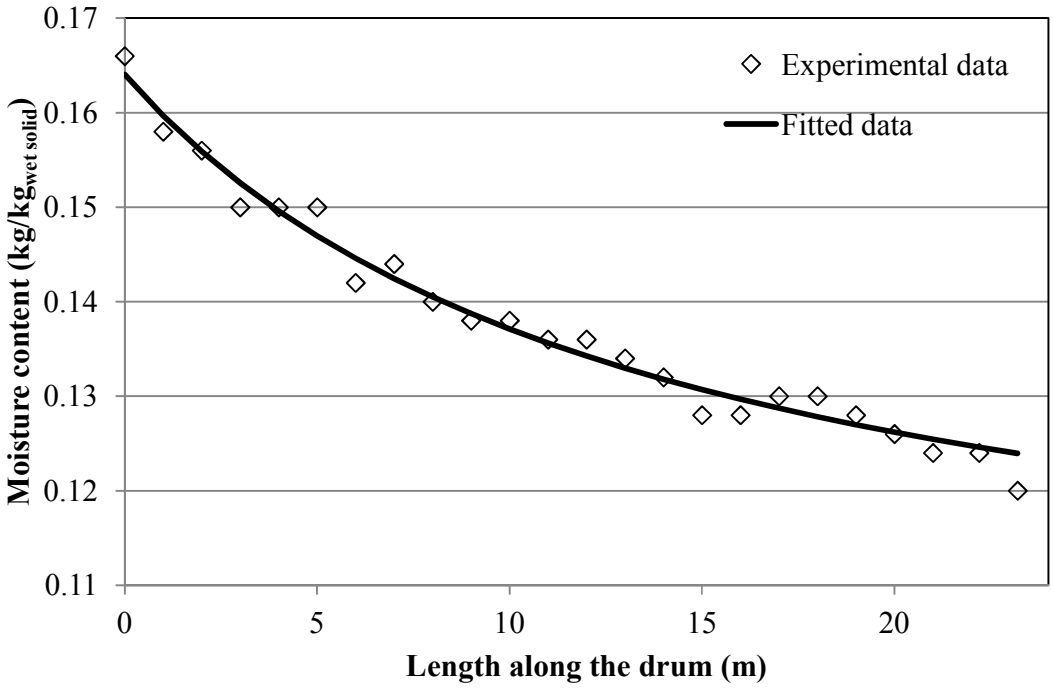

Figure 3.3: Moisture content profile along the length of the dryer

$$x_w = \frac{0.1006L + 2.218}{L + 13.51} \qquad \textbf{3.1}$$

where x_w and L are the solid moisture content (kg/kg$_{wet\ solid}$) and axial position within the dryer (m) respectively.

3.4.2 Dynamic angle of repose

The dynamic angle of repose describes the flowability of solid within the flights. Experiments were carried out in a pilot scale dryer by placing a subset of sampled zinc concentrate solid in a container. The filled container was affixed to the front-end Perspex of the drum (see Figure 3.4). Photographs of the front end of the rotating drum were taken and the dynamic angle of repose was measured using ImageJ software.

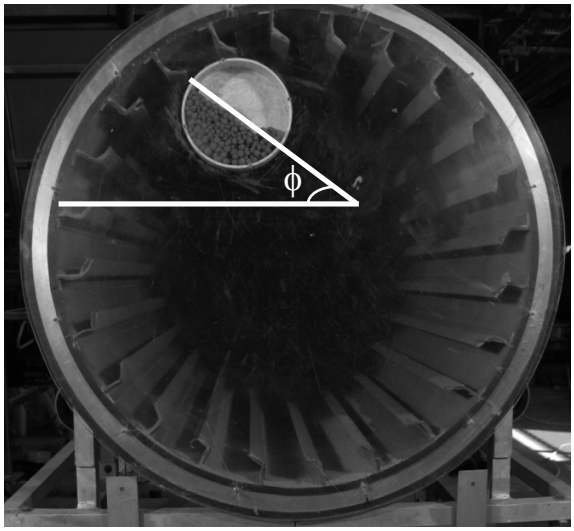

Figure 3.4: Experimental apparatus to measure dynamic angle of repose

The dynamic angle of repose as a function of the corresponding moisture content of the solid is shown in Table 3.3 and plotted in Figure 3.5. The fitted linear equation was used in all further modelling to relate moisture content to dynamic angle of repose (Equation 3.2). The standard deviation of the angle of repose reduces as the moisture content of the solid reduces. This is a common observation with a decrease in solid cohesion (Lee & Sheehan, 2010).

Table 3.3: Dynamic angle of repose

Position along the length of the drum(m)	Moisture content	Dynamic angle of repose(^{o})	Standard deviation(^{o})
0	0.166	60.6	4.7
3	0.150	56.6	4.4
6	0.142	54.2	4.3
9	0.138	48.8	4.0
14	0.132	46.8	2.6
15	0.128	45.6	3.3
21	0.124	43.4	2.4
23	0.120	43.3	0.9

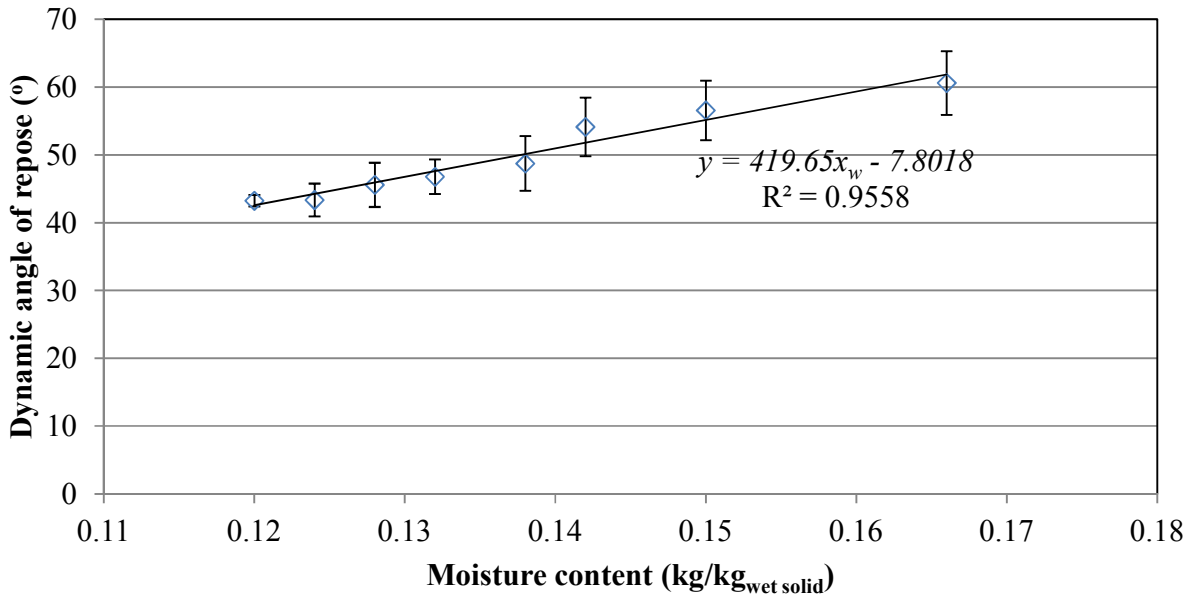

Figure 3.5: Dynamic angle of repose versus moisture content

$$\emptyset = 419.6x_w - 7.801 \qquad \textbf{3.2}$$

where ϕ and x_w are dynamic angle of repose (degrees) and the corresponding solid moisture content ($kg/kg_{wet\ solid}$) respectively.

3.4.3 Particle size

The particle size distribution of the zinc concentrate at different sections of the dryer was carried out using dry sieving. Sieves used were 38 mm, 19 mm, 9.5 mm, 4.75 mm, 2.36 mm, 1.18 mm, and 600 µm. The mass of solid in each sieve was measured. Thirteen samples of zinc concentrate at different sections of the dryer were sieved. Samples n = 0 to 23 are zinc concentrates samples taken at every one meter of the dryer. The mass percentage passing is plotted in Figure 3.6.

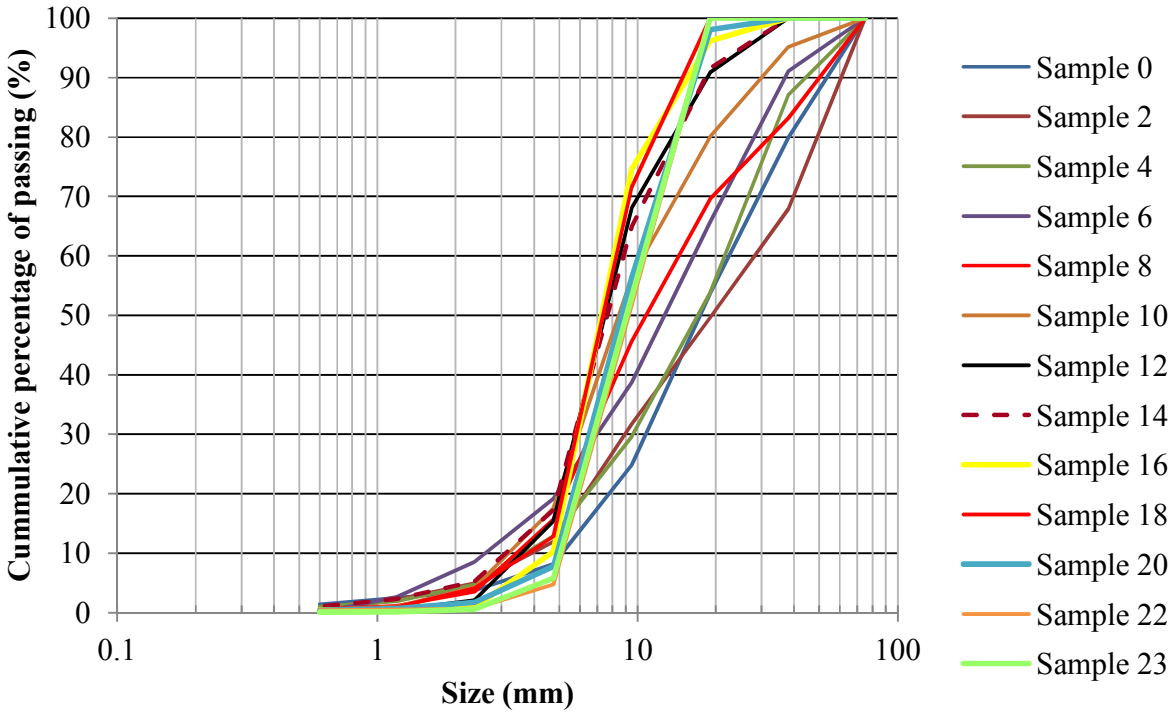

Figure 3.6: Mass percentage of the passing (*Samples n = 0 to 23 are zinc concentrates samples that were taken every one meter along the length of the dryer)*

3.4.4 Bulk density

The consolidated bulk densities of the inlet and outlet solids were determined in the laboratory (Table 3.4). The process involved weighing an empty 200 ml volumetric cylinder and filling it with zinc concentrate. The cylinder was tapped until no more consolidation occurred and the sample was measured. The consolidated bulk density was calculated using Equation 3.3. Density measurements were repeated five times to determine averages and standard deviations. Consolidated bulk density was assumed to change linearly with respect to moisture content (Equation 3.4).

$$\rho_b = \frac{Mass}{Volume} \qquad \textbf{3.3}$$

Table 3.4: Consolidated bulk densities of the solid

Solid	Consolidated bulk density (kg/m^3)	Standard deviation (kg/m^3)
Inlet	1530	12
Outlet	1660	31

$$\rho_b = 2043.8 - 3095.2x_w \qquad \textbf{3.4}$$

where ρ_b and x_w are bulk density (kg/m^3) and moisture content (kg/kg$_{\text{wet solid}}$) respectively.

3.5 Residence Time Distribution (RTD) Tests

3.5.1 Experimental studies

The residence time distributions (RTD) are usually obtained by tracer tests. In a tracer test, an inert chemical (tracer) is injected at the inlet of the dryer while the concentration of the tracer at the outlet as a function of time is monitored. There are two common ways to inject the tracer, namely: pulse input and step change. The pulse input involves rapid injection of a known amount of tracer and the outlet concentration is measured as a function of time.

The accurate determination of RTD largely depends on proper selection and introduction of the tracer. Sheehan et al. (2002) presented residence time distributions for an industrial sugar dryer. Three different tracer compounds were used in their experiment and a pulse tracer testing lithium chloride solution produced the best results. Other studies have also used lithium chloride (LiCl) as a tracer in both pilot scale and industrial rotary dryers (Renaud et al, 2000; Britton et al., 2006; Owens, 2006). Important characteristics of a tracer are: analysis of the tracer should be convenient, sensitive and reproducible, inexpensive, easy to handle and unable to be absorbed on or react with the surface of the dryer.

The first moment of the RTD (mean residence time) and residence time distribution function were calculated using Equations 3.5 and 3.6. As shown in Equations 3.5 and 3.6, the time limit tends to infinity but the RTD experiments were truncated at finite time of 1.5 hours. After this length of time, the Lithium concentrations were below background and because of their low values were prone to high relative error. Curl and McMillan (1966) developed error models to quantify the errors when estimating RTD moments at finite time. Their study found there was significant error between the values estimated at infinity time and finite time. However, the primary focus of this study was not specifically to determine mean residence time and other

moments of the distributions. The objective of the RTD study is to provide sufficient data for fitting and validating the developed model in Chapters 5 and 6, in which case the error in neglecting the tail was considered not significant.

$$\tau = \int_0^\infty tE(t)dt \qquad \textbf{3.5}$$

where

$$E(t) = \frac{C(t)}{\int_o^\infty C(t)dt} \qquad \textbf{3.6}$$

3.5.2 RTD test methodology

Previous characterization of MMG rotary dryer showed there was poor tracer recovery when standard solution of lithium chloride was injected into the inlet of the dryer (Owen, 2006). As a result, two different approaches to introducing the tracer into the inlet of the dryer were investigated: preparation of a standard solution of lithium chloride (LiCl), and pre-mixing the LiCl powder with a certain amount of zinc concentrate.

The lithium concentrations in the samples taken at the outlet were determined using Inductively Coupled Plasma Mass Spectrometry (ICP-MS) available at the JCU Advanced Analytical Centre (AAC). The background lithium concentration in the sample was determined to ensure its concentration was low and would not interfere with the tracer analysis.

Each RTD test was carried out when the dryer was as close as possible to steady state. It was difficult to have a complete steady state in an industrial setting considering all factors that affect the steady operation of the plant. For example, the dryer feed rate is affected by the discharge from the five batch filter presses used in the operation. Standard deviations from PI data were used to quantify the variation. The Process Information (PI) data for the two approaches are

presented in Tables 3.5 and 3.6. The experimental procedures for the two approaches are described below.

3.5.2.1 Tracer standard solution approach (Test 1)

1.25 kg of LiCl powder (99.0% purity, Chem-supply) was dissolved in four litres volume of de-ionised water (51.15g lithium /L). The prepared tracer solution was injected into the dryer directly, over a period of one minute. Solids are fed directly from the hopper to the dryer via a screw feeder. The time taken for the solid to reach the inlet of the dryer from the hopper was approximately 20 seconds. Samples from the outlet were taken at intervals of 30 seconds for the first 30 minutes and every 60 seconds for the remaining 1.5 hours.

3.5.2.2 Solid tracer pre-mixed with inlet solid (Test 2)

1.25 kg of LiCl powder (99.0% purity, Chem-supply) was mixed thoroughly with 8 kg of inlet feed and the prepared material was placed onto the inlet conveyor at the mouth of the hopper. Samples from the outlet were taken at intervals of 30 seconds for the first 30 minutes and every 60 seconds for the remaining 1.5 hours.

Table 3.5: Operating conditions for Test 1

PI Description	Average value	Standard deviation
Solid feed rate	134 ton/hr	18 ton/hr
Gas inlet temperature	517 ^{o}C	41 ^{o}C
Solid inlet moisture content	17.6%	0.79%
Gas outlet temperature	155 ^{o}C	23 ^{o}C
Product outlet temperature	49 ^{o}C	2 ^{o}C
Product moisture content	11.9%	
Rotational speed of the drum	3 rpm	-
Internal condition	Unscaled	

Table 3.6: Operating conditions for Test 2

PI Description	Average value	Standard deviation
Solid feed rate	170 ton/hr	16 ton/hr
Gas inlet temperature	531 ^{o}C	32 ^{o}C
Solid inlet moisture content	18.6%	1.38%
Gas outlet temperature	124 ^{o}C	13 ^{o}C
Product outlet temperature	50 ^{o}C	1 ^{o}C
Product moisture content	12.5%	
Rotational speed of the drum	3 rpm	-
Internal condition	Unscaled	

3.5.3 Data analysis

To quantify the reliability of Residence Time Distribution (RTD) tests, the quantity of tracer recovered from the outlet was determined by mass balance on lithium across the dryer and compared to the quantity of tracer added to the dryer (Equation 3.7). Trapezoidal rule was used to solve Equation 3.7 and that resulted in Equation 3.8.

$$Total\ mass\ of\ tracer = \int_0^{t_f} C.F(out).dt \qquad \textbf{3.7}$$

where C, F and t_f are tracer concentration (kg/kg), solid flow rate ($kg_{wet\ solid}/s$) and final trial time (seconds) respectively

$$\int_0^{t_f} C.Feed\ rate(out).dt = \Delta t\left(\frac{C_0F_0}{2} + C_1F_1 + C_2F_2 + \cdots + \frac{C_tF_t}{2}\right) \qquad \textbf{3.8}$$

Raw data of lithium concentration versus time for the experiments can be found in Appendix B. The solid tracer approach (Test 2) showed improved tracer recovery compared to the standard solution approach (Test 1) and was used for all further RTD trials (Table 3.7). It can be concluded that the tracer solution approach (Test 1) may lead to poor localized mixing and a pulse of sludgy solids, which then increased the probability of zinc concentrates sticking to the walls of the hopper or inlet of the dryer. Premixed concentrate provides more uniform mixing and reduces the loss of tracer compound.

An assumption made in the treatment of the error in the RTD experimental data, was that the variance in lithium concentration throughout the test remained constant. Comparing two data sets for test 2 led to a standard error estimate of 0.15 ppm for each sample across the entire data set, which was within the instrument error (range from 0.01 to 0.5ppm). It is assumed this is the case

for all tests undertaken. The standard error was within the bounds used in later model parameter estimations to fit the model to the RTD data (range of 0.01 to 10ppm).

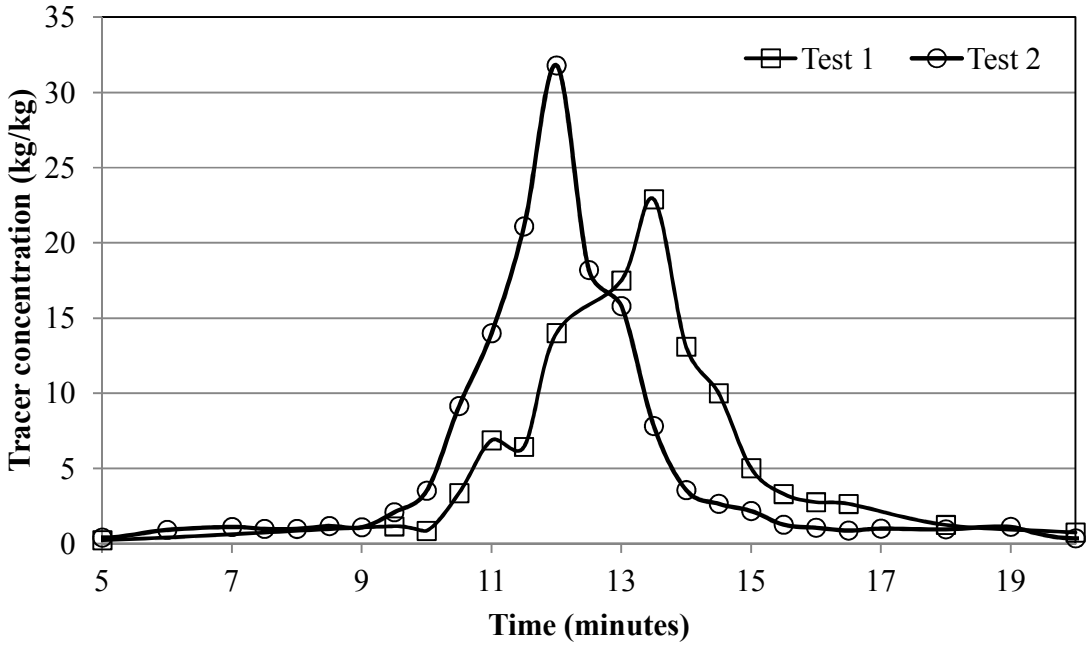

Figure 3.7: Lithium concentration versus time *(for method testing RTD trials)*

Table 3.7: Mass of lithium recovered

Approach	Mass of lithium injected to the dryer (g)	Mass of lithium recovered (g)	Percentage of recovery (%)
Test 1	205.9	127	60
Test 2	205.9	191	91

3.5.4 RTD operational conditions

Using the premixed methodology for tracer injection, a series of RTD experiments were carried out under different operating conditions. To determine the effect of scaling of flights and walls, two tests were conducted: prior to a scheduled shutdown (Test 3) and just after a scheduled shutdown where internal cleaning had occurred (Test 4). To determine the effect of rotational speed, two tests were undertaken (Test 5: 2 rpm and Test 6: 3 rpm). The operating conditions and tracer quantities for all RTD trials are presented in Tables 3.8–3.11.

Table 3.8: Operating conditions for Test 3

Description	Average value	Standard deviation
Solid feed rate	188 ton/hr	12 ton/hr
Gas inlet temperature	500 ^{o}C	10 ^{o}C
Solid inlet moisture content	16.2%	0.3%
Gas outlet temperature	165 ^{o}C	1.8 ^{o}C
Product outlet temperature	46 ^{o}C	0.3 ^{o}C
Product outlet moisture content	13.6%	-
Rotational speed of the drum	3 rpm	-
Internal condition of the dryer	Scaled	
Tracer quantity (LiCl powder)	2 kg	

Table 3.9: Operating conditions for Test 4

Description	Average value	Standard deviation
Solid feed rate	146 ton/hr	7 ton/hr
Gas inlet temperature	500 ^{o}C	16.05 ^{o}C
Solid inlet moisture content	16.3%	1.5%
Gas outlet temperature	131 ^{o}C	4 ^{o}C
Product outlet temperature	46 ^{o}C	0.4 ^{o}C
Product outlet moisture content	12.4%	-
Rotational speed of the drum	3 rpm	-
Internal condition of the dryer	Unscaled	
Tracer quantity (LiCl powder)	2 kg	

Table 3.10: Operating conditions for Test 5

Description	Average value	Standard deviation
Solid feed rate	116 ton/hr	9 ton/hr
Gas inlet temperature	509 ^{o}C	23 ^{o}C
Solid inlet moisture content	16.53%	0.12%
Gas outlet temperature	155 ^{o}C	7.98 ^{o}C
Product outlet temperature	45 ^{o}C	0.3 ^{o}C
Product outlet moisture content	12%	-
Rotational speed of the drum	2 rpm	-
Internal condition of the dryer	Unscaled	
Tracer quantity (LiCl powder)	2 kg	

Table 3.11: Operating conditions for Test 6

Description	Average value	Standard deviation
Solid feed rate	162 ton/hr	3 ton/hr
Gas inlet temperature	515 ^{o}C	11 ^{o}C
Solid inlet moisture content	16.6%	0.1%
Gas outlet temperature	150 ^{o}C	5 ^{o}C
Product outlet temperature	47 ^{o}C	0.4 ^{o}C
Product outlet moisture content	12.2%	-
Rotational speed of the drum	3 rpm	-
Internal condition of the dryer	Unscaled	
Tracer quantity (LiCl powder)	2 kg	

The results of the RTD tests are plotted in Figure 3.8. The percentages of tracer recovered during the experiments are presented in Table 3.12. Test 3 had low recovery, which may be due to high solid feed rate and the scaled internal condition of the dryer. The scale build-up in the dryer may enhance the adhesion of the material resulting in loss of the tracer within the dryer. The percentage recovery in Test 5 was also relatively low compared to other tests (Tests 2, 4 and 6) with similar internal conditions.

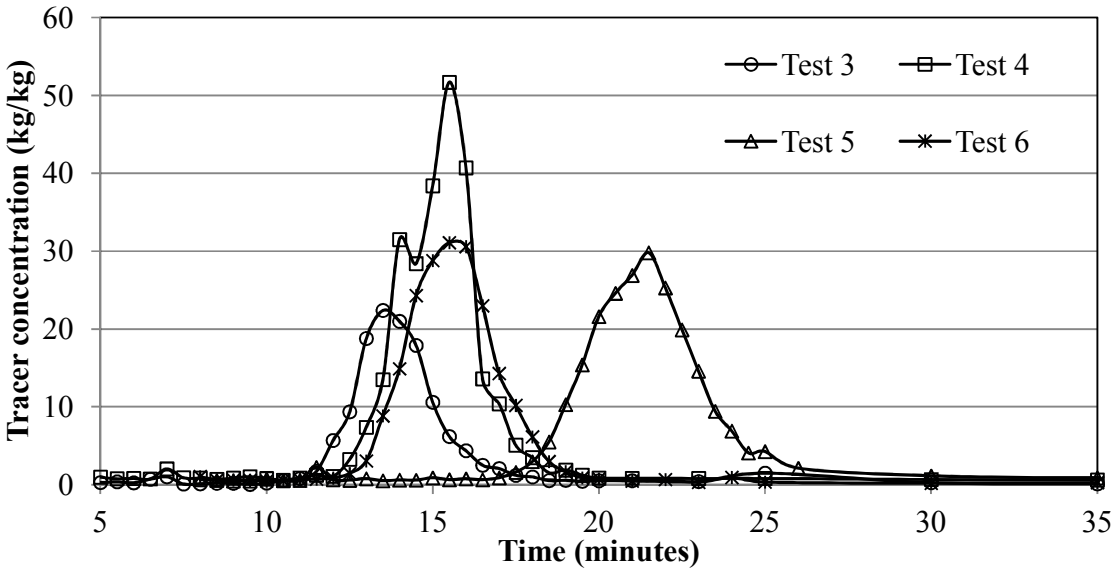

Figure 3.8: Lithium concentration versus time for test runs

Table 3.12: Mass of lithium recovered

Condition of the dryer	Actual Tracer (g) (Li)	Recovered Tracer (g) (Li)	Recovery (%)
Test 3	327.4	194	59
Test 4	327.4	307	94
Test 5	327.4	252	77
Test 6	327.4	273	84

The distribution of residence times is represented by an exit age distribution *(E(t))*. Equation 3.8 was used to transform the lithium concentration curves (Figures 3.7 and 3.8) into residence time distribution curves (Figure 3.9).

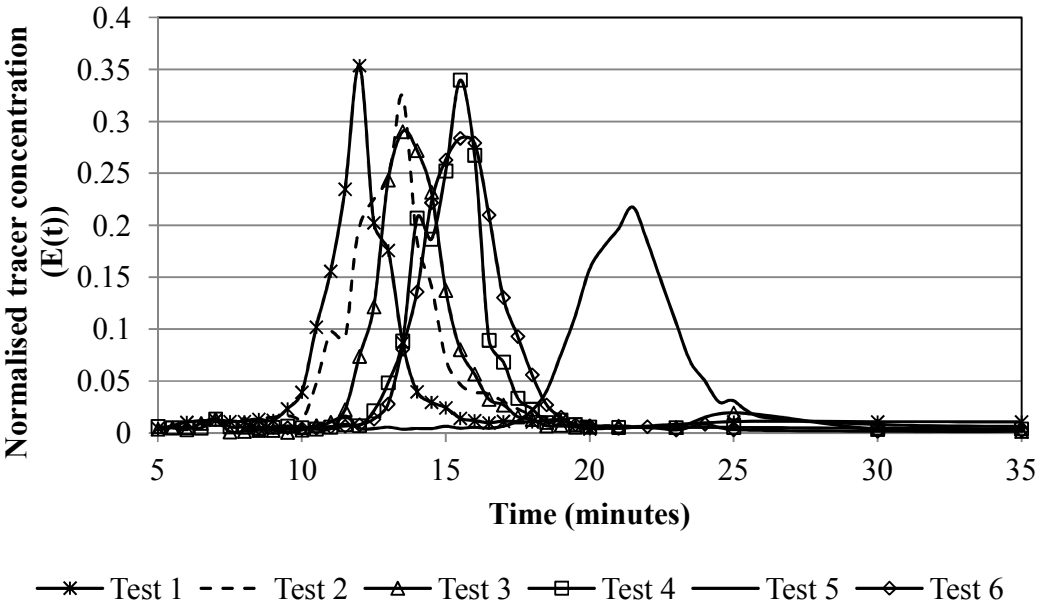

Figure 3.9: Normalised residence time distribution functions for all tests

Table 3.13 presents the first moment of the RTD trials. The most obvious observation is the effect of rotational speed on mean residence time.

Table 3.13: Moment of RTD

Test	Condition of Dryer	Rotational speed (rpm)	Solid feed rate ($kg_{wet\ solid}$/min)	1st moment τ (minutes)
Test 1	Unscaled	3	2230	13.20
Test 2	Unscaled	3	2840	12.02
Test 3	Scaled	3	3140	14.00
Test 4	Unscaled	3	2440	15.21
Test 5	Unscaled	2	1940	21.73
Test 6	Unscaled	3	2690	15.61

3.5.4.1 Hold-up

The hold-up of the dryer for the different operating conditions was calculated using Equation 2.1. The average P1 data was used as the solid feed rate for all the conditions. The hold-up values for all of the RTD trials are presented in Table 3.14.

Table 3.14: Holdup values for different conditions

Test	Condition of Dryer	Rotational speed (rpm)	τ (minutes)	Solid feed rate ($kg_{wet\ solid}$/min)	Holdup ($kg_{wet\ solid}$)
Test 1	Unscaled	3	13.20	2230	29,400
Test 2	Unscaled	3	12.02	2840	34,100
Test 3	Scaled	3	14.00	3140	43,900
Test 4	Unscaled	3	15.21	2440	37,100
Test 5	Unscaled	2	21.73	1940	42,200
Test 6	Unscaled	3	15.61	2690	41,990

3.6 Shell temperature measurement

The shell temperature distribution across the length of the dryer was measured using an infrared heat gun (Kane-May Infratrace 801). The measurement was undertaken both prior to and after cleaning of the internal walls of the dryer. The gas inlet temperatures for the scale accumulated dryer and the clean dryer were 501 ^{o}C and 498 ^{o}C respectively. Figure 3.10 shows the smoothed shell temperature profiles of the scale accumulated and the unscaled dryer.

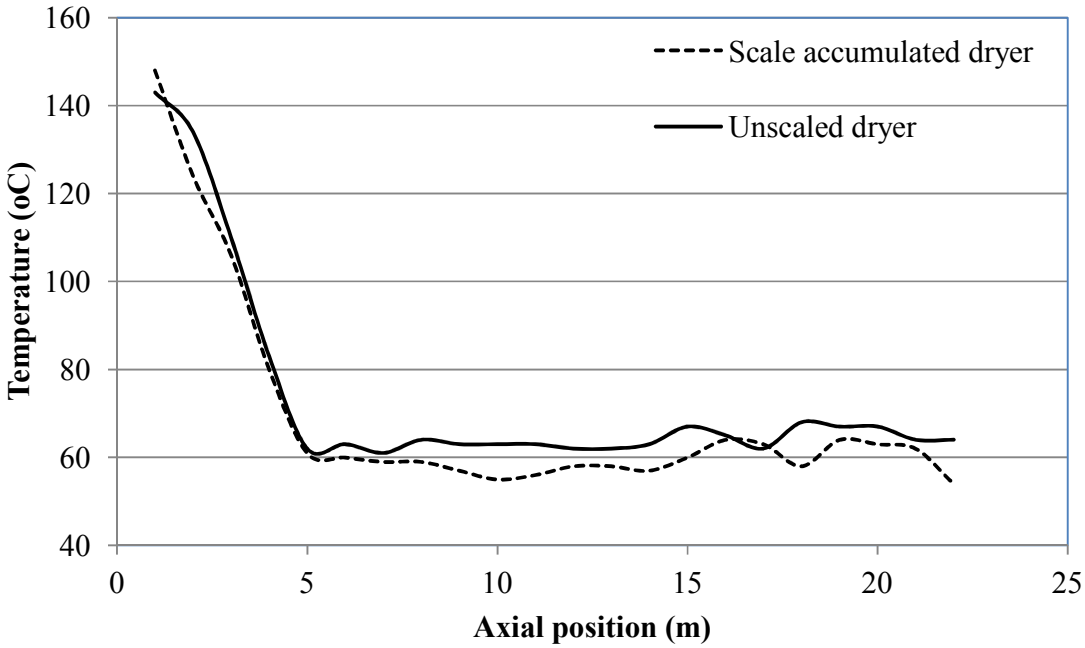

Figure 3.10: Shell temperature profile along the length of the dryer

CHAPTER FOUR

4. DESIGN LOADING IN FLIGHTED ROTARY DRYERS

The amount of solids contained within the flights and in the airborne phase of a flighted rotary dryer is critical to the analysis of performance and the optimal design of these units. In order to validate design loading states in flighted rotary dryers, there is a need to carry out experiments at different solid loadings. Previous studies have described the determination of flight holdup using photographs of the cross-sectional area of a rotating drum (Matchett & Sheikh, 1990; Revol et al., 2001). This technique has also been used to determine angle of repose as a function of the angular position of the flights and has demonstrated that accurate analysis of the photographs is vital to the proper estimation of the design load.

Image analysis and image processing has been used widely in the biological science literature and many of the techniques used to filter and process images have arisen from these fields. Similarities between particles and cells and the ability to capture real time images have led to explosion of its applications in particle engineering systems such as fluidised beds. In the last decade, there has been substantial increase in the number of publications in image analysis of particle/solid behaviour. An ISI web knowledge search (Engineering) using terms image analysis and particles shows an increase from 57 articles in 2001 to 143 articles in 2010. Examples of studies demonstrating the use of image analysis to resolve critical engineering problems include Heffels et al. (1996), Obadiat et al. (1998), and Boerefijn and Ghadiri (1998). Dagot et al. (2001) used image analysis to confirm the assumption that there is a decrease in the quantity or quality of filamentous bacteria in a Sequencing Batch Reactor (SBR). The study concluded that image analysis can be used to control and monitor the SBR in real time. Poletto et al. (1995) used image analysis to establish a linear correlation between voidage pixel intensity within a fluidised bed.

Boerefijn and Ghadiri (1998) developed an image analysis technique to characterise particle flow behaviour for fluidised bed jets. In another study, image analysis was used to describe particle curtain behaviour in a solar particle receiver (Kim et al., 2009). Their study showed variation in the solid volume fraction and the falling particle velocity at different heights within the curtain. It can be concluded that image analysis is a powerful tool for solving different engineering challenges in particle technology.

Image analysis is the process of extracting important information from images; mainly from digital images by means of digital image processing techniques. An image can be defined as a two-dimensional function, $f(x, y)$, where x and y are plane coordinates and the magnitude of f at any pair of coordinates (x,y) is called the pixel intensity of the image at that location.

There are four basic types of images, namely: binary, grayscale, true-colour or red-green-blue (RGB) and indexed. In binary images, the pixels are either black or white and they are represented as 0 and 1 for black and white respectively. The grayscale image consists of shades of gray and the pixels range from 0 (black) to 255 (white). This type of image is predominantly used in image analysis for engineering applications due to its distinctive and easily analysed colour variation. For the true colour image, each pixel has a colour which is described by the amount of red, green, and blue in it. Each of these components can have range of values from 0 to 255 giving a total of 255^3 different possible colours in the image and every pixel in the image corresponds to three values, complicating analysis. An indexed image has each pixel with a value that does not give its colour but an index to the colour in an associated colour map. The knowledge of the types of images facilitates appropriate choice of image analysis technique to be implemented.

Different image analysis techniques are available in engineering applications and they are mostly implemented using image processing software. These techniques can be sub-categorised into the following algorithms: image enhancement, image restoration and image segmentation. Image enhancement can be regarded as the pre-processing of an image and involves the sharpening of the image, highlighting the edges, improving image contrast or brightness. The next step in the algorithm is the image restoration and it entails repairing the damage done to an image by a known cause. Examples of image restoration are removal of optical distortions or periodic interference. The image segmentation involves isolating certain regions of interest within the image or subdividing the image into component parts. This process can include estimating the area within the region of interest or finding and counting particular shapes in the image. Figure 4.1 shows a typical algorithm structure used in image processing.

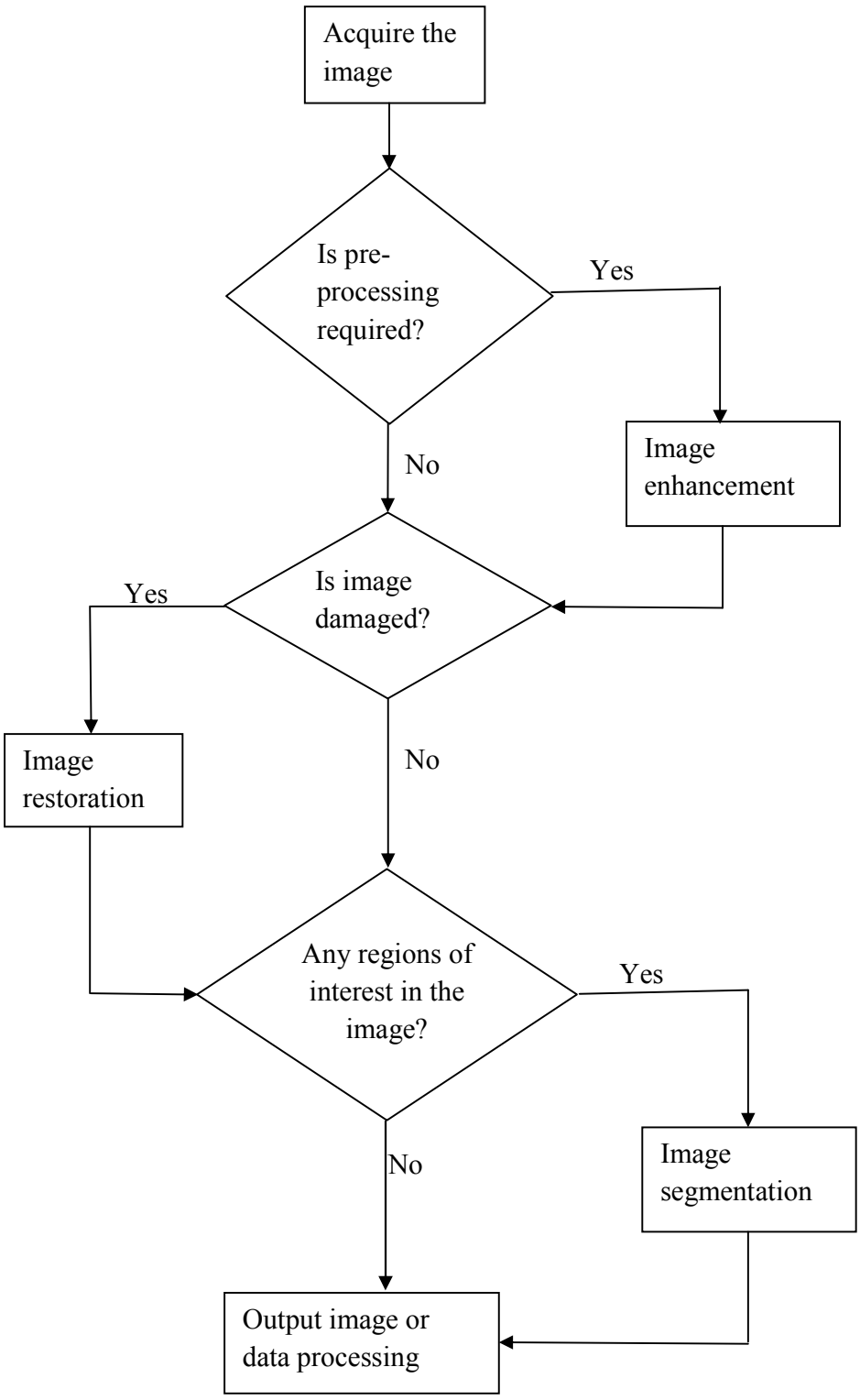

Figure 4.1: Algorithm for image analysis

4.1 Experimental set-up

A series of experiments were carried out at pilot scale in order to determine dryer design loadings. The experimental conditions examined in this study are stated in Table 4.1. The flighted rotary dryer used in the experiments is rotated in a clockwise direction and aligned to be perfectly horizontal. The geometrical configuration of the dryer is described in Table 4.2 and a diagram defining the flight geometry is provided in Figure 4.2. Figure 4.2 illustrates a typical two-staged flight defined by the flight base length (s_1), flight tip length (s_2), the angle between the flight base and the drum wall (α_1) and angle between the flight segments (α_2). A camera on a tripod stand was placed 1.5 metres in front of the end of the drum and positioned around the 9 o'clock axis of the drum, so as to minimise parallax error. The photographs were taken using a Nikon D80 camera which was adjusted to manual focus settings with focal length of 18 mm and aperture size of 3.5. The shutter speed was 1/60 second. The images were taken using the continuous operation mode and in grayscale (2592 x 3872 pixels). Six 500 watt spotlights on tripod stands were placed to illuminate the drum cross section. The laboratory room was blackened so as to reduce variation in the ambient light. A polished Perspex plate with a 5 mm thickness was used on the front end of the dryer and a black screen was used on the back end of the dryer throughout the experiment. The built-in flash system of the camera could not be used because of its reflective effect on the Perspex front end of the drum.

Table 4.1: Operating conditions for the design load experiments

Experimental conditions	
Material	Filter sand
Rotational speed	2.5 rpm, 3.5 rpm and 4.5 rpm
Moisture content	0.4 wt% fluid content sand
	0.75 wt% fluid content sand
	1.25 wt% fluid content sand
	2.1 wt% fluid content sand

Table 4.2: Experimental set up and geometrical configuration of the drum

Parameter	Value
Length of dryer (L)	1.150 m
Diameter of dryer (D)	0.750 m
Flight base length (s_1)	0.033 m
Flight tip length (s_2)	0.030 m
Flight base angle (α_1)	90 ^{o}
Flight tip angle (α_2)	124 ^{o}
Flight thickness	0.002 m
Number of flights	24

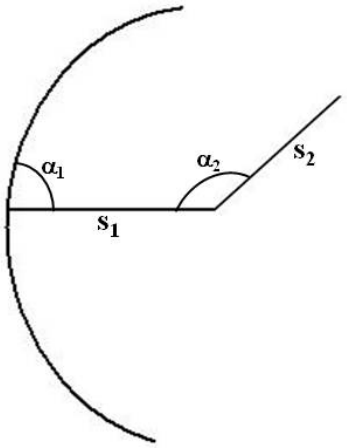

Figure 4.2: Schematic diagram of the flight geometry

4.1.1 Material and its properties

Filter sand was sieved, washed and dried in the oven for 12 hours prior to loading. Pretreatment of the filter sand was necessary to remove fine particles which, because of electrostatic interference, obscured the cross-sectional photographs. The particle size distribution of the filter sand was determined using sieves and the average particle size of the treated filter sand was 300 μm. Low volatility Dow Corning 200 fluid, 350CS (laboratory grade) within the range of 0.4 wt% to 2.1 wt% was added to the filter sand so as to investigate the effect of fluid content or solids cohesion on design load. Small quantities of low volatility Dow corning fluid can be used to carefully alter the angle of repose of the solids without evaporating during the experiments. However, un-wetted filter sand was not used because of the electrostatic obscuration due to dust particles abraded during an experiment. The characteristics of the filter sand with different fluid contents are outlined in Table 4.3. The free-flowing characteristic was described by the flow index (ff_c) and is the ratio of consolidation stress and unconfined yield strength, which was measured using a ring shear tester. The loose bulk density was determined in the laboratory by

pouring the material into an empty 200ml volumetric cylinder. The consolidated density was determined by tapping the sides of the cylinder until no more consolidation occurred. The samples were weighed to determine the consolidated density. Density measurements were repeated five times to determine the average value and the standard deviations. The effect of fluid content on the bulk density and the free-flowing nature of the sand was significant. Care was taken prior to each experimental run to ensure even solids distribution along the drum length.

Table 4.3: Characteristics of the material at different moisture content

Fluid content (%wt)	Flow index (ff_c)	Loose Bulk density (kg/m^3)	Consolidated Bulk density (kg/m^3)
0.40	11	1406 ± 8	1559 ± 13
0.75	6	1374 ± 10	1560 ± 15
1.25	3.7	1326 ± 14	1564 ±15
2.10	2.2	1262 ± 14	1537 ± 20

4.2 Image segmentation and manual analysis

Previous studies have used ImageJ software to manually determine the area of solid within the flights (Christensen, 2008) and to measure angle of repose (Lee, 2008; Lee & Sheehan, 2010). In the manual process, ImageJ software is used to trace regions of interest such as the boundaries defining the enclosed area within a flight (see Figure 4.3) and computing the enclosed area. The photographs were scaled in ImageJ to determine the length of a pixel and the in-built area function was used to determine the cross-sectional area of both flight-borne solids and airborne solids. The scaling process involved using the diameter of the dryer (75 cm) as the reference

length. Computed areas were segmented into four regions of interest. These regions are the First Unloading Flight (FUF), flight-borne solids in upper half of the drum (UHD), flight-borne solids in lower half of the drum (LHD), and airborne solids in the free-falling curtains (AP) defined as any solids within the circle enscribed by the flight tips. These regions are pictorially described in Figure 4.3 and defined in Table 4.4. In Figure 4.3a, the UHD area lies within the range of angle $(\gamma + \theta)$, the LHD area lies within the range of angle (β) and the FUF lies within the range of angle (γ). Manual use of ImageJ software is a good analytical tool which enables intuition to be used to determine the boundary of solid within the flights. However, a major limitation of manual tracing is that it is very time consuming to analyse multiple photographs.

(a) (b)

Figure 4.3: Drum cross section including the angles used to define the regions of interest for the Image segmentation.

Table 4.4: Regions of interest corresponding to Figure 4.3

Region of interest	Location
FUF	γ
UHD	$\gamma + \theta$
LHD	β

4.2.1 Image enhancement

In view of the thousands of photographs analysed, this study developed an automated process for computing the cross-sectional area of solids in the regions of interest for batches of photographs. A number of approaches using MATLAB and ImageJ were tested and compared to manual tracing to assess their accuracy. The initial MATLAB process involved cropping the image and counting the total number of pixels in the region of interest to estimate the area. The cropping process required removing the airborne solids (AP) from the image and also excluding the background by cropping the edges of the drum. The cropped image contained the solid retained in the flights as well as the voids between the flights. The MATLAB calculation entailed determining the pixel intensity cut-off point for the entire image. The concept of pixel intensity cut-off, also referred to as thresholding, was to remove pixel values of the flight components and voids, thereby retaining only solid within the flight. To determine the exact minimum brightness value (B_{min}) or cut-off point for the region of interest, matrix indexing was done. The matrix indexing gave an insight into the exact brightness value within the region of interest. It was observed that portions of solid within the flight had the same pixel value as the flight components, and appropriate B_{min} values differed between the upper and lower half of the drum due to subtle variation in lighting. Camera location also led to unavoidable difficulties in

determining the edges of the flight-borne solids in the bottom half of the drum due to parallax. It is interesting to note that the naked eye can discern subtle differences making manual tracing more reliable. The results presented in Tables 4.5 and 4.6 demonstrate the inconsistency in the approach and the overestimation of the region of interest and provide justification for both image enhancement and segmentation.

Table 4.5: Comparative estimation of regions of interest *(2.5 rpm, 0.4 wt% moisture content, 32 kg loading condition)*

Technique	Area at FUF (cm^2)	Area of UHD (cm^2)	Area of UHD + LHD (cm^2)
ImageJ manual calculation	26.00	102.47	220.74
MATLAB calculation	29.08	125.34	259.95

Table 4.6: Comparative estimation of regions of interest *(3.5 rpm, 0.4 wt% moisture content, 33 kg loading condition)*

Technique	Area at FUF (cm^2)	Area of UHD (cm^2)	Area of UHD + LHD (cm^2)
ImageJ manual calculation	26.37	83.27	213.35
MATLAB calculation	28.80	103.68	258.53

Further investigation observed variation in the brightness and contrast properties within images of the same experimental run. The variation in the brightness properties could be attributed to experimental conditions such as fluctuation in the lightning set-up. Image enhancement techniques used to overcome these issues are discussed in the following section.

4.2.1.1 Filtering and thresholding in ImageJ software

The images were filtered in batches using ImageJ software prior to the processing for the cross-sectional area in MATLAB. The filtering macro was developed in ImageJ and the three-step process involved adjusting the brightness/contrast of the image, the smoothing and edge enhancement of the pixels of the bulk solid within the flight, followed by thresholding. The brightness/contrast of the image was adjusted by increasing the brightness/contrast using the in-built ImageJ function. The smoothing filter (ImageJ plugin) was based on the sigma probability of the Gaussian distribution and was defined by the parameters outlined in Table 4.7. The sigma filter smoothes the image noise by averaging only those neighbourhood pixels which have intensities within a fixed sigma range of the centre pixel (ImageJ plugins, 2007). In this way, image edges are preserved, and subtle details within the image are maintained. The next process in the developed macro was the thresholding of the image. An example of a filtered and thresholded image is presented in Figure 4.4. The thresholding values of the upper and lower halves were different due to subtle contrast difference arising from spotlight location. The developed macro was implemented across the stack of images for a particular experimental condition. The thresholding reduced the longitudinal background effect of the drum by turning every pixel value within the background to black (zero pixel value). The regions of interest within the flights were the non-zero pixel values.

Table 4.7: Values for the thresholding process

Filtering and thresholding process	Upper half of the drum ($\alpha + \theta$)	Lower half of the drum (β)
Brightness and contrast value	140	160
Sigma filtering	Radius = 4, use = 3, minimum = 1	Radius = 4, use = 2, minimum = 0.9
Thresholding value	168	177

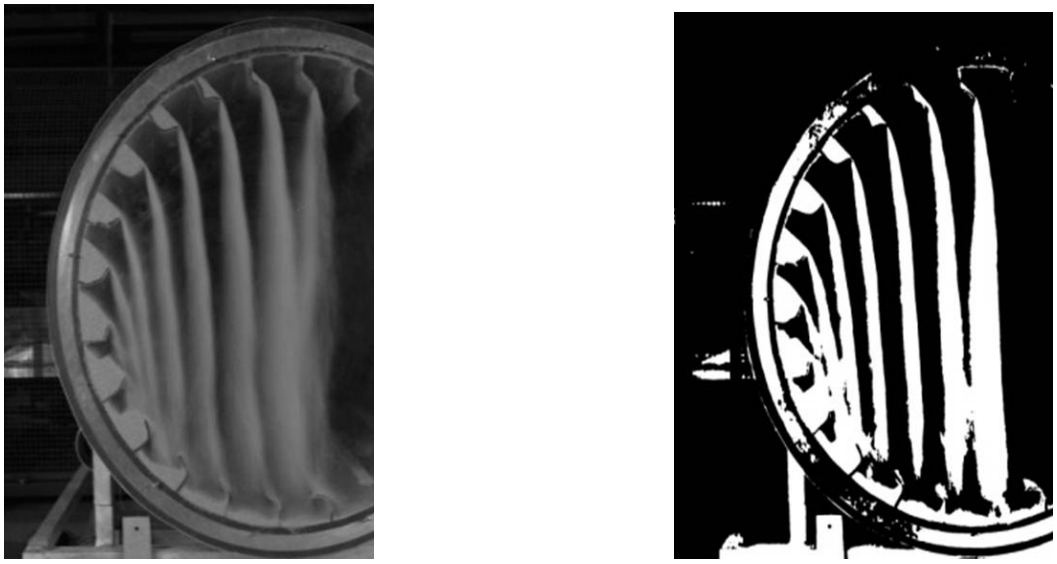

(a) Original image example (b) Filtered image example

Figure 4.4: Original and filtered images in ImageJ software *(upper half filter)*

4.3 Validation of image analysis

In order to validate the image processing techniques, five photographs at different loading conditions of 0.4 wt% fluid content experimental run were analysed manually and averages calculated. The comparisons between techniques are presented in Tables 4.8- 4.10.

The combined ImageJ enhancement and MATLAB calculation technique slightly over-estimated the area when compared with ImageJ manual calculation. The deviation was attributed to the presence of solid stuck to corners and surface junctions between flights, which have high degree of pixel intensity but are excluded in the manual calculation because of intuition elimination. The discrepancies in the results are found to be consistent for different loading conditions and thus introduced an assumed consistent bias in the data, which makes it appropriate for analysis of design loading. A t-test at 95% confidence interval was performed and indicated that for the FUF, the ImageJ manually calculated approach and the combined ImageJ enhancement and MATLAB approach are equivalent. The automated combined ImageJ enhancement and MATLAB calculation technique was used to process the remaining photographs. MATLAB code is presented in Appendix C.

Table 4.8: Comparative estimation of regions of interest *(3.5 rpm, 0.4 wt% moisture content, 33 kg loading condition)*

Technique	Area at FUF (cm^2)	Area of UHD (cm^2)	Area of TP (cm^2)
ImageJ enhancement and MATLAB calculation	27.32	93.48	234.07
ImageJ manual calculation	26.37	83.27	213.35

Table 4.9: Comparative estimation of regions of interest *(3.5 rpm, 0.4 wt% moisture content, 35 kg loading condition)*

Technique	Area at FUF (cm^2)	Area of UHD (cm^2)	Area of TP (cm^2)
ImageJ enhancement and MATLAB calculation	27.39	95.18	245.58
ImageJ manual calculation	26.96	89.54	233.34

Table 4.10: Comparative estimation of regions of interest *(4.5 rpm, 0.4 wt% moisture content, 34.5kg loading condition)*

Technique	Area at FUF (cm^2)	Area of UHD (cm^2)	Area of TP (cm^2)
ImageJ enhancement and MATLAB calculation	29.58	98.64	250.99
ImageJ manual calculation	29.02	92.52	237.39

4.4 Estimation of design load

Matchett and Baker (1988) established a criterion to estimate the design load experimentally. They observed a change in the slope of the plot of holdup versus feed rate (Figure 4.5). Their study concluded that the change in slope indicated a transition from under-loaded to over-loaded conditions and the transition point was regarded as the design load. Their study also observed saturation of mass within the airborne phase at design loading.

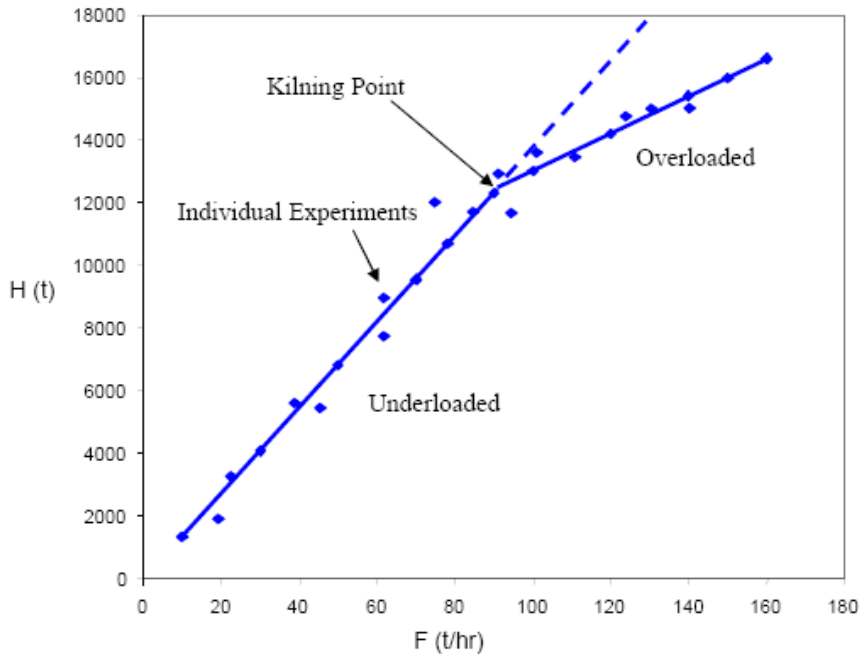

Figure 4.5: Plot of holdup against feed rate (Matchett & Baker, 1988)

In line with the Matchett and Baker (1988) concept of saturation, four different approaches were considered in this study: visual analysis, change in gradient with respect to loading of flight-borne solids, saturation of the airborne solids, saturation of the upper flight-borne solids, and saturation of the FUF. The concept of these approaches is discussed in subsequent sections.

4.4.1 Visual analysis approach

The visual analysis approach involved examining all the photographs at different loading conditions to determine the loading at which there is discharge of solids at precisely the 9 o'clock position as shown in Figure 2.1b. However, because of the fluctuating nature of flight loading, the visual approach gave a range of design load conditions for the set of photographs and is excessively time consuming. It assumed that the design load lies between the loading condition when the discharge was first observed and the next loading condition. This approach may not be suitable for high moisture content solids because of its avalanche discharge pattern as

the drum rotates. Hence, the visual analysis was not considered appropriate to determine the design loading.

4.4.2 Change in gradient of total flight-borne solids

The total flight-borne solids was estimated by summing the areas of flight-borne solids in both the upper half of the drum (UHD) and the lower half of the drum (LHD). Figure 4.6 shows the increase in the total flight-borne solids as the loading condition increases. Qualitatively, it was evident that there is a change in the slope as the loading condition passes a certain point. However, it is difficult to determine the exact loading condition where the gradient changes. Piecewise regression analysis was carried out on the data but is subject to considerable error as a result of the uncertainty in the gradient past the design point.

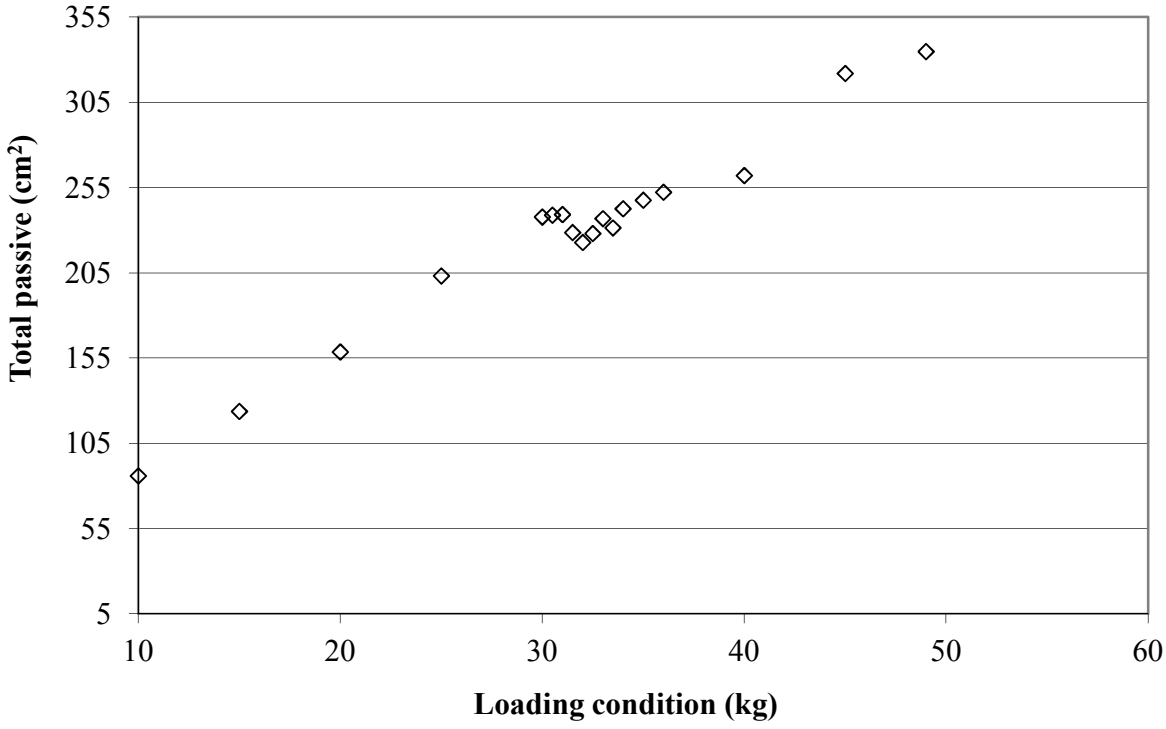

Figure 4.6: Total passive *(UHD + LHD)* versus loading for 0.4 wt% moisture content solids at 3.5 rpm

4.4.3 Saturation of the airborne solids and of the flight-borne solids in the upper half of the drum

Prior to the estimation of the area covered by airborne solids, the image enhancement technique described in section 4.2.1.1 was implemented across the stack of images using threshold values of 104 and 120 for the upper half airborne solids and the lower half airborne solids of the drum respectively. The drum was segmented by excluding anything outside the radius defined by the flight tips. The percentage coverage by the airborne solids was determined using Equation 4.1. The flight tip radius was calculated as 0.3262 metres using Lee and Sheehan (2010) geometric model.

$$Area\ of\ covered = \frac{Area\ of\ covered\ by\ airborne\ solids}{Area\ of\ the\ drum\ bounded\ by\ the\ flight\ tips} \times 100\% \qquad \textbf{4.1}$$

Figure 4.7 shows the percentage coverage by the airborne solids (AP) and the area of the flight-borne solids in the upper half of the drum (UHD) at different loading conditions. It is interesting to note that the profiles of both areas with respect to loading are independently very similar. The peaks in the graphs can be regarded as the point where there is maximum interaction between solids and gas. They may also be considered to be the transition point from under-loaded to overloaded, i.e. the design load. It can be seen there was a relative saturation in the areas in the later stages of loading after this transition point. At this stage, the reason for the peak in the UHD and AP, repeatable at different rotational speeds, is unclear. Variation in both the consolidated density within the flights and solids voidage within the falling curtains may contribute to this phenomenon and will be the subject of further investigation. The standard deviations for the areas of flight-borne solids in UHD are high and the complexity of determining the solids

voidage of the airborne solids propagated errors and could introduce significant bias in estimation of the design load. Using the peak in the approaches to quantity design load relies on the accuracy of individual data points.

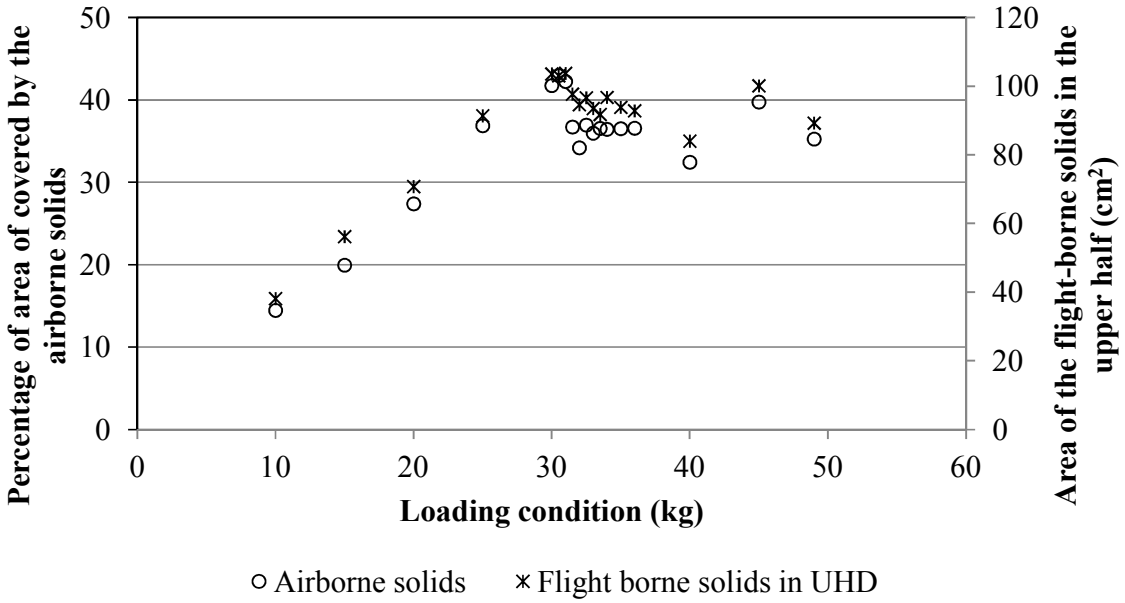

Figure 4.7: Saturation of the airborne solids and flight-borne solids in the upper half of the drum (3.5 rpm)

4.4.4 Saturation of the First Unloading Flight (FUF)

The study assumed that the design load was achieved when the mass at FUF was at maximum capacity, i.e. saturated. This relies on the assumption that the flight-borne mass becomes constant when the dryer is over loaded. Under this assumption, the average area in the FUF from each experimental run was plotted against loading as shown in Figure 4.8 (a-c). The shape language modelling (SLM) technique developed by D'Errico (2009) was used in the regression of piecewise functions to these data sets. The SLM approach is based on least squares splines subjected to simple constraints. It should be noted that the right hand slope in the SLM approach

was constrained to zero (assumed saturation) and the left hand line was constrained to be linear but not constrained to pass through the origin. The discontinuity/break location along the curve indicates the estimated design load. This approach offers significant advantage with respect to quantification of experimental error when compared to the change in gradient approach described in section 4.4.2. The SLM fitting technique was implemented in the MATLAB Optimization Toolbox (see Appendix D for the user-defined part of the MATLAB code). It can also be seen from the graphs that relatively constant FUF area values were achieved from the design load to the overloading condition. The results for the FUF data and the calculated design loadings are presented in Table 4.11. Confidence intervals were determined via rules of propagation of errors (Harrison & Tamaschke, 1984; Oosterbaan et al., 1990). The detailed process of estimating the confidence intervals is presented in Appendix E.

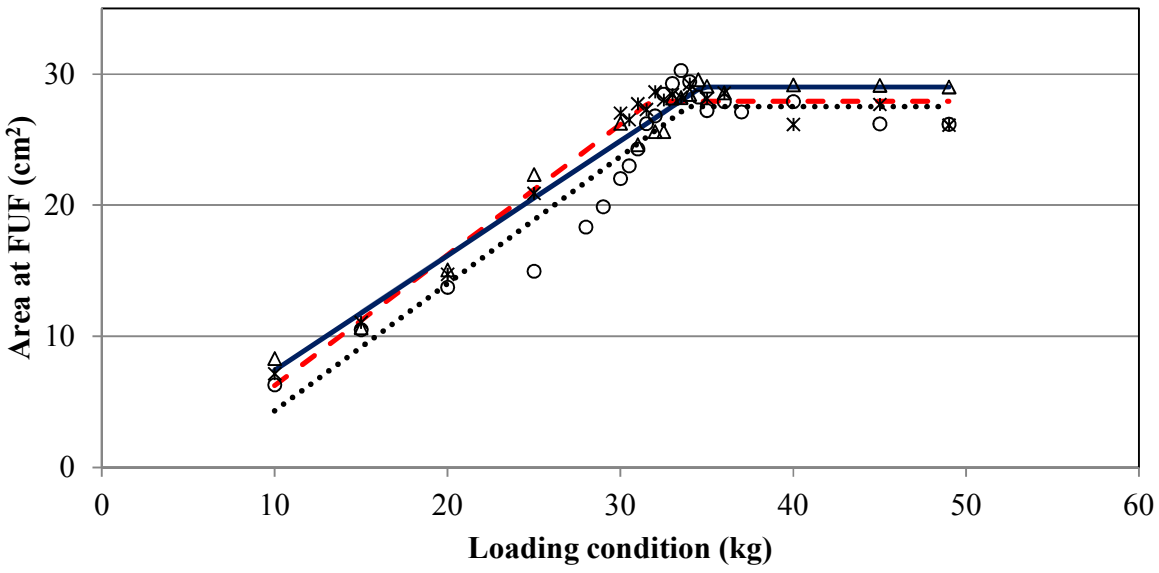

(a)

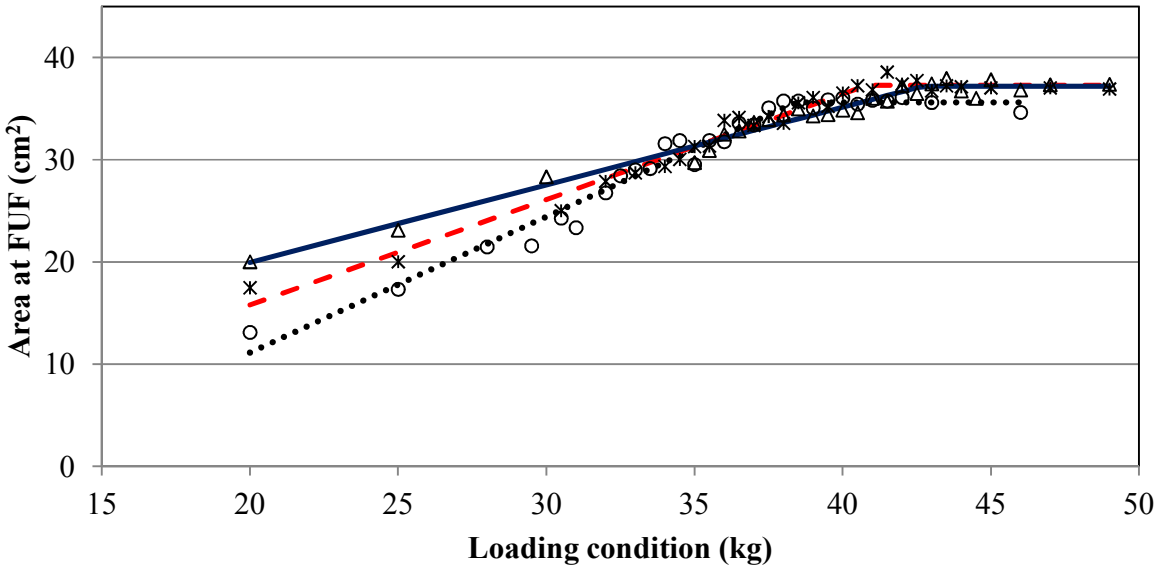

(b)

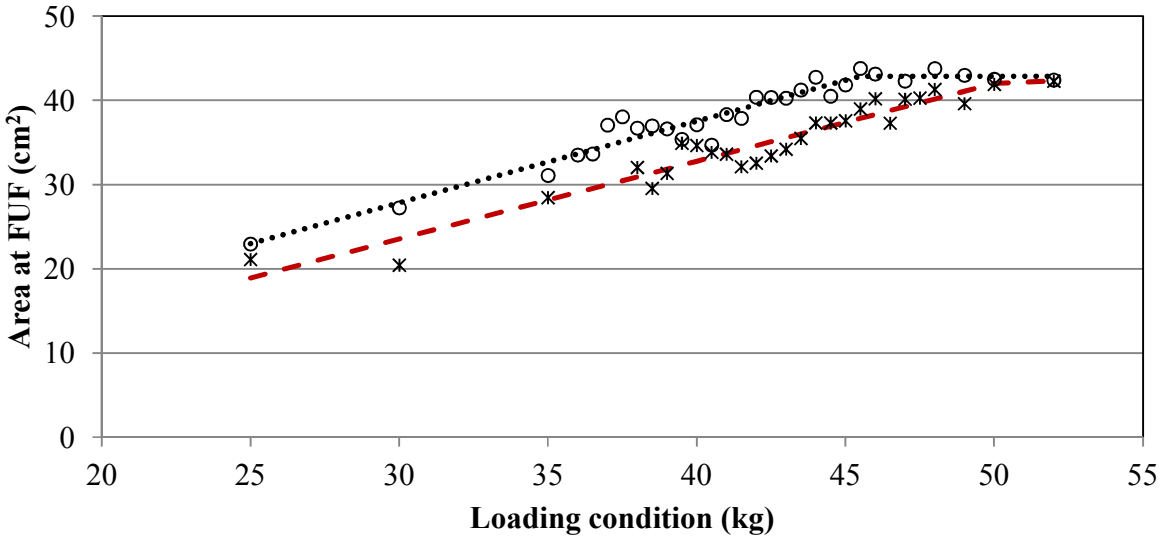

(c)

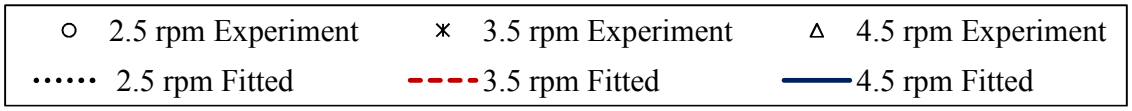

Figure 4.8: Design load of (a) low (0.75 wt% 2.5 rpm, 0.4 wt% (3.5 rpm and 4.5 rpm)), (b) medium (1.25 wt%) and (c) high (2.1 wt%) moisture content solids at different rotational speeds

Table 4.11: Design load based on constant area at FUF *(at different experimental conditions)*

Rotational speed (rpm)	Moisture content (wt%)	Dynamic angle of repose (degrees)	Design Load (kg)	Area at FUF (cm^2)
	0.75	46.7 ± 2.9	33.9 ± 7.7	27.3 ± 0.92
2.5	1.25	51.1 ± 1.6	38.4 ± 4.8	35.6 ± 0.43
	2.10	58.3 ± 2.3	45.5 ± 8.1	42.9 ± 0.60
	0.40	44.7 ± 2.0	31.8 ± 3.7	27.9 ± 0.47
3.5	1.25	54.3 ± 2.6	40.8 ± 4.4	37.3 ± 0.34
	2.10	59.4 ± 1.7	50.3 ± 8.0	42.3 ± 1.00
	0.40	45.0 ± 2.5	34.7 ± 4.4	29.0 ± 0.53
4.5	1.25	56.7 ± 2.4	42.7 ± 4.6	37.2 ± 0.32
	2.10	62.3 ± 2.8	54.3 ± 5.3	44.5 ± 0.71

Rotational speed had significant effect on the design load of the dryer as observed in the results presented above. This can be attributed to a number of factors. Increased rotational speed leads to an increase in the dynamic angle of repose of the solids and a potential increase in the bulk density of the flight-borne solids. Higher rotational speeds also lead to an increased rate of discharge of solids into the airborne phase which increases the total dryer holdup. This is further supported by the observed decrease (with respect to rotational speed) in the gradient of the area versus load line, particularly evident in Figure 4.8(b). The relationship between rotational speed

and angle of repose has been presented in Schofield and Glikin (1962). Fluid content or level of cohesion has a significant effect on the design load of the drum. As the fluid content of the sand material increases, its cohesive nature increases and thus increases the angle of repose of the material within the flights.

The design loading at 3.5 rpm for example, showed increasing uncertainty as the fluid content or cohesion increases (3.7 kg to 4.8 kg to 8.0 kg). This was attributed to the avalanching flow behaviour of the more cohesive material as it discharges from the flight, and the resultant increase in scatter of the measured data points. Similar discontinuous discharging patterns were observed in the flight unloading experiments described in Lee and Sheehan (2010). Additionally, in the cohesive solids loading experiments, the solids tended to adhere to the Perspex plate in the small junctions and spaces around the flights, which reduced the quality of the processed images. Qualitative observations of the images of airborne solids from the cohesive solids loading experiments were substantially different to those observed using free-flowing solids. The widths of the free-falling curtains were considerably narrower for the cohesive solids compared to the particle curtains in the free-flowing solids experiments, as demonstrated in Figure 4.9. This indicates that the density and flow development of the particle curtains are not comparable, and in the cohesive system significant clumping of solids was observed. This clumping behaviour has also been observed in industrial raw sugar flighted rotary dryers (Britton et al., 2006).

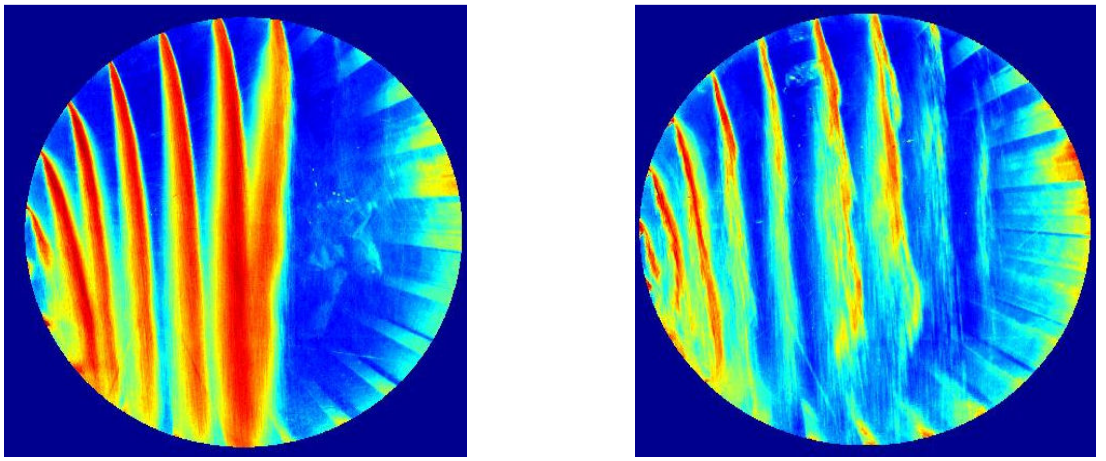

(a) Low moisture content (0.4%) **(b) High moisture content (2.1%)**

Figure 4.9: Variation in the cropped image pixel intensity for free-flowing and cohesive falling particle curtains (3.5 rpm)

4.5 Estimation of the airborne solids

The amount of solids within the airborne or active phase is important to accurate determination of the total dryer holdup and is also an important property in flighted rotary dryer solid transport modelling. In addition, proper understanding of the exact amount of solid in contact with the drying gas is important to ascertain the efficiency of interaction between the gas and solids within the dryer. In determining the airborne solids, different approaches were considered. The first approach involved subtracting the total passive (TP), which is the mass of flight-borne solids during rotation, from the total mass within the drum which can be determined by stopping the dryer and collecting photographic images of the cross section. The deficiency of this approach is the high degree of sensitivity of the difference in masses to the accurate determination of the bulk density of the solids in the flights during drum rotation. In this study, the laboratory-determined consolidated bulk density of the solids was assumed to be the bulk density of the solids within the rotating flights, which over-estimated the passive mass in

comparison to the total mass and led to unrealistic masses for the airborne solids. An alternative approach was to estimate the airborne solids by manually tracing the area covered by falling particle curtains within each photograph (see Figure 4.10 for example). Consequently, a method to determine the solids voidage within the falling particle curtain was required. Computational Fluid Dynamics (CFD) was used to facilitate calculation of the solid volume fraction in the cascaded solid.

Figure 4.10: The manually traced falling curtains

Previous studies have modelled gas-solid interaction and particle curtain behaviour using CFD (Wardjiman et al., 2008; Kim et al., 2009; Wardjiman et al., 2009). CFD involves the numerical solution of mass, momentum and energy conservation equations in the flow system of interest. The two most common approaches to modelling this type of multiphase flow are Eulerian-Eulerian and Eulerian-Lagrangian models. The Eulerian-Langrangian method provides a direct physical interpretation of particle-particle and particle-wall interactions but requires large

computational capacity to simulate the enormous numbers of particles simultaneously. In the Eulerian-Eulerian approach, both phases are treated as interpenetrating continua, and therefore this approach has less computing requirement than Langrangian approach. Both 2D (Kim et al., 2009) and 3D (Wardjiman et al., 2009) Eulerian-Eulerian approaches have been successfully used to model voidage and shape of free-falling particle curtains.

The governing equations for the Eulerian-Eulerian approach are presented below. The standard k-ε turbulence model was used and the conservation equations for the solid phases were based on the kinetic theory for granular flow.

The continuity equation for each phase ($k = g, s$) can be stated as:

$$\frac{\partial(\alpha_k \rho_k)}{\partial t} + \nabla.(\alpha_k \rho_k U_k) = 0 \qquad \textbf{4.2}$$

The momentum balance for gas phase is:

$$\frac{\partial(\alpha_g \rho_g U_g)}{\partial t} + \nabla.(\alpha_g \rho_g U_g U_g) = -\alpha_g \nabla P - \nabla.(\alpha_g \tau_g) + \alpha_g \rho_g \bar{g} + \beta(U_g - U_s) \qquad \textbf{4.3}$$

The momentum balance for solid phase can be written as:

$$\frac{\partial(\alpha_s \rho_s U_s)}{\partial t} + \nabla.(\alpha_s \rho_s U_s U_s) = -\alpha_s \nabla P - \nabla.(\alpha_s \tau_s) + \alpha_s \rho_s \bar{g} + \beta(U_s - U_g) \qquad \textbf{4.4}$$

where α, ρ, U, P and g are the volume fraction, density, velocity vector, pressure and gravity respectively. The term β is the interphase transfer coefficient which can be computed from the drag coefficient, the Reynolds number and the solids volume fraction.

β is expressed as:

$$\beta = \frac{3}{4} C_D \frac{\alpha_s \alpha_g \rho_g}{d_p} |U_g - U_s| \alpha_g^{-2.65} \qquad \textbf{4.5}$$

The drag coefficient was evaluated using the commonly used Schiller–Naumann (1935) drag correlation stated in Equation 4.6.

$$C_D = \begin{cases} \dfrac{24}{\mathrm{Re}} & \mathrm{Re} < 0.2 \\ \dfrac{24}{\mathrm{Re}}\left(1 + 0.15\,\mathrm{Re}^{0.687}\right) & \mathrm{Re} < 1000 \\ 0.44 & \mathrm{Re} > 1000 \end{cases} \qquad \textbf{4.6}$$

The granular kinetic theory based models introduce several additional terms in the solid stresses, which in turn modify momentum conservation equations for solid phases.

The solid stress for the solid phase can be written as:

$$\alpha_s \bar{\tau}_s = -P_s \bar{I} + 2\alpha_s \mu_s \bar{S} + \alpha_s \left(\lambda_s - \frac{2}{3}\mu_s\right) \nabla . U_s \bar{I} \qquad \textbf{4.7}$$

where P_s is the solids pressure, μ_s is the solids (shear) viscosity, and λ_s is the solids bulk viscosity. $\bar{S}$ is given by:

$$\bar{S} = \frac{1}{2}(\nabla U_s + (\nabla U_s)^T) \qquad \textbf{4.8}$$

In the literature, several different expressions have been derived for solids pressure, solids shear viscosity and solids bulk viscosity by employing different approximations and assumptions while applying the kinetic theory of granular flows. The constitutive equations used in this study were as follows:

The total solid shear viscosity was expressed as follows (Lun et al., 1984):

$$\mu_s = \frac{4}{5}\alpha_s \rho_s g_0 (1 + e_s)\left(\frac{\theta_s}{\pi}\right)^{1/2} \qquad \textbf{4.9}$$

The solids pressure, P_s is:

$$P_s = \alpha_s \rho_s \theta_s \big(1 + 2(1 + e_s)\big)\alpha_s g_{0s} \qquad \textbf{4.10}$$

where e_s is the value of the restitution coefficient of solid particles, g_{0s} is a radial distribution function and θ_s is the granular temperature which was defined via:

$$\theta_s = \frac{1}{3}u_i^2 \qquad \textbf{4.11}$$

The radial distribution can be seen as a measure of the probability of inter-particle contact and was described using the Gidaspow (1994) correlation:

$$g_{0s} = \frac{3}{5}\left[1 - \left(\frac{\alpha_s}{\alpha_{s\,max}}\right)^{\frac{1}{3}}\right]^{-1} \qquad \textbf{4.12}$$

$$\alpha_{s\,max} = 0.62$$

The turbulence effect of the solid phase was estimated using the zero equation turbulence model. On the other hand, the eddy viscosity in the stress tensor of the gas phase was estimated using Equation 4.13. It contains two unknown variables, k and ε, which refer to turbulent kinetic energy and turbulent energy dissipation rate. Previous studies in gas-solids interaction modelling have found the standard $k-\varepsilon$ model to be suitable in modelling turbulence in the continuous (gas) phase in free-falling particle curtains (Koksal & Hamdullahpur, 2005; Wardjiman et al., 2008; Wardjiman et al., 2009). Consequently, the turbulence prediction of the gas phase was obtained using the standard $k-\varepsilon$ model.

$$\mu_t = \rho C_\mu \frac{k^2}{\varepsilon} \qquad \textbf{4.13}$$

Turbulence kinetic energy was determined via:

$$\rho\frac{\partial k}{\partial x_i} = \mu_t\left(\frac{\partial \overline{u_j}}{\partial x_i} + \frac{\partial \overline{u_l}}{\partial x_j}\right)\frac{\partial \overline{u_j}}{\partial x_i} + \frac{\partial}{\partial x_i}\left[\left(\frac{\mu}{\sigma_k}\right)\frac{\partial k}{\partial x_i}\right] - \rho\varepsilon \qquad \textbf{4.14}$$

The turbulent energy dissipation rate was determined via:

$$\rho\frac{\partial\varepsilon}{\partial x_i}=C_{\varepsilon1}\frac{\varepsilon}{k}\mu_t\left(\frac{\partial\overline{u}_J}{\partial x_i}+\frac{\partial\overline{u}_l}{\partial x_j}\right)\frac{\partial\overline{u}_J}{\partial x_i}+\frac{\partial}{\partial x_i}\left[\left(\frac{\mu}{\sigma_\varepsilon}\right)\frac{\partial\varepsilon}{\partial x_i}\right]-C_{\varepsilon2}\rho\frac{\varepsilon^2}{k} \qquad \textbf{4.15}$$

$$C_{\varepsilon1}=1.44, C_{\varepsilon2}=1.92, C_\mu=0.92, \sigma_k=1, \sigma_\varepsilon=1.3$$

4.5.1 Vessel geometry and grid generation

In this study, the modelled curtain was the discharging flight at an angular position of 150^o within the pilot scale rotary dryer (Figure 4.11). This location was selected for two reasons: the 150^o curtain was the best centred falling solid with respect to the image orientation and geometrical calculations showed the 150^o curtain to provide an average mass flow rate, with respect to rotation. Geometric calculations based on the experimentally observed dynamic angle of repose, measured at the 9 o'clock position, were performed using the model described in Lee and Sheehan (2010). The mass flow rate profiles across the entire range of rotational angles that were generated using this model are presented in Figure 4.12 and show the mass flow rate at angular position of 150^o to be a reasonable representation of the average flow rate of the flights. Experimentally measured and geometrically derived model inputs are outlined in Table 4.12.

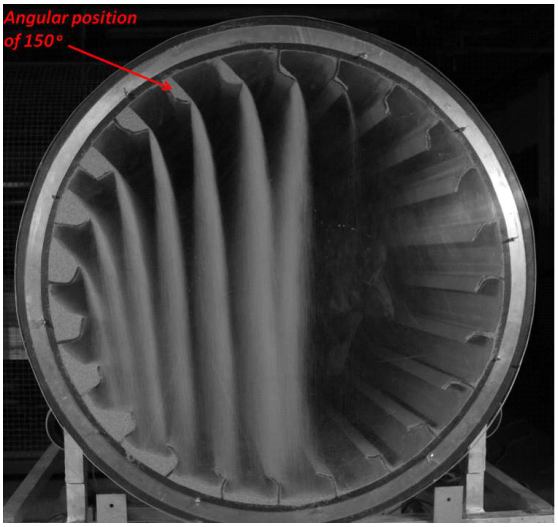

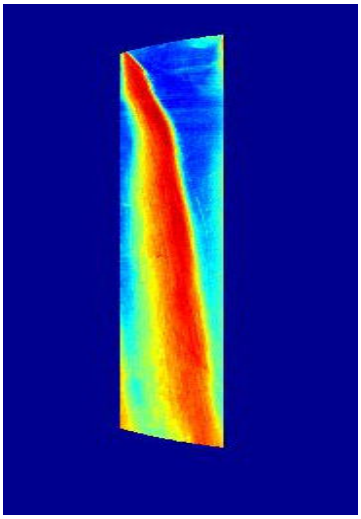

(a) Original image

(b) Colour map of cropped original image

(coloured by pixel intensity)

Figure 4.11: Experimental images of the discharged solid at angular position of 150°

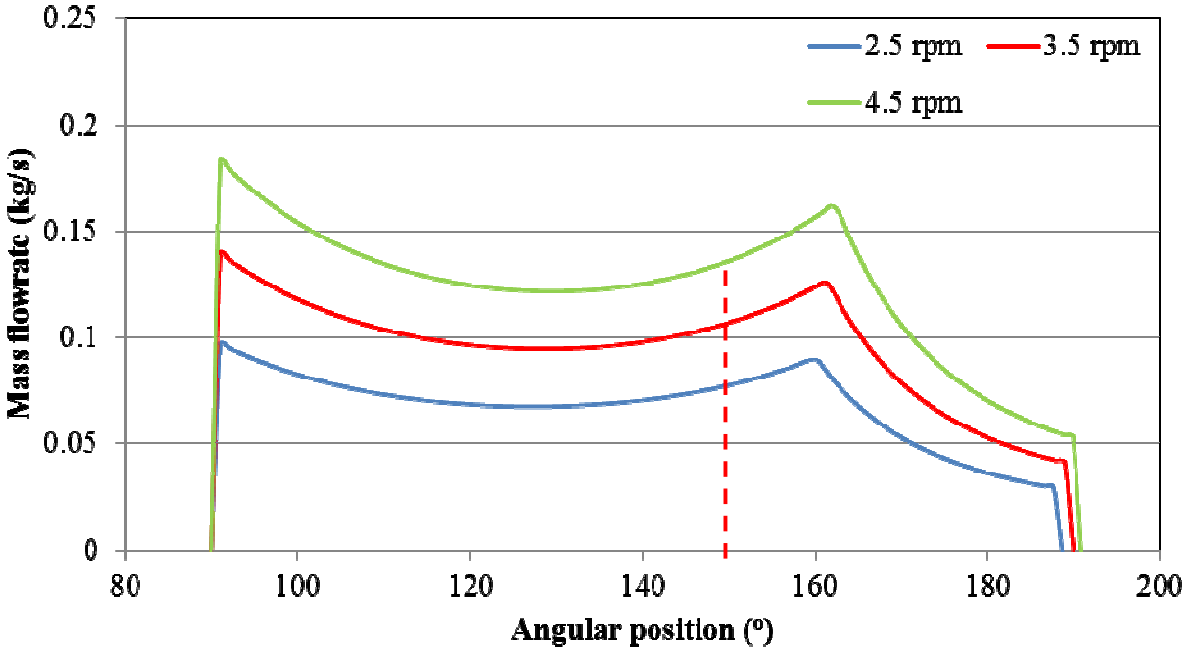

Figure 4.12: Geometrically calculated flight discharge mass flow rate profiles at varying rotational speed

Table 4.12: Experimental conditions for the 150^o free-falling particle curtain

Parameters	**2.5 rpm**	**3.5 rpm**	**4.5 rpm**
Mass flow rate (modelled)	0.073 kg/s	0.103 kg/s	0.134 kg/s
Bulk density	1361 kg/m^3	1361 kg/m^3	1361 kg/m^3
Particle density	2630 kg/m^3	2630 kg/m^3	2630 kg/m^3
Particle size	300 μm	300 μm	300 μm
Dynamic angle of repose*	46.9^o	44.7 ^{o}	45.0^o
Width of discharged solid at the flight tip	0.006 m	0.006 m	0.006 m
Vertical height of curtain	0.59 m	0.59 m	0.59 m
Modelled curtain depth	0.15 m	0.15 m	0.15 m

The schematic diagram of the three-dimensional CFD model is shown in Figure 4.13. The commercial grid generation package (ANSYS Inc.) was used to create body-fitted, structured grid nodes for the geometry studied.

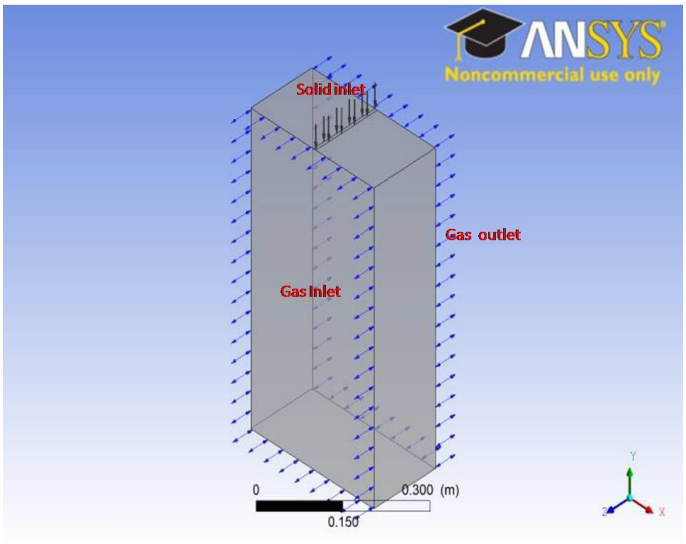

Figure 4.13: Schematic diagram of the CFD model

4.5.2 Boundary conditions

The input values for the CFD analysis were the experimental and modelled conditions outlined in Table 4.12, determined from images of a design loaded dryer and via the geometry model. The inlet solid volume fraction was specified as a function of particle density and bulk density as shown in Equation 4.16. The gas inlet and outlet were modelled as opening boundary conditions. The reference pressure of zero Pa was specified and the speed of the air phase was zero. The solid inlet was modelled as inlet only. The other parts of the geometry were modelled as walls, and a 'no slip' boundary condition was specified for the vessel walls.

$$\rho_b = \rho_{pt}(1 - \varepsilon_v) \qquad \textbf{4.16}$$

where $\rho_b, \rho_{pt}, \varepsilon_v$ are the bulk density, particle density and voidage.

4.5.3 Simulation

The solving of the Eulerian-Eulerian equations was done on a Pentium 4, 2GB RAM, 1.86 GHz PC. The average computing time was approximately one hour and thirty minutes for each run. A high resolution discretisation scheme was used for all the equations in the study. In the analysis,

a solution was considered to have converged when the total normalised residual for the continuity equation dropped below 1 x 10^{-4}.

4.5.4 Results and Discussion

Preliminary runs were carried out for the geometry to ensure the solutions were independent of grid size. The results revealed that the differences in mean solid volume fraction were negligible, between 223,200 cells and 438,900 cells. The cut-off point for defining the curtain edge was taken to be a solids volume fraction of 1 x10^{-5} (Lee, 2008; Wardjiman et al., 2009). Referring to Figure 4.13, solid volume fractions were extracted from the *xy* plane through the middle of the box (*z=0.15m*). An example of this plane is shown in Figure 4.14. Solids volume fraction was averaged across a line in the *x* direction and within the curtain edges for a range of vertical heights. These results are presented in Table 4.13.

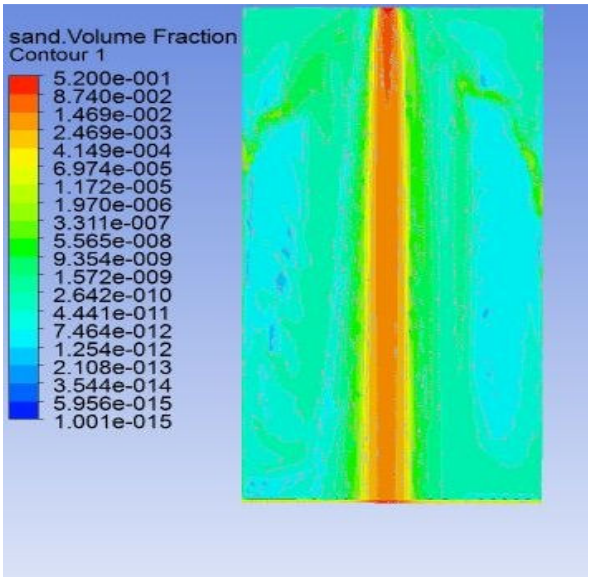

Figure 4.14: Contour profile of the solid volume fraction

The solid volume fraction contour profile presented in Figure 4.14 was compared with the cross-sectional photograph taken during the equivalent experiment such as that shown in Figure

4.11(a). For comparison, Figures 4.15 and 4.16 show the area profiles of the pixel intensity and solid volume fraction in the experimental image and the CFD respectively, which are qualitatively well matched. Taking the average area by integration of area profiles, both graphs gave the same area of 0.0278 m^2, illustrating similarity between the CFD profile and the image profile. The pixel intensities within the curtains in the photographic images reduce with vertical distance of the curtain as illustrated qualitatively in Figure 4.11(b) and quantitatively in Table 4.13. A comparable reduction in solid volume fraction was observed in the CFD results as well. However, contrary to expectations (Poletto et al., 1995) a linear correlation between the pixel intensity of the image and voidage could not be established across the entire range of volume fractions. At low solids volume fraction (<0.003) a direct correlation between volume fraction and pixel intensity was observed. However, at higher solids volume fractions the image pixel intensity becomes saturated. Pixel saturation is a result of both high volume fraction and also the significant depth (1.15 m) of curtain being photographed. If a significantly reduced depth of field was used, then the approach described in Nopharantana et al. (2003) may be applicable. In this approach, thresholding could be used to determine area fractions covered by the particles and then converted into volume fraction. However, a depth of field in the range of 10mm would be required. Unfortunately wall effects would also be more significant in this experimental setup.

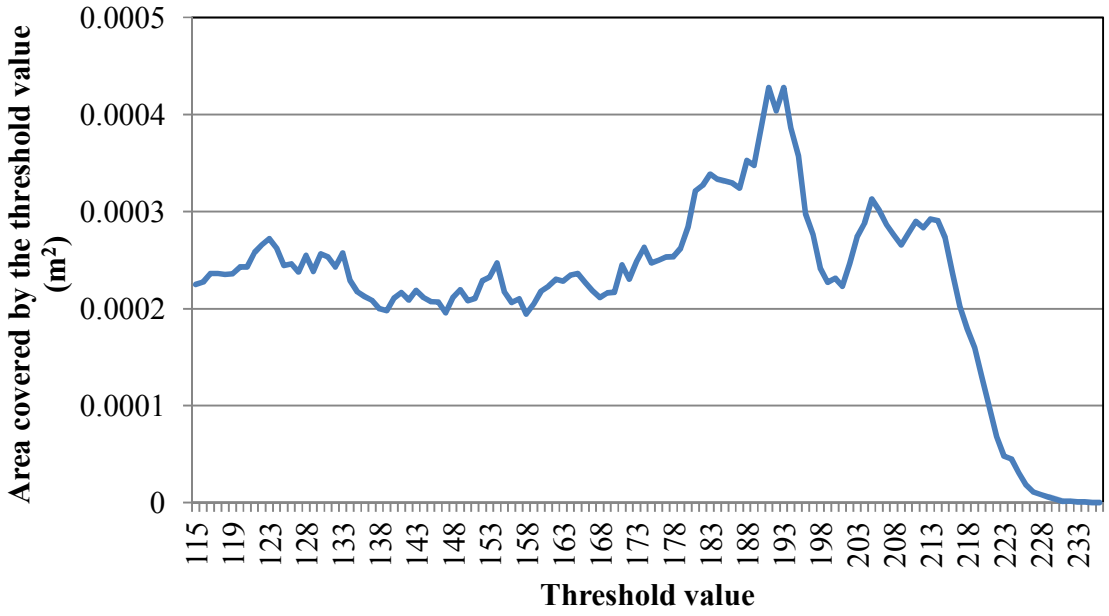

Figure 4.15: Area covered by the threshold values within the original image *(0.4 wt%, 4.5 rpm)*

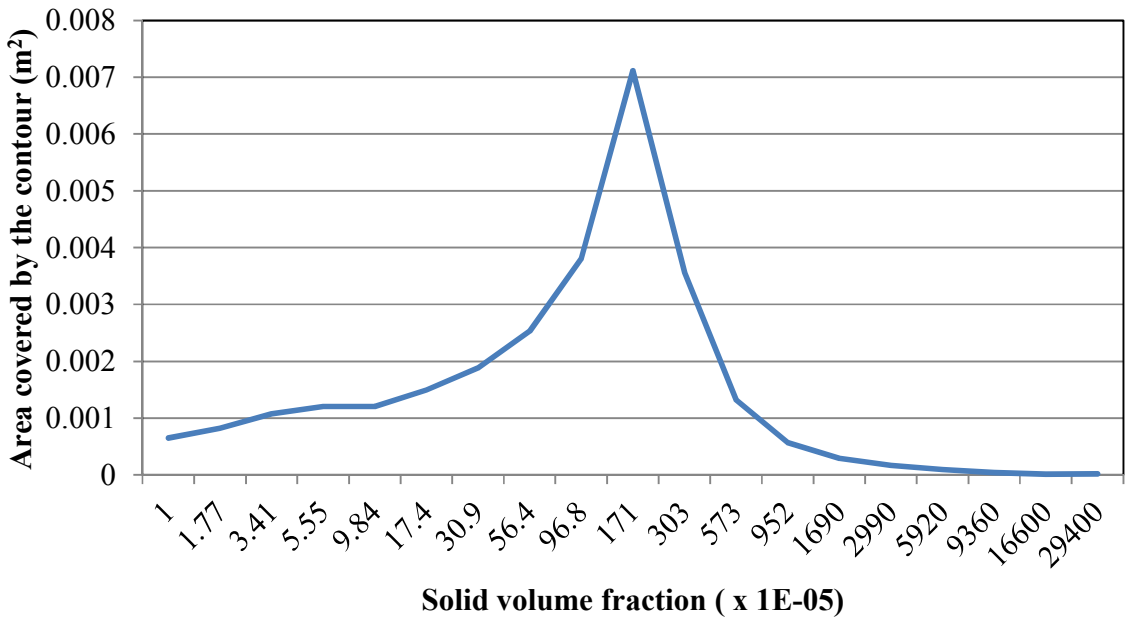

Figure 4.16: Area with CFD contour profiles, which are defined by their solid volume fraction

Table 4.13: Threshold value and solid volume fraction

Position from the solid inlet (m)	**0.1180**	**0.1967**	**0.2950**	**0.3933**	**0.4720**
Average image threshold value	189.9	183.0	182.2	172.8	169.1
Average CFD modelled Solid volume fraction	0.2180	0.0043	0.0031	0.0026	0.0023

In order to combine CFD results with the experimental images, an area averaged solids volume fraction (α_{ct}) was obtained. Again referring to Figure 4.13, solid volume fractions were extracted from the *xy* plane through the middle of the box (*z=0.15 m*). The solids volume fraction was averaged across the entire particle curtain from the curtain entrance to a set distance below the entrance (h_{ct}). These results are presented in Figure 4.17. By way of example, the average volume fraction of solids within a curtain 50 cm long would be 0.0049. In order to use the CFD results in combination with a matching experimental image, empirical equations for average solids volume fractions versus curtain height were derived from the data sets in Figure 4.17, and are presented in Table 4.14.

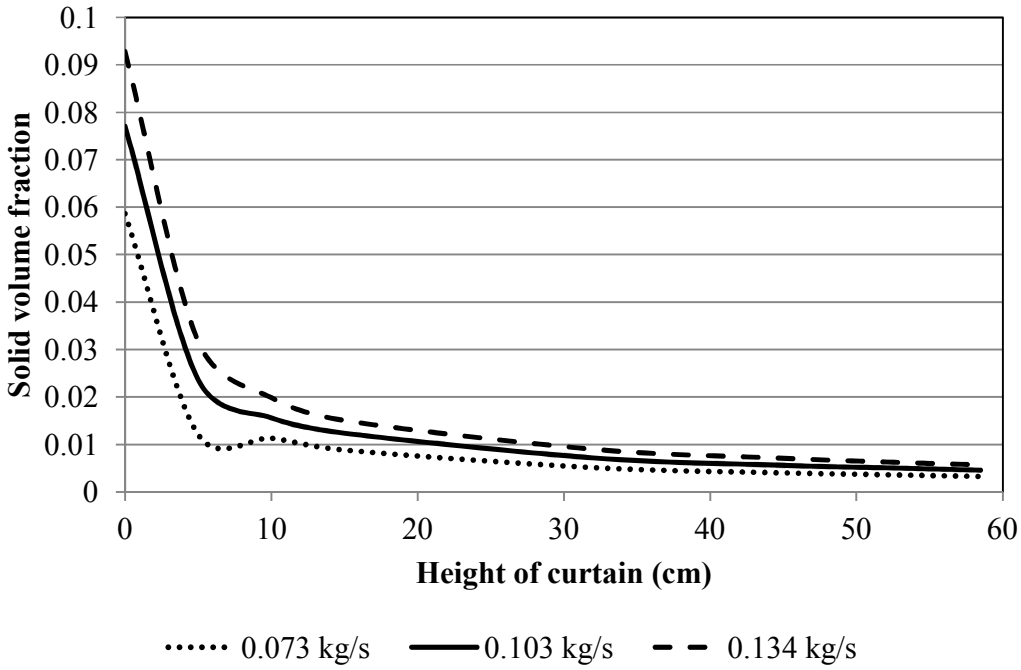

Figure 4.17: Effect of curtain height on solid volume fraction at different mass flow rates *(for free-flowing solids)*

Table 4.14: Empirical equations for determining solids volume fraction (α_{ct}) within the curtain as a function of curtain vertical drop distance in cm (h_{ct}) *(for free-flowing solids)*

Mass flow rate (kg/s)	Empirical equations
0.073	$\alpha_{ct} = \frac{0.003043h_{ct} + 0.07083}{h_{ct} + 1.209}$
0.103	$\alpha_{ct} = \frac{0.002479h_{ct} + 0.1592}{h_{ct} + 2.065}$
0.134	$\alpha_{ct} = \frac{0.00237h_{ct} + 0.2236}{h_{ct} + 2.409}$

Within a flighted rotating dryer there are multiple curtains and the height of each curtain within the drum varies according to flight location. In determining the mass of airborne solids, all

curtains within a single experimental data set were assumed to be discharging solids at the average mass flow rate determined via the geometry code. Curtain discharge rates are a complex function of flight and drum geometry, and Figure 4.12 illustrates the profiles as a function of rotational angle. Averaging is thought to be a reasonable simplification in line with the approach taken in compartment process models of flighted rotary dryers such as those of Sheehan et al. (2005) and Britton et al. (2006). The mass of solids in each curtain (m_{ct_i}) of length h_{ct} was calculated using Equation 4.17, where A_c is the cross-sectional area of each curtain in an image and L is the length of the dryer (1.15 m). The bulk density of each curtain (ρ_{bct}) in Equation 4.17 was determined using Equation 4.16, where the voidage (ε_v) was equal to $(1 - \alpha_{ct})$ and the solids volume fraction (α_{ct}) was calculated via the relationships described in Table 4.14.

$$m_{ct_i} = \rho_{b_{ct}} \times A_{ct} \times L \qquad \textbf{4.17}$$

The total mass of the airborne phase (m_a) was estimated by summing the masses of all the curtains contained in each image, via Equation 4.18, where n_{ct} is the total number of curtains.

$$m_a = \sum_{i=1}^{n_{ct}} m_{ct_i} \qquad \textbf{4.18}$$

The estimated masses of airborne solids are presented in Table 4.15 for the low moisture content experimental runs. The masses presented are the average from a selection of five images taken from the batch of photos closest to the determined design loading state. Images were also selected with the FUF as close as possible to the 9 o'clock position. It is noted that the proportion of airborne solids in a design loaded dryer is not constant and increased with increasing rotational speed. It is also well known that an increase in rotational speed reduces solids residence time. Airborne masses for the higher moisture content solids were more problematic to

determine because of the cohesive nature of the solids and the complexity of modelling these flows using CFD. CFD modelling of cohesive particle curtain flows was not attempted in this work.

Table 4.15: Active phase for different angles of repose

Rotational speed (rpm)	Moisture content (wt%)	Dynamic angle of repose (degrees)	Active phase (kg)	Design load (kg)	% active phase
2.5	0.75	46.9 ± 2.9	1.4	33.9	4.0
3.5	0.40	44.7 ± 2.0	1.9	31.8	6.2
4.5	0.40	45.0 ± 2.5	2.4	34.7	7.2

4.6 Application of geometric modelling to predict design loading

The design loadings obtained experimentally were compared to predicted design loadings using geometric models from the literature. The precise design loading condition was determined from Figure 4.8(a-c) as described in the previous section. A selection of images was taken from the batch of photos closest to the determined loading state and having the FUF tip closest to the 9 o'clock position. The total flight-borne holdup was estimated based on the average of the five images selected from the set. ImageJ software was used to trace the regions of interest so as to minimise potential errors in the validation process. Experimentally determined values for the areas of the FUF and the UHD at design load were used in Equations 2.2 to 2.4. Table 4.16 presents the percentage of deviation of the model prediction from the experimental design loading, based on area. The models suggested by Porter (1963) and Kelly (1977) overestimate the design load and are less consistent (7.5% and 7.8% standard deviation respectively) when compared to the predictions using the Baker (1988) model, which under-estimates the design

load but is more consistent (4.4% standard deviation). The propagated error in the validation process was within 3%.

Table 4.16: Percentage of deviation of the design load model

Experimental conditions		Experimental	Percentage of model deviation		
Solid	Rotational speed (rpm)	Design load (kg)	Porter (1963)	Kelly (1977)	Baker (1988)
0.4 wt%	3.5	31.5	37.8	43.5	-25.8
0.4 wt%	4.5	34.5	33.0	38.5	-31.5
0.75 wt%	2.5	33.9	24.3	29.5	-27.5
1.25 wt%	2.5	38	37.2	43.0	-21.3
1.25 wt%	3.5	41	22.3	27.3	-21.0
1.25 wt%	4.5	43	29.4	34.8	-19.3
2.1 wt%	2.5	43	20.1	25.1	-23.9

It is worth noting that Baker's model was based on the flight-borne mass only and excluded the airborne solids. The relevant holdups for the other two models (Porter, 1963; and Kelly, 1977) were not clearly defined in the original sources. In Table 4.16, these latter model predictions are compared to the flight-borne solids only. In order to compare these model predictions against total drum hold-up, two options were considered. The first involved determining the design loading hold-up (for example, see Figure 4.8a). The cross-sectional area of the solid within the drum was calculated by dividing the design loading mass by the solid consolidated density. The second involved approximating the airborne hold-up from previous calculations (roughly 5–10%). Using either of these approaches, the match of these models to the experimentally

observed design loadings still remains poor and they are also inconsistent across the spectrum of experimental conditions. Based on the reasonable consistency of deviation in the results, a correction factor which modifies Baker's (1988) model is recommended for modelling the flight-borne solids in a design loaded dryer (Equation 4.19).

$$Design\ load_{passive} = \left(1.24 \times M_{design}\right) \qquad \textbf{4.19}$$

where M_{design} is given by Equation 2.4 and $Design\ load_{passive}$ is the design loading of the passive or flight-borne solids.

The potential to use geometric modelling to determine airborne mass and thus develop predictive models for the total flighted rotary dryer holdup was considered. The flighted rotary dryer compartment model described in Britton et al. (2006) uses transport coefficients based on average solids cycle times to determine the ratio of airborne to flight-borne solids. In their model, transport coefficients regulating the flow between the airborne and flight-borne phases were related to the mass averaged time for a solid particle to fall though the air phase (termed the mass averaged fall time: *maft*) and the mass averaged time (t_p) for the solid particle to return, via flight rotation, back to the mass averaged discharge location (θ_D). The derivation of the mass averaged discharge location (θ_D) via a flight discharge geometry model is described in Britton et al. (2006) and Lee (2008).

Referring to Figure 4.18, the mass averaged falling height of a solid particle (*mafh*) can be expressed as a function of the dryer radius (R) and the mass averaged discharge location Equation 4.20. The first term in the right hand side of the equation represents the height when the solid particle falls into the active phase (point *i*) to the tip of another flight at the base of the

drum (point *ii*) as shown in Figure 4.18 while the second term is the height from flight tip (point *ii*) to the base of the drum (point *iii*). It should be noted that the derivation of the second term is based on one's judgment on where the particles should fall.

$$mafh = sin(\theta_D - 90^o) \times 2 \times R_F + \left(\left(\frac{R + R_F}{2}\right) - R_F\right) \quad \textbf{4.20}$$

The mass averaged falling time (*maft*) of the solid can be calculated using Newton's equations of motion (in this case neglecting drag and assuming that the initial velocity of the falling particle is zero) via Equation 4.21, where $\bar{g}$ is the acceleration due to gravity.

$$maft = \sqrt{\frac{2 \times mafh}{\bar{g}}} \quad \textbf{4.21}$$

The time for a particle to return to the discharge point (t_p) is a function of rotational speed (ω) in radians per second and of the dryer geometry, such as the slope of the drum (θ).

$$t_p = \frac{acos\left(1 - \left(\frac{(mafh \times cos\,\theta)^2}{2 \times {R_F}^2}\right)\right)}{\omega} \quad \textbf{4.22}$$

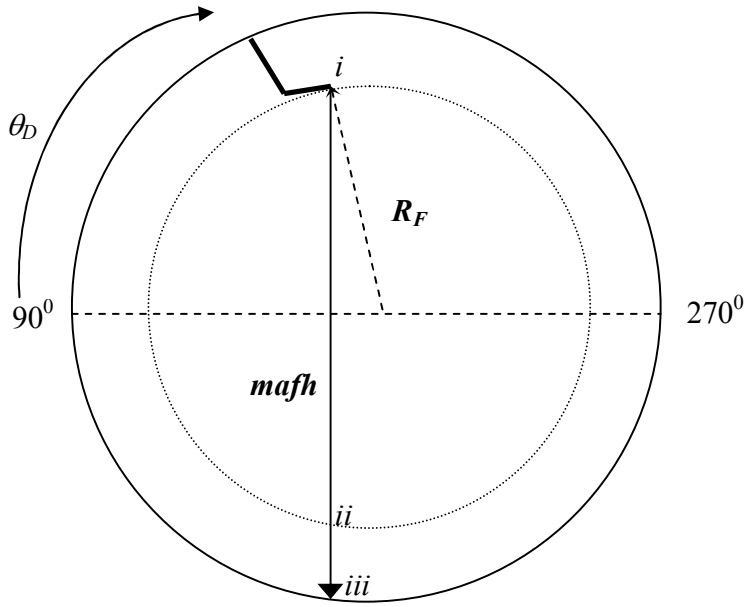

Figure 4.18: Drum cross section showing the mass averaged falling height geometrical details

At steady state, the mass ratio of airborne (m_a) to flight-borne (m_p) solids at design loading can be derived from a mass balance on the compartments within the model described in Britton et al. (2006).

$$\mathcal{R} = \frac{maft}{t_p} = \frac{m_a}{m_p} \qquad \textbf{4.23}$$

In Table 4.17, the ratios of the airborne to flight-borne solids based on the experimental images coupled with CFD are compared to the ratios determined via the geometric modelling described in Equations 4.20 to 4.23. Considering the propagated uncertainty in obtaining these ratios, the results are in good agreement and demonstrate a very high degree of correlation ($R^2 \approx 1$). Enhancing the quality of the geometric modelling with more realistic values, such as non-zero

initial velocity and a reduced *mafh* to account for contact with flight-borne solids, would only improve the match between these ratios.

Table 4.17: Ratio of airborne to flight-borne solids at design loading *(with different angles of repose)*

Rotational speed (rpm)	Dynamic angle of repose (degrees)	CFD approach	Geometric model
2.5	46.9 ± 2.9	0.042	0.047
3.5	44.7 ± 2.0	0.064	0.067
4.5	45.0 ± 2.5	0.078	0.085

It is suggested that total dryer holdup under design loading (M_{design}^{TOT}) can be determined using a geometric flight unloading model, such as described in Britton et al. (2006), Lee (2008), Lee and Sheehan (2010). Equation 4.19 can be used to determine the total flight-borne solids and the ratio of cycle times in Equation 4.23 can be used to determine the airborne solids. Combining these two holdup phases, the total holdup can be expressed as:

$$M_{design}^{TOT} = \left(1.24\left(2 \times \sum_{f}^{n} m_i\right) - m_{FUF}\right)(1 + \mathcal{R}) \qquad \textbf{4.24}$$

4.7 Summary

The design loading for a pilot scale flighted rotary dryer was determined using image analysis. The automated image analysis technique used contrast enhancement, filtering and thresholding to enhance image quality and allow multiple images to be processed in order to quantify the amount

of solid within the flights of a rotating drum. Processed images were used to determine the design load via different approaches and were reasonably similar. The approach based on the saturation of the airborne solids and of the flight-borne solids in the upper half of the drum demonstrated similar profiles and new phenomena. The peaks in the areas of the airborne solids and of the flight-borne solids in the upper half of the drum may be used as a criterion to estimate the design load but require highly accurate determination of area and also understanding flight-borne solids bulk densities. The areas of first unloading flight (FUF) at different loading conditions were fitted using a piecewise regression analysis and it is argued that they offer a more suitable means to estimate the design load. The effects of rpm (2.5rpm, 3.5rpm, and 4.5 rpm) and solids cohesion on the design load were determined and found to be significant. Additionally, airborne solids demonstrated increasingly dense and increasingly discontinuous curtains as the degree of solids cohesion increased from a flow index *(ff_c)* of 11 to 2.2.

A new methodology was developed to integrate image analysis and Eulerian-Eulerian CFD simulation of free-falling curtains to estimate the mass of airborne solids at the design load. CFD simulations of free-falling, non-cohesive curtains were well matched to the observed curtain images. A consistent increase in the mass of airborne solids with increasing drum rotational speed was observed. Image pixel intensities could be correlated to predicted CFD curtain solids volume fractions at low solids volume fraction but became saturated at high volume fractions, limiting the potential to use image analysis alone to determine curtain voidage. The experimentally determined design loads were compared to common geometry-based design load models available in literature and a modified equation based on the Baker (1988) model was recommended. The ratio of airborne to flight-borne solids at the design load determined via geometric analysis were similar and highly correlated to the ratios determined experimentally.

CHAPTER FIVE

5. SOLID TRANSPORT MODELLING

This chapter outlines the development of a pseudo-physical compartment model for the MMG industrial dryer. The MMG rotary dryer contains both unflighted and flighted sections. To the best knowledge of the author, there is no literature describing these mixed mode dryers or their modelling. However, there is extensive description of modelling both unflighted and flighted drums in isolation. In this study, the modelling strategy for the flighted sections was based on a compartment modelling approach. This modelling approach is a series-parallel formulation of well-mixed tanks whereby the solid distributions between the compartments are estimated via geometric modelling and design loading. The kilning phase occurring in the unflighted sections was modelled using the axially-dispersed plug flow equation. RTD undertaken at different dryer operating conditions (see Section 3.5) were used for model parameter estimation. The operating conditions for all RTD trials presented in Tables 3.6, 3.8–3.11 are used as model inputs. The geometrical configuration of the MMG industrial dryer presented in Section 3.2 is used to describe the dryer in the geometric model. Simulations and parameter fitting were undertaken using gPROMS (process modelling software). To verify the model structure and parameters, the effect of operating conditions on RTD is investigated.

5.1 Model development

The model structure is presented in Figure 5.1. Following typical criterion (Matchett & Baker, 1988; Sheehan et al., 2005; Britton et al., 2006), airborne solids are regarded as active solids and flight and drum borne solids are regarded as passive solids. Distinguishing between these two solids phases is critical to the development of energy balances on these dryers. Studies have modelled the solid transport in the flighted rotary dryer using different approaches: empirical

correlations, semi-empirical correlations, mechanistic, and compartment modelling. All these approaches except compartment modelling do not account for the effect of flight configuration, solid distribution, drum loading capacity and solid properties such as dynamic angle of repose. The compartment model parameters are determined through geometric modelling based on dryer geometry and solids physical properties. In this study, modelling of the flighted sections was based on the pseudo-physical compartment modelling approach (Sheehan et al., 2005). The original structure described in Sheehan et al. (2005) and Britton et al. (2006) accounted for counter-current gas flow and flights that were of constant geometry and frequency down the entire length of the dryer. The dryer examined in this study is a co-current dryer in which hot gas flows in the same direction as the solids. Furthermore, different flight configurations are used along the dryer length including the non-flighted sections.

Previous studies have assumed the solid transport within the unflighted dryer as plug flow with (Danckwerts, 1953; Fan & Ahn, 1961; Mu & Perlmutter, 1980; Sai et al., 1990) or without (Ortiz et al., 2003; Oritz et al., 2005) axial mixing. However, experimental studies have established the occurrence of axial mixing phenomenon within the unflighted sections (Sai et al., 1990; Bensmann et al., 2010). In this study, the unflighted sections were modelled as an axial dispersed plug flow system.

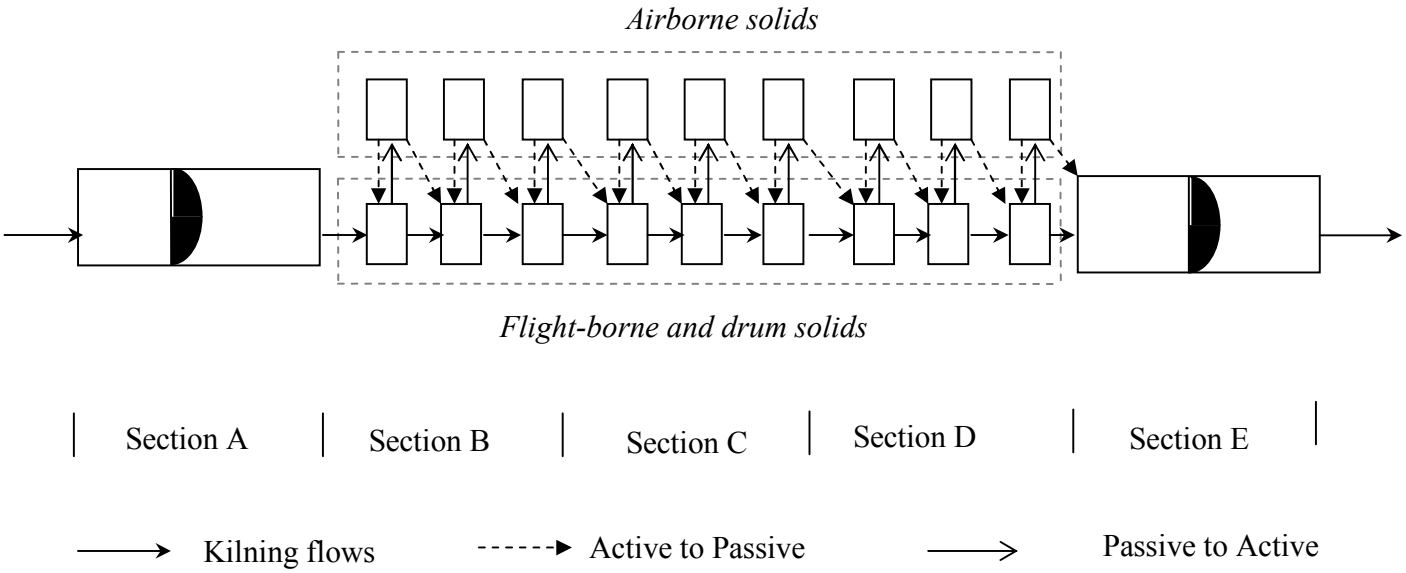

Figure 5.1: Model structure

5.1.1 Flighted section

The flow from the passive phase into the active phase in a given cell is characterised by transport coefficient k_2. The kilning flow is the movement of solids from passive cell to passive cell and is characterised by transport coefficient k_4. Previous studies have estimated the kilning flow transport coefficient (k_4) which was a function of kilning bed angle and rotational speed (Sheehan et al., 2005; Britton et al., 2006). However, their approach did not utilize an obvious physical representation of the kilning phase because the kilning or passive phase was modelled as a well-mixed tank. A more physically realistic structure would be to use a dispersed plug model or series of partial differential equations rather than ordinary differential equations. Unfortunately, it is significantly more computational demanding to solve a system of partial differential equations (plug flow model), particularly when coupled to the active phase which is modelled using compartment modelling approach. A study by Lee et al. (2005) observed no difference in the solutions obtained using either plug flow model or well-mixed tanks for the

active phase. In this study, the kilning flow was modelled using what is considered to be a more physical realistic approach: dispersed plug flow model for the unflighted section.

The flow of solid from the active phase $(k_3 m_a)$ is divided into two different paths: axial movement of falling solid into the next passive cell and the return of falling solid into the corresponding passive cell. The splitting of the flow is governed by the forward step coefficient (C_F). Another important difference in the model structure between this study and that of Britton et al. (2006) is the back-mixing flow caused by the airflow drag on the solids particles into the active phase. In this study, there is no back-mixing flow into the active phase. The drag force analysis showed there was minimal airflow drag effect on the solid particles and this can be attributed to the physical properties of the solids. The mean particle size in this current study varied from 18 mm to 6 mm while the mean particle size in Britton et al. (2006) was 0.84 mm. Based on the model structure presented in Figure 5.2, the mass balances on solids for the two phases and the tracer are described in Equations 5.1–5.3.

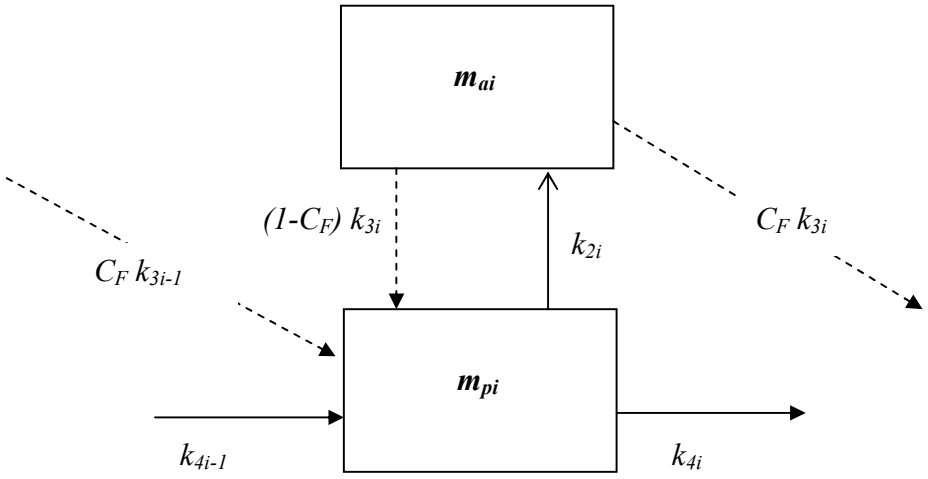

Figure 5.2: Model structure for the flighted section

The mass balance on solids in the passive cell *i*:

$$\frac{dm_{pi}}{dt} = k_{4i-1}m_{pi-1} + k_{3i-1}C_F m_{ai-1} + k_{3i}(1 - C_F)m_{ai} - k_{2i}m_{pi} - k_{4i}m_{pi} \quad \textbf{5.1}$$

The mass balance on solids in the active cell *i*:

$$\frac{dm_{ai}}{dt} = k_{2i}m_{pi} - k_{3i}C_F m_{ai} - k_{3i}(1 - C_F)m_{ai} \quad \textbf{5.2}$$

The mass balance on tracer in the passive cell *i*:

$$\frac{dt_{pi}m_{pi}}{dt} = k_{4i-1}t_{pi-1}m_{pi-1} + k_{3i-1}C_F t_{ai-1}m_{ai-1} + k_{3i}t_{ai}(1 - C_F)m_{ai} - k_{2i}t_{pi}m_{pi} - k_{4i}t_{pi}m_{pi} \quad \textbf{5.3}$$

where m_{pi}, m_{ai}, t_{ai} and t_{pi} are passive mass (kg), active mass (kg), tracer concentration in active phase (ppm) and tracer concentration in passive phase (ppm) respectively

5.1.2 Unflighted section

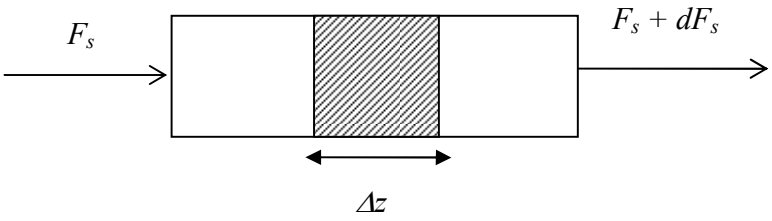

Figure 5.3: Model structure of the unflighted section characterised by its feed rate (F_s) and length

Considering an unflighted section of the dryer as the system in Figure 5.3, the mass balance equation across a differentiable element *(Δz)* along the length of the drum is:

$$\frac{\partial}{\partial t}(\rho_s A_s \Delta z) = F_s|_z - F_s|_{z+\Delta z} \quad \textbf{5.4}$$

Mass flow rate *(F_s)* for the axially dispersed plug flow (Davis & Davis, 2003) is defined as:

$$F_s = u_s A_s \rho_s - \frac{\wp A_s \rho_s}{\Delta z} \qquad \textbf{5.5}$$

where u_s, m_s, A_s and ρ_s are the solid velocity *(m/s),* kilning mass per length *(kg/m),* cross-sectional area occupied by the solid *(m^2)* and solid consolidated density *(kg/m^3)* respectively.

By substitution,

$$\frac{\partial}{\partial t}(\rho_s A_s \Delta z) = \left(u_s A_s \rho_s - \frac{\wp A_s \rho_s}{\Delta z}\right)\Big|_z - \left(u_s A_s \rho_s - \frac{\wp A_s \rho_s}{\Delta z}\right)\Big|_{z+\Delta z} \qquad \textbf{5.6}$$

Dividing by Δz and taking the limit $\Delta z \to 0$, and assuming $\wp$ is constant with respect to length

$$\frac{\partial}{\partial t}(A_s \rho_s) = \wp \frac{\partial^2}{\partial z^2}(A_s \rho_s) - \frac{\partial}{\partial z}(u_s A_s \rho_s) \qquad \textbf{5.7}$$

The term $A_s \rho_s$ is the mass of solids per unit length and is an important property of the model as it represents drum holdup

$$m_s = A_s \rho_s \qquad \textbf{5.8}$$

By substitution, the axially dispersed plug flow model for the unflighted drum is given as:

$$\frac{\partial}{\partial t}(m_s) = \wp \frac{\partial^2}{\partial z^2}(m_s) - \frac{\partial}{\partial z}(u_s m_s) \qquad \textbf{5.9}$$

In similar manner, the mass balance for the tracer is:

$$\frac{\partial}{\partial t}(x_t m_s) = \wp \frac{\partial^2}{\partial z^2}(x_t m_s) - \frac{\partial}{\partial z}(x_t u_s m_s) \qquad \textbf{5.10}$$

where, x_t is the tracer concentration*(kg/kg)*.

5.1.3 Boundary conditions

The Danckwerts boundary conditions (Danckwerts, 1953) for Equations 5.9 and 5.10 were used and are shown in Equations 5.11–5.14.

For Equation 5.9

$$z = 0, \qquad m_s(0) = {}^{F_s}/_{u_s} \tag{5.11}$$

At the outlet, the solids do not disperse back into the dryer and thus, the outlet boundary condition is stated as follows:

$$z = L, \qquad \wp \frac{\partial^2 m_s}{\partial z^2} = 0 \tag{5.12}$$

For Equation 5.10

$$z = 0, \qquad x_t(0) = x_{in} \tag{5.13}$$

$$z = L, \qquad \wp \frac{\partial^2 m_s}{\partial z^2} = 0 \tag{5.14}$$

5.2 Model parameters

Important model parameters include active cycle time $(\bar{t}_a)$, passive cycle time $(\bar{t}_p)$, and mass average forward step *(D_{avg})*. The active cycle time is the mass averaged falling time of the solid (Figure 5.4). The passive time can be defined as the time it takes the discharge particle to travel within the drum from the point it enters the passive phase to the original discharge position (Figure 5.4). The average forward step is the axial distance the particle travels from the flight tip to the dryer base, which is due to the inclination of the drum and the effect of airflow drag on the particle (Figure 5.5). The average forward step (*D_{avg})* provides bounds on the maximum number of cells since solids are constrained not to fall (geometrically) further than one cell ahead. In this study, a drag force analysis on the particles indicated that drag can be neglected because of large particle sizes of the zinc concentrate across the length of dryer. These model parameters

$(\bar{t}_a, \bar{t}_p, D_{avg})$ were determined via geometric modelling based on the mass contained within the flights.

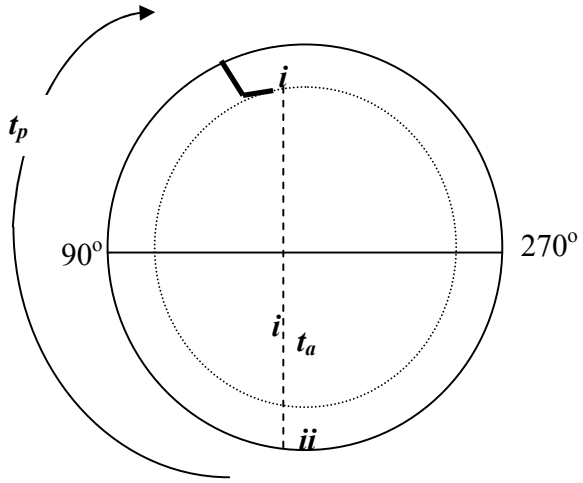

Figure 5.4: Drum cross section showing geometrical details *(Active cycle time is the time taken for the solids to fall from point ii to point i while passive cycle time is the time taken for the discharge particle at point i to move to original discharged point ii).*

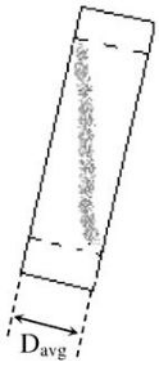

Figure 5.5: Axial displacement of particle

5.2.1 Geometric modelling

The cross-sectional area of solids within the flights and solids discharge rate from the flight are calculated using geometric modelling described in Lee and Sheehan (2010). Lee and Sheehan (2010) developed a geometric model based on the geometric characterisation of two-staged flight using the number of flights, flight configuration, dryer geometry and mean surface angle. In their study, the following model assumptions were made: the mean surface angle remains constant and describes the behaviour of the solid across the entire rotation of the flight, the solids are free-flowing and there is a continuous unloading process. Their experimental results showed that the mean surface angle was not constant because of the avalanche discharge pattern of the solids from the flights. However, their experimental flight unloading profile was within 95% confidence interval of the predicted data, which indicated that the model assumptions are suitable for this current study.

The geometric model (Microsoft Excel platform) which was developed by Lee (2008) was used in this study. The key elements of the geometric model are the calculation of flight areas as a function of rotation angle and the corresponding cycle times determined using Newton's equations of motion. Flight areas are differentiated with respect to time to obtain mass flow rates. Mass averaged properties(Ψ) are determined within the geometric model using the Equation 5.15 (Britton et al., 2006). The mass averaged properties determined in the geometric model are mass averaged falling height, mass averaged falling time, mass average passive cycle time.

$$\Psi = \frac{\sum_j m_j \, t_a}{\sum_j m_j} \qquad \textbf{5.15}$$

The geometric model was modified to include the new design load model discussed in section 4.6. The modified equation based on Baker's (1988) model is presented again in Equation 5.16. The accurate estimation of the design load and loading state of the dryer directly influences determination of the aforementioned model parameters.

$$Design\ load_{passive} = 1.24 \times \left[\left(2 \times \sum_{f}^{n} m_i \right) - m_{FUF} \right] \quad \textbf{5.16}$$

The interaction between the geometric model and the process model is shown in Figure 5.6. The process model data (passive mass (m_p) and moisture content (x_w)) were exported into the geometric model so as to calculate the model parameters $(\bar{t}_a, \bar{t}_p)$ and the geometric constraints of $\left(D_{avg}, m_{p_{design}}\right)$. In order to simplify the initial fitting process, energetic processes were excluded and a moisture content profile was assumed. The fitted equations for moisture content and consolidated bulk density (Equations 3.1 and 3.4) as function of length along the drum were used. In order to reflect the inlet and outlet moisture content for each RTD test, Equation 3.1 was scaled for different RTD trials. The fitted linear equation of dynamic angle of repose versus moisture content (Equation 3.2) was used to obtain the dynamic angle of repose for each model compartment.

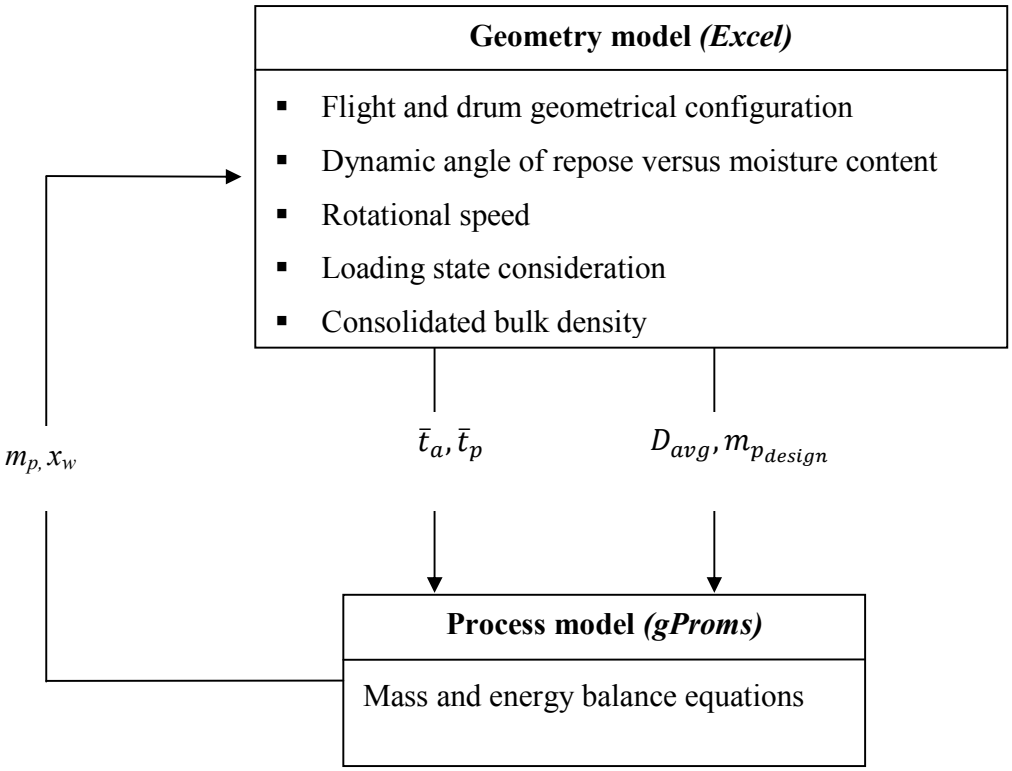

Figure 5.6: Geometric model structure

Regression models for the active and passive cycle times, mass averaged falling height and design load were derived using the geometric model across a range of dynamic angle of repose and loading state. These equations were used in gProms and are presented in Appendix F (sub-section: geometric modelling for sections B, C and D). The regression model for the active and passive cycle times were a function of the dynamic angle of repose, the loading condition of the drum and the angle of inclination of the drum (Sheehan et al, 2005; Britton et al., 2006).

5.2.2 Flighted section

The transport coefficients k_2 and k_3 were calculated as the inverse of the passive and active cycle times respectively (see Equation 5.17) (Sheehan et al., 2005; Britton et al., 2006). If the

mass in flight and drum solids exceeds the design load condition, the flow from the flight and drum borne phase to airborne phase is set to maximum (Equation 5.18).

$$k_2 = \frac{1}{\bar{t}_p} \quad , \qquad k_3 = \frac{1}{\bar{t}_a} \tag{5.17}$$

$$\begin{aligned} m_p > m_{p_{design}}, \quad & \left|k_2 m_p\right|_{MAX} = k_2 m_{p_{design}} \\ m_p \leq m_{p_{design}}, \quad & k_2 m_p = k_2 m_p \end{aligned} \tag{5.18}$$

Equation 5.19 shows the relationship between the kilning flow transport coefficient, solid velocity and length of the compartment cell.

$$k_{4_{(i)}} = \frac{u_{s_{(i)}}}{L_{(i)}} \tag{5.19}$$

where $k_{4_{(i)}}, u_{s_{(i)}}, L_{(i)}$ are kilning flow transport coefficient *(s^{-1}),* solid velocity (*m/s)*, and length of the compartment cell *(m)* respectively.

The splitting of the flow from the active cell is governed by the forward step *(C_F)*, which was calculated as the ratio of the average forward step (D_{avg}) to the representative physical length of the cell (Sheehan et al., 2005). The physical length of each compartment cell was calculated geometrically based on the solids not falling further than one cell ahead, which constrained the numbers of compartment cells within the flighted sections and is a key component in forcing physical realism upon the system. The effect of compartment numbers is well described in Lee (2010), as such reference to that analysis is provided. Thus, Equation 5.20 was used to determine

the number of cells within each flighted section. Table 5.1 gives the number of cells in the each flighted section.

$$N_c = \frac{L_s}{D_{avg}} \tag{5.20}$$

where N_c, L_s and D_{avg} are number of cells within the section, length of the section *(m)* and average forward step *(m)* respectively.

Table 5.1: Number of cells in each flighted section

Section	Number of cells *(N_c)*
B	8
C	12
D	22

5.2.3 Unflighted section

The solid velocity and axial dispersion coefficients were assumed to be constant throughout the dryer. Their estimation will be discussed in the parameter estimation section (Section 5.3.1).

5.2.4 Scaling effects

An internal examination of the dryer prior to the RTD experiment (Test 3) revealed significant scale accumulation within the flights and the internal walls of the drum. Consequently, the study assumed that the flight loading capacity was reduced by 80%. Figures 5.7 and 5.8 illustrate the changes in the dryer geometry and flight configuration due the scale accumulation. A scale accumulation factor *(S_F)* was introduced in order to modify the geometrical configuration of the flights and the drum. All the modified dimensions due to the scale build-up were used in the

geometric modelling. Equation 5.21 provides information on the calculation of the scale accumulation factor.

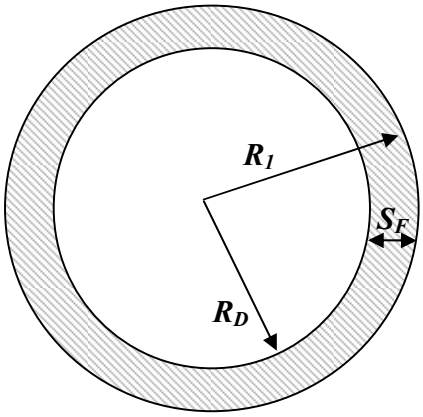

Figure 5.7: Internal radius of a scale accumulated dryer

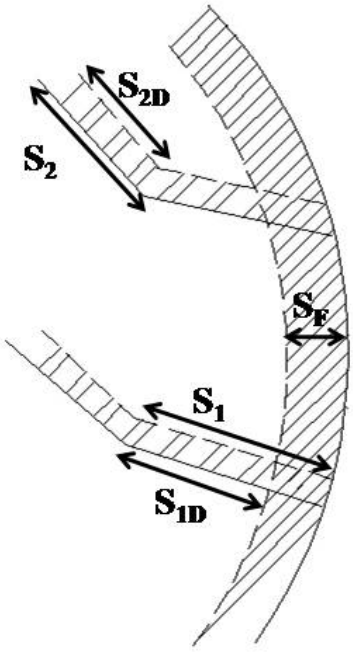

Figure 5.8: Scale accumulation around the flight base *(s_1)* and the flight tip *(s_2)*

The scale accumulation factor (S_F) was calculated as follows:

$$S_F = s_1 \times A_{SF} \quad \textbf{5.21}$$

where s_1 and A_{SF} are flight base and percentage of area covered by scale accumulation respectively. The percentage ranges between 0–100%.

5.3 Multi-scale model architecture

In this study, gPROMS (general process modelling system) numerical modelling software was used in simulating the developed process models. The software has capability to solve systems of integral, partial, ordinary and algebraic equations. There are different entities in the software: model, process, estimation and experiment. The process entity provides the operating conditions of the process, which includes the initial conditions, control variables and solution parameters. The estimation and experiment entities are used for the parameter estimation and process optimisation. The provision to build a model and sub-models is available in gPROMS, which is suitable for multiscale modelling. The model and sub-models are linked via the defined data streams. A detailed description of the components, programming approach and solvers in gPROMS can be found in gPROMS (2004).

The numerical solver in gPROMS lacks the capacity to execute iterative model simulation. For instance, an "IF or FOR loop" available in other programming languages is difficult to implement in gPROMS. However, the advantage of gPROMS software is the interface with other softwares such as FLUENT (Computational Fluid Dynamics software package), Microsoft Excel and programming languages like FORTAN and C++. Due to the iterative nature of the geometric model, Microsoft Excel was used. The linking of gPROMS to Microsoft Excel was not undertaken because it is more computationally demanding. As a result, the regression models for geometric modelling were developed in Microsoft Excel. gPROMS code for this study can be

found in Appendix F. Figure 5.9 shows the interaction between the geometry model and process models.

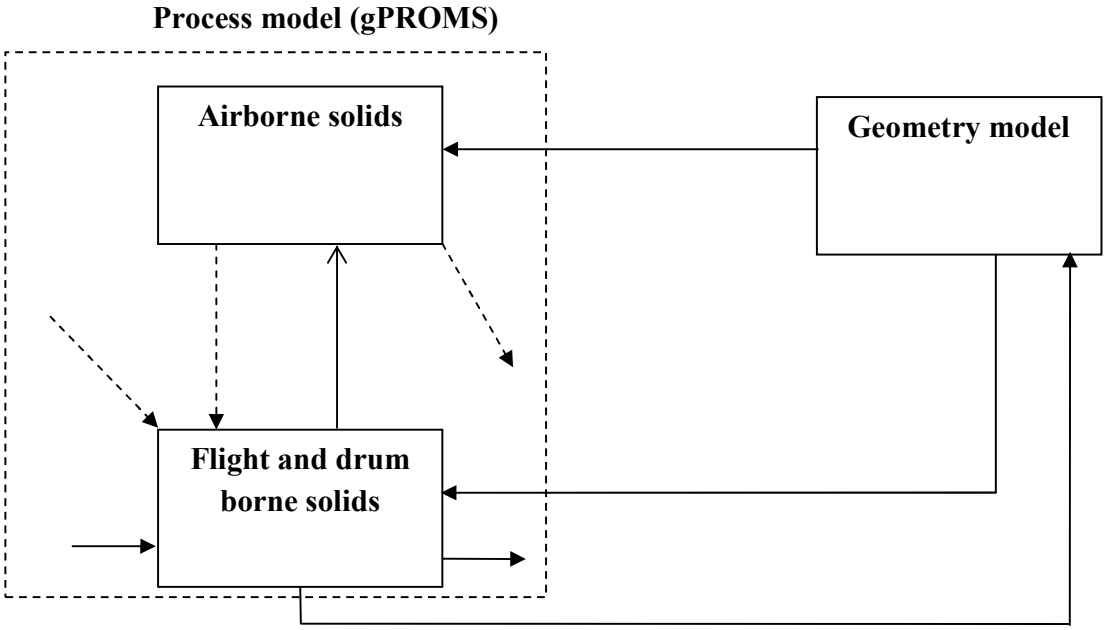

Figure 5.9: Interaction between the process model and geometric model

5.3.1 Numerical solution and parameter estimation

The solid velocity and the axial-dispersion co-efficient ($\wp$) were the parameters estimated. The parameter estimation process was executed in gPROMS software and was based on minimising the sum of square errors between the modelled RTD and experimental RTD data points. The following objective function (Equation 5.22) was used. There are different variance models in gPROMS software and an appropriate variance model is chosen based on the magnitude of standard deviation within the predicted or experimental data. In this study, the constant relative variance model was used because the standard deviation values of the RTD data varied with the magnitude of the tracer concentration. An initial guess value, and lower and upper limits of the

standard deviation are required. In this study, the initial guess value was 0.5, lower and upper limits were 0.01 and 10 respectively.

$$\Gamma = \frac{z}{2} In(2\pi) + \frac{1}{2} \min_{\vartheta} \left\{ \sum_{i=1}^{\alpha_i} \sum_{j=1}^{\beta_j} \left[In\left(\sigma_{ij}^2\right) + \frac{\left(\bar{Y}_{ij} - Y_{ij}\right)^2}{\sigma_{ij}^2} \right] \right\} \qquad \textbf{5.22}$$

where Z is the total number of measurements taken during the experiments, ϑ, α and β_i, are the set of model parameters to be estimated (u_s, $\wp$), the number of experiments, and the number of variables measured in *i*th experiment: 1 and the number of measurements of *j*th variable in the ith experiment. $\bar{Y}_{ij}$ is the *k*th measured value of variable *j* in experiment *i*. Y_{ij} is the *j*th predicted value of variable *j* in experiment *i*. σ_{ij}^2 is the variance of the *j*th measurement of variable *j* in experiment *i*. σ_{ij}^2 is described by the models available in gPROMS.

Preliminary runs found that discretisation scheme and number of discretised cells within the plug flow models have significant effect on the accurate estimation of the parameters and the fitting of the RTD profile. Figure 5.10 shows the effect of grid spacing within the unflighted sections on the fitting of the RTD profile. Large grid sizes (0.3 m and 0.15 m) resulted in numerical instability. The grid independency study revealed that the fitted RTD profiles of 0.075 m grid size and 0.0375 m grid size were similar. Based on 0.075 m grid size, the number of discretised cells for sections A and E were 28 and 100 respectively. It should be noted that the two unflighted sections (sections A and E) were discretised using second order backward finite difference scheme.

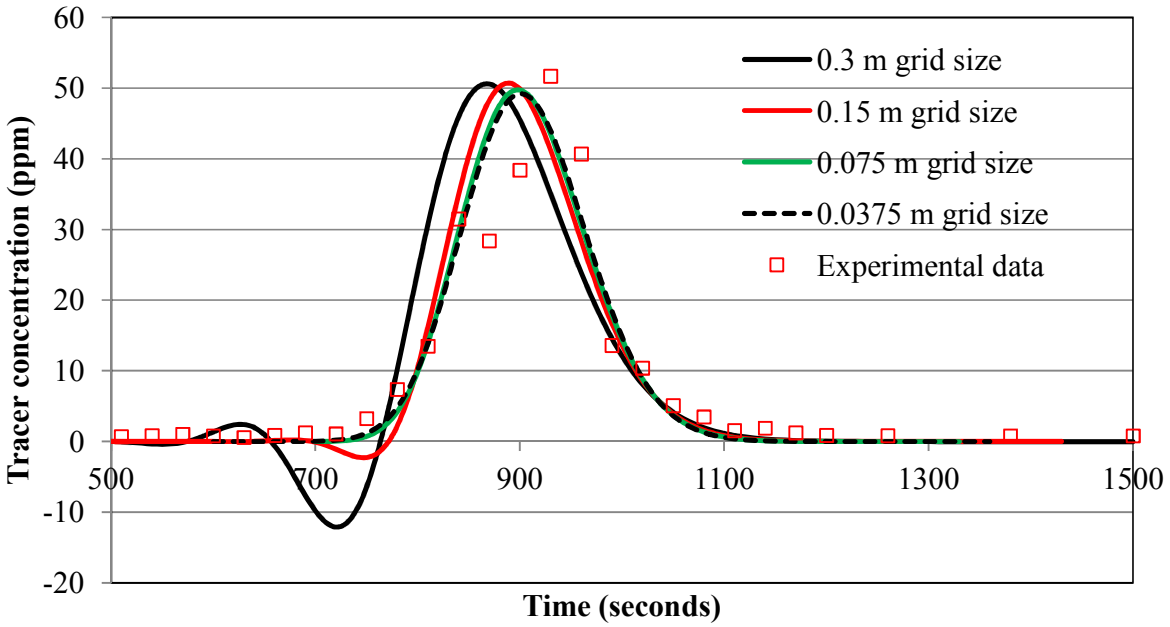

Figure 5.10: Effect of grid size within the unflighted section

Table 5.2 presents the estimated model parameters for different RTD trials. Lee (2008) reported estimated kilning velocity of 0.04 m/s for a counter-current industrial sugar dryer. The value is approximately of the same order of magnitude as that of this study (0.01–0.03 m/s). The low solid velocity suggested that the kilning flow is a dominant flow path in the model structure because there were more solids in the passive phase.

Sherritt et al. (2003) performed a non-invasive technique to measure the axial mixing in a rotating drum and the axial dispersion coefficients were calculated. The estimated axial dispersion coefficient values in this current study (Table 5.2) were within their proposed range of 10^{-07} to 10^{-04} m^2/s. Sherritt et al. (2003) also concluded that the axial dispersion coefficient is proportional to the diameter of the drum and to the square root of the rotational speed. This relationship could not be verified due to limited experimental data.

Table 5.2: Estimated parameters for different conditions in the dryer

Trials	u_s (m/s)	$\wp$ (m^2/s)
Test 2	0.020	0.0023
Test 3	0.030	0.00024
Test 4	0.016	0.00040
Test 5	0.011	0.00044
Test 6	0.015	0.00090

In order to understand the effect of operating conditions on the estimated parameters, the relationships between the estimated parameters and operating conditions were examined using the Pearson correlation technique (Mendenhall, 1979). The Pearson correlation technique is used to determine the significance of interaction between the variables. The Pearson correlation technique in Microsoft Excel was used to analyse the data presented in Table 5.2. The Pearson linear correlation coefficients between the estimated parameters and operating conditions are presented in Table 5.3.

Table 5.3: Pearson correlation coefficients between the axial dispersion coefficient and experimental conditions

Parameters	Pearson correlation coefficient		
	Rotational speed (rpm)	Internal diameter of the drum (m)	Inlet dynamic angle of repose (^{o})
u_s	0.67	- 0.77	0.22
$\wp$	0.27	0.41	0.98

Results indicate there was a significant correlation between the axial dispersed coefficient and the inlet dynamic angle of repose *(r = 0.98).* There was weak relationship between the internal diameter of the drum and the axial dispersed coefficient. The correlation coefficients showed the main operating conditions affecting the solid velocity are rotational speed *(r = 0.67)* and the internal diameter of the drum *(r = -0.77).* However, a t-test at 95% confidence interval indicated that they were not statistically significant and this can be attributed to the limited experimental data. At a wider range of experimental conditions, there is a greater chance of demonstrating a significant relationship.

To ensure the solids transport model for the unflighted sections is responsive to geometric and operating variables, it is necessary to derive a suitable model for the solid velocity and dispersion coefficient based on the abovementioned operating conditions. Solid velocity was modelled as a function of the rotational speed and internal diameter of the drum. The axial dispersed coefficient was modelled as function of inlet dynamic angle of repose. Estimated values for solid velocity and axial dispersed coefficient are presented in Table 5.2 and the corresponding operating conditions $(D, \omega, \emptyset)$ were used in Microsoft Excel's multiple regression analysis to develop Equations 5.23 and 5.24 for estimating the solid velocity and axial dispersed coefficient respectively. The regression models were implemented in the solid transport model to study the effect of operating variables.

$$u_s = 0.161318 + 0.006533\ \omega - 0.04198\ D \qquad (R^2 = 0.82) \tag{5.23}$$

$$\wp = 0.000197\emptyset - 0.01154 \qquad (R^2 = 0.97) \tag{5.24}$$

5.4 Model results

The fitted data and experimental data for different conditions are plotted in Figures 5.11–5.15. The model RTD profiles well matched the experimental RTD profiles for the different operating conditions of the dryer, which indicated that the proposed model structure was appropriate for the studied rotary dryer. The key features of initial steep rise and extended tail in the RTD profiles were also reproduced by the model.

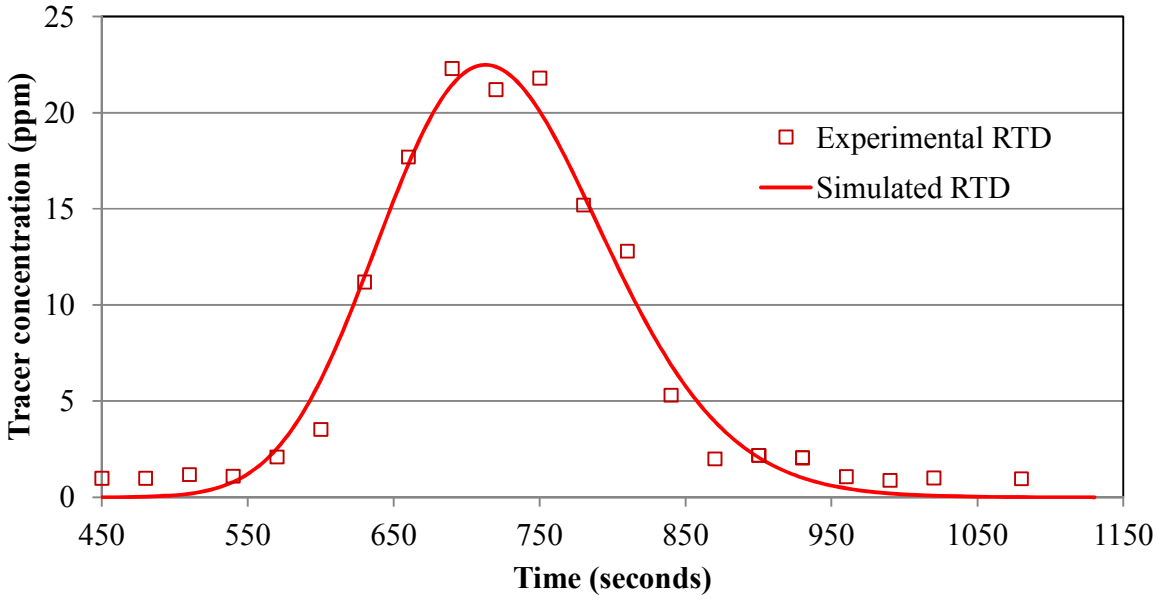

Figure 5.11: RTD profile (Test 2)

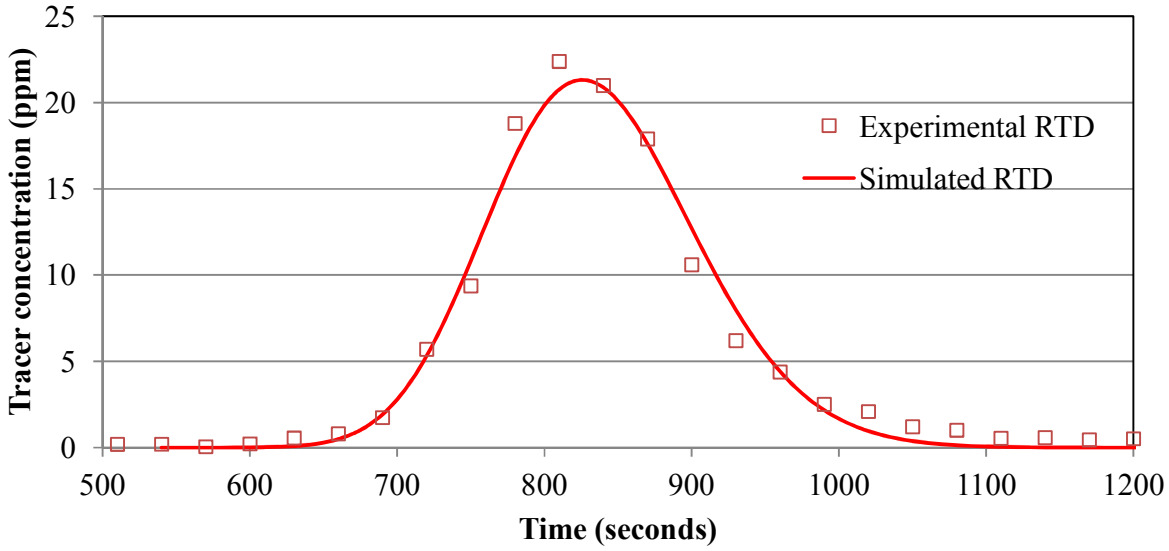

Figure 5.12: RTD profile *(Test 3)*

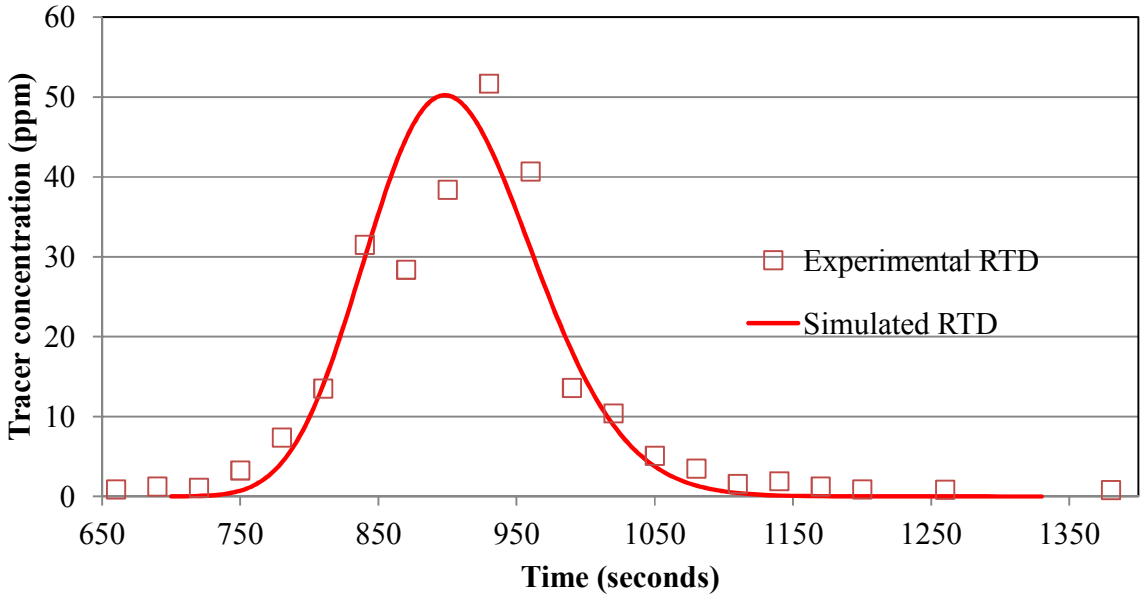

Figure 5.13: RTD profile *(Test 4)*

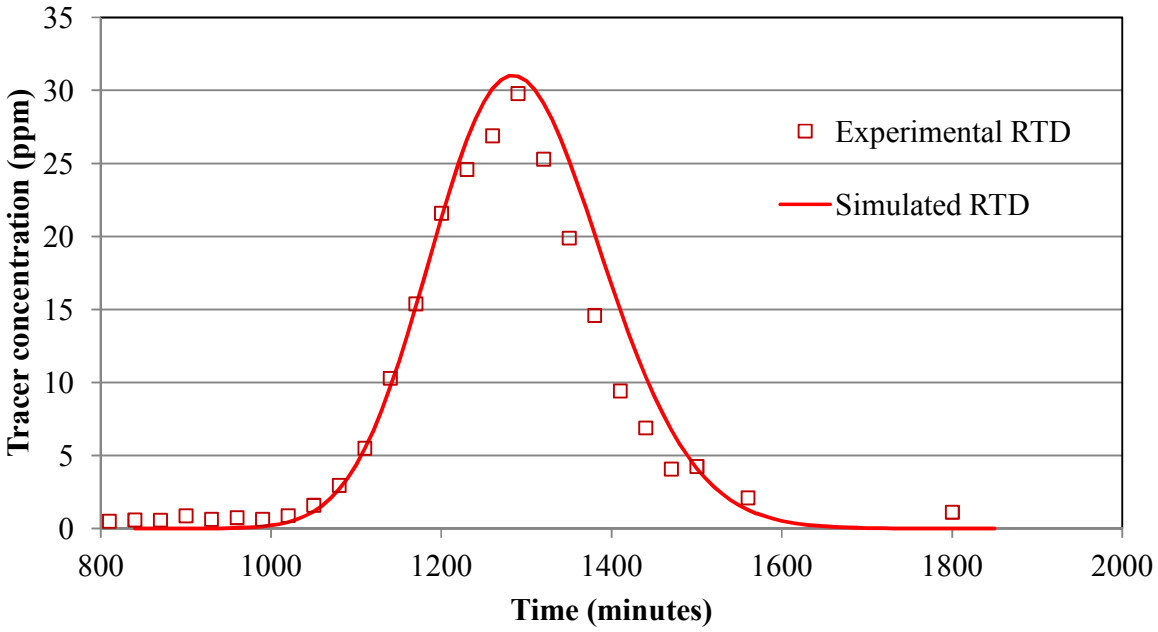

Figure 5.14: RTD profile (Test 5)

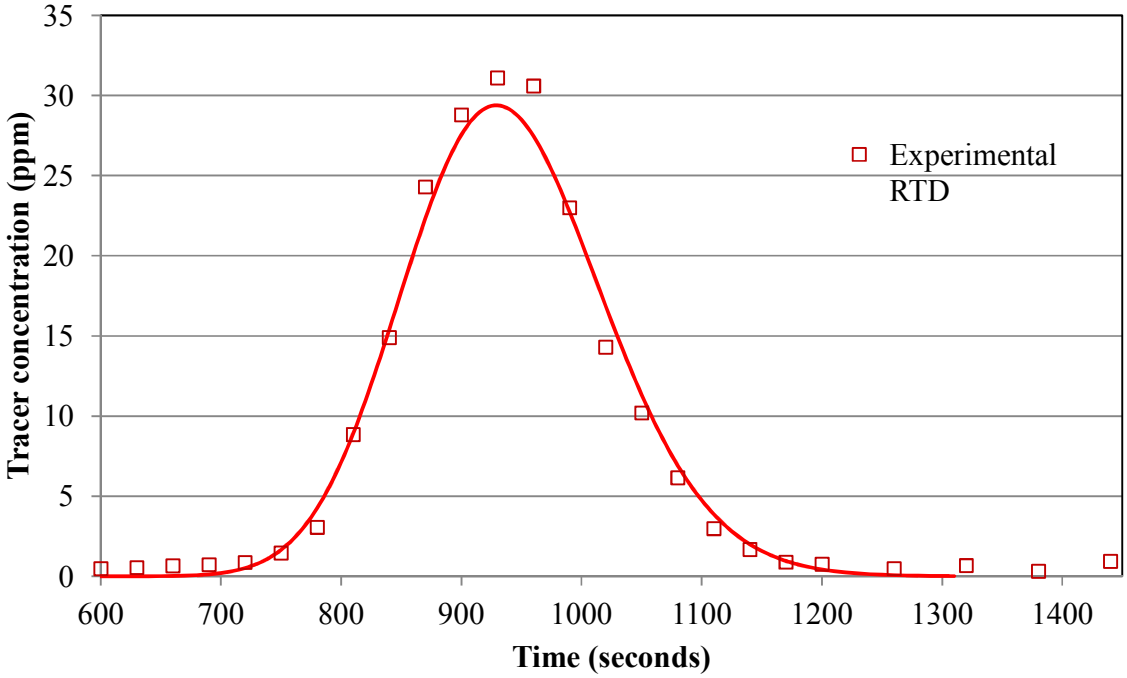

Figure 5.15: RTD profile *(Test 6)*

Table 5.4 outlines the mean residence time and holdups for different conditions of the dryer. The model predictions of the mean residence time and hold-ups were comparable to the experimental values presented in Table 3.14. Design load considerations within the compartment model facilitated better estimation of solids distribution within the dryer as shown Figure 5.16–5.21 for Tests 2, 3, 4, 5 and 6 respectively. The study noticed that movement of solids was faster in the flighted sections compared to the unflighted sections. As a result, the solid holdups within the unflighted sections were large. On the other hand, the experimental solid outlet moisture content for Test 3 was high (Table 3.8), which indicated there was minimal gas-solids interaction and is confirmed by Figure 5.17. The reduction in its flight loading capacity also resulted in an overloaded condition as there were excess solids rolling in the base of the dryer (Figure 5.17) .

Table 5.4: Holdup for different operating conditions of the dryer

Test	Mean residence time (minutes)	Average feed rate ($kg_{wet\ solid}$/min)	Holdup ($kg_{wet\ solid}$)
Test 2	12.08	2840	34,300
Test 3	13.93	3140	43,700
Test 4	15.26	2440	37,200
Test 5	21.58	1940	41,900
Test 6	15.68	2690	42,000

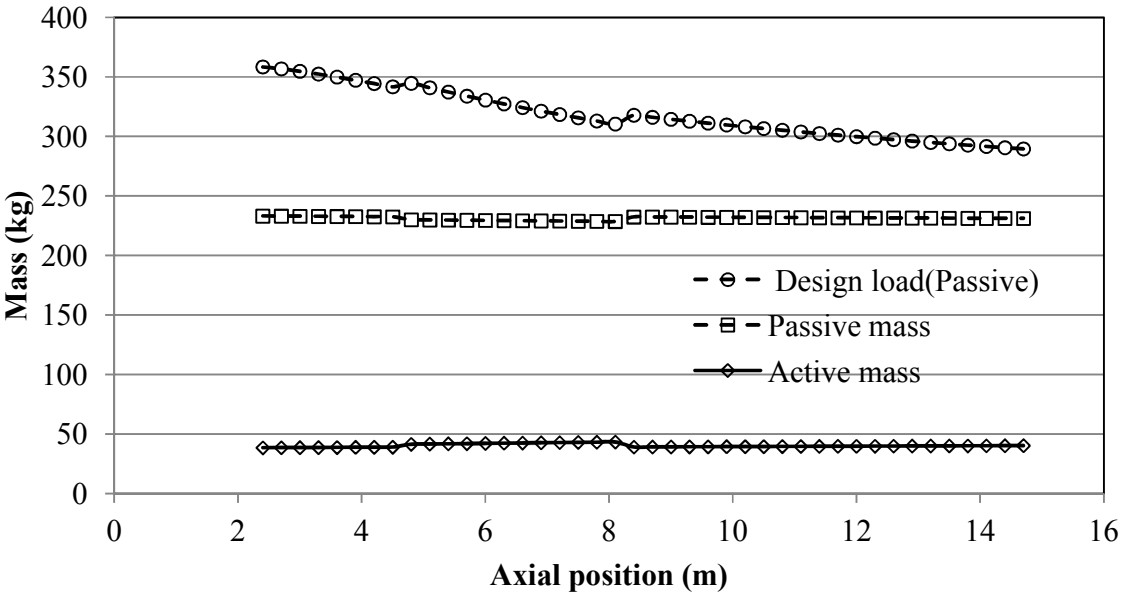

Figure 5.16: Solids distribution within the flighted sections for Test 2 *(Holdup in the unflighted sections: 2237 kg/m)*

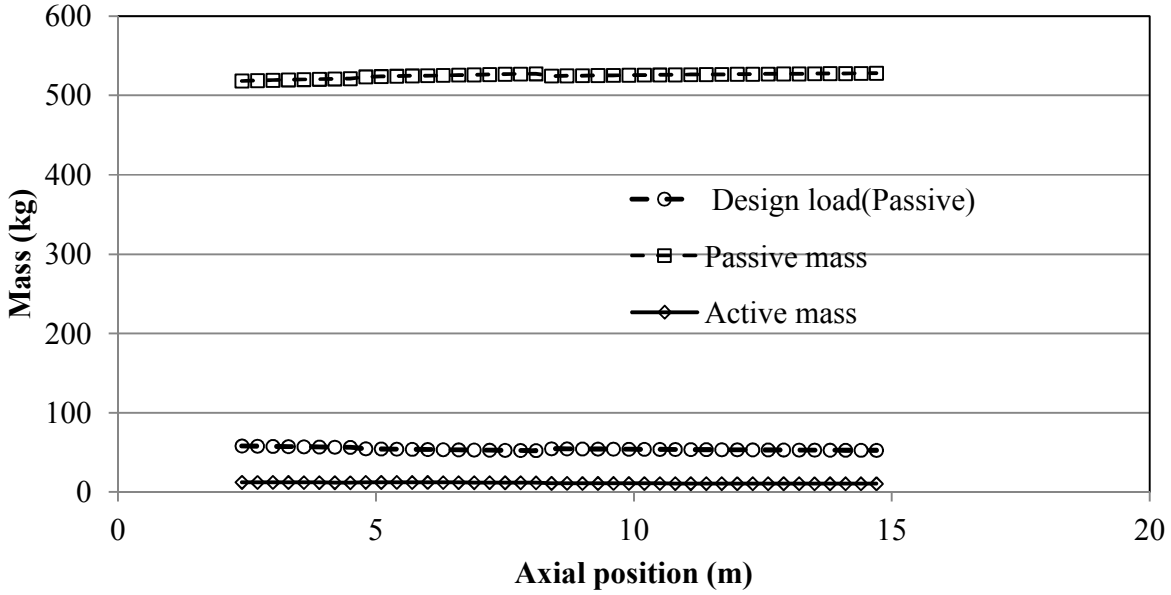

Figure 5.17: Solids distribution within the flighted sections for Test 3 *(Holdup in the unflighted sections: 2044 kg/m)*

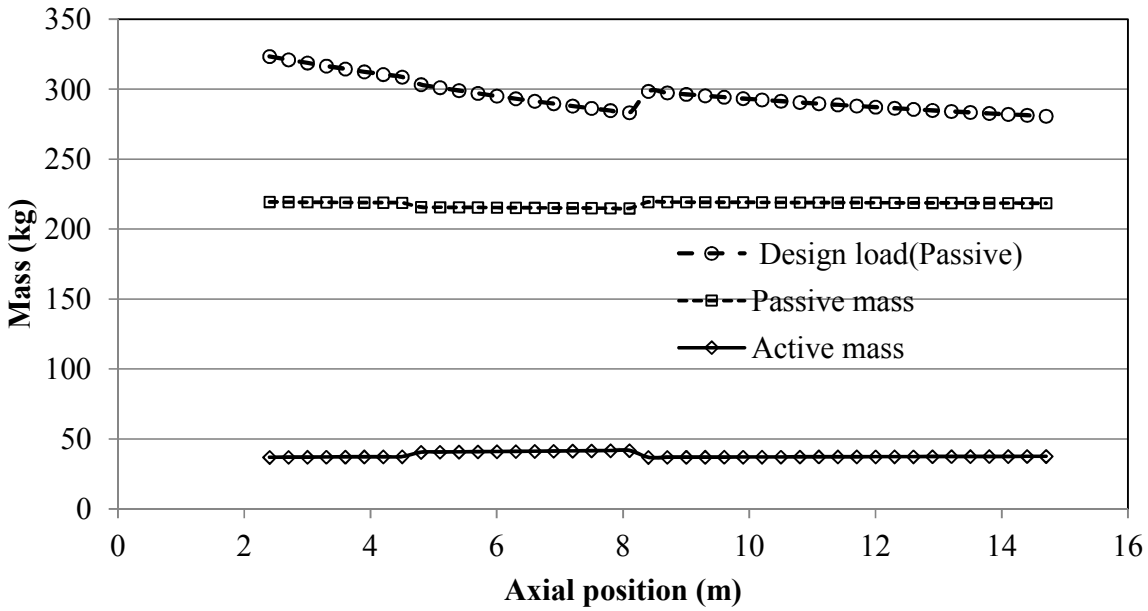

Figure 5.18: Solids distribution within the flighted sections for Test 4 *(Holdup in the unflighted sections: 2593 kg/m)*

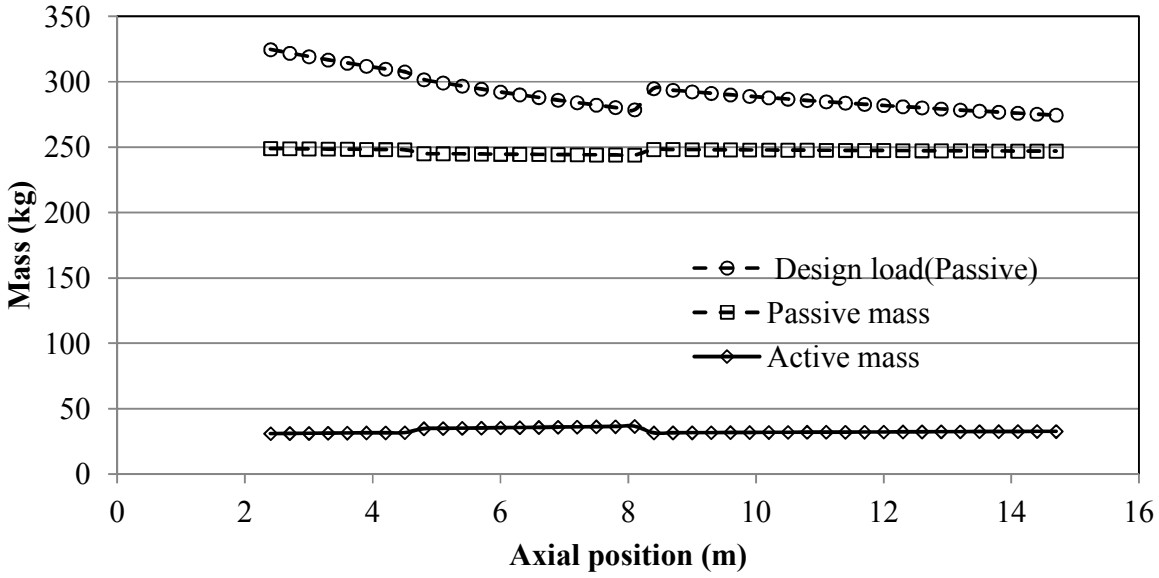

Figure 5.19: Solids distribution within the flighted sections for Test 5 *(Holdup in the unflighted sections: 3039 kg/m)*

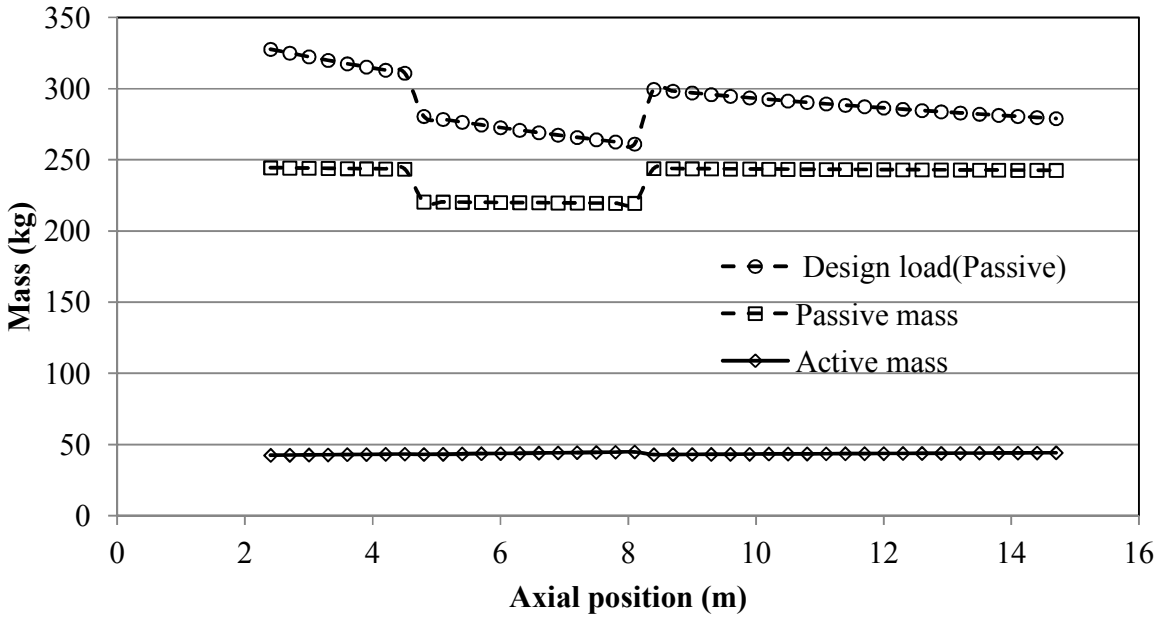

Figure 5.20: Solids distribution within the flighted sections for Test 6 *(Holdup in the unflighted sections: 3024 kg/m)*

5.4.1 Model sensitivity

In order to verify the model structure and the parameters, the effects of operating conditions on the RTD profile and the solid distribution between the active and passive phases within the model were examined.

5.4.1.1 Effect of internal diameter

The internal diameter of the dryer and the flight dimensions change as the solid adheres to the walls and flights of the dryer. In order to investigate its effect on the dryer performance indicators, the rate of solid accumulation on the walls was achieved by varying the scaling percentage presented in Equation 5.21. The other operating conditions for the investigation are presented in Table 3.8 (Test3) and remained constant. Figure 5.21 shows the effect of the internal diameter on the RTD profiles. In this study, the effect of the internal diameter was

similar to the Friedman and Marshall (1949a) correlation that mean residence time is inversely proportional to the internal diameter. Figures 5.22 and 5.23 illustrate the solid distribution within the flighted section of the dryer. The active phase reduces significantly with an increase in the hard scale build-up in the drum.

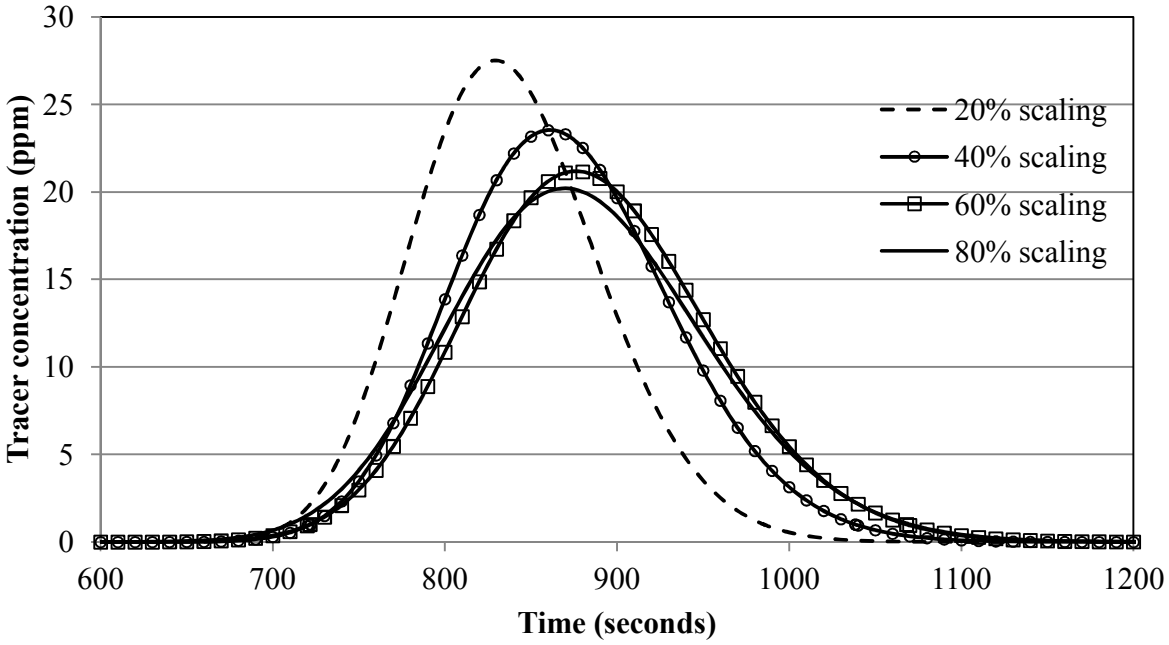

Figure 5.21: Effect of internal diameter and flight loading capacity on RTD

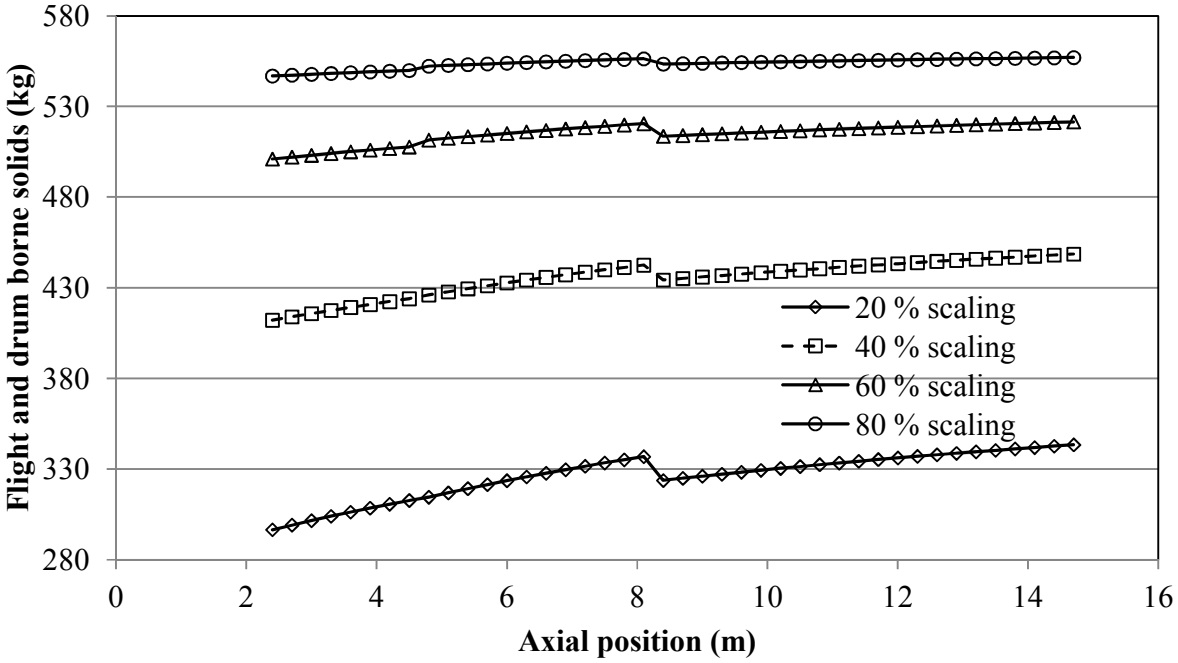

Figure 5.22: Effect of internal diameter on solid distribution *(passive)*

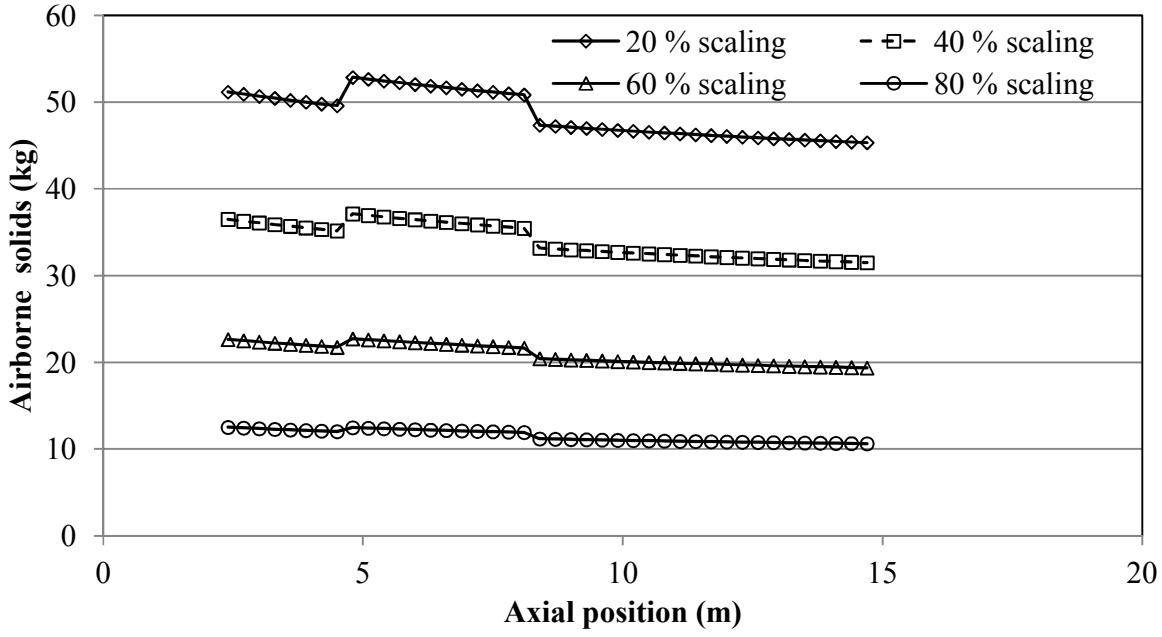

Figure 5.23: Effect of internal diameter on solid distribution *(active)*

5.4.1.2 Effect of rotational speed

The effect of rotational speed on the RTD and solid distribution between the compartments was investigated. The rotational speed was varied between 2 rpm and 5 rpm while the other operating conditions presented in Table 3.9 remained constant. Figure 5.24 shows the effect of the rotational speed on RTD. The mean residence time decreases with an increase in the rotational speed. This trend was observed in Hatzilyberis and Androutsopoulos's (1999) experimental RTD study for the flow of lignite particles through a rotary dryer. Figures 5.25 and 5.26 describe the effect of rotational speed on the solid distribution in the flighted sections of the dryer. As the rotational speed increases, the active cycle time reduces, which means solids spend less time within the airborne phase (Figure 5.26). However, the ratio of airborne solids to flight-borne solids increases with an increase in the rotational speed. The study has further established the ability of the pseudo-physical compartment model as a design and control tool for industrial applications. Therefore, it is necessary to develop and incorporate energy balances into the validated solid transport model in order for it to be used as a design and control tool in the industry.

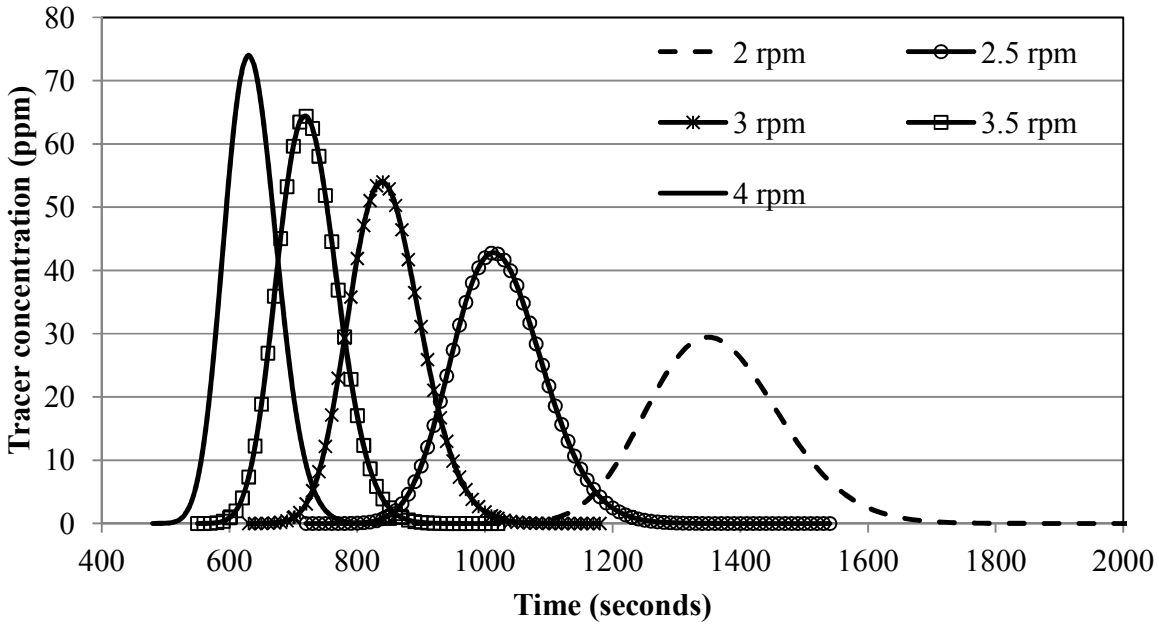

Figure 5.24: Effect of rotational speed on RTD

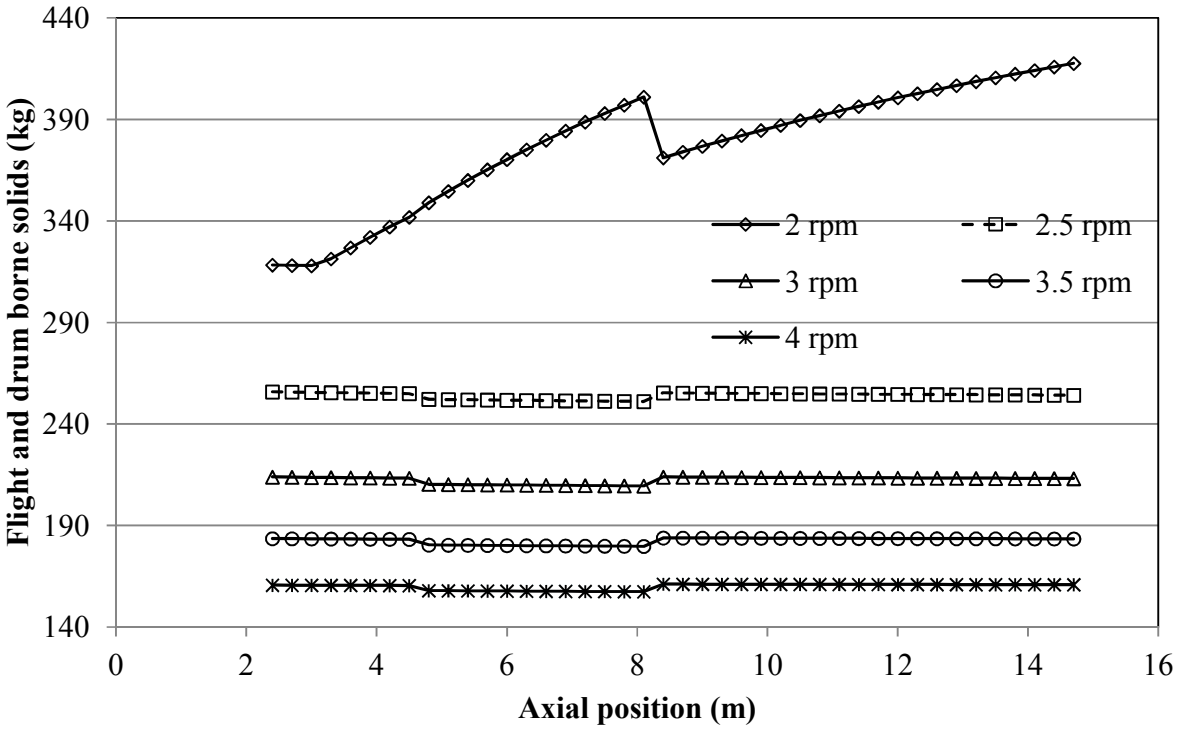

Figure 5.25: Effect of rotational speed on solid distribution *(passive)*

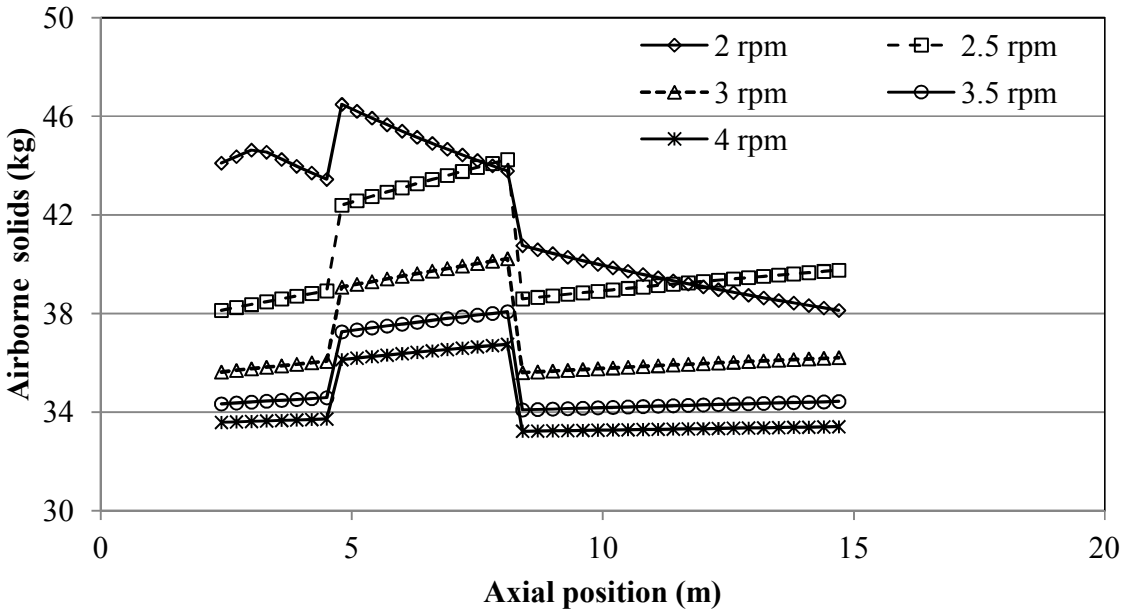

Figure 5.26: Effect of rotational speed on solid distribution *(active)*

5.5 Summary

The modelling of solid transport within an industrial rotary dryer was undertaken. The unflighted sections of the dryer were modelled as axial dispersed plug flow systems and compartment modelling approach was used to model the flighted sections. A parameter estimation technique based on the constant relative variance model was used to determine the solid velocity and the axial dispersion coefficient. A test of Pearson correlation showed the relationship between the estimated parameters and the operating conditions. The study also investigated the effect of solid adhesion to the walls of the dryer and found the active mass decreases sharply as the scale accumulation within the drum increases. The model's response to operating variables demonstrated its capability as a design and control tool.

CHAPTER SIX

6. MATHEMATICAL MODELLING OF AN INDUSTRIAL FLIGHTED ROTARY DRYER

This chapter focuses on the development and integration of energy balances into the validated solid transport model (Chapter 5). In order to facilitate the drying process, a gas phase model is introduced. The gas phase in both unflighted and flighted sections was modelled as a plug flow system. Simulations and parameter estimation were undertaken using gPROMS (process modelling software). Parameter estimation and model validation was carried out using the experimental moisture content and RTD data. The model was used to predict the gas and solid internal temperature profiles.

6.1 Model development

6.1.1 Model structure

The solid transport model structure developed in Chapter 5 is extended to include the gas phase (Figure 6.1). Heat and evaporated water were transferred between these phases. Heat was transferred to the solid from the gas by convection (Q_{conv}) and radiation (Q_{rad}). The study assumed that most of the drying process occurred in the active phase of the flighted sections while minimal drying occurred in the unflighted sections. There is uncertainty in the modelling and dynamics of the gas phase. The mean residence time of the gas phase was around 5 seconds compared to the solid phase of 15 minutes. As a result, the gas phase in both the flighted and unflighted sections was assumed to be a plug flow system without dispersion. The study assumed heat is lost through the shell from the gas phase and the contact between the shell and solids was ignored in the heat loss calculation.

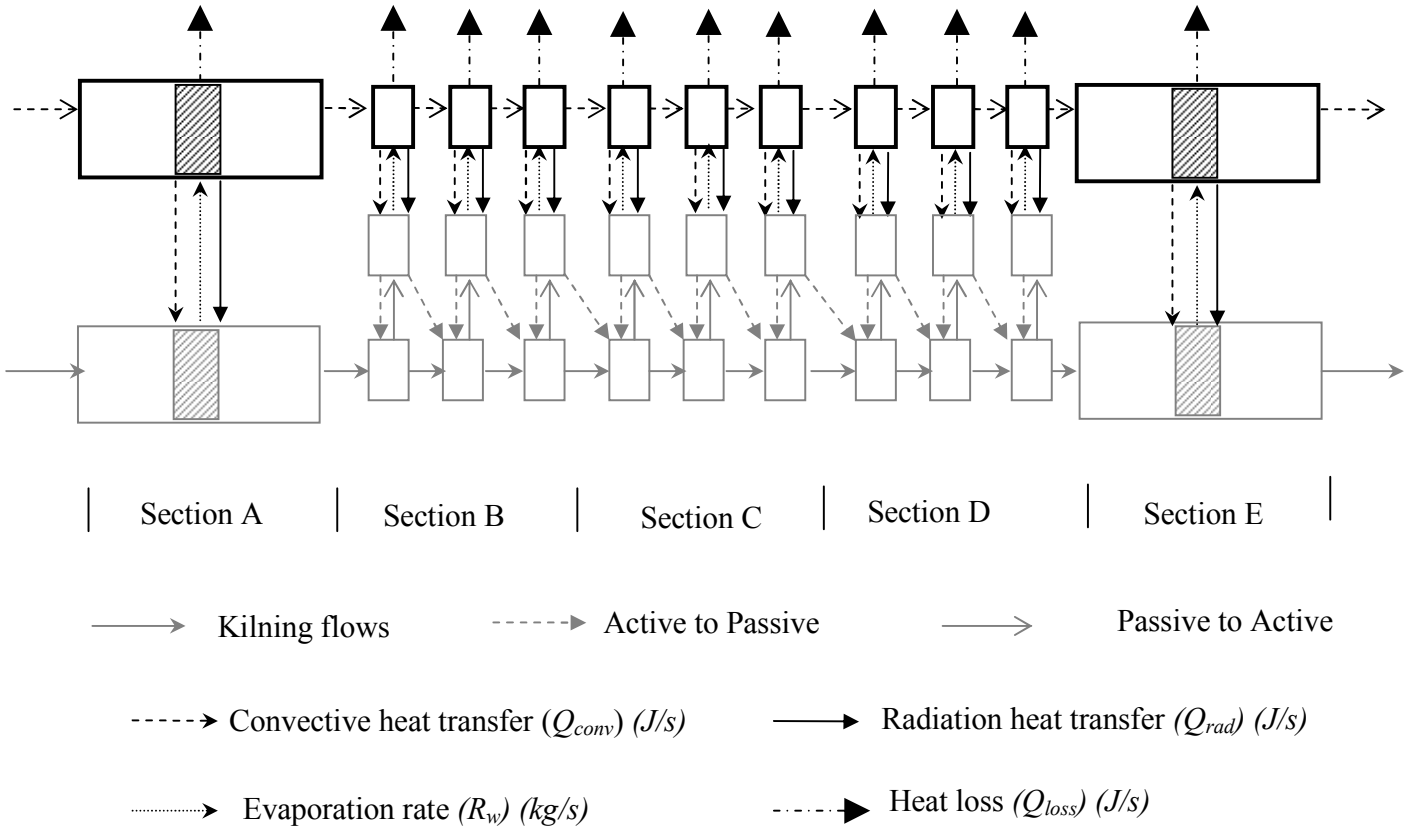

Figure 6.1: Model structure

6.1.1.1 Reference states

The reference state for water was liquid at 0 °C and 1 atm. The reference states for the solid and gas were 0 °C and 101.325 kPa.

6.1.1.2 Flighted section

6.1.1.2.1 Solid phase

Figure 6.2 represents the model structure for the flighted section. Equations 5.1 and 5.2 are the dry solid mass balance in passive and active phases respectively. To facilitate energy balance, it

is necessary to augment the dry solids mass balance with a solids moisture balance. Equations 6.1 and 6.2 describe the solid moisture balance for the passive and active phases.

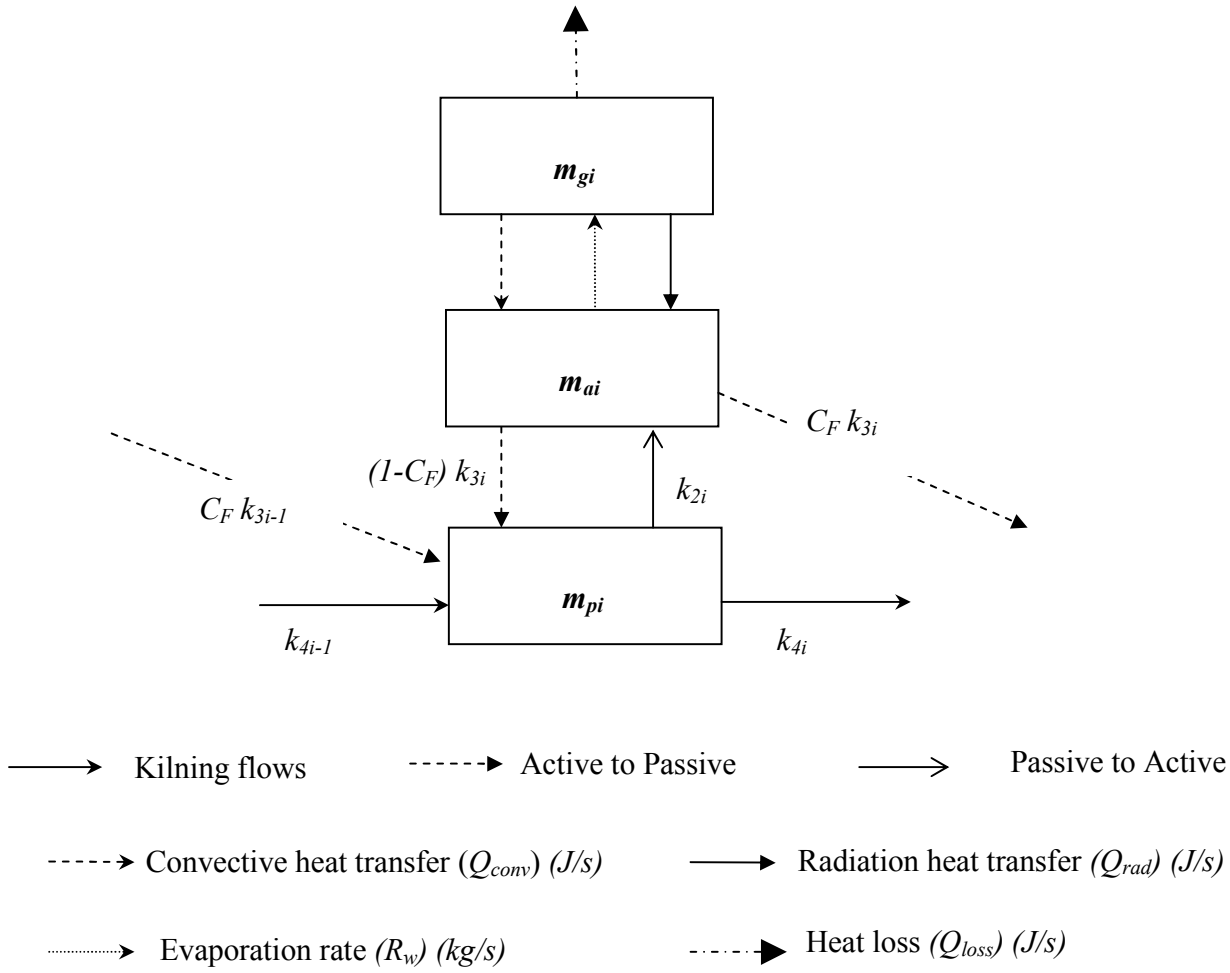

Figure 6.2: Model structure of the flighted section

The moisture balance on solids in the passive cell *i*:

$$\frac{d(x_i m_{pi})}{dt} = x_{wi-1} m_{pi-1} k_{4i-1} + x_{wi-1} m_{ai-1} k_{3i-1} C_F + x_{wi} m_{ai} k_{3i}(1 - C_F) - x_{wi} m_{pi} k_{2i} - x_{wi} m_i k_{4i} \quad \textbf{6.1}$$

The moisture balance on solids in the active cell *i*

$$\frac{dx_{wi}m_{ai}}{dt} = x_{wi}m_{pi}k_{2i} - x_{wi}m_{ai}k_{3i}C_F - x_{wi}m_{ai}k_{3i}(1 - C_F) - R_{w(i)} \quad \textbf{6.2}$$

Energy balance on solids in the passive cell *i* (assuming incompressible solid phase):

$$\begin{aligned}
&\frac{d\left(m_{pi}x_{wi}Cp_wT_{s_{pi}} + m_{pi}(1 - x_{wi})Cp_sT_{s_{pi}}\right)}{dt} \\
&= \left(x_{wi-1}Cp_wT_{s_{pi-1}} + (1 - x_{wi-1})Cp_sT_{s_{pi-1}}\right).k_{4i}m_{pi-1} \\
&+ \left(x_{wi-1}Cp_wT_{s_{ai-1}} + (1 - x_{wi-1})Cp_sT_{s_{ai-1}}\right).k_{3i-1}C_Fm_{ai-1} \\
&+ \left(x_{wi}Cp_wT_{s_{ai}} + (1 - x_{wi})Cp_sT_{s_{ai}}\right).k_{3i}(1 - C_F)m_{ai} \\
&- \left(x_{wi}Cp_wT_{s_{pi}} + (1 - x_{wi})Cp_sT_{s_{pi}}\right).k_{2i}m_{pi} \\
&- \left(x_{wi}Cp_wT_{s_{pi}} + (1 - x_{wi})Cp_sT_{s_{pi}}\right).k_{4i}m_{pi}
\end{aligned} \quad \textbf{6.3}$$

Energy balance on solids in the active cell *i* (assuming incompressible solid phase):

$$\begin{aligned}
&\frac{d\left(x_{wi}m_{ai}Cp_wT_{s_{ai}} + (1 - x_{wi})m_{ai}Cp_sT_{s_{ai}}\right)}{dt} \\
&= \left(x_{wi}Cp_wT_{s_{pi}} + (1 - x_{wi})Cp_sT_{s_{pi}}\right).k_{2i}m_{pi} \\
&- \left(x_{wi}Cp_wT_{s_{ai}} + (1 - x_{wi})Cp_sT_{s_{ai}}\right).k_{3i}C_Fm_{ai} \\
&- \left(x_{wi}Cp_wT_{s_{ai}} + (1 - x_{wi})Cp_sT_{s_{ai}}\right).k_{3i}(1 - C_F)m_{ai} \\
&- R_{w(i)}\left(H_v + Cp_wT_{s_{ai}}\right) + Q_{conv(i)} + Q_{rad(i)}
\end{aligned} \quad \textbf{6.4}$$

In Equations 6.1–6.4, m_a, m_p, x_w ,Cp_s, Cp_w, H_v, T_s and R_w, are active mass *(kg)*, passive mass (kg), moisture content *(*kg/kg$_{\text{wet solid}}$*)*, specific heat capacity of zinc concentrate *(J/(kg.K))*, specific heat capacity of liquid water *(J/(kg.K))*, latent heat of vaporization *(KJ/kg)* at temperatature = 0 ^{o}C,

solid temperature (^{o}C) and evaporation rate (kg/s) respectively. The specific heat capacities for liquid water and solid were assumed to be constant across the anticipated temperature range (25 to 55 ^{o}C).

6.1.1.2.2 Gas phase

The gas dynamics in terms of residence time is significantly different to the solid phase. The gas velocity across the dryer was between 3–5 m/s compared to the solid phase of 0.0155 m/s. As a result, the gas phase within the flighted section was modelled algebraically as a plug flow system, i.e. a steady state system (Duchesne et al., 1997). The equations for the mass balances and enthalpy balance are stated in Equations 6.5–6.7.

The mass balance equation of the gas is:

$$F_{g_{i+1}} = F_{g_i} + R_{w(i)} \qquad \textbf{6.5}$$

The equation for the moisture balance in the gas is:

$$F_{g_{i+1}} y_{w_{i+1}} = F_{g_i} y_{w_i} + R_{w(i)} \qquad \textbf{6.6}$$

Taking the following energy pathways into consideration, the water was heated to 100 ^{o}C, energy was required to evaporate the water and later heated to the operating temperature. The equation for the enthalpy balance in the gas is:

$$
\begin{aligned}
&F_{g_{i+1}}(1-y_{w_{i+1}})Cp_gT_{wg_{i+1}} + F_{g_{i+1}}y_{w_{i+1}}Cp_wT_{wg_{i+1}} + F_{g_{i+1}}y_{w_{i+1}}H_v \\
&\quad + F_{g_{i+1}}(1-y_{w_{i+1}})Cp_g(T_{gi+1}-100) \\
&\quad + F_{g_{i+1}}y_{w_{i+1}}Cp_v(T_{gi+1}-100) \\
&\quad = F_{g_i}(1-y_{w_i})Cp_gT_{wg_i} + F_{g_i}y_{w_i}Cp_wT_{wg_i} + F_{g_i}y_{w_i}H_v \\
&\quad + F_{g_i}(1-y_{w_i})Cp_g(T_{gi}-100) + F_{g_i}y_{w_i}Cp_v(T_{gi}-100) \\
&\quad + R_{w(i)}(H_v + Cp_wT_{s_{ai}}) - Q_{conv(i)} - Q_{rad(i)} - Q_{loss(i)}
\end{aligned}
\qquad \textbf{6.7}
$$

where F_g, Cp_g, Cp_w, Cp_v T_{wg} , T_g and Ql_{oss} are gas flow rate (*kg/s),* specific heat capacity of gas, specific heat capacity of liquid water(*(J/(kg.K))*, specific heat capacity of water vapour (*(J/(kg.K))*, gas temperature (0–100 ^{o}C), operating gas temperature and heat lost through the shell respectively.

6.1.1.3 Unflighted section

Figure 6.3 shows the model structure in the unflighted sections. The solid phase in the unflighted sections was modelled as an axially-dispersed plug flow (Section 5.1.2). The gas phase in this section was also assumed to be a plug flow system without dispersion.

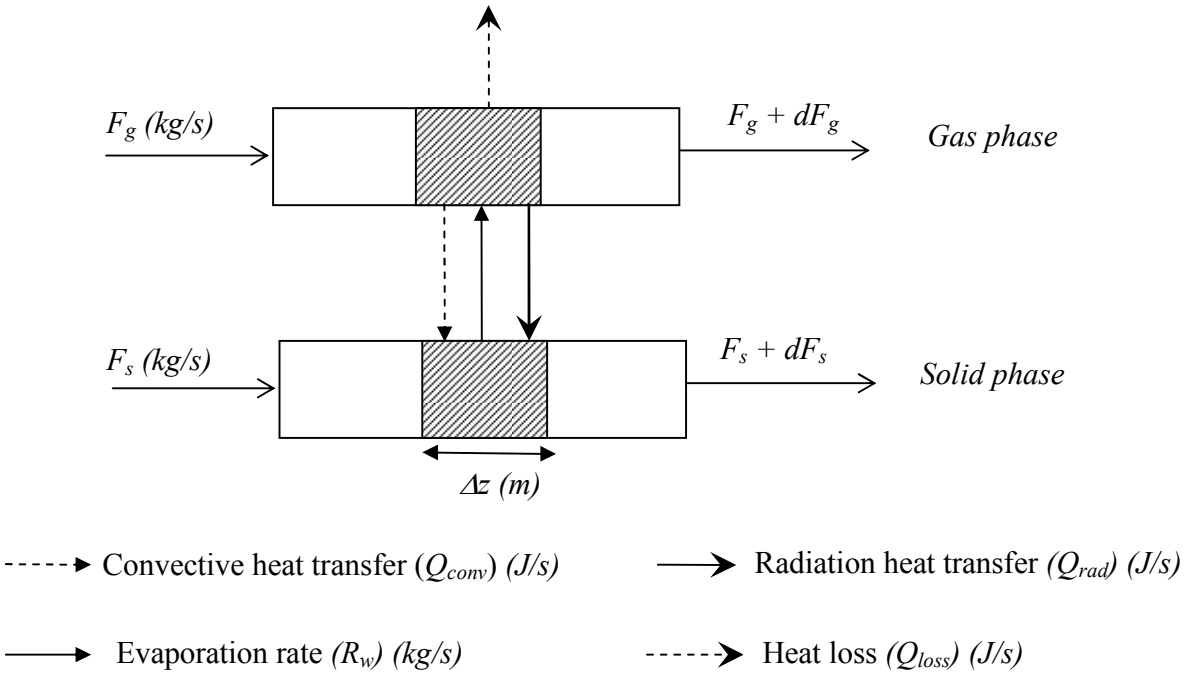

Figure 6.3: Model structure of the unflighted section

6.1.1.3.1 Solid phase

To facilitate energy balance and drying, it is necessary to augment the dry solids mass balance (Equation 5.9) with the solids moisture balance. Following the approach taken in Section 5.1.2, the mass balance on moisture content in the solid phase is:

$$\frac{\partial}{\partial t}(x_w m_s) = \wp \frac{\partial^2}{\partial z^2}(x_w m_s) - \frac{\partial}{\partial z}(u_s x_w m_s) - \frac{R_w}{\Delta z} \qquad \textbf{6.8}$$

where m_s and R_w are the mass per length (kg/m)and the rate of moisture removal (kg/s) within a slice (Δz) respectively.

Energy balance in the solid phase including convection (Q_{conv}), radiation (Q_{rad}) and evaporation is expressed as:

$$\frac{\partial}{\partial t}(\rho_s \bar{U}_s A_s \Delta z) = F_s \bar{H}|_z - F_s \bar{H}|_{z+\Delta z} - R_w(H_v + Cp_w T_s) + Q_{conv} + Q_{rad} \qquad \textbf{6.9}$$

where $\bar{U}, \bar{H}$ are the internal energy *(J/kg)* and enthalpy energy *(J/kg)* respectively.

As a result of the assumed incompressibility of the solids (i.e. $\overline{PV} \cong 0$), internal energy $\bar{U}_s$ was simplified to:

$$\partial \bar{U}_s = \partial \bar{H}_s = Cp \partial T_s \qquad \textbf{6.10}$$

Substituting for F_s *(Equation* 5.5*)* and $\bar{H}_s$ in Equation 6.9 and dividing by Δz and taking the limit $\Delta z \rightarrow 0$, Equation 6.9 becomes:

$$\begin{aligned} &\frac{\partial}{\partial t}(x_w m_s Cp_w T_s + (1 - x_w) m_s Cp_s T_s) \\ &= \wp \frac{\partial^2}{\partial z^2}(x_w m_s Cp_w T_s + (1 - x_w) m_s Cp_s T_s) \\ &- u_s \frac{\partial}{\partial z}(x_w m_s Cp_w T_s + (1 - x_w) m_s Cp_s T_s) \\ &- \frac{R_w}{\Delta z}(H_v + Cp_w T_s) + \frac{Q_{conv}}{\Delta z} + \frac{Q_{rad}}{\Delta z} \end{aligned} \qquad \textbf{6.11}$$

6.1.1.3.2 Gas phase

Assuming plug flow without dispersion, the mass balances on dry gas and moisture can be derived (Equations 6.12–6.14). As the hot gas flows through the dryer, heat is transferred to the solids and the moisture content of the gas increases due to the evaporated water. This leads to variation in the gas density along the length of the dryer such that $\rho_g = f(z)$.

The mass balance equation on the gas across a differential element (Δz) is

$$\frac{\partial}{\partial t}(\rho_g A_g \Delta z) = v_g A_g \rho_g\big|_z - v_g A_g \rho_g\big|_{z+\Delta z} \qquad \textbf{6.12}$$

Substituting the term $A_g \rho_g = m_g$ into Equation 6.12, then dividing by Δz and taking the limit $\Delta z \rightarrow 0$, gives

$$\frac{\partial}{\partial}(m_g) = -\frac{\partial}{\partial z}(v_g m_g) \qquad \textbf{6.13}$$

The mass balance on moisture in the gas is:

$$\frac{\partial}{\partial t}(y_w m_g) = -\frac{\partial}{\partial z}(v_g y_w m_g) + \frac{R_w}{\Delta z} \qquad \textbf{6.14}$$

In Equations 6.12 –6.14, A_g, ρ_g, m_g, y_g and R_w are the area *(m^2),* density *(kg/m^3),* mass per length *(kg/m),* gas humidity *(kg/kg Total wet gas)* and drying rate *(kg/s)* respectively. The gas velocity is calculated as follows:

$$v_g = \frac{F_g}{\rho_g A_g} \qquad \textbf{6.15}$$

Energy balance on the gas across a differential element (*Δz)* is:

$$\begin{aligned} &\frac{\partial}{\partial t}(\rho_g U_g A_g \Delta z) \\ &= v_g A_g \rho_g \overline{H}\big|_z - v_g A_g \rho_g \overline{H}\big|_{z+\Delta z} + R_w(H_v + Cp_w T_s) - Q_{conv} \\ &- Q_{rad} - Q_{loss} \end{aligned} \qquad \textbf{6.16}$$

Noting the compressible nature of the gas phase, the following substitution, assuming ideal gas behaviour is made:

$$\overline{U}_g = \overline{H}_g - \overline{PV}_g = \overline{H}_g - \overline{RT}_g \qquad \textbf{6.17}$$

Dividing by Δz and taking the limit $\Delta z \rightarrow 0$ and substituting the ideal gas equation for $\overline{PV}$, gives:

$$\frac{\partial\left(y_w A_g \rho_g Cp_w T_g + (1-y_w) A_g \rho_g Cp_g T_g + y_w A_g \rho_g H_v - (nRT)_g - (nRT)_w\right)}{\partial t}$$

$$= -\frac{\partial\left(v_g y_w A_g \rho_g\, Cp_w T_g + v_g (1-y_w) A_g \rho_g Cp_g T_g + v_g y_w A_g \rho_g H_v\right)}{\partial z} \qquad \textbf{6.18}$$

$$+ \frac{R_w}{\Delta z}(H_v + Cp_w T_s) - \frac{Q_{conv}}{\Delta z} - \frac{Q_{rad}}{\Delta z} - \frac{Q_{loss}}{\Delta z}$$

Taking the following energy pathways into consideration, the water was heated to 100 ^{o}C, energy was required to evaporate the water and later heated to the operating temperature (for instance, 500 ^{o}C). Equation 6.18 becomes:

$$\frac{\partial\begin{pmatrix} y_w m_g Cp_w T_{wg} + (1-y_w) m_g Cp_g T_{wg} + y_w m_g H_v + y_w m_g Cp_v\left(T_g - 100\right) + \\ (1-y_w) Cp_g\left(T_g - 100\right) - (nRT)_g - (nRT)_w \end{pmatrix}}{\partial t}$$

$$= -\frac{\partial\begin{pmatrix} v_g y_w m_g\, Cp_g T_{wg} + v_g (1-y_w) m_g Cp_g T_{wg} + v_g y_w m_g H_v + \\ v_g y_w m_g Cp_v\left(T_g - 100\right) + \; v_g (1-y_w) m_g Cp_g\left(T_g - 100\right) \end{pmatrix}}{\partial z} \qquad \textbf{6.19}$$

$$+ \frac{R_w}{\Delta z}(H_v + Cp_w T_s) - \frac{Q_{conv}}{\Delta z} - \frac{Q_{rad}}{\Delta z} - \frac{Q_{loss}}{\Delta z}$$

In Equation 6.19*, R* and *n* are the ideal gas constant *(J/(mol·K))* and the number of moles *(mol))* respectively.

6.1.1.3.3 Boundary conditions

The Danckwerts boundary conditions (Danckwerts, 1953) for Equations 5.9, 6.8, 6.11, 6.13, 6.14 and 6.19 were used and are shown below.

For Equation 5.9

$$z = 0, \qquad m_s(0) = {}^{F_s}/_{u_s} \tag{6.20}$$

At the outlet, the solids do not disperse back into the dryer and thus, the outlet boundary condition is stated as follows:

$$z = L, \qquad \wp \frac{\partial^2 m_s}{\partial z^2} = 0 \tag{6.21}$$

For Equation 6.8

$$z = 0, \qquad x_w(0) = x_{inlet} \tag{6.22}$$

$$z = L, \qquad \wp \frac{\partial^2 x_w m_s}{\partial z^2} = 0 \tag{6.23}$$

For Equation 6.11

$$z = 0, \qquad T_s(0) = T_{s(inlet)} \tag{6.24}$$

$$z = L, \qquad \wp \frac{\partial^2 (Cp_w T_s x_w m_s + Cp_s T_s (1 - x_w) m_s)}{\partial z^2} = 0 \tag{6.25}$$

For Equation 6.13

$$z = 0, \qquad m_g(0) = {}^{F_g}/_{v_g} \tag{6.26}$$

$$z = L, \qquad \frac{\partial m_g}{\partial z} = 0 \tag{6.27}$$

For Equation 6.14

$$z = 0, \qquad y_w(0) = y_{inlet} \tag{6.28}$$

$$z = L, \quad \frac{\partial y_w m_g}{\partial z} = 0 \tag{6.29}$$

For Equation 6.19

$$z = 0, \quad T_g(0) = T_{g(inlet)} \tag{6.30}$$

$$z = L, \quad \frac{\partial \begin{pmatrix} v_g y_w m_g \, Cp_w T_{wg} + v_g(1 - y_w) m_g Cp_g T_{wg} + v_g y_w m_g H_v + \\ v_g y_w m_g Cp_v(T_g - 100) + v_g(1 - y_w) Cp_g(T_g - 100) \end{pmatrix}}{\partial z} = 0 \tag{6.31}$$

6.1.1.4 Drying rate

The drying rate in the rotary dryer depends on the drying gas, the properties of the solid and the geometrical configuration of the dryer. The drying rate is controlled by either the rate of internal migration of water molecules to the surface or the rate of evaporation of water molecules from the surface into the air. It can be characterised experimentally by measuring the moisture content loss as a function of time. Studies have also used thin-layer drying experiments to study the rate of evaporation and to derive drying rate correlations (Cao & Langrish, 2000; Igauz et al, 2003). Wang et al. (1993) suggested the drying rate in the falling rate period can be determined by using Sharples et al. correlation (1964). These approaches are not suitable for this study because the thin layer experiments and the correlations were carried out at a lower temperature range compared to the typical operating temperature of this study.

In a non-experimental approach, the drying rate has been typically modelled as the process of water molecules transferring into the gas stream and the driving force was provided by the difference in the vapour pressures of the gas and the wet surface (Duchesne et al. 1997; Didriksen, 2002; Raffak et al. 2008). The rotary dryer examined in Duchesne et al. (1997) and

Raffak et al. (2008) were used in drying zinc concentrates and phosphate ore respectively. In this study, the drying rate was assumed to be proportional to the difference between the water partial pressure in the gas phase and the water vapour pressure at the temperature of the solids being dried (Equation 6.32). The vapour pressure was calculated using the solid temperature of the active phase and was estimated using Antoine equation (Equation 6.33)

$$R_w = h_m A_s (P_w - P_v) \qquad \textbf{6.32}$$

where h_m, P_w, P_v and A_s are the mass transfer coefficient, water vapour pressure at the temperature of the solids being dried, partial pressure of water vapour in the gas phase and surface area of solid particles in contact with the incoming gas respectively. The estimation of the surface area of solid particles for unflighted section and flighted section will be discussed in subsequent section (where $A_s = A_a$ or $A_s = A_{AL}$).

Vapour pressure at the temperature of the airborne solids is expressed by Felder and Rousseau (2005) as:

$$P_w = \exp\left(23.561 - \frac{4030.182}{T_s + 235}\right) \qquad \textbf{6.33}$$

P_w and T_s are water vapour pressure (Pa) and temperature of the solids (^oC)

Partial pressure of water vapour in the gas phase is calculated by:

$$P_v = \acute{y}_w P \qquad \textbf{6.34}$$

$\acute{y_w}, P$ are the gas humidity (mol/mol) and total pressure (Pa) respectively.

6.1.1.5 Heat and mass transfer

During drying of wet solids in rotary dryers, heat and mass transfer occurs simultaneously. In this thesis, the heat is assumed to be transferred from the gas to the solid particles through radiation and convection.

6.1.1.5.1 Convective heat transfer

The convective heat transfer (Q_{conv}) is dependent on the temperature difference between the drying gas and the solid. The equation for convective heat transfer can be expressed in Equation 6.35:

$$Q_{conv} = h_c A_s (T_s - T_g) \qquad \textbf{6.35}$$

where Q_{conv}, h_c, A_s, T_s and T_g are the convective heat transfer, convective heat transfer coefficient, surface area, temperature of the solid and temperature of the air respectively.

The process of estimating the convective heat transfer coefficient can be achieved through the correlation of the heat transfer coefficient and the dimensionless Nusselt number *(Nu)*. The general form of this type of correlation is as follows:

$$Nu = \frac{h_c L}{k_g} = f(Re, Pr, Gu) \qquad \textbf{6.36}$$

where *Nu, , h_c, L, k_g, Re, Gu* and *Pr,* are the Nusselt number, heat transfer coefficient, characteristic length scale, thermal conductivity, Gukhman number, and Prandtl number respectively.

The most commonly used Nusselt correlation in rotary dryer modelling studies is the Ranz and Marshall (1952) correlation (Equation 6.37). The correlation was based on evaporation of water

droplets experiments and non-interaction between the droplets was assumed. This assumption is not valid for solid particles within the rotary dryer.

$$Nu = 2 + 0.6Re^{0.5}Pr^{0.33} \quad \textbf{6.37}$$

Hirosue (1989) introduced a correction factor into the Ranz-Marshall (1952) correlation to address the limitation of non-interaction between the falling particles. The correction factors are stated in Equations 6.38 and 6.39.

Range 1

$$K_h = 37.5A_{\bar{N}}^{-1/4}, \qquad 3 \times 10^5 \leq A_{\bar{N}} \leq 1.5 \times 10^8 \quad \textbf{6.38}$$

Range 2

$$K_h = 4190A_{\bar{N}}^{-1/2}, \qquad 1.5 \times 10^8 \leq A_{\bar{N}} \leq 2 \times 10^{10} \quad \textbf{6.39}$$

$$A_{\bar{N}} = \frac{X^{1.37}Fr^{0.41}S}{d_p^3} \quad \textbf{6.40}$$

In Equations 6.38–6.40, K_h, *Fr, S, X* and *dp* are the correction factor, Froude number, cross-sectional area of the dryer, holdup and particle diameter respectively.

Previous studies in rotary dryer modelling (Kelly, 1987; Didriksen, 2002; Raffak et al., 2008) have also used Nusselt number correlation (Equation 6.41) developed for air flow over spherical particles. Equation 6.41 was used to determine the convective heat transfer coefficient in this thesis.

$$Nu = 0.33Re^{0.6} \qquad \textbf{6.41}$$

6.1.1.5.2 Radiation heat transfer

The study assumed that the heat transferred from the gas to the solid by convection and radiation. It should be noted that most of the drying process was assumed to occur in the active phase of the flighted sections while minimal drying occurred in the unflighted sections. This is a typical approach taken in flighted rotary dryer literature (Duchesne et al, 1997; Sheehan et al., 2005). The exposure of both the active phase and the active layer of the unflighted sections to freeboard gas promote gas-solids interactions within the dryer. The description and implications of the choice of the active layer will be discussed in Section 6.1.1.7.1. Equation 6.42 presented in previous studies (Didriksen, 2002; Dhanjal et al., 2004) was used to calculate the radiative heat transfer from the gas to the solid. This equation represents the radiative exchange between the freeboard gas and the active solids within an active phase cell, and also within the unflighted sections. The radiative exchanges that are neglected in this work are the exchange between the freeboard gas and passive solids as well as the exchange between the internal walls and the solids. A more comprehensive approach described in rotary kiln and combustion chamber literature (where gas temperatures are typically much higher) is the zone method. This has been used to determine the radiative heat transfer within complex geometries (Gorog et al (1981), Barr, 1986; Batu and Selcuk, 2002). This approach involves subdividing the enclosure into zones and summing the exchanges of radiation between the neighbouring zones. The model developed in this thesis would provide a good basis with which to implement such an approach because the model is already geometrically segmented. However, the shortcomings of this approach are large computing requirements and numerical instability due to large number of non-linear equations. It should also be noted that the effect of radiative heat transfer in the current study is expected to be

relatively small because the gas temperature is lower than 700^{o}C, where radiation is known to dominate. The radiative heat transfer from the gas to inside wall of the dryer was also considered and discussed in section 6.1.1.6. The end walls were neglected because their areas only account for roughly 5% of the total exposed area.

$$Q_{rad} = \varepsilon_r \sigma_r \left(T_g^4 - T_s^4\right) \quad \textbf{6.42}$$

6.1.1.5.3 Mass transfer

The mass transfer coefficient *(h_m)* can be calculated from the Ranz and Marshall (1952) correlation stated in Equation 6.43, which was based on single particle approach.

$$Sh = 2 + 0.6Re^{0.5}Pr^{0.33} \quad \textbf{6.43}$$

where *Sh* is the Sherwood number (Equation 6.44)

$$Sh = \frac{h_m L}{\wp_{AB}} \quad \textbf{6.44}$$

In this study, the mass transfer coefficient was calculated via the Chilton-Colburn analogy ($j_H = j_m$) used to relate mass and heat transfer coefficients, as previously used in other rotary dryer modelling studies (Didriksen, 2002; Raffak et al., 2008)

$$j_H = StPr^{2/3} \quad \textbf{6.45}$$

$$j_m = \left(\frac{h_m P_v}{v_g \rho_g}\right) Sc^{2/3} \quad \textbf{6.46}$$

where j_H, j_m, P_v, v_g, ρ_g, Sc and St are the heat transfer factor, mass transfer factor, vapour pressure, gas velocity, gas density, Stanton number, Schmidt number and Prandtl number respectively

Thus, the mass transfer coefficient (h_m) is:

$$h_m = \left(\frac{St\ v_g \rho_g}{P_v}\right)\left(\frac{Pr}{Sc}\right)^{2/3} \quad \textbf{6.47}$$

The Stanton (St) and Schmidt (Sc) numbers can be estimated using Equations 6.48 and 6.49 respectively.

$$St = \frac{h_c}{Cp_g\ v_g \rho_g} \quad \textbf{6.48}$$

$$Sc = \frac{\mu_g}{\wp_{AB} \rho_g} \quad \textbf{6.49}$$

where h_c, Cp_{air} and $\wp_{AB}$ are heat transfer coefficient, specific heat capacity of the air and vapour diffusivity in the air respectively.

6.1.1.6 Heat loss

The heat loss from the dryer shell was calculated by determining individual thermal resistances and the overall temperature gradient, according to Equation 6.50 (Sheehan, 2002).

$$Q_{loss} = \theta_{loss}\left(\frac{T_g - T_{amb}}{\sum R_j}\right) \quad \textbf{6.50}$$

where T_g, T_{amb} and R_j, are gas temperature, ambient temperature and resistance respectively. A heat loss turning factor (θ_{loss}) is introduced in order to fit the gas outlet temperature, and its estimation process is discussed in the parameter estimation section.

In this study, the contact between the solids and the walls that acts as an insulator was ignored in the resistance analysis. Hence, the heat loss over the entire circumference of the shell was assumed. The following mechanisms of heat transfer were considered in the resistance analysis: forced convection from the hot gas to the dryer inside surface, free convection from the outside dryer surface, radiation from the hot gas to the dryer inside surface, radiation from the outside of the dryer surface and conduction.

$$\sum R_j = \frac{1}{\left(h_{in} 2\pi r_{in} L + h_{rad_{in}} 2\pi R L\right)} + \frac{\ln(R_o/r_{in})}{k_c 2\pi r_{in} L} + \frac{1}{\left(h_{out} 2\pi R_o L + h_{rad_{out}} 2\pi R_o L\right)} \quad \textbf{6.51}$$

The total heat coefficient (convection(h_{in}) and radiation ($h_{rad_{in}}$)) at the internal surface of the dryer was determined. The Sieder and Tate (1936) correlation was used to calculate the forced convective heat transfer coefficient (Equation 6.52) because the effect of variation in the gas temperature and its properties across the dryer was taken into account. The radiation heat transfer coefficient was estimated using Equation 6.53 (Incropera & DeWitt, 2002).

$$h_{in} = \left(\frac{k_g}{D_{in}}\right) \times \left(0.027 Re^{4/5} Pr^{1/3} \left(\frac{\mu}{\mu_s}\right)^{0.14}\right) \quad \textbf{6.52}$$

$$h_{rad_{in}} = \varepsilon_r \sigma_r \left(T_g + T_w\right)\left(T_g^2 + T_w^2\right) \quad \textbf{6.53}$$

The total heat coefficient (convection(h_{out}) and radiation ($h_{rad_{out}}$) at the external surface of the dryer was calculated using available correlations. The Churchill and Chu (1975) correlation was

used to calculate the convective heat transfer coefficient (Equation 6.54) and Equation 6.55 was used to calculate the external radiation heat transfer coefficient (Incropera & DeWitt, 2002).

$$h_{out} = \left(\frac{k_{g_{out}}}{D_{out}}\right) \times \left(0.60 + \frac{0.387Ra^{1/6}}{\left(1 + \left({}^{0.559}/_{Pr}\right)^{9/16}\right)^{8/27}}\right)^2 \qquad \textbf{6.54}$$

$$h_{rad_{out}} = \varepsilon_r \sigma_r (T_w + T_{amb})(T_w^2 + T_{amb}^2) \qquad \textbf{6.55}$$

6.1.1.7 Surface area consideration

The surface area exposed to the drying gas stream influences the drying rate. In a study, the contact surface area was assumed to be equal to the sum of the particle area of the suspended mass in the flighted rotary dryer (Didriksen, 2002). However, the accurate estimation of this surface area without experiments can be difficult because of the effect of the dryer operating conditions and the solid properties such as the particle size, void fraction and cohesion.

In unflighted dryers, the surface area in contact with the gas largely depends on the solids bed motions within the drum. The solids bed motion is dependent on the rotational speed and internal geometry of the dryer. The solids move in different modes: rolling, slipping and slumping (Mellmann, 2001). The most common solid movement in an industrial rotary drum is the rolling mode because of its low rotational speed. Consequently, this study assumed that the rolling mode occurs in the unflighted sections. Studies have shown that the rolling mode is characterised by two distinct regions: active layer and passive layer. The active layer is characterised by vigorous mixing of particles and hence a high rate of surface renewal which promotes heat transfer. In the passive region, it is commonly assumed that little or no mixing occurs. The estimation of the

thickness of the active layer has been a subject of interest for researchers (Boateng, 1993; Jauhari et al., 1998; Mellmann et al., 2004; Liu et al., 2006). There may be a need for a correction factor to address the uncertainty in the theoretical estimation of these surface areas in both the unflighted and the flighted sections of the dryer.

6.1.1.7.1 Unflighted section

In the unflighted sections, convection, radiation and evaporation are assumed to occur. However, unlike the airborne solids, the available area is assumed to be reduced. Heinen et al. (1983a) measured the thickness of the active layer to be less than eight particle diameters. Previous studies have also modelled the active layer as a thin layer with the assumption of flat bed surface (Ding et al, 2001; Heydenrych et al., 2002). The difference in the experimental observations by Heinen et al (1983a) and the latter modelling approach clearly shows that the estimation of the thickness of the active layer remains ambiguous. As a result, this study assumed a single particle diameter as the depth of the active layer and a correction factor was introduced to address the uncertainty in the assumption. The implications of this assumption are discussed in Section 6.2.1. Thus, to determine the surface area of solid particles in contact with the gas stream within the active layer (Figure 6.4) and Equations 6.56–6.61 were used in the calculation.

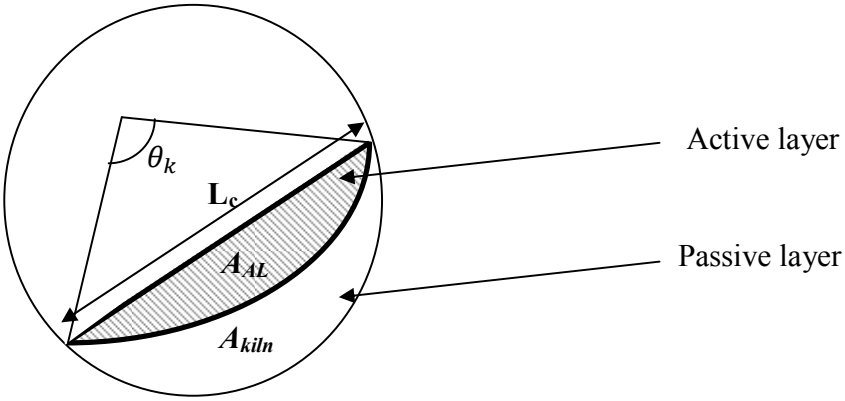

Figure 6.4: Active layer and passive layer in the kilning section *(A_{AL} is area of active layer, A_{kiln} is the chordal area (kilning area))*

Referring to Figure 6.4, to determine the kilning angle(θ_k), the drum mass (both active layer and passive layer) was converted to the chordal area *(A_{kiln})* using Equation 6.56 (Britton et al., 2006). The area of the active layer was calculated using Equation 6.57. In this thesis, the thickness of the active layer was assumed to be the diameter of a particle.

$$\frac{m_{kiln}}{\rho} = A_{kiln} = \frac{R^2}{2}(\theta_k - \sin\theta_k) \qquad \textbf{6.56}$$

$$A_{AL} = L_c \times d_p \qquad \textbf{6.57}$$

where m_{kiln}, θ_k, L_c and D_p are kilning mass *(kg/m)*, kilning angle *(radian)*, chordal length *(m)* and particle diameter *(m)* respectively.

The mass of the active layer (both solid particles and void) was determined using Equation 6.58.

$$M_{AL} = \left(\frac{A_{AL}}{A_{kiln}}\right) \times (m_s \times \Delta z) \qquad \textbf{6.58}$$

where $m_s, \Delta z$ are the mass of solid in each cell *(kg/m)* and length of the discretised cell *(m)* respectively. The length of the discretised cell was calculated using Equation 6.59

$$\Delta z = {}^{L}/_{N_c} \qquad \textbf{6.59}$$

where L, N_c are length of the unflighted section and number of discretised cells respectively.

The surface area of the estimated active layer in contact with the gas stream was then calculated by determining the number of solid particles within the active layer. It is then assumed that half of the total surface area of a solid particle is exposed to the gas stream (Equation 6.60).

$$A_{AL} = \frac{M_{AL}}{\left({}^{4}/_{3}\,\pi\left(0.5d_p\right)^3\right)\rho_{pt}}\left(\frac{4\pi\left(0.5d_p\right)^2}{2}\right) \qquad \textbf{6.60}$$

where ρ_P is the density of a particle.

Because of the uncertainty in estimating surface area, a correction factor *(θ_{AL})* is introduced, (Equation 6.61). The estimation of θ_{AL} will be discussed in the parameter estimation section.

$$A_{AL} = \theta_{AL}\left\{\frac{M_{AL}}{\left({}^{4}/_{3}\,\pi\left(0.5d_p\right)^3\right)\rho_{pt}}\left(\frac{4\pi\left(0.5d_p\right)^2}{2}\right)\right\} \qquad \textbf{6.61}$$

where θ_{AL} is the correction factor for the surface area of solid particles in the active layer.

6.1.1.7.2 Flighted section

As the solids cascade through the gas stream, there are voids within the falling solid particles. To determine the surface area (A_a) of airborne (or active) particles in contact with the gas stream, the

number of solid particles was calculated. It is then assumed that half of the surface area of a particle was exposed to the gas stream (Equation 6.62). A correction factor (θ_a) was also introduced to account for uncertainty in the estimated surface area. For future study, CFD analysis can also be used to determine the void fraction within the airborne solids.

$$A_a = \frac{M_a}{\left({}^4/_3\,\pi\left(0.5d_p\right)^3\right)\rho_{pt}}\left(\frac{4\pi\left(0.5d_p\right)^2}{2}\right) \qquad \textbf{6.62}$$

With the inclusion of the correction factor (θ_a), Equation 6.62 becomes:

$$A_a = \theta_a\left\{\frac{M_a}{\left({}^4/_3\,\pi\left(0.5d_p\right)^3\right)\rho_{pt}}\left(\frac{4\pi\left(0.5d_p\right)^2}{2}\right)\right\} \qquad \textbf{6.63}$$

6.2 Model solution

The model equations in Section 6.1 were solved using gPROMS modelling software. gPROMS code for this study can be found in Appendix F. Parameter estimation was carried out using the RTD and the moisture content profiles of the operating conditions presented in Table 6.1 (Test 4). The operating conditions represent the ideal condition of the dryer because the data were collected immediately after internally cleaning of the dryer and the operating conditions were close to its original design criteria. The predictability of the model was further tested by using these estimated values under the conditions of Tables 3.8, 3.10– 3.11. The mean particle sizes presented in Section 3.4.3 were used in the estimation of the solid surface area in contact with the gas stream in different sections of the dryer. As a result, the assumed mean particle diameters for sections A,B,C,D and E in the dryer were 0.02 m, 0.015 m, 0.012 m, 0.008 m, 0.007 m respectively. The gas properties such as density, thermal conductivity and dynamic viscosity

were modelled as a function of gas temperature (Incropera & DeWitt, 2002). The specific heat capacity of the water vapour was also modelled as a function of operating temperature (Incropera & DeWitt, 2002).

Table 6.1: Operating conditions for Test 4

Description	Average value	Standard deviation
Solid feed rate	146 ton/hr	7 ton/hr
Gas inlet temperature	500 ^{o}C	16.05 ^{o}C
Solid inlet moisture content	16.3%	1.5%
Gas outlet temperature	131 ^{o}C	4 ^{o}C
Product outlet temperature	46 ^{0}C	0.4 ^{o}C
Product outlet moisture content	12.4%	-
Rotational speed of the drum	3 rpm	-
Internal condition of the dryer	Unscaled	
Tracer quantity (LiCl powder)	2 kg	

6.2.1 Parameter estimation

The scaled moisture content profile shown in Figure 6.5 was the key experimental data used for model parameter fitting. The surface area correction factors (θ_{AL} and θ_a) in Equations 6.61 and 6.63 were used for parameter estimation. The parameter estimation was done manually because of the complexity within the model that resulted in numerical instability and significant computing requirements.

Different approaches were taken to investigate the dependence on these terms. The correction factor was assumed to be constant across the different sections of the dryer, which indicates a degree of confidence in both theoretical approaches to surface area determination. The fitted moisture content profile shown in Figure 6.5 was based on constant area correction factors (θ_{AL} and θ_a) equal to 1 (no correction factor) and 1.3 (constant correction factor). Both approaches resulted into poor fitting of the experimental moisture content data. It can be seen from the graph that without suitable correction factors, the fitting of the solid moisture content profile of the dryer was difficult (Figure 6.5).

To improve the fit to the moisture content profile, different correction factors were used for the different sections of the drum. The correction factors were obtained by manually tuning to fit the moisture content profile. The manually tuned surface area correction factors for the unflighted sections (A and E) were 2.4 and 1.4, which could indicate that the active layer is more than one particle diameter thick. However, the true thickness of the active layer is difficult to define accurately because of the complexity of the drying mechanism. The correction factors for the flighted sections B, C and D were 1.2, 0.6 and 0.42 respectively. It can be deduced from Figure 6.6 that the loss of moisture occurred mostly in the flighted sections but at the unflighted sections of the dryer, the evaporation rate was reduced. The difference in evaporation rate in the different sections can also be attributed to the amount of solids in contact with the incoming gas. The estimated interfacial surface areas for flighted sections B, C and D were 0.086 m^2/kg, 0.054 m^2/kg and 0.056 m^2/kg respectively while for the unflighted sections A and E were 0.0047 m^2/kg and 0.0029 m^2/kg. The small interfacial area at unflighted sections of the dryer indicated minimal drying. This observation further established the assumption of negligible drying in the passive phase of the flighted sections.

In order to match the gas outlet temperature, the heat loss correction factor in Equation 6.50 was also manually tuned but was assumed to be a constant value across the dryer. The manually tuned value was 15.

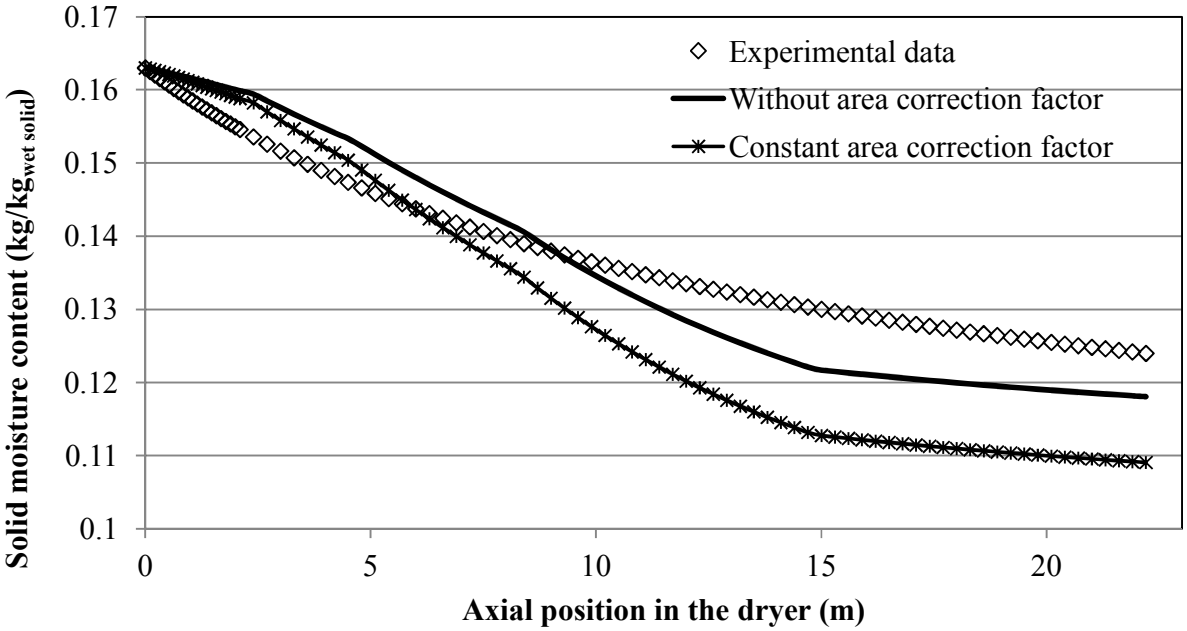

Figure 6.5: Effect of area correction factor on moisture content profile

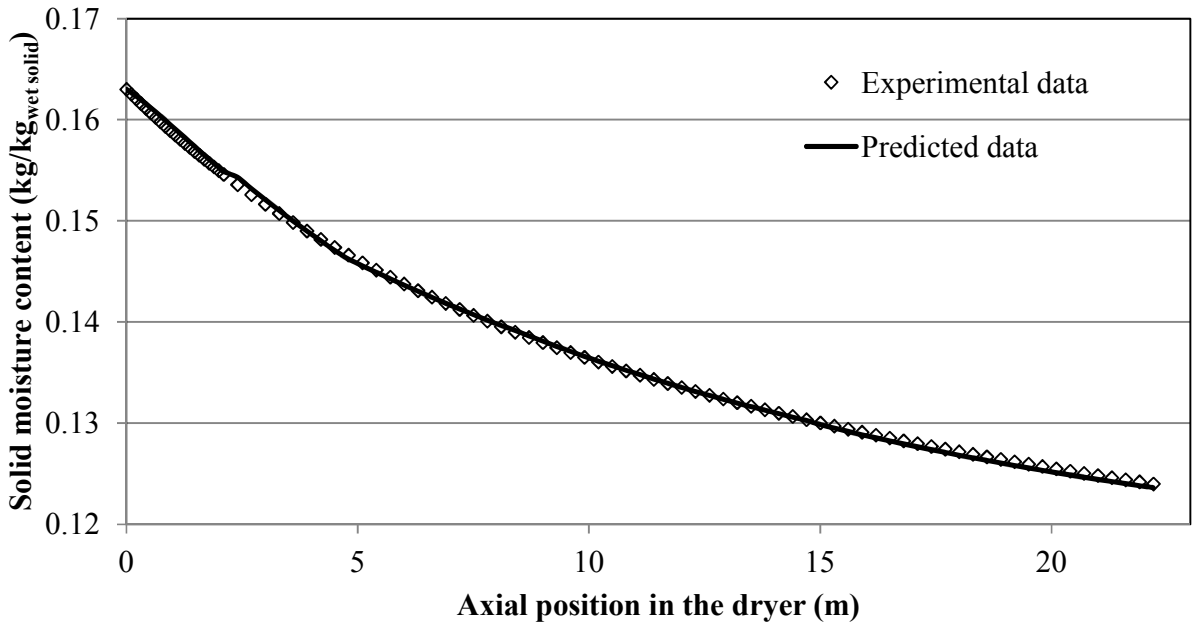

Figure 6.6: Solid moisture content profile

6.3 Model verification

To verify the model, mass and energy balances across the dryer were examined. Under steady state conditions, both mass and energy were conserved. For further verification, the mass of the tracer leaving the dryer was also compared to the mass of the tracer added to the dryer. The mass of the tracer that exited from the dryer was equal to the mass of the tracer added to the dryer. Figure 6.7 shows the predicted RTD profile well matched to the experimental RTD data.

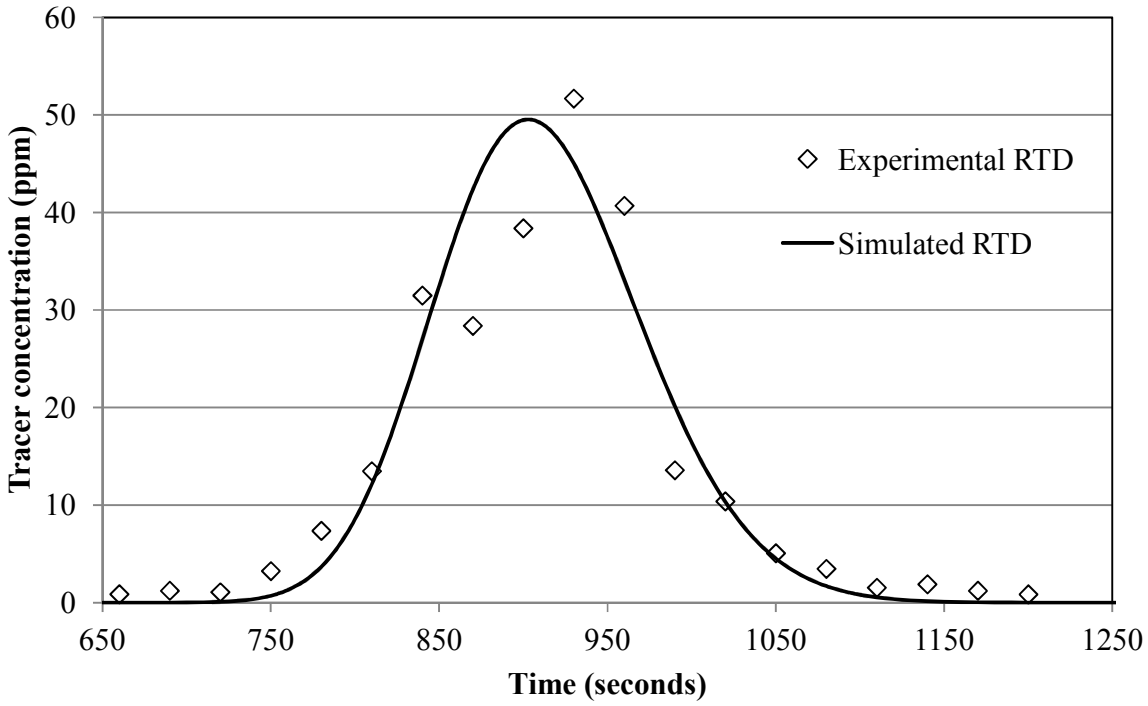

Figure 6.7: RTD profile ***(Test 4)***

The internal gas and solid temperature profiles across the dryer were not available and as a result, the study assumed if the outlet predicted values agree with the experimental values, the predicted profile was assumed to be appropriate. Figures 6.8 and 6.9 show the solid temperature profile, and gas and shell temperature profiles respectively.

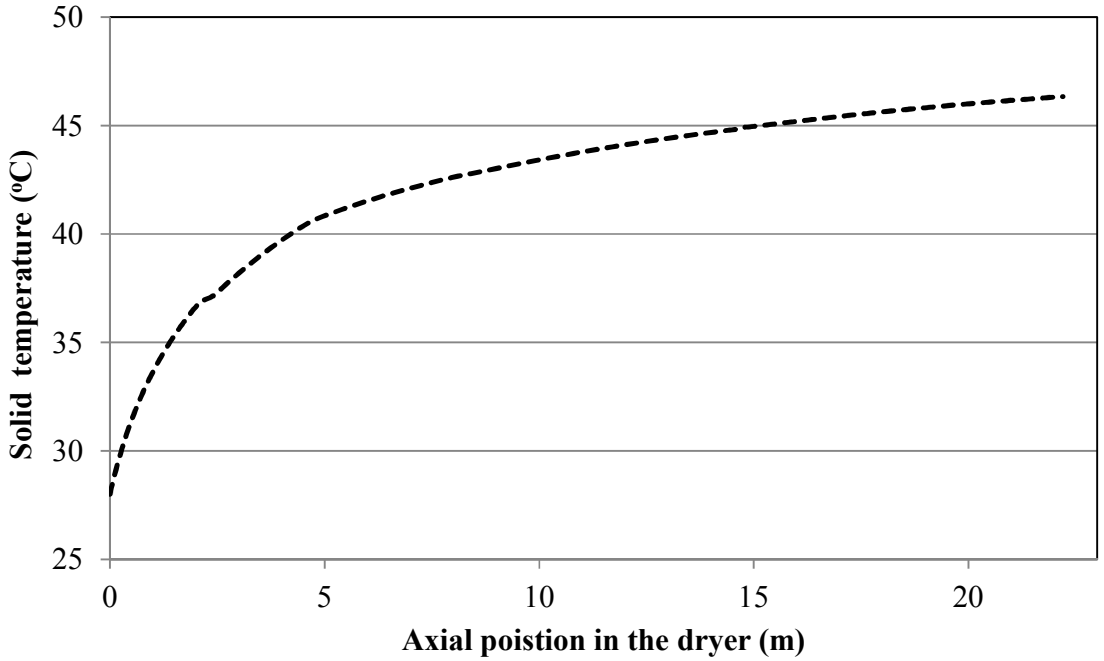

Figure 6.8: Solid temperature profile *(Test 4)*

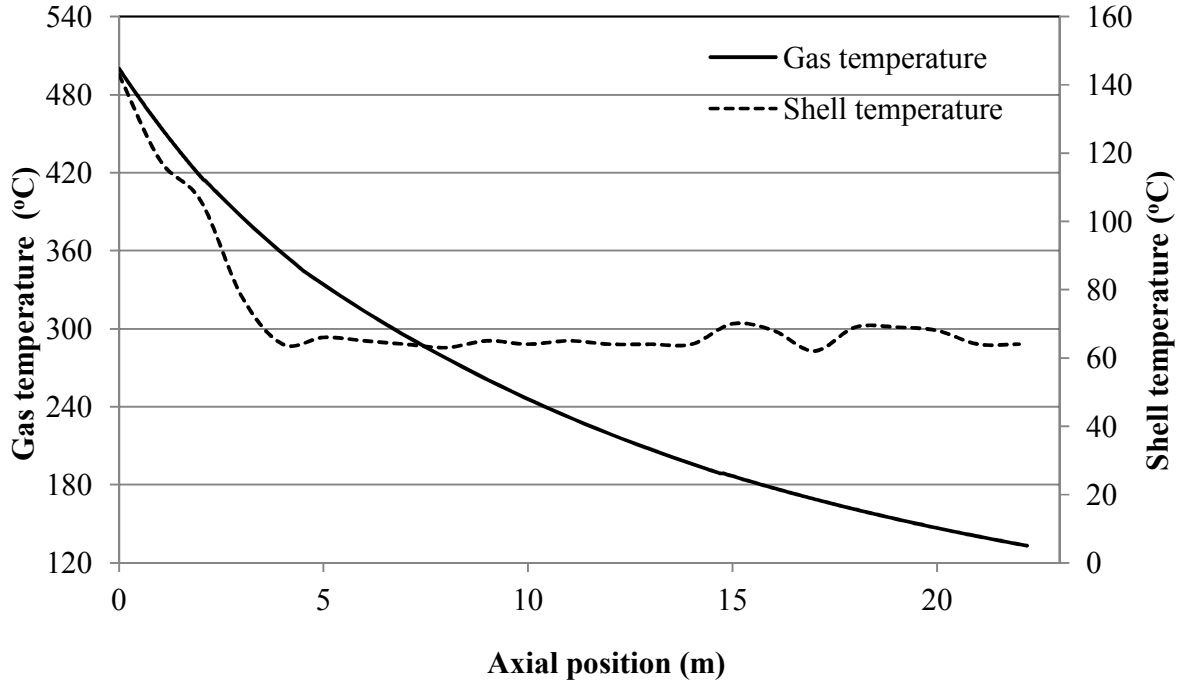

Figure 6.9: Gas and shell temperature profiles *(Test 4)*

The model was further tested using the operating conditions presented in Tables 3.8, 3.10–3.11. The predicted values of product moisture content, product temperature and gas outlet temperature are presented in Tables 6.2–6.4. The predicted values of product moisture content and product temperature at different operating conditions were comparable with the experimental data demonstrating the strong predictability of the model. There is some discrepancy in the gas outlet temperature but the trends are consistent.

Table 6.2: Product moisture content

	Experimental value ($kg/kg_{wet\ solid}$)	**Predicted value ($kg/kg_{wet\ solid}$)**
Test 3	0.136	0.143
Test 5	0.12	0.116
Test 6	0.122	0.127

Table 6.3: Product temperature

	Experimental value (^oC)	**Predicted value (^oC)**
Test 3	46	41
Test 5	45	47
Test 6	47	48

Table 6.4: Gas outlet temperature

	Experimental value (^oC)	Predicted value (^oC)
Test 3	165	168
Test 5	155	137
Test 6	150	130

6.4 Summary

A dynamic multiscale model was developed and validated for an industrial rotary dryer based on the assumption that the predicted and measured outlet temperature values should be similar. In order to facilitate the drying, the energy balances of both solid and gas phases were incorporated into the validated solid transport model presented in Chapter 5. The gas phase in both unflighted and flighted sections was modelled as plug flow systems. The correction factors were introduced to account for the uncertainty in the estimated surface areas of solids at different sections of the dryer. These correction factors were manually parameter estimated using the experimental moisture content. The heat loss via the shell was calculated using the resistance analysis. In order to match the gas outlet temperature, a heat loss correction factor was also introduced and was manually tuned.

CHAPTER SEVEN

7. MODEL APPLICATION

The key issues for MMG dryer management are those of controlling outlet moisture content, controlling outlet solids temperature and optimising fuel economy. The generation of solutions to these issues is complicated by the progressive scaling that occurs within the dryer, which leads to changing dryer performance over time. It is clear that complex multiscale dynamic dryer models, such as that developed in this thesis, are well suited to informing the development of control schemes, assisting the understanding of these complexities and predicting the effects of scaling on dryer outputs. In this chapter, the dynamic dryer model developed in Chapter 6 was utilised to gain insight on how to operate the dryer at both unscaled and scaled conditions and to provide insight into the complexities of drying. As a result of observations, the model was further used to investigate potential solutions to maximize heat retention within dryer and to reduce fuel consumption.

A typical dryer control scheme consists of three main factors: manipulated variables, controlled variables and disturbance variables. Currently, a distributed control system (DCS) based on feed forward control is used to control the MMG rotary dryer. The control algorithm calculates the amount of water to be removed from the solid using the following operating variables: solid inlet and target product moisture content, solid feed rate and air flow into the combustion chamber. The estimated amount of water is then used to determine the amount of fuel oil required for the combustion process, in effect increasing the gas inlet temperature. Scaling is not accounted for in MMG's control schemes. Despite the current control strategy, there is significant variation in the product moisture content due to changes in the solid feed rate and inlet moisture content, which

largely depends on the operation and performance of the five batch filter presses preceding the drying process.

The scale build-up within the dryer also affects the product quality because the gas-solids interaction is reduced in a scaled dryer (as observed in Section 5.4.1.1) and to compensate, MMG increases their fuel consumption in order to achieve product quality targets. It should be noted that the increase in fuel consumption is based on operator's judgment and experience. Despite the significant increase in fuel consumption, the desired product quality is commonly not achieved. Therefore, it is evident that there is a need to gain insight into the process performance under scaled and unscaled operations using the developed dynamic model.

To operate the dryer at an optimum condition, it is vital to identify the most suitable manipulated variables for different operating conditions. In this work, the suitability of a manipulated variable is defined by the following characteristic: can be adjusted in order to maintain the controlled variable at its set value. To identify the manipulated variable, the approach developed by Duchesne et al. (1997) was used. The approach measures the relative indices of the outlet variables to changes in the inlet variables.

The operational issues associated with MMG rotary dryer are high fuel consumption and scale build-up within the dryer. High fuel consumption results into significant increase in operating cost and carbon dioxide emission into the environment. With the newly introduced carbon price mechanism, it is important to investigate ways to reduce carbon pollution via reduction in fuel consumption. A novel solution rapidly gaining momentum is to maximise the heat energy within the dryer by insulating the outside shell. Prior to insulating dryers, the model should be used to examine the shell temperature profile in order to avoid shell degradation and external

temperature measurements should be taken so as to verify these findings. The dynamic model developed in this thesis provides an effective tool for examining potential benefits and identifying thermal constraints.

7.1 Relative indices analysis

The manipulated variables were identified using an approach used in a similar dryer modelling study by Duchesne et al. (1997). The approach involves determining the relative indices of the output variables to changes in the input variables using Equation 7.1. The significance of relative index was determined by how large its magnitude is in either a negative or positive direction. For example, a large positive relative index indicates that either increases or decreases in input variables will have significant effect on the corresponding output variables.

$$\eta = \frac{(\psi - \psi_{ref})/\psi_{ref}}{(\chi - \chi_{ref})/\chi_{ref}} \qquad \textbf{7.1}$$

here η is the relative index, ψ_{ref} and ψ are the values of the output variables before and after the change respectively. χ_{ref} is the initial value of the input variable and χ is its new value.

Five input variables were changed consecutively and their effects on product moisture content and product temperature were monitored. In this analysis, the temperature units were taken as degrees centigrade. The following input variables were selected for investigation: gas inlet temperature, gas inlet humidity, dryer's rotational speed, solid inlet temperature and solid feed rate. Gas inlet temperature is currently used as the manipulated variable in the industry control scheme. Rotational speed greatly affects the solid residence time and active mass (as observed in Section 5.4.1.2). Its potential as a manipulated variable was examined in this study. The gas inlet humidity was considered because in the sugar industry, the inlet air is conditioned prior to its

introduction into the dryer. The prospect of solid temperature as a manipulated variable was investigated because it contributes to the magnitude of the drying rate (Equation 6.33). It has also been observed in sugar drying that steam is added to the inlet sugar in order to increase moisture removal. This approach to dryer control may offer new opportunity to the mineral industry but care must be taken to avoid storage issues associated with high solid temperature. The effect of solid feed rate was investigated because the loading state plays a significant role in the efficiency of the dryer. As observed in Section 5.4.1.1, the active mass reduces as the scale accumulation increases. Therefore, reduction in solid feed rate may potentially be used to facilitate better gas-solids interaction, particularly within a scaled dryer. However, the practicability of this option remains to be examined (by the industry).

Product moisture content and temperature were considered as output (controlled) variables because there is a need to maintain transportable moisture content limit (12%) for MMG's products. In addition, MMG's current operating policy is to maintain product temperature within the range of 45 ^{o}C to 50 ^{o}C so as to avoid internal movement of water molecules to the external surface of the solid particles, which could lead to uncontrolled stickiness in the storage area.

In this study, the dryer's internal scaling condition was examined across the range of 0% to 80%. To obtain the references values, the steady state solutions from simulations carried out using the operating conditions presented in Table 6.1 under scenarios of 0% scaled to 80% scaled. For an overloaded scenario; the solid feed rate in Table 6.1 was changed to 63.89 $kg_{wet\ solids}/s$. The relative indices were determined by changing the specified input variable and performing the new simulations. The gas inlet temperature and gas inlet humidity were varied by positive 10% and negative 30% respectively. The solid inlet temperature and solid feed rate were varied by changing its initial values by positive 30% and negative 20% respectively. The maximum

rotational speed limit for MMG rotary dryer is 3 rpm, thus it was varied by reducing the speed by 30%. The relative indices of the output variables are presented in Tables 7.1- 7.5. Note in these tables that an increase in reference variable will result in a positive denominator in Equation 7.1 and a decrease will result in a negative denominator.

Table 7.1: Relative indices of output variables for a change in gas inlet temperature

Solid feed rate ($kg_{wet\ solid}/s$)	Dryer condition	Product moisture content	Product temperature
40.64	0% scaled	-0.425	0.410
40.64	40% scaled	-0.354	0.379
40.64	60% scaled	-0.287	0.387
40.64	80% scaled	-0.228	0.390
63.89	0% scaled	-0.284	0.375

Table 7.2: Relative indices of output variables for a change in gas inlet humidity

Solid feed rate ($kg_{wet\ solid}/s$)	Dryer condition	Product moisture content	Product temperature
40.64	0% scaled	0.030	0.092
40.64	40% scaled	0.025	0.103
40.64	60% scaled	0.025	0.120
40.64	80% scaled	0.026	0.141
63.89	0% scaled	0.019	0.074

Table 7.3: Relative indices of output variables for a change in rotational speed

Solid feed rate ($kg_{wet\ solid}/s$)	Dryer condition	Product moisture content	Product temperature
40.64	0% scaled	0.110	-0.094
40.64	40% scaled	-0.092	0.093
40.64	60% scaled	-0.056	0.071
40.64	80% scaled	-0.023	0.037
63.89	0% scaled	-0.089	0.116

Table 7.4: Relative indices of output variables for a change in solid inlet temperature

Solid feed rate ($kg_{wet\ solid}/s$)	Dryer condition	Product moisture content	Product temperature
40.64	0% scaled	-0.053	0.084
40.64	40% scaled	-0.044	0.082
40.64	60% scaled	-0.043	0.097
40.64	80% scaled	-0.041	0.115
63.89	0% scaled	-0.040	0.096

Table 7.5: Relative indices of output variables for a change in solid feed rate

Dryer condition	Product moisture content	Product temperature
0% scaled	0.198	0.124
40% scaled	0.337	0.0003
60% scaled	0.274	-0.008
80% scaled	0.211	-0.005

7.1.1 Discussion

The relative indices showed that the gas inlet variable temperature has most significant effect of all inlet variables on both product moisture content and temperature (Table 7.1). The product temperature responded to change in the gas inlet temperature in the opposite direction when compared with product moisture content. This phenomenon indicates that the solid temperature profile along the dryer is an important driving force in evaporative drying i.e. the higher the solid temperature, the higher the evaporation rate. However, the relative indices presented in Table 7.4 showed that increasing the solid inlet temperature does not enhance drying rate to the same extent. This observation demonstrates the complex relationship between the mechanisms involved in the rotary drying process. As the scale build up increases within the dryer, there is reduction in the effectiveness of using gas inlet temperature to control product moisture content, which is assumed to be a result of loading state. It should be noted that increasing gas inlet temperature in a scaled dryer increases the fuel consumption within the combustion chamber without necessarily achieving the product specification. This has been also observed by MMG operations controlling under high scaling situations. Similar conclusions can be made regarding high solid feed rate scenarios, which also reduce the effectiveness of gas temperature as a manipulated variable. The relative indices in Table 7.1 could be used to modify the existing control strategies under these scenarios

Gas inlet humidity has a reduced effect on the output variables for the different operating conditions compared to gas inlet temperature (Tables 7.2 and 7.3). Its effect is to decrease both the solid outlet moisture content and temperature. Under scaled conditions, inlet gas humidity could be used in conjunction with inlet gas temperature to better control the dryer. With 30% decrease in the gas inlet humidity, the decrease in the exhaust gas humidity ranged from 5% to

8% for the studied conditions. It is evident that the driving force for drying the solid also depends on the temperature difference between the gas and solids.

The effect of rotational speed on temperature and moisture presented in Table 7.3 is complicated. Rotational speed affects both the residence time and the proportion of solids in the active and passive phases. Lower speed results in more solids rolling on the base of the drum at both scaled and overloaded conditions compared to unscaled condition. For example, in section B of the dryer, the passive masses at different scaling conditions are: 1970 kg (0% scaling), 4006 kg (40 % scaling), 4400 kg (60% scaling) and 4600 kg (80% scaling). On the other hand, the active mass decreases with increase in the scaling condition: 250kg (0% scaling), 194 kg (40% scaling), 125 kg (60% scaling) and 70 kg (80% scaling). It can be concluded that the increase in the passive solids at different scaling conditions has an opposing effect to the increased residence time resulting from decreased rotational speed. Intuitively these effects are hard to predict without the use of models such as that developed in this thesis.

Table 7.5 shows that the loading state of the dryer (induced by varying solid feed rate) has significant effect on the product moisture content. Solid feed rate as a manipulated variable for scaled conditions is a potential solution to achieving target product moisture content in comparison to using the gas inlet temperature as manipulated variable. Similar to the observations regarding rotational speed, a predictive model is considered essential to implementing this approach. However, the practicability of this option largely depends on the production targets of the industry.

7.2 Optimising fuel consumption

The gas inlet temperature was recognized in the previous section to be one of the most important manipulated variables. The gas inlet temperature to the dryer is manipulated by increasing fuel consumption in the combustion chamber. The cost of fuel consumed is one of the major operating costs for the MMG rotary dryer and typical rate of consumption is 750 kg/hr of fuel to generate hot inlet gas temperature at 500 ^{o}C. With increasing cost of fuel and increased emphasis on reducing carbon dioxide emission to the environment, the model is used to examine engineering design options to reduce the daily fuel consumption.

It is a common practice in process industries to externally insulate the dryer so as to increase its thermal efficiency and reduce heat losses. However, mild steel degradation can occur when wall temperatures exceed 593 ^{o}C (according to API standard 521). This constraint is often used to justify the absence of thermal insulation on dryer walls. The model can be easily manipulated through minor adjustment in model parameters to represent such common engineering design solutions. The model was used to investigate options to maximize the retention of heat within the dryer. In the model developed in this thesis, the heat loss was assumed over the entire circumference of the shell and was modeled by determining individual thermal resistances through the shell as stated in Equation 6.50. To examine the option of externally insulating the dryer, the heat loss factor in Equation 6.50 was set to zero, effectively removing completely heat losses through the shell. The effect on output variables such as gas outlet temperature and product moisture content was monitored.

Table 6.1 presents the operating conditions used for the investigation. Figure 7.3 presents gas temperature profiles with and without heat loss. Figures 7.4 and 7.5 are the solids temperature and moisture content respectively. The study observed a 90% and a 22% increase in the solid and

gas outlet temperatures respectively when the heat loss factor was set to zero. The increase in the product temperature indicates that by insulating dryer shells, the convective heat transfer to solids can be increased, which enhances the drying process and, leads to decrease in the product moisture content. However, care must be taken to avoid increases in the product temperature that can result in downstream storage problems.

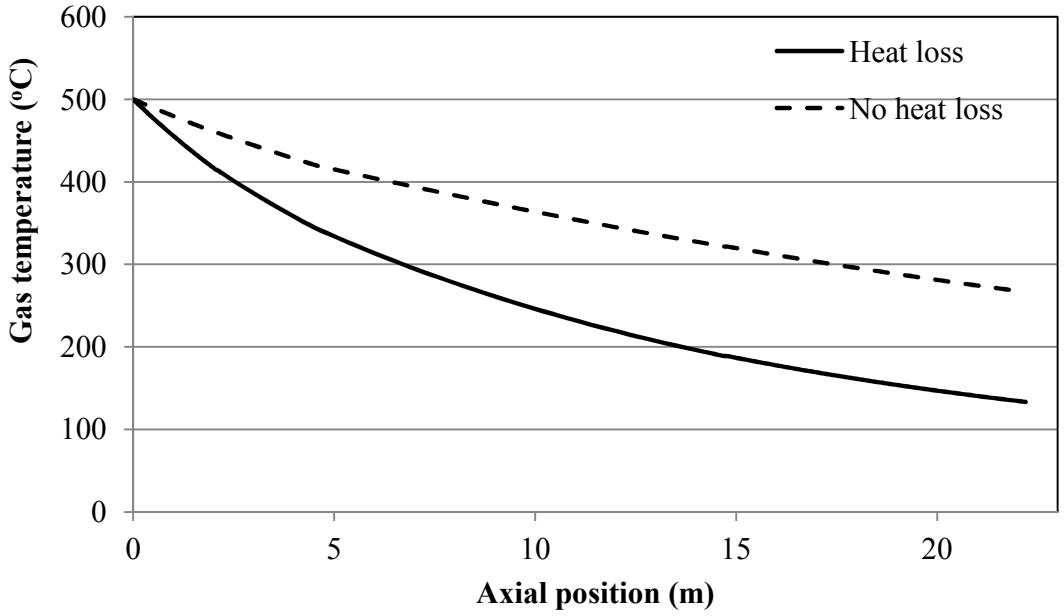

Figure 7.1: Effect of external heat loss on gas temperature profile

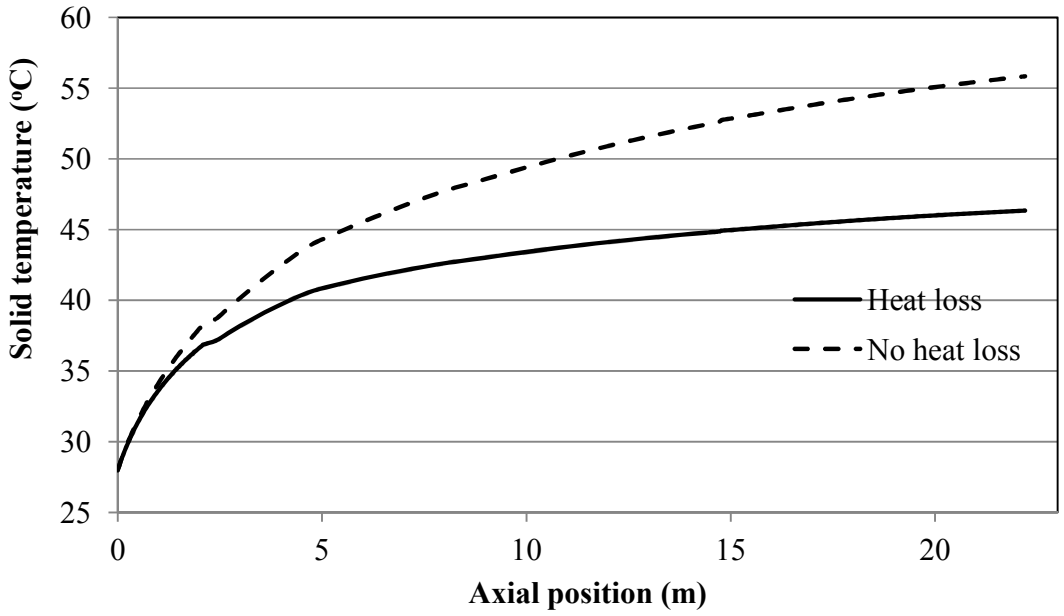

Figure 7.2: Effect of external heat loss on solid temperature profile

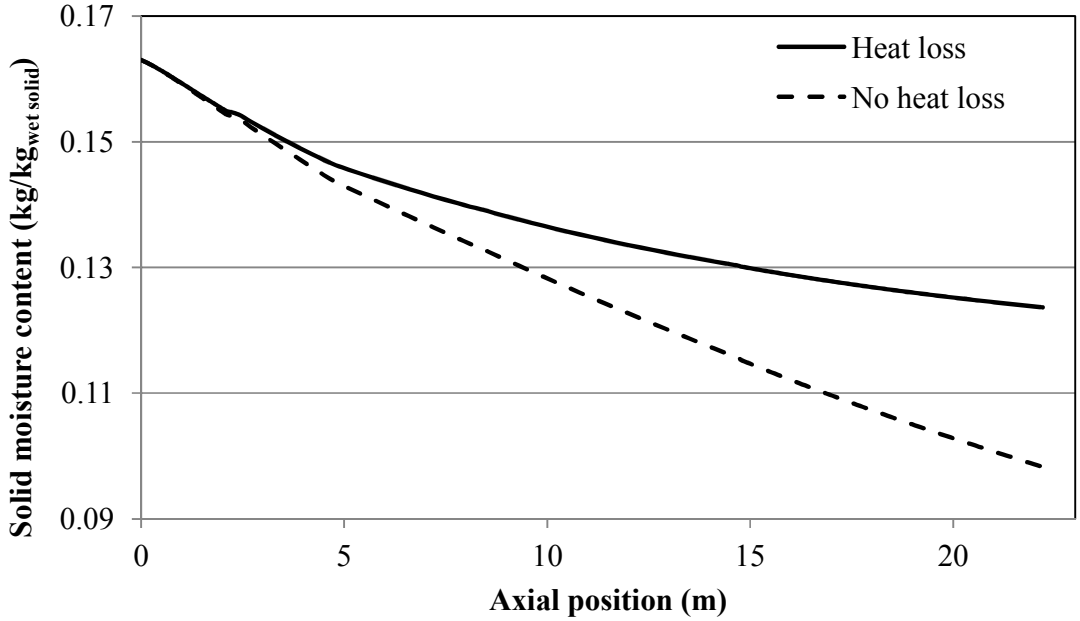

Figure 7.3: Effect of external heat loss on solid outlet moisture content profile

In an attempt to avoid high gas and solid outlet temperatures, the gas inlet temperature was reduced for the insulated rotary dryer. Figures 7.6 and 7.7 show the resulting moisture profile and solid temperature profile for a reduced inlet gas temperature (350 ^{o}C) respectively. The figures illustrate a potential reduction in fuel consumption through external insulation of the dryer whilst maintaining the desired product quality for the proposed externally insulated dryer. The difference in the solid temperature and moisture profiles for heat loss and no heat loss scenarios can be attributed to variation in gas temperature profiles along the length of the drum. Another retrofit modification is to recycle back the exhaust gas from the dryer into the combustion chamber, thereby further reducing the amount of fuel consumed within the dryer. However, this option was not quantified in this current study.

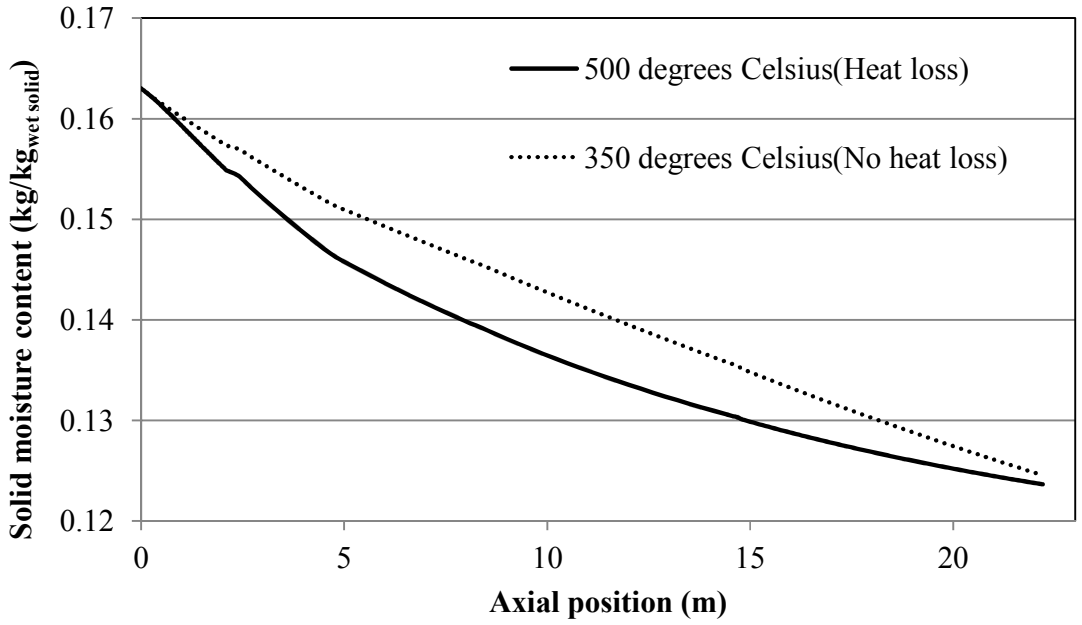

Figure 7.4: Effect of gas inlet temperature on solid moisture content profile in an insulated dryer

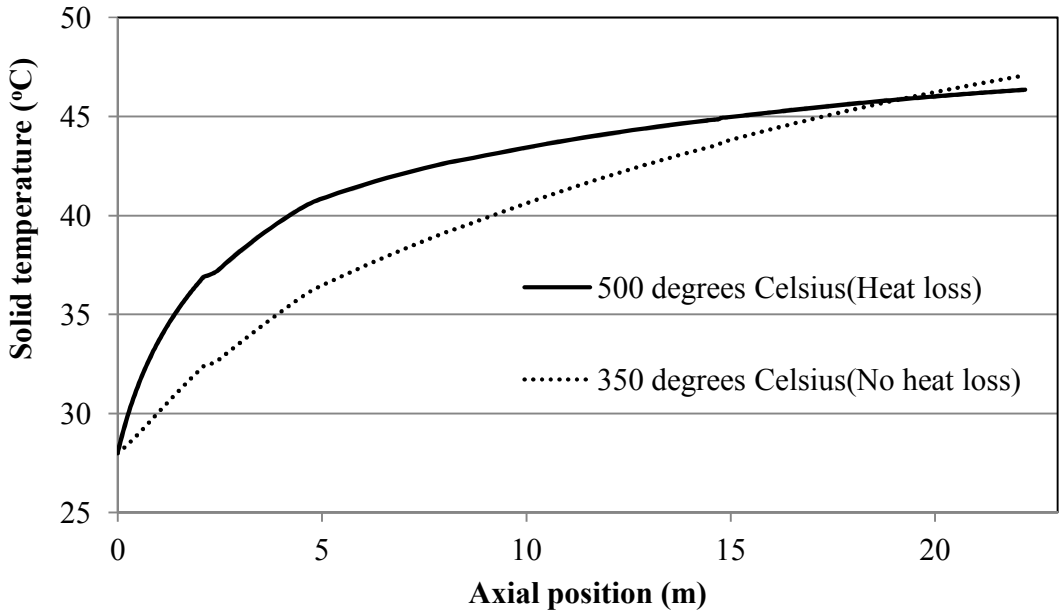

Figure 7.5: Effect of gas inlet temperature on solid temperature profile in an insulated dryer

7.4. Summary

The most suitable manipulated variables under both scaled and unscaled conditions were determined. The criterion for choosing a suitable manipulated variable was determined using the approach developed by Duchesne et al. (1997). The approach measured the relative indices of the outlet variables to changes in the inlet variables. The gas inlet temperature was found to be the most suitable manipulated variable to control and optimise the drying process but its effectiveness depends on scaling and loading states within the dryer. The model was found to be necessary to understand the complex effects of rotational speed and gas humidity on output variables. The study also suggested the solid feed rate be reduced for a scaled dryer (i.e. modifying the loading state) so as to achieve optimum gas-solid interaction. To further utilize the model to reduce the amount of fuel consumed, the study investigated options to maximize the

retention of heat within the dryer. Although the model presents a simplified description of thermal profile within a dryer shell, insulating the dryer coupled with reduction in the gas inlet temperature appears to be a promising option for meeting the desired product quality and reducing fuel consumption.

CHAPTER EIGHT

8. CONCLUSION AND RECOMMENDATIONS

8.1 Conclusion

A dynamic multiscale model was developed and validated for the MMG rotary dryer. The gas phase in both the unflighted and flighted sections of the dryer was modelled as a plug flow system. The solid phase in the unflighted sections was modelled as an axial dispersed plug flow system. Following typical convention, a compartment modelling approach was used to model the solid transport in the flighted sections. This approach is a series-parallel formulation of well-mixed tanks and solids distribution between the compartments was estimated through geometric modelling and consideration of design loading constraints. The modelling approach was able to account for variation in flight configuration and geometry. Model parameters were estimated via a combination of geometric modelling (flight geometry, dryer geometry and solid properties) and parameter estimation.

Flight loading experiments were carried out at pilot scale to determine the effect of moisture content and rotational speed on dryer design loadings. Multiple photographs of the cross-sectional area of the drum were taken and analysed. The study developed an automated combination of ImageJ and MATLAB code to enhance the image quality and to estimate the regions of interest. The regions of interest were the first unloading flight, the upper half of the drum, the total flight-borne solids and the airborne phase.

To determine the design loading, different approaches were investigated. The estimated design load values based on all the approaches were similar, however, the piecewise regression analysis of the saturated first unloading flight data were found to be more consistent, after consideration

of the error in the estimated values. Similar profiles were obtained using the approaches based on the saturation of the airborne solids and of the flight-borne solids in the upper half of the drum. The study observed a sudden peak in the plotted areas of the airborne solids and of the flight-borne solids in the upper half of the drum. The peaks may be used as a criterion to estimate the design load but require highly accurate determination of area and also an understanding of the flight-borne solids bulk density. The design loading increased with an increase in moisture content and an increase in rotational speed.

The mass of airborne solids at the design load was determined using a combination of image analysis and Eulerian-Eulerian simulation of free-falling curtains. The airborne solids increase with an increase in rotational speed but challenges with analysing high moisture content situation remain. The study also carried out experimental validation of design load models available in the literature and a modified equation based on the Baker (1988) model was proposed. The modified design load model was used in this study as a constraint within the compartment model.

In order to validate the dynamic multiscale model of the dryer and parameter estimate unknown model parameters, a series of residence time distribution (RTD) pulse tracer tests were performed using lithium chloride as the tracer. Solid velocity and axial dispersion coefficients were parameter estimated using the RTD experimental data. The experimental moisture content profile was used for model parameter fitting. The gas and solid temperature profiles were also predicted.

There was uncertainty in the estimation of the solid surface area in contact with the gas stream, which led to introducing correction factors within the surface area terms for different sections of the dryer. The correction factors were manually tuned to fit the experimental moisture content

profile. The study observed the interfacial surface areas at the unflighted sections were small in comparison to the airborne solids, which indicated the gas-solids interaction in the kilning phase was minimal. This observation validated the commonly made assumption of negligible drying in the passive phase or kilning phase of the flighted sections of flighted rotary dryers.

The main manipulated variables for different operating conditions were identified using the relative sensitivity indices of output variables to changes in the input variables. Gas inlet temperature was identified as the manipulated variable for MMG rotary dryer. Both rotational speed and gas inlet humidity have small effect on the output variables. At scaled internal condition, the study suggested the solid feed rate should be reduced so as to achieve optimum gas-solid interaction. To address high fuel consumption associated with MMG rotary dryer, the study proposed the dryer should be externally insulated so as to maximize the thermal efficiency of the dryer. It should be noted that mild steel degradation can occur when the dryer's wall temperature exceeds 593 ^{o}C. However, the wall temperature for the studied dryer is expected to be less than 593 ^{o}C because the gas inlet temperature for the proposed externally insulated dryer will be around 350 ^{o}C.

8.2 Recommendations

Based on the findings in this thesis, the following recommendations are made:

- This study observed a sudden peak in the airborne and upper flight-borne mass during the flight loading experiments. To further investigate this phenomenon and also investigate voidage variation in the airborne solids, there is a need to improve the experimental set-up. These improvements include: reducing the length of the drum so as to avoid background interference of the falling solid particles and the lighting set-up should be

improved so as to achieve consistent pixel intensity within a set of photographs for a particular experimental condition.

- In this study, the geometric model calculates the cross-sectional area of flight-borne solids and a consolidated density was assumed to determine the flight holdup. It is a challenge to quantify density in both flights and in the airborne phase. There is need to determine the density profile of flight-borne solids, which could be facilitated by improved image analysis and more controlled particle properties.

- This study developed correlations for solid velocity and axial dispersion coefficient correlations based on limited RTD experimental data. It is important to carry out a comprehensive parametric study to determine how the operating parameters such as rotational speed, dynamic angle of repose, diameter of the drum and loading state of the drum affect the residence time and axial dispersion in the kilning phase. These RTD experiments should be carried out on pilot scale dryer because of the complexity involved in manipulating the operating variables within an industrial setting.

- There is a need for better understanding of the dynamics of the gas phase. Residence time distribution tests for the gas phase in flighted rotary dryers should be undertaken in conjunction with collection of velocity and high quality humidity measurements.

- In literature, there is no heat transfer correlation developed for curtaining particles. An experimental and CFD study needs to be undertaken to investigate heat transfer mechanism within the curtains. The study can provide information on how to model the heat transfer coefficient in the multiscale model and provide greater certainty regarding airborne solid interfacial contact areas. There is also a need to investigate the complex

relationship between the evaporation rate and the convective heat transfer as observed in this study as this is critical to dryer control.

- A dynamic model was developed but there was uncertainty in the responses of the outlet variables to step change in the inlet parameters. Thus, a validation of the dynamic response is required through the collection of dynamic data from the Process Information (PI) data.

REFERENCES

Alvarez, P.I, Shene, C., 1994. Experimental study of residence time in a direct rotary dryer. *Drying Technology*, 12(7), 1629–1651.

American Petroleum Institute, 2007. *ANSI/API Std 521:guide for Pressure-relieving and Depressuring Systems: Petroleum petrochemical and natural gas industries-Pressure relieving and depressuring systems,* 5th Edition, API Publishing Services, Washington, United States.

Arbuckle, D., Brash, I., 2001. Technical report on the monitoring conducted at the Pasminco Century zinc mine Portside in Karumba: Unilabs Environmental, Australia: Draft report May 01078.

Baker, C.G.J., 1988. The design of flights in cascading rotary dryers. *Drying Technology*, 6(4), 631–653.

Baldwin, T., 2005. Determining and modelling the heat loss from QNI's rotary ore dryer. B.Eng. Thesis, James Cook University, Australia.

Barr, P.V., 1986. Heat transfer processes in rotary kilns. PhD Thesis, University of British Columbia, Canada.

Batu, A., Selcuk, N., 2002. Modelling of radiative heat transfer in the freeboard of fluidized bed combustor using the zone method of analysis, *Turkish Journal of Engineering and Environmental Science,* 26, 49-58.

Benlyamani, M., Ajersch, F., 1986. Agglomeration of particles during roasting of zinc sulphide concentrates, *Metallurgical Transactions,* 17B, 647-656.

Bensmann, S., Subagyo, A., Walzel, P., 2010. Residence time distribution of segregating sand particles in a rotary drum. *Particulate Science and Technology*, 28, 319–331

Boateng, A.A., 1993. Rotary Kiln Transport Phenomena: Study of the bed motion and heat transfer. PhD Thesis, University of British Columbia, Canada.

Boateng, A.A., Barr, P. V.R, 1996. Modelling of particle mixing and segregation in the transverse plane of a rotary kiln. *Chemical Engineering Science*, 51, 4167–4181.

Boerefijn, R., Ghadiri, M., 1998. High speed video image analysis of flow of fine particles in fluidized bed jets. *Advanced Powder Technology*, 9(3), 229–243.

Britton, P.F., Sheehan, M.E., Schneider, P.A., 2006. A physical description of solids transport in flighted rotary dryers. *Powder Technology*, 165, 153–160.

Bureau of Meteorology (BOM), 2010. Retrieved 07 July 2011, from http://www.bom.gov.au/climate/

Cao, W.F., Langrish, T.A.G., 2000. The development and validation of a system model for a counter-current cascading rotary dryer. *Drying Technology*, 18(1 & 2), 99–115.

Chen, T.T., Dutrizac, J.E., 2004. Mineralogical changes occurring during the fluid-bed roasting of zinc sulfide concentrates. *Journal of the Minerals, Metals and Material Society,* 56(12), 46-51.

Cholette, A., Cloutier, L., 1959. Mixing Efficiency Determinations for Continuous Flow Systems. *Canadian Journal of Chemical Engineering*, 37, 105–112.

Christensen, M., 2008. Evaluating Porter's assumption to determine rotary dryer design loads. B.Eng. Thesis, James Cook University, Australia.

Churchill, S.W., Chu, H.S., 1975. Correlation equations for laminar and turbulent free convection from a vertical plate. *International Journal of Heat and Mass Transfer*, 18, 1323–1329.

Dagot, C., Pons, M.N., Casellas, M., Guiband, G., Dollet, P., Baudu, M., 2001. Use of image analysis and rheological studies for control of settleability of filamentous bacteria: application in SBR reactor. *Water Science and Technology*, 43(3), 27–33.

Danckwerts, P.V., 1953. Continuous flow systems distribution of residence times. *Chemical Engineering Science*, 2, 1–13.

Davis, M.E., Davis, R.J., 2003. *Fundamentals of Chemical Reaction Engineering*. McGraw-Hill Higher Education, United States.

D'Errico, J., 2009. Shape language modeling. (http://www.mathworks.com/matlabcentral/fileexchange/24443), MATLAB central file exchange, Retrieved December 18, 2009.

Dhanjal, S.K., Barr, P.V., Watkinson, A.P., 2004. The rotary kiln: an investigation of bed transferr in transverse plane. *Metallurgical and Minerals Transactions,* 35B, 1059-1070.

Didriksen, H., 2002. Model based predictive control of a rotary dryer. *Chemical Engineering Journal*, 86, 53–60.

Ding, Y.L., Seville, J.P.K., Forster, R., Parker, D.J., 2001. Solids motion in rolling mode rotating drums operated at low to medium rotational speeds. *Chemical Engineering Science,* 56, 1769–1780.

Douglas, P.L., Kwade, A., Lee, P.L., Mallick, S.K., 1993. Simulation of a rotary dryer for sugar crystalline. *Drying Technology*, 11(1), 129–155.

Duchesne, C., Thibault, J., Bazin, C., 1996. Modelling of the solids transportation within an industrial rotary dryer: A simple model. *Industrial Engineering Chemistry Research*, 35, 2334–2341.

Duchesne, C., Thibault, J., Bazin, C., 1997. Modelling and dynamic simulation of an industrial rotary dryer. *Developments in Chemical Engineering and Mineral Processing Journal*, 5(3–4), 155–182.

Fan, L.T, Ahn, Y.K., 1961. Axial dispersion of solids in rotary flow systems. *Applied Scientific Research*, 10(1), 465–470.

Felder, R.M., Rousseau, R.W., 2005. *Elementary Principles of Chemical Processes*, Third edition. John Wiley & Sons, New York.

Friedman, S.J., Marshall, W.R., 1949a. Studies in Rotary Drying. Part 1 – Holdup and Dusting. *Chemical Engineering Progress*, 45(8), 482–493.

Friedman, S.J., Marshall, W.R., 1949b. Studies in Rotary Drying. Part 2 – Heat and Mass Transfer. *Chemical Engineering Progress*, 45(9), 573–588.

Gidaspow, D., 1994. *Multiphase Flow and Fluidization: Continuum and Kinetic Theory Descriptions*. Academic Press, San Diego.

Gorog, J.P., Brimacombe, J.K., Adams, T.N., 1981. Radiative heat transfer in rotary kilns. *Metallurgical Transactions B,* 12B, 55-70.

Harrison, S.R., Tamaschke, H.U., 1984. *Applied Statistical Analysis*. Prentice-Hall of Australia Pty Ltd.

Hatzilyberis, K.S., Androutsopoulos, G.P., 1999. An RTD study for the flow of lignite particles through a pilot rotary dryer. Part II: flighted drum case. *Drying Technology*, 17(4 & 5), 759–774.

Heffels, C., Willemse, A., Scarlett, B., 1996. Possibilities of near backward light scattering for characterizing dense particle systems. *Powder Technology*, 86, 127–135.

Henein, H., Brimacombe, J.K., Watkinson, A.P., 1983a. Experimental study of transverse bed motion in rotary kilns. *Metallurgical transcations B,* 14B, 191–203.

Heydenrych, M.D., Greff, P., Heesink, A.B.M., Versteeg, G.F., 2002. Mass transfer in rolling rotary kilns: a novel approach. *Chemical Engineering Science,* 57, 3851–3859.

Hirosue, H., 1989. Influence of particles falling from flights on volumetric heat transfer coefficient in rotary dryers and coolers. *Powder Technology*, 59, 125–128.

Incropera, F.P., DeWitt, D.P., 2002. *Fundamentals of Heat and Mass Transfer*, Fifth Edition. John Wiley & Sons, New York.

ImageJ plugins. (2007). Sigma filter [online]. Available: http://rsbweb.nih.gov/ij/plugins/sigma-filter.html [accessed 9 October 2009].

Iguaz, A., Esnoz, A., Martinez, G., Lopez, A., Virseda, P., 2003. Mathematical modelling and simulation for the drying process of vegetable wholesale by-products in a rotary dryer. *Journal of Food Engineering*, 59, 151–160.

Iguaz,A., Budman, H., Douglas, P.L., 2002. Modelling and control of an alfalfa rotary dryer. *Drying Technology,* 20(9), 1869-1887.

Jauhari, R., Gray, M.R., Masliyah, J.H., 1998. Gas-solid mass transfer in a rotating drum. *The Canadian Journal of Chemical Engineering*, 76, 224–232.

Kelly, J.J., O'Donnell, J.P., 1968. Dynamics of granular material in rotary dryers and coolers. *Institution of Chemical Engineers Symposium Series*, 29, 33–41.

Kelly, J.J., O'Donnell, J.P., 1977. Residence time model for rotary drums. *Transactions of the Institution of Chemical Engineers*, 55, 243–252.

Kelly, J.J., 1987. Rotary Drying. In: Mujumdar, A.S., ed., *Handbook of Industrial Drying,* 1st edition. Marcel Dekker Incorporated, New York.

Kelly, J., 1992. Flight design in rotary dryers. *Drying Technology*, 10(4), 979–993.

Kelly, J.J., 1995. Rotary Drying. In: Mujumdar, A.S., ed., *Handbook of Industrial Drying,* 2nd edition. Marcel Dekker Incorporated, New York.

Kim, K., Siegel, N., Kolb, G., Rangaswamy, V., Moujaes, S., 2009. A study of solid particle flow characterization in solar particle receiver. *Solar Energy*, 83, 1784–1793.

Kohav, T., Riachardson, J.T., Luss, D., 1995. Axial dispersion of solid particles in continuous rotary kiln. *American Institute of Chemical Engineers Journal*, 41(11), 2465–2475.

Koksal, M., Hamdullahpur, F., 2005. CFD simulation of the gas-solid flow in the riser of a circulating fluidized bed with secondary air injection. *Chemical Engineering Communications*, 192, 1151–1179.

Lee, A., Sheehan, M.E., Britton, P.F., Schneider, P.A., 2005. A comparison of compartment models for solids transport in flighted rotary dryers. In, *Proceedings of Chemeca conference, 2005*, September 25–28, Brisbane, Australia.

Lee, A., 2008. Modelling transport phenomena within flighted rotary dryers. PhD Thesis, James Cook University, Australia.

Lee, A., Sheehan, M.E., 2010. Development of a geometric flight unloading model for flighted rotary dryers. *Powder Technology*, 198(3), 395–403.

Levenspiel, O., 1999. *Chemical Reaction Engineering*, 3rd edition. Wiley, New York.

Lisboa, M.H., Vitorino, D.S., Delaiba, W.B., Finzer, J.R.D., Barrozo, M.A.S., 2007. A study of particle motion in rotary dryer. *Brazilian Journal of Chemical Engineering*, 24(3), 365–374.

Liu, X., Specht, E., Gonzalez, O.G., Walzel, P., 2006. Analytical solution for the rolling-mode granular motion in rotary kilns. *Chemical Engineering and Processing*, 45, 515–521.

Lun, C.K.K., Savage, S.B., Jeffery, D.J., 1984. Kinetic theories for granular flow: inelastic particles in couette flow and slightly inelastic particles in general flow field. *Journal of Fluid Mechanics*, 140, 223–256.

Matchett, A.J., Baker, C.G.J., 1987. Particle residence times in cascading rotary dryers, Part 1 – Derivation of the two-stream model. *Journal of Separation Process Technology*, 8, 11–17.

Matchett, A.J., Baker, C.G.J., 1988. Particle residence times in cascading rotary dryers, Part 2 – Application of the two-stream model to experimental and industrial data. *Journal of Separation Process Technology*, 9, 5–13.

Matchett, A.J., Sheikh, M.S., 1990. An improved model of particle motion in cascading rotary dryers. *Transactions of the Institution of Chemical Engineers*, 68, Part A, 139–48.

Mellmann, J., 2001.The Transverse Motion of Solids in Rotating Cylinders—Forms of Motion and Transition Behaviour. *Powder Technology*, 118(3), 251–270.

Mellmann, J., Specht, E., Liu, X., 2004. Prediction of rolling bed motion in rotating cylinders. *American Institute of Chemical Engineers Journal*, 50, 2783–2793.

Mendenhall, W., 1979. *Introduction to Probability and Statistics*. Wadsworth Publishing Company, Inc., United States of America.

Mu, J., Perlmutter, D.D., 1980. The mixing of granular solids in a rotary cylinder. *American Institute of Chemical Engineers Journal*, 26 (6), 928.

Myklestad, O., 1963. Heat and mass transfer in rotary dryers. *Chemical Engineering Progress Symposium Series,* 59(41), 129–137.

Nopharatana, M., Mitchell, D.A., Howes, T., 2003. Use of confocal scanning laser microscopy to measure the concentrations of aerial and penetrative hyphae during growth of Rhizopus oligosporus on a solid surface. *Biotechnology and Bioengineering,* 84 (1), 71-77.

Obadiat, T.M., Al-Masaeid, H.R., Gharaybeh, F., Khedaywi, T.S., 1998. An innovative digital image analysis approach to quantify the percentage of voids in mineral aggregates of bituminous mixtures. *Canadian Journal of Civil Engineering*, 25(6), 1041–1049.

Oosterbaan, R.J., Sharma, D.P., Singh, K.N., Rao, K.V.G.K., 1990. Crop production and soil salinity: Evaluation of field data from India by segmented linear regression with breakpoint. In: *Proceedings of the Symposium on land drainage for salinity control in arid and semi-arid regions*, 25 February–2 March, Cairo, Egypt, 3, 373–383.

Ortiz, O.A., Martinez, N.D., Mengual, C.A., Noriega, S.E., 2003. Steady state simulation of a rotary kiln for charcoal activation. *Latin American Applied Research*, 33, 51–57.

Ortiz, O.A., Su′arez, G.I., Nelson, B., 2005. Dynamic simulation of a pilot rotary kiln for charcoal activation. *Computers and Chemical Engineering*, 29, 1839–1848.

Owens, P., 2006. Experimental characterisation of an industrial zinc concentrate rotary dryer. B.Eng. Thesis, James Cook University, Australia.

Perez-Correa, J.R., Cubillos, F., Zavala, E., 1998. Dynamic simulation and control of direct rotary dryers. *Food Control*, 9(4), 195–203.

Perron, J., Bui, R.T., 1990. Rotary cylinders: solids transport prediction by dimensional and rheological analysis. *Canadian Journal of Chemical Engineering*, 68, 61–68.

Perry, R.H., Green, D.W., 1984. *Perry's chemical engineers' handbook,* 6th edition. McGraw-Hill, New York.

Poletto, M., Bai, R., Joseph, D.D., 1995. Propagation of voidage waves in two-dimensional liquid-fluidized bed. *International Journal of Multiphase Flow*, 21(2), 223–239.

Porter, S.J., 1963. The design of rotary driers and coolers. *Transactions of the Institution of Chemical Engineers*, 41, 272–280.

Process Systems Enterprise, 2004. *gPROMS Advanced User Guide*, Bridge Studios, 107a Hammersmith Bridge Rd, Condon W6 9DA, UK.

Prutton, C.F., Miller, C. O, Schuette, W.H., 1942. Factors influencing the performance of rotary dryers. *Transactions of American Institute of Chemical Engineers,* 38, 123-141.

Raffak, T., Agouzoul, M., Mabsate, M., Chik, A., Alouani, A., 2008. Recent patent and modelling of Phosphate rotary dryer. *Recent Patents on Engineering*, 2, 132–141.

Ranz, W.E., Marshall, W.R., 1952. Evaporation from drops. Part 1 and 2, *Chemical Engineering Progress*, 48(3), 141–146 and 173–180.

Renaud, M., Thibault, J., Trusiak, A., 2000. Solids transportation model of an industrial rotary dryer. *Drying Technology*, 18(4 & 5), 843–865.

Renaud, M., Thibault, J., Alvarez, P.I., 2001. Influence of solids moisture content on the average residence time in a rotary dryer. *Drying Technology*, 19(9), 2131–2150.

Revol, D., Briens, C.L., Chabagno, J.M., 2001. The design of flights in rotary dryers. *Powder Technology*, 121, 230–238.

Sai, P.S.T., Surender, G.D., Damodaran, A.D., Sureh, Z.G.P, Sankaran, K., 1990. Residence time distribution and material flow studies in a rotary kiln. *Metallurgical Transactions B*, 21B, 1005–1011.

Schiller, L., Naumann, Z., 1935. A drag coefficient correlation. *Z Ver. Deutsch. Ing.*, 77, 318-320.

Schofield,E.R., Glikin, P.G., 1962. Rotary driers and coolers for granular fertilisers. *Transactions of the Institution of Chemical Engineers,* 40, 183–190.

Shahhosseini, S., Cameron, I.T. and Wang, F.Y. (2000). A simple model for solids transport in rotary dryers, *Drying Technology*, 18(4&5), 867-886.

Shahhosseini, S., Cameron, I.T., Wang, F.Y., 2001. A dynamic model with on-line identification for rotary sugar drying processes. *Drying Technology*, 19(9), 2103–2129.

Sharples, K., Glikin, P.G, Warne, R., 1964. Computer simulations of rotary dryers. *Transactions of the Institution of Chemical Engineers*, 42. T275–T284.

Sheehan, M.F., 1993. A study of the material transport in a flighted rotary dryer. B.Eng. Thesis, University of Queensland, Australia.

Sheehan, M.E., Schneider, P.A., Monro, A., Vigh, S., 2002. Transport and axial dispersion of sugar in flighted rotary dryers. In: *Proceedings of Australian Society of Cane Technology*, 101–108.

Sheehan, M.E., Britton, P.F., Schneider, P.A., 2005. A model for solids transport in flighted rotary dryers based on physical considerations. *Chemical Engineering Science*, 60, 4171–4182.

Sherritt, R.G., Caple, R., Behie, L.A., Mehrotra, A.K., 1993. The movement of solids through flighted rotating drums. Part I: Model formulation, *Canadian Journal of Chemical Engineering*, 71, 337–346.

Sherritt, R.G., Chaouki, J., Mehrotra, A.K., Behie, L.A., 2003. Axial dispersion in the three-dimensional mixing of particles in a rotating drum reactor. *Chemical Engineering Science*, 58, 401–415.

Sieder, E.N., Tate, G.E., 1936. Heat transfer and pressure drop of liquids in tubes. *Industrial and Engineering Chemistry*, 28, 1428–1436.

Sullivan, J.D., Maier, C.G., Ralson, O.C., 1927. Passage of solid particles through cylindrical kilns. U.S Bureau of Mines Technical paper, No. 384.

Wang, F.Y., Cameron, I.T., Litster, J.D., Douglas, P.L., 1993. A distributed parameter approach to the dynamics of rotary drying process. *Drying Technology*, 11(7), 1641–1656.

Wang, F.Y., Cameron, I.T., Litster, J.D, Rudolph, V. 1995. A fundamental study on particle transport through rotary dryers for flight design and system optimization. *Drying Technology,* 13(5-7), 1261-1278.

Wardjiman, C., Lee, A., Sheehan, M.E., Rhodes, M., 2008. Behaviour of a curtain of particles falling through a horizontally-flowing gas stream. *Powder Technology*, 188, 110–118.

Wardjiman, C., Lee, A., Sheehan, M.E., Rhodes, M., 2009. Shape of a particle curtain falling in stagnant air. *Powder Technology*, 192, 384–388.

Yang, S., Thibault, J., Kudra, T., 2003. Dynamic characteristics of solids transportation in rotary dryers. *Drying Technology*, 21(5), 755–773.

Yliniemi, L., 1999. Advanced control of a rotary dryer. PhD Thesis, University of Oulu, Finland.

APPENDINCES

APPENDIX A: COMBUSTION CHAMBER

The air enters the combustion chamber and is heated by burning the fuel oil. The hot gas leaves the combustion chamber at an approximate temperature of 500 ^{0}C. The gas flow rate into the dryer is not measured directly. This section presents the mass balances around the combustion chamber to determine its value.

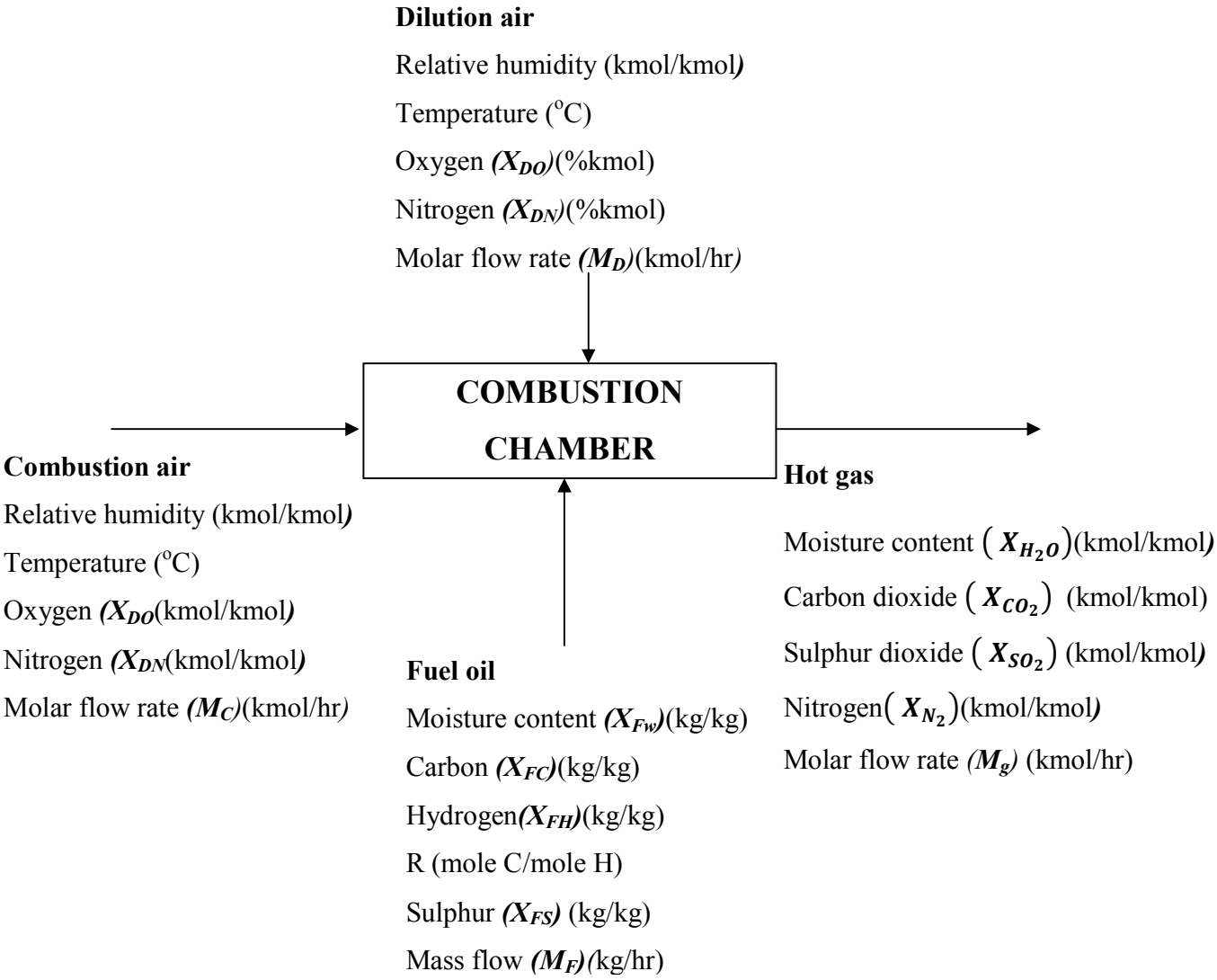

Figure A1: Block diagram of the combustion chamber

Air properties

Arbuckle and Brash (2001) carried out experimental measurements in 2001 to determine the relationship between the percentage of the fan opening (PI data) and the experimental volumetric flow rate (Figures A2 and A3). Fitted Equations A1 and A2 were used to determine the volumetric flow rates for dilution air and combustion air respectively.

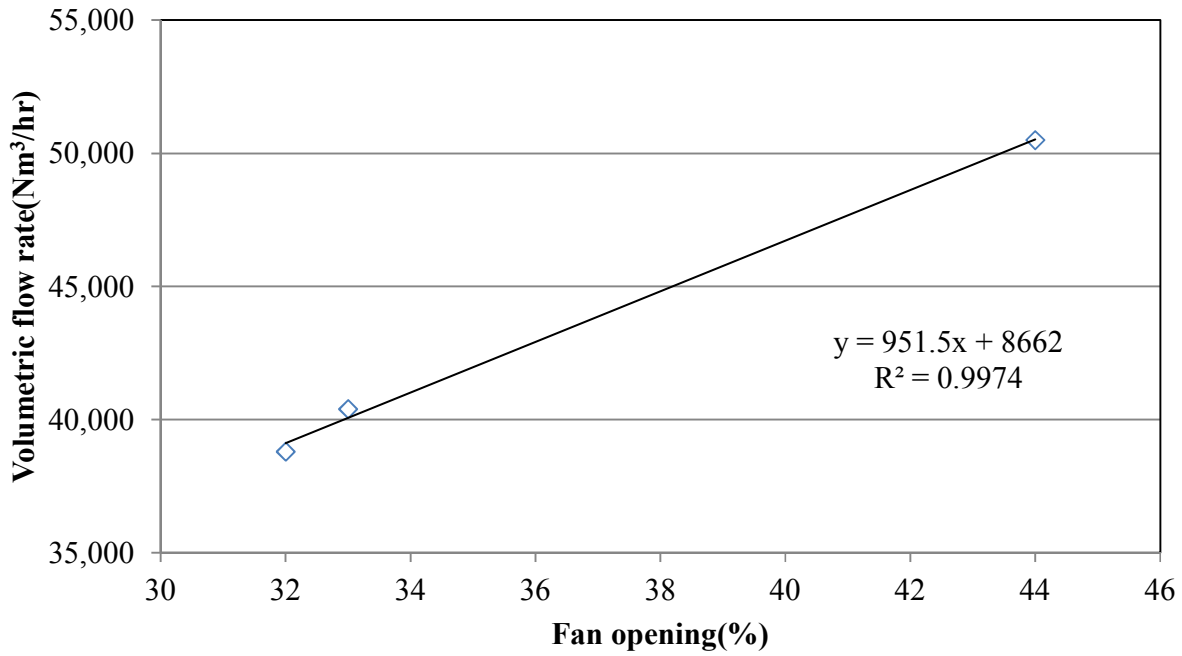

Figure A2: Dilution air (Arbuckle and Brash, 2001)

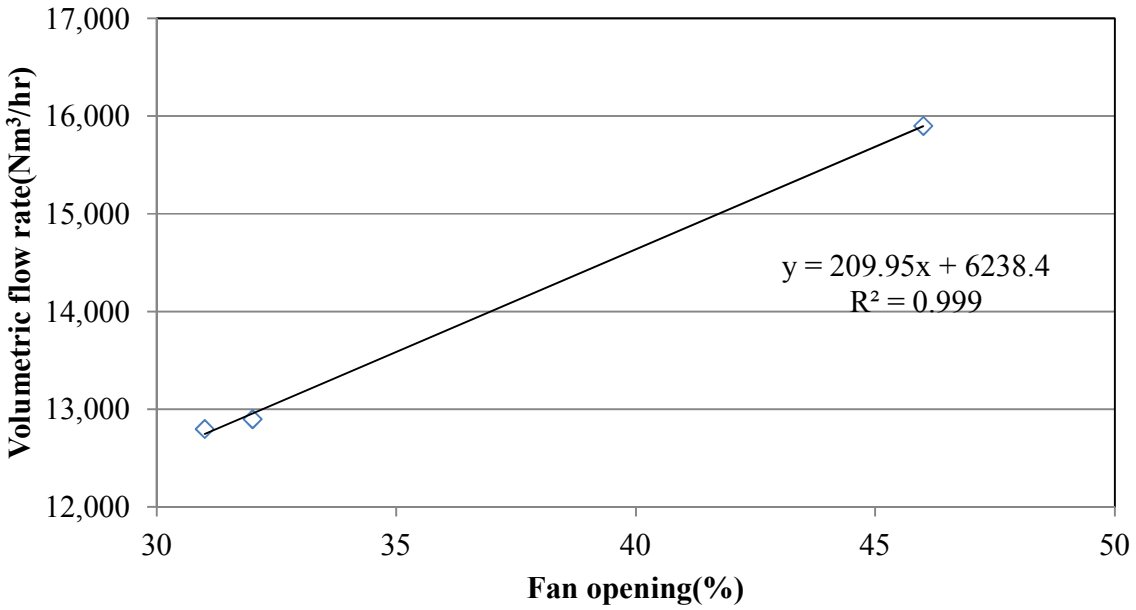

Figure A3: Combustion air (Arbuckle and Brash, 2001)

$$951.5x + 8662 \quad \textbf{A1}$$

$$209.95x + 6283.4 \quad \textbf{A2}$$

Table A1: Fan opening and volumetric flow rate

	Fan opening (%)	Amount(Nm^3/hr)	kmol/hr
Dilution air	83.43	88050	3928
combustion air	15.80	23698	1057

The moisture content of dilution and combustion air were calculated based on the relative humidity and temperature of air when the RTD experiments were undertaken (BOM, 2010). Equation A3 was used to estimate the moisture content (kmol of water/kmol dry air).

$$x_{CW} = \frac{P_{i_{H_2O}}}{P} \quad \textbf{A3}$$

$$P_{i_{H_2O}} = \frac{Rh}{100} \times P^*_{i_{H_2O}} \quad \textbf{A4}$$

$P^*_{i_{H_2O}}$ is the vapour pressure at the air temperature obtained from the vapour pressure table(Felder and Rousseau, 2005). $P_{i_{H_2O}}, P, Rh$ are vapour partial pressure, atmospheric pressure *(assumed to be 1 atm)* and relative humidity respectively.

Recycled oil properties

The composition of the recycled fuel oil is stated in Table A2 and was based on the data presented in Bladwin (2005). The mass flow rate of the fuel oil was obtained from the Process Information (PI) data.

Table A2: Composition of Recycled fuel oil

Content	
Water content	0.35 wt%
Sulphur content	0.95 wt%
Carbon to Hydrogen(C:H)	7.6 (mol/mol)

Hot gas

Elemental mass balances were carried out to determine the composition and molar flow rate of the hot gas leaving the unit.

Carbon:

$$0 = M_F X_{FC} - M_g \, X_{CO_2} MW_{CO_2} \left(\frac{MW_c}{MW_{CO_2}}\right)\left(\frac{1 \; kmol \; C}{1 \; kmol \; CO_2}\right) \quad \textbf{A5}$$

Hydrogen:

$$0 = M_F X_{FH} + M_F X_{FW} MW_{H_2O}\left(\frac{2}{18}\right) + (M_c + M_D) X_{CW} MW_{H_2O}\left(\frac{2}{18}\right) - M_g\, X_{H_2O} MW_{H_2O}\left(\frac{2}{18}\right) \quad \textbf{A6}$$

Nitrogen:

$$0 = (M_c + M_D) X_{DN} - M_g\, X_{N_2} \quad \textbf{A7}$$

Sulphur:

$$0 = M_F X_{FS} - M_g\, X_{SO_2}(32) \quad \textbf{A8}$$

Oxygen:

$$0 = (M_c + M_D) X_{cw} MW_{H_2O}\left(\frac{MW_{O_2}}{MW_{H_2O}}\right)\left(\frac{1\ kmol\ O_2}{1\ kmol\ H_2O}\right) + (M_c + M_D) X_{DO_2} MW_{O_2}\left(\frac{2\ kmol\ O_2}{1\ kmol\ O_2}\right) + M_F X_{FW}\left(\frac{MW_{O_2}}{MW_{H_2O}}\right)\left(\frac{1\ kmol\ O_2}{1\ kmol\ H_2O}\right) - M_g\, X_{H_2O} MW_{H_2O}\left(\frac{MW_{O_2}}{MW_{H_2O}}\right)\left(\frac{1\ kmol\ O_2}{1\ kmol\ H_2O}\right) - M_g\, X_{CO_2} MW_{CO_2}\left(\frac{MW_{O_2}}{MW_{CO_2}}\right)\left(\frac{2\ kmol\ O_2}{1\ kmol\ CO_2}\right) - M_g\, X_{SO_2} MW_{SO_2}\left(\frac{MW_{O_2}}{MW_{SO_2}}\right)\left(\frac{2\ kmol\ O_2}{1\ kmol\ SO_2}\right) \quad \textbf{A9}$$

Total components in hot gas *(M_g)* stream

$$X_{SO_2} + X_{CO_2} + X_{H_2O} + X_{N_2} = 1 \quad \textbf{A10}$$

APPENDIX B: RTD DATA (Lithium concentration as a function of time)

TEST 1

Time (minutes)	Concentration (kg/kg)
2	0.202
5	0.237
9.5	1.16
10	0.86
10.5	3.37
11	6.88
11.5	6.44
12	14
13	17.5
13.5	22.9
14	13.1
14.5	10
15	5.02
15.5	3.31
16	2.76
16.5	2.65
18	1.25
20	0.743

TEST 2

Time (minutes)	Concentration (kg/kg)	Time (minutes)	Concentration (kg/kg)
2	0.462	14.5	2.66
4	0.976	15	2.18
5	0.412	15.5	1.27
6	0.928	16	1.07
7	1.12	16.5	0.881
7.5	0.993	17	1.009
8	0.991	18	0.963
8.5	1.18	19	1.13
9	1.1	20	0.362
9.5	2.1	25	0.974
10	3.53	30	0.972
10.5	9.16	35	0.963
11	14	45	1.01
11.5	21.1	60	1.08
12	31.8		
12.5	18.2		
13	15.8		
13.5	7.83		
14	3.57		

TEST 3

Time (minutes)	Concentration (kg/kg)	Time (minutes)	Concentration (kg/kg)	Time (minutes)	Concentration (kg/kg)
3	0.259	13	18.8	40	0.259
3.5		13.5	22.4	45	0.293
4	0.314	14	21		
4.5	0.31	14.5	17.9		
5	0.289	15	10.6		
5.5	0.383	15.5	6.2		
6	0.255	16	4.38		
6.5	0.721	16.5	2.51		
7	1.03	17	2.09		
7.5	0.0943	17.5	1.21		
8	0.127	18	1.01		
8.5	0.193	18.5	0.541		
9	0.194	19	0.578		
9.5	0.049	19.5	0.452		
10	0.217	20	0.513		
10.5	0.554	21	0.523		
11	0.803	23	0.415		
11.5	1.74	25	1.5		
12	5.7	30	0.273		
12.5	9.38	35	0.121		

TEST 4

Time (minutes)	Concentration (kg/kg)	Time (minutes)	Concentration (kg/kg)	Time (minutes)	Concentration (kg/kg)
3	1.53	13	7.38	40	0.603
3.5	0.076	13.5	13.5	45	0.511
4	1.47	14	31.5		
4.5	1.36	14.5	28.4		
5	0.983	15	38.4		
5.5	0.772	15.5	51.7		
6	0.814	16	40.7		
6.5	0.750	16.5	13.6		
7	2.04	17	10.4		
7.5	0.902	17.5	5.09		
8	0.852	18	3.49		
8.5	0.693	18.5	1.55		
9	0.855	19	1.90		
9.5	1.04	19.5	1.24		
10	0.805	20	0.869		
10.5	0.584	21	0.839		
11	0.886	23	0.813		
11.5	1.24	25	0.810		
12	1.09	30	0.677		
12.5	3.26	35	0.613		

TEST 5

Time (minutes)	Concentration (kg/kg)	Time (minutes)	Concentration (kg/kg)
8	0.636	18	2.97
8.5	0.583	18.5	5.51
9	0.489	19	10.3
9.5	0.488	19.5	15.4
10	0.743	20	21.6
10.5	0.531	20.5	24.6
11	0.562	21	26.9
11.5	2.24	21.5	29.8
12	0.656	22	25.3
12.5	0.579	22.5	19.9
13	0.776	23	14.6
13.5	0.506	23.5	9.43
14	0.602	24	6.9
14.5	0.585	24.5	4.08
15	0.883	25	4.26
15.5	0.641	26	2.11
16	0.758	30	1.13
16.5	0.637	35	0.885
17	0.897	40	1.1
17.5	1.6		

TEST 6

Time (minutes)	Concentration (kg/kg)	Time (minutes)	Concentration (kg/kg)
8	1.05	18	6.15
8.5	0.578	18.5	2.98
9	0.609	19	1.68
9.5	0.567	19.5	0.885
10	0.475	20	0.763
10.5	0.545	21	0.486
11	0.660	22	0.672
11.5	0.727	23	0.315
12	0.867	24	0.937
12.5	1.46	25	0.347
13	3.06	30	0.191
13.5	8.85	35	0.272
14	14.9		
14.5	24.3		
15	28.8		
15.5	31.1		
16	30.6		
16.5	23.0		
17	14.3		
17.5	10.2		

APPENDIX C: MATLAB CODE

```
%To calculate the area at 9 o' clock position
jpegFiles = dir('*.jpg'); % directory of pictures
for a = 1:length(jpegFiles)  % loop to run large number of pictures
filename = jpegFiles(a).name;
data1 = imread(filename);
red = data1(:,:,1);  % Extracting on
mass9 = red;
[m n] = size(mass9);
[I J] = meshgrid(1:n,1:m);
radiusa = 950; % Radius of the drum in the image(You can use imageJ software to determine)
Center =[2320,1250];
Circle = (I-Center(1)).^2 + (J-Center(2)).^2 >= radiusa^2; % To remove the active phase.
mass9(Circle) = 0;
radius = 815;%inner radius where the active phase lies(You can use imageJ software to
determine)
Center =[2330,1240];
Circle = (I-Center(1)).^2 + (J-Center(2)).^2 <= radius^2; % To remove the active phase.
mass9(Circle) = 0;
mass9(1315:2700,:)=0; % removing lower limit
mass9(1:1070,:)=0; % removing upper limit
mass9(:,1500:3700)= 0; % removing where there is no flight
nmass9=nnz(mass9);% number of pixels in the passive phase
```

```
imagesc(mass9)
len =(radiusa*2)/75; % the scale of pixel/cm
Area = len^2; % pixel/cm^2
mass9oclock = nmass9/Area;
y(a) = mass9oclock;
%disp(mass9oclock);%area @ 3 o clock position
end
FUF = y';
x = char(jpegFiles.name);
t = cellstr(x);
xlswrite('C:\nineoclockAreacalculation.xlsx', t, 'area', 'A1');
xlswrite('C:\nineoclockAreacalculation.xlsx', FUF, 'area', 'B1');

%To calculate the area of the upper half of the drum
jpegFiles = dir('*.jpg'); % directory of pictures
for a = 1:length(jpegFiles)  % loop to run large number of pictures
filename = jpegFiles(a).name;
data1 = imread(filename);
red = data1(:,:,1);  % Extracting on
upperpassive = red;
[m n] = size(upperpassive);
[I J] = meshgrid(1:n,1:m);
radiusa = 950; % Radius of the drum in the image(You can use imageJ software to determine)
```

```
Center =[2320,1250];% center of the drum in the image(You can use imageJ software to
determine)
Circle = (I-Center(1)).^2 + (J-Center(2)).^2 >= radiusa^2; % Isolate the drum
upperpassive(Circle) = 0;
radius = 815;%inner radius where the active phase lies(You can use imageJ software to
determine)
Center =[2330,1240];% center of the drum in the image(You can use imageJ software to
determine)
Circle = (I-Center(1)).^2 + (J-Center(2)).^2 <= radius^2; % To remove the active phase.
upperpassive(Circle) = 0;
%upperpassive(1:700,:)=0;
upperpassive(700:2700,:)=0;% removing lower half of the drum
upperpassive(:,2800:3700)= 0;  % removing where the flights are empty
nupperpassive=nnz(upperpassive);% number f pixels in the passive phase
imagesc(upperpassive)
len = (radiusa*2)/75; % the scale of pixel/cm
Area = len^2; % pixel/cm^2
upperpassive= nupperpassive/Area;
u(a) = upperpassive;
end
UHD = u';
x = char(jpegFiles.name);
t = cellstr(x);
```

```
xlswrite('C:\UHDAreacalculation.xlsx', t, 'area', 'A1');
xlswrite('C:\UHDAreacalculation.xlsx', UHD, 'area', 'B1');


%To calculate the area of the lower half of the drum
jpegFiles = dir('*.jpg'); % directory of pictures
for a = 1:length(jpegFiles)  % loop to run large number of pictures
filename = jpegFiles(a).name;
data1 = imread(filename);
red = data1(:,:,1);  % Extracting on
lowerpassive = red;
[m n] = size(lowerpassive);
[I J] = meshgrid(1:n,1:m);
radiusa = 950; % Radius of the drum in the image(You can use imageJ software to determine)
Center =[2320,1250];%center of the drum in the image(You can use imageJ software to
determine)
Circle = (I-Center(1)).^2 + (J-Center(2)).^2 >= radiusa^2; % Isolate the drum
lowerpassive(Circle) = 0;
radius = 815;%inner radius where the active phase lies(You can use imageJ software to
determine)
Center =[2330,1240];%center of the drum in the image(You can use imageJ software to
determine)
Circle = (I-Center(1)).^2 + (J-Center(2)).^2 <= radius^2; % To remove the active phase.
lowerpassive(Circle) = 0;
```

```
lowerpassive(1:700,:)=0; %removing the upper half of the drum
lowerpassive(:,2800:3700)= 0;  % removing where the flights are empty
nlowerpassive=nnz(lowerpassive);% number of pixels in the passive phase
imagesc(lowerpassive) % image showing lower half of the drym
len = (radiusa*2)/75; % the scale of pixel/cm
Area = len^2; % pixel/cm^2
lowerpassive = nlowerpassive/Area;
l(a) = lowerpassive;
%totalpassive = upperpassive + lowerpassive; % total passive area of the drum
end
 LHD = l';
x = char(jpegFiles.name);
t = cellstr(x);
xlswrite('C:\LHDAreacalculation.xlsx', t, 'area', 'A1');
xlswrite('C:\LHDAreacalculation.xlsx', LHD, 'area', 'B1');
```

APPENDIX D: MATLAB CODE FOR ESTIMATING DESIGN LOAD

```
sslm = slmengine(x,y,'knots',3,'rightslope',0,'degree',1,'interiorknots','free','plot','on')

xlabel('Loading condition(kg)'), ylabel('Area of 3 o clock, cm^2')

c = sslm.knots(2)

slmeval(c,sslm)

slmeval(x,sslm)
```

APPENDIX E: CONFIDENCE INTERVAL OF DESIGN LOAD

Figure E1 shows the piecewise regression analysis of FUF area data. The breaking point of piecewise regression analysis was regarded as the design load discussed in Section 4.4.4. The confidence interval of estimated design load is discussed below.

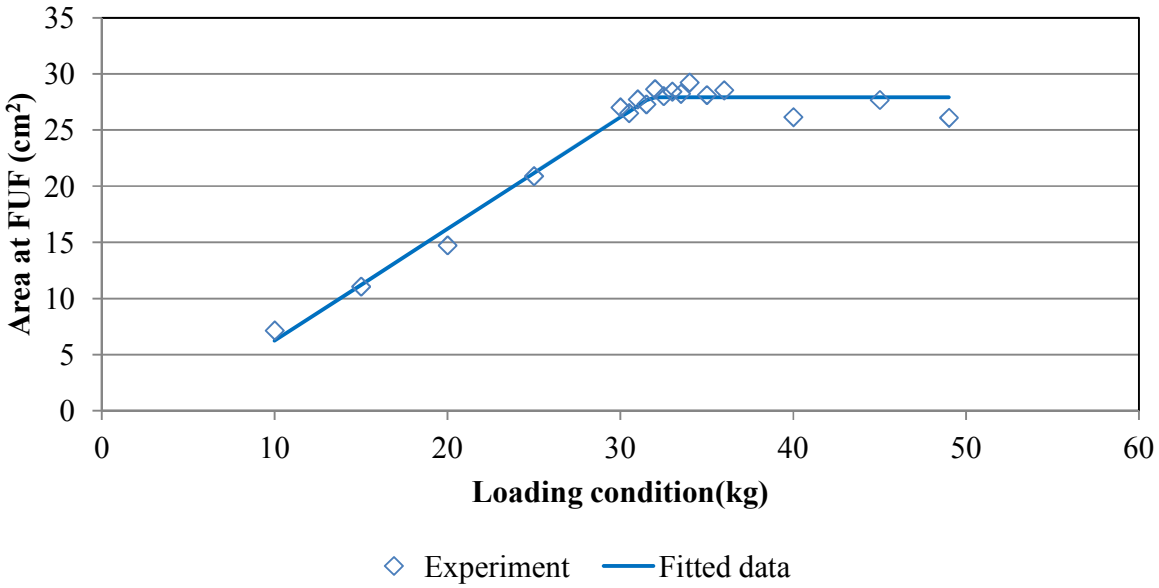

Figure E1: Design load estimation

The two lines in the above graph are represented by two different equations:

$$y_b = A_b x + C_b \quad \textbf{E1}$$

$$y_a = A_a x + C_a \quad \textbf{E2}$$

Equations E1 and E2 represent the equations of the lines before and after the break point respectively

A_b is the slope of the line before the break point

A_a is the slope of the line after the break point and this was constrained to zero.

C_b is the intercept of the line before the break point

C_a is the intercept of the line after the break point and this was average of the data points after the break point

The break point (B) is design load value and it can be derived from the two equations by subbing *x* for B for the Equations E1 and E2. This gives Equation E3:

$$A_b B + C_b = A_a B + C_a \quad \textbf{E3}$$

Therefore

$$B = \frac{C_a - C_b}{A_b - A_a} = \frac{G}{H} \quad \textbf{E4}$$

The standard error of B (design load) was estimated based on the rule of propagation of errors as stated in Equation E5.

$$SE_B = B \times \left(\sqrt{\left(\frac{SE_G}{G}\right)^2 + \left(\frac{SE_H}{H}\right)^2} \right) \quad \textbf{E5}$$

here SE_G, SE_H are the standard errors of *G* and *H* in Equation D4 and they were obtained based on the principle of propagation of errors.

Therefore, the 95% confidence interval for the design load is $\mathbf{1.96\ x\ SE_B}$

The standard error of G was calculated as follows,

$$SE_G = \sqrt{\left(\frac{E_{ca}}{C_a}\right)^2 + \left(\frac{E_{cb}}{C_b}\right)^2} \quad \textbf{E6}$$

here E_{ca}, E_{cb} are the error in intercepts before and after the break point(design load) respectively.

Similarly for *H*,

$$SE_H = \sqrt{\left(\frac{E_{Ab}}{A_b}\right)^2 + \left(\frac{E_{Aa}}{A_a}\right)^2} \quad \textbf{E7}$$

here E_{Ab}, E_{Aa} are the error in slope before and after the break point (design load) respectively. It should be noted that the error in slope after the break point is zero.

APPENDIX F: gPROMS Code

Process model

```
UNIT
D          AS Dryer_Clean
PARAMETER
L1                  AS REAL    # Length of 1st Stage (m)
L2                  AS REAL    # Length of 2nd Stage (m)
L3                  AS REAL    # Length of 3rd Stage (m)
L4                  AS REAL    # Length of 4th Stage (m)
L5                  AS REAL    # Length of 4th Stage (m)
R                   AS REAL    # Drum Radius (m)
theta               AS REAL    # Inclination of Drum (degrees)
# Flight Geometry in 3rd Stage of Dryer
Nf_2                AS INTEGER  # No. Flights
s1_2                AS REAL    # Flight Length 1
s2_2                AS REAL    # Flight Length 2
alpha1_2            AS REAL    # Flight Angle 1
alpha2_2            AS REAL    # Flight Angle 2
# Flight Geometry in 4th Stage of Dryer
Nf_3                AS INTEGER  # No. Flights
s1_3                AS REAL    # Flight Length 1
s2_3                AS REAL    # Flight Length 2
alpha1_3            AS REAL    # Flight Angle 1
```

```
alpha2_3        AS REAL     # Flight Angle 2
Nf_4            AS INTEGER  # No. Flights
s1_4            AS REAL     # Flight Length 1
s2_4            AS REAL     # Flight Length 2
alpha1_4        AS REAL     # Flight Angle 1
alpha2_4        AS REAL     # Flight Angle 2
N2              AS INTEGER  # No. Cells in Section 2
N3              AS INTEGER  # No. Cells in Section 3
N4              AS INTEGER  # No. Cells in Section 4
Cp_w            AS REAL       # Specific heat capacity of water
Cp_z            AS REAL       # Specific heat capacity of zinc
landa           AS REAL       # Heat of vaporisation
Cp_air          AS REAL         # Specific capacity of air
P               AS REAL     # Pressure within the dryer
rho_p           AS REAL     # particle density of zinc
MONITOR
D.O.T_ppm;
D.O.tau;
D.O.T_flow;
D.C1.me;
D.C2(*).P.x_p;
D.C3(*).P.x_p;
D.C4(*).P.x_p;
```

D.C6.me;

D.C1.tair;

D.C2(*).AIR.T_airout;

D.C3(*).AIR.T_airout;

D.C4(*).AIR.T_airout;

D.C6.tair;

D.C1.H_out;

D.C2(*).AIR.H_out;

D.C3(*).AIR.H_out;

D.C4(*).AIR.H_out;

D.C6.H_out;

D.C1.ts;

D.C4(*).P.tp;

D.C3(*).P.tp;

D.C2(*).P.tp;

D.C6.ts;

D.Energy;

D.Energy_1;

D.Energy_2;

D.Energy_3;

SET

L1 := 2.1;

L2 := 2.4;

```
L3      := 3.6;
L4      := 6.6;
L5      := 7.5;
R       := 1.95;
theta   := 4;
Cp_w    := 4182;
Cp_z    := 505;
Cp_air  :=1070;
landa  :=(2257*1000);
rho_p     := 2800;
P   := 101045;
# Flight Geometry in 3rd Stage of Dryer
Nf_2    := 30;
s1_2    := 0.120;
s2_2    := 0.21;
alpha1_2:= 90;
alpha2_2:= 135;
# Flight Geometry in 4th Stage of Dryer
Nf_3    := 30;
s1_3    := 0.130;
s2_3    := 0.220;
alpha1_3:= 90;
alpha2_3:= 150;
```

```
Nf_4    := 30;
s1_4    := 0.120;
s2_4    := 0.210;
alpha1_4:= 90;
alpha2_4:= 130;
#Number of cells
N2      := 8;
N3      := 12;
N4      := 22;
ASSIGN
D.F_ain  := 112675.6688;    # Gas flow rate into section 1 and used as correlation for section 5
D.C1.H_ain  := 0.0193;              # Gas inlet humidity
D.C1.T_airin :=500;             # Gas inlet temperature
D.Tamb :=26;                    # Ambient temperature
D.C1.F_k_in  := 146320/3600;        # Solid mass flow rate
D.C1.T_k_in  := 0;                # Tracer concentration
D.C1.u:=0.01557;                # kilning time
D.C1.x_in:=0.163;               # Solid moisture content
D.C1.tink:= 28;                 # solid temperature
D.omega    :=3;
D.y         :=   0.000399686;       # axial dispersed coefficient
D.f         :=2.4;          # area correction factor for section A
D.ha        := 1.2;    # area correction factor for section B
```

```
D.hb        :=0.6;        # area correction factor for section C
D.hc        := 0.42;      # area correction factor for section D
D.n         :=1.4;        # area correction factor for section E
D.lo_factor  :=15;        # heat loss correction factor for all sections
INITIAL
D.O.T_flow = 0;
D.O.xtime = 0;
D.O.tau = 0;
FOR i := 0|+ TO L1|- DO
   D.C1.r(i) = (32250/D.L)*L1;
   D.C1.T(i) = 0;
   D.C1.me(i) = 0.168;
   D.C1.Ts(i) = 25;
   D.C1.Air(i) = (D.C1.F_ain/3600)/D.C1.v_g(0);
   D.C1.tair(i) =500;
   D.C1.H_out(i) = 0.0193;
END
FOR i:= 1 TO N2 DO
   D.C2(i).P.m_p = (32250/D.L)*(L2/N2);
   D.C2(i).P.T_p = 0;
    D.C2(i).P.x_p = 0.15;
    D.C2(i).P.tp = 32;
   D.C2(i).A.m_a = (4/D.L)*(L2/N2);
```

```
    D.C2(i).A.T_a = 0;
    D.C2(i).A.x_a = 0.15;
    D.C2(i).A.ta = 30;
 END
FOR i:= 1 TO N3 DO
    D.C3(i).P.m_p = (32250/D.L)*(L3/N3);
    D.C3(i).P.T_p = 0;
    D.C3(i).P.x_p = 0.14;
    D.C3(i).P.tp = 32;
    D.C3(i).A.m_a = (4/D.L)*(L3/N3);
    D.C3(i).A.T_a = 0;
    D.C3(i).A.x_a = 0.14;
   D.C3(i).A.ta = 30;
 END
FOR i:= 1 TO N4 DO
    D.C4(i).P.m_p = (32250/D.L)*(L4/N4);
    D.C4(i).P.T_p = 0;
     D.C4(i).P.x_p = 0.13;
     D.C4(i).P.tp = 35;
    D.C4(i).A.m_a = (4/D.L)*(L4/N4);
    D.C4(i).A.T_a = 0;
    D.C4(i).A.x_a = 0.13;
     D.C4(i).A.ta = 35;
```

```
  END
FOR i := 0|+ TO L5|- DO
   D.C6.r(i) = (32250/D.L)*L5;
   D.C6.T(i) = 0;
   D.C6.me(i) = 0.125;
  D.C6.Ts(i) = 40;
 D.C6.Air(i) = D.C4(N4).AIR.A_out/D.C4(N4).AIR.v_g;
   D.C6.tair(i) = 120;
   D.C6.H_out(i) = 0.1;
END
SOLUTIONPARAMETERS
   LASolver := "MA28"
   DASolver := "DASOLV"
   REPORTINGINTERVAL      :=10
#gExcelOutput          := "checkit.xls" ;
SCHEDULE
# Method 1
#CONTINUE FOR 3600
# Tracer Study
SEQUENCE
   CONTINUE FOR 1500
   RESET
```

```
    D.C1.T_k_in :=1.255E-04; # IMPORTANT: If you change this you need to change the
value in the Dryer Model as well.
  END
  CONTINUE FOR 60  # IMPORTANT: If you change this you need to change the value in the
Dryer Model as well.
  RESET
    D.C1.T_k_in := 0;
  END
  CONTINUE FOR 2500
END
#Dynamic studies
{SEQUENCE
  CONTINUE FOR 3500
  RESET
   #D.C1.F_k_in :=60000/3600;
  # D.F_ain := 60000;
  #D.C1.T_airin :=350;
  #D.C1.H_ain  := 0.002;
   #D.C1.tink:= 25;              # solid temperature
  #D.C1.x_in:=0.15 ;            # Solid moisture content
 # D.omega:=2;
  END
```

CONTINUE FOR 4500 # IMPORTANT: If you change this you need to change the value in the Dryer Model as well.

END}

Dryer Model

PARAMETER

N2	AS INTEGER	# Number of cells in Section B
N3	AS INTEGER	# Number of cells in Section C
N4	AS INTEGER	# Number of cells in Section D
L1	AS REAL	# Length of Section A
L2	AS REAL	# Length of Section B
L3	AS REAL	# Length of Section C
L4	AS REAL	# Length of Section D
L5	AS REAL	# Length of Section E
Cp_w	AS REAL	#Specific heat capacity of water
Cp_z	AS REAL	# Specific heat capacity of zinc
Cp_air	AS REAL	# Specific heat capacity of air
landa	AS REAL	#Heat of vaporisation
R	AS REAL	# Radius of the drum

VARIABLE

Omega	AS no_unit	# rotational speed
Tot_moist	AS no_unit	# moisture content balance
Tot_solid	AS no_unit	# Solid balance across unflighted section A
Tot_air	AS no_unit	# Gas balance across unflighted section A
k4_2	AS no_unit	# Solid velocity
k4_3	AS no_unit	# Solid velocity
k4_4	AS no_unit	# Solid velocity

```
f           AS no_unit        ## area correction factor for section A
ha          AS no_unit        # area correction factor for section B
hb          AS no_unit        # area correction factor for section C
hc          AS no_unit        # area correction factor for section D
n           AS no_unit         ## area correction factor for section E
L           AS no_unit        # Length
f           AS no_unit        ## area correction factor for section A
y           AS no_unit        # axial dispersed coefficient
Energy_1    AS no_unit       # Energy balance across unflighted section A
F_ain       AS mass_flowrate    # Gas flow rate
Tamb        AS temperature       # Ambient temperature
Energy      AS no_unit        # Energy balance across the dryer
lo_factor   AS no_unit        # Heat loss factor
Tot_solid_2 AS no_unit       #Solid balance across flighted sections
Tot_air_2   AS no_unit         #Gas balance across flighted sections
Energy_2    AS no_unit       # Energy balance across flighted section
Energy_3    AS no_unit       # Energy balance on unflighted section E
UNIT
C1          AS  Kilning_Cell_1
C2          AS ARRAY(N2) OF Cell1
C3          AS ARRAY(N3) OF Cell2
C4          AS ARRAY(N4) OF Cell3
C5          AS Mixing
```

```
C6                AS  Kilning_Cell_2

O                 AS Outflow

SET

C1.sl := [BFDM,2, 60];

C6.sl     := [BFDM, 2, 100];

#C1.sl := [OCFEM,3, 30];

#C6.sl     := [OCFEM, 3, 30];

EQUATION

L = L1 + L2 + L3 + L4 + L5;

#C1.U:= 0.161318 +(0.006533*omega) –(0.04198*(R*2));

k4_2=C1.u;

k4_3= C1.u;

k4_4= C1.u;

C6.u = C1.u;

# Area and heat loss factors

C1.f =f ;      # factor

C1.lo = lo_factor;

C6.lo = lo_factor;

C6.n =n;

 # axial dispersion coefficient

C1.k =y ;      # axial dispersion coefficient

C6.k =y;       # axial dispersion coefficient

C1.F_ain = F_ain;
```

```
C1.Tamb = Tamb;
C6.Tamb = Tamb;
# Section 2
FOR i:=1 TO N2-1 DO
   C2(i).P.Kiln_out IS C2(i+1).P.Kiln_in;
   C2(i).A.Axial    IS C2(i+1).P.Axial;
   C2(i).AIR.Air_out  IS C2(i+1).AIR.Air_in;
END
C2(1).P.F_x = 0;
C2(1).P.T_x = 0;
C2(1).P.x_x = 0;
C2(1).P.tx = 0;
# Section 3
FOR i:=1 TO N3-1 DO
   C3(i).P.Kiln_out IS C3(i+1).P.Kiln_in;
   C3(i).A.Axial    IS C3(i+1).P.Axial;
  C3(i).AIR.Air_out  IS C3(i+1).AIR.Air_in;
END
FOR i:=1 TO N4-1 DO
   C4(i).P.Kiln_out IS C4(i+1).P.Kiln_in;
   C4(i).A.Axial    IS C4(i+1).P.Axial;
      C4(i).AIR.Air_out  IS C4(i+1).AIR.Air_in;
END
```

```
#Connecting Sections 1 and 2
C1.Kiln_out IS C2(1).P.Kiln_in;
C1.Air_out IS C2(1).AIR.Air_in;
# Connecting Sections 2 and 3
C2(N2).P.Kiln_out IS C3(1).P.Kiln_in;
C2(N2).A.Axial IS C3(1).P.Axial;
C2(N2).AIR.Air_out is C3(1).AIR.Air_in;
C3(N3).P.Kiln_out IS C4(1).P.Kiln_in;
C3(N3).A.Axial IS C4(1).P.Axial;
C3(N3).AIR.Air_out is C4(1).AIR.Air_in;
# Connecting Sections 3 and 4
C4(N4).P.Kiln_out IS C5.Passive;
C4(N4).A.Axial IS C5.Axial;
C5.out IS C6.Kiln_in;
C4(N4).AIR.Air_out is C6.Air_in;
# Setting Coefficients
FOR i:=1 TO N2 DO
 C2(i).P.k_4 =  k4_2/(L2/N2);
C2(i).A.h = ha;
C2(i).G.Phi = (419.6*C2(i).P.x_p)-7.801;
 C2(i).AIR.lo= lo_factor;
C2(i).AIR.Ts =105 ;
 C2(i).AIR.Tamb =  Tamb;
```

```
C2(i).G.rhob = (-3095.24*C2(i).P.x_p)+ 2043.81;
C2(i).AIR.L = L2/N2 ;
 C2(i).A.dp = 0.015;
C2(i).AIR.dp = 0.015;
C2(i).G.omega = omega;
END
FOR i:=1 TO N3 DO
C3(i).P.k_4 =  k4_3/(L3/N3);
C3(i).AIR.dp = 0.012;
C3(i).A.dp = 0.012;
C3(i).A.h = hb;
C3(i).G.Phi = (419.6*C3(i).P.x_p)-7.801;
 C3(i).AIR.lo= lo_factor;
C3(i).AIR.Ts =100;
 C3(i).AIR.Tamb =  Tamb;
C3(i).AIR.L = L3/N3 ;
C3(i).G.rhob = (-3095.24*C3(i).P.x_p)+ 2043.81;
C3(i).G.omega = omega;
END
FOR i:=1 TO N4 DO
 C4(i).P.k_4 =  k4_4/(L4/N4);
   C4(i).A.h = hc;
C4(i).G.Phi = (419.6*C4(i).P.x_p)-7.801;
```

```
C4(i).AIR.Ts =100 ;
C4(i).AIR.L = L4/N4 ;
 C4(i).AIR.Tamb =  Tamb;
   C4(i).AIR.dp = 0.008;
    C4(i).A.dp = 0.008;
 C4(i).AIR.lo= lo_factor;
C4(i).G.rhob = (-3095.24*C4(i).P.x_p)+ 2043.81;
C4(i).G.omega = omega;
END
O.Passive IS C6.Kiln_out;
O.Air_in  IS C6.Air_out;
O.T_mass = 0.304;     # This value must match the value of the tracer conc. in the Process entity.
#Overall Mass and energy balances
Tot_air = (C1.A_o*(1-C1.H_o))- ((C1.F_ain/3600)*(1-C1.H_ain));
Tot_air_2 = (C4(22).AIR.A_out*(1-C4(22).AIR.H_out))- ((C1.A_o)*(1-C1.H_o));
Tot_solid =C1.F_k_out*(1-C1.x_out) - C1.F_k_in*(1-C1.x_in);
Tot_moist =(C6.A_o*(C6.H_o)+ O.F_o*(O.x_o))-
(C1.F_k_in*(C1.x_in)+((C1.F_ain/3600)*(C1.H_ain)));
Tot_solid_2 =C5.F_t*(1-C5.x_t) - C1.F_k_out*(1-C1.x_out);
#Overall energy balance around the first unflighted section
Energy_1 = C1.F_k_out*(1-C1.x_out)*Cp_z*C1.Tout + C1.F_K_out*C1.x_out*Cp_w*C1.tout
+ C1.A_o*Cp_air*(1-C1.H_o)*100 + C1.A_o*Cp_w*C1.H_o*100 + C1.A_o*Cp_air*(1-
C1.H_o)*(C1.T_o-100) + C1.A_o*C1.Cpw_v(L1)*C1.H_o*(C1.T_o-100) +
```

```
C1.A_o*landa*C1.H_o- (C1.F_k_in*(1-C1.x_in)*Cp_z*C1.tink +
C1.F_k_in*C1.x_in*Cp_w*C1.tink + (C1.F_ain/3600)*Cp_air*(1-C1.H_ain)*(C1.T_airin-100)
+(C1.F_ain/3600)*C1.Cpw_v(0)*C1.H_ain*(C1.T_airin-100) + (C1.F_ain/3600)*Cp_air*(1-
C1.H_ain)*100 +(C1.F_ain/3600)*Cp_w*C1.H_ain*100  + (C1.F_ain/3600)*landa*C1.H_ain);
#Overall energy balance around flighted sections
Energy_2 = (C5.F_t*(1-C5.x_t)*Cp_z*C5.tt + C5.F_t*C5.x_t*Cp_w*C5.tt +
C4(22).AIR.A_out*Cp_air*(1-C4(22).AIR.H_out)*100 +
C4(22).AIR.A_out*Cp_w*C4(22).AIR.H_out*100 +
C4(22).AIR.A_out*landa*C4(22).AIR.H_out+ C4(22).AIR.A_out*Cp_air*(1-
C4(22).AIR.H_out)*(C4(22).AIR.T_airout -100) +
C4(22).AIR.A_out*C4(22).AIR.Cpw_v*C4(22).AIR.H_out*(C4(22).AIR.T_airout-100)) -
(C1.F_k_out*(1-C1.x_out)*Cp_z*C1.tout + C1.F_k_out*C1.x_out*Cp_w*C1.tout +
(C1.A_o)*Cp_air*(1-C1.H_o)*100 + C1.A_o*Cp_w*C1.H_o*100 + C1.A_o*landa*C1.H_o +
(C1.A_o)*Cp_air*(1-C1.H_o)*(C1.T_o-100) + C1.A_o*C1.Cpw_v(0)*C1.H_o*(C1.T_o-100));
#Overall energy balance around last unflighted section
Energy_3 =  (O.F_o*(1-O.x_o)*Cp_z*O.tout + O.F_o*O.x_o*Cp_w*O.tout +
C6.A_o*Cp_air*(1-C6.H_o)*100 + C6.A_o*Cp_w*C6.H_o*100 + C6.A_o*landa*C6.H_o +
C6.A_o*Cp_air*(1-C6.H_o)*(C6.T_o-100) + C6.A_o*C6.Cpw_v(L5)*C6.H_o*(C6.T_o-100)) -
(C5.F_t*(1-C5.x_t)*Cp_z*C5.tt + C5.F_t*C5.x_t*Cp_w*C5.tt +
C6.A_air*C6.H_out(0)*100*Cp_w +C6.A_air*(1-C6.H_out(0))*100*Cp_air +
C6.A_air*landa*C6.H_out(0) + C6.A_air*C6.H_out(0)*(C6.tair(0)-100)*C6.Cpw_v(0)
+C6.A_air*(1-C6.H_out(0))*(C6.tair(0)-100)*Cp_air);
```

#Overall energy balance across the dryer

Energy = O.F_o*(1-O.x_o)*Cp_z*O.tout + O.F_o*O.x_o*Cp_w*O.tout + C6.A_o*Cp_air*(1-C6.H_o)*100 + C6.A_o*Cp_w*C6.H_o*100 + C6.A_o*landa*C6.H_o +C6.A_o*Cp_air*(1-C6.H_o)*(C6.T_o-100) + C6.A_o*C6.Cpw_v(L5)*C6.H_o*(C6.T_o-100)- C1.F_k_in*(1-C1.x_in)*Cp_z*C1.tink - C1.F_k_in*C1.x_in*Cp_w*C1.tink - (C1.F_ain/3600)*Cp_air*(1-C1.H_ain)*C1.T_airin -(C1.F_ain/3600)*Cp_w*C1.H_ain*C1.T_airin - (C1.F_ain/3600)*landa*C1.H_ain;

Air phase

PARAMETER

landa	AS REAL	# Heat of vaporization
Cp_w	AS REAL	# specific heat capacity of water
Cp_air	AS REAL	# specific heat capacity of air

VARIABLE

Rw	AS mass_flowrate	# Evaporation
A_in	AS mass_flowrate	#Gas inlet mass flow rate
A_out	AS mass_flowrate	# Gas outlet mass flow rate
H_in	AS mass_fraction	# Gas inlet humidity
H_out	AS mass_fraction	# Gas outlet humidity
T_airout	AS temperature	# Gas outlet temperature
T_airin	AS temperature	# Gas inlet temperature
ta	AS temperature	# Moisture Content in Active Phase
Area	AS no_unit	# Area of solid in contact with gas
conv_a	AS no_unit	# convective heat transfer(active)
R	AS no_unit	# Total resistance
h_rad	AS no_unit	# radiation heat transfer coefficient
e	AS no_unit	# Surface emissivity
e_s	AS no_unit	# emissivity for solid
et	AS no_unit	#stefan boltmanz
Ts	AS temperature	# Shell temperature
Re_in	AS no_unit	# Inside Reynolds number

```
k_air          AS no_unit      # Thermal conductivity
mu_g           AS no_unit      # Viscosity of gas
mu_s           AS no_unit      # Viscosity @ d surface
Pr             AS no_unit      # Prandtl number
rho_g          AS no_unit      # Density of gas
v_g            AS no_unit      # Velocity of gas
Cpw_v          AS no_unit      # specific heat capacity of water vapour
hout           AS no_unit      # Outside Convective heat transfer coefficient
hinside        AS no_unit      # Inside Convective heat transfer coefficient
Q              AS no_unit      # Heat loss
Ra             AS no_unit      # Rayleigh number
conv_in        AS no_unit      # Inside convection
conv_out       AS no_unit      # Outside convection
L              AS no_unit      # Length of cell
D_out          AS no_unit      # Outside diameter
D_in           AS no_unit      # Inside diameter
Cond           AS no_unit      # Conduction
Rad            AS no_unit      # Radiation
g              AS no_unit      # Acceleration due to gravity
B              AS no_unit      #  expansion coefficient
Tamb           AS no_unit      # Ambient temperature
v              AS no_unit      # kinematic viscosity
alpha          AS no_unit      #Thermal diffusivity
```

```
R_out           AS no_unit      # Outside radius
R_in            AS no_unit      # Inside radius
K_airo          AS no_unit  # Air thermal conductivity based on shell temperature
h_rad_w         AS no_unit      # radiation heat transfer coefficient internal
St              AS no_unit      # Staton number
dp              AS no_unit      # diffusivity
hc              AS no_unit      # diffusivity
k_s             AS no_unit      # diffusivity
rad_solid       AS no_unit      # Heat transferred to the solid via radiation
Rad_w           AS no_unit      # Radiation from gas to wall
lo              AS no_unit      # heat loss factor
STREAM
Air_in          :A_in,H_in,T_airin          AS AIRFLOW
Air_out         :A_out,H_out,T_airout       AS AIRFLOW
Evaporation     :Rw,area, ta                AS EVAPORATION
Convection      :conv_a                     AS CONVECTION
masstransfer    :mu_g,rho_g,st              AS masstransfer
Radiation       :rad_solid                  AS RADIATION
EQUATION
# Mass and energy balance
A_out = A_in + Rw;
A_out*H_out = A_in*H_in + Rw;
```

```
A_out*100*Cp_air*(1-H_out)+ A_out*100*Cp_w*(H_out) + A_out*H_out*landa +
A_out*(T_airout-100)*Cp_air*(1-H_out)+ A_out*(T_airout-100)*Cpw_v*(H_out) =
A_in*100*Cp_air*(1-H_in) +  A_in*100*Cp_w*(H_in) +  A_in*H_in*landa + A_in*(T_airin-
100)*Cp_air*(1-H_in) +  A_in*(T_airin-100)*Cpw_v*(H_in)+ Rw*(landa + (Cp_w*Ta))-
conv_a- rad_solid-Q;
# Properties of air
Pr = 0.70752;
v_g = A_in/(rho_g*3.142*(1.95^2));
mu_s    = -7.479E-12*(ts^2) + 3.746E-08*(ts) + 1.824E-05;
k_air =  -1.249E-08*(t_airin^2) + 6.699E-05*(t_airin) + 2.541E-02;
rho_g =   6.417E-13*(t_airin^4) - 2.673E-09*(t_airin^3) + 4.129E-06*(t_airin^2) - 3.037E-
03*t_airin + 1.225E+00;
mu_g =   -7.479E-12*(t_airin^2) + 3.746E-08*(t_airin) + 1.824E-05;
# specific heat capacity of water vapour
Cpw_v = -0.00000000031759*(t_airin +273)^3 + 0.00000091451537*(t_airin +273)^2 -
0.00014971847134*(t_airin +273) + 1.84044937134494;
#Estimation of convective heat transfer to solid
hc = (0.33*(((v_g*rho_g*dp)/mu_g)^0.6)*(k_air/dp));
St = hc/(cp_air*rho_g*v_g);
conv_a = hc*Area*(T_airout-Ta);
#Estimation of radiation heat transfer to solid
e_s = 0.9;
rad_solid = e_s*et*Area*(((T_airout+273)^4)-((Ta+273)^4));
```

```
#Heat loss calculation

# Radiation from the environment

h_rad = e*et*((Ts+273) + (Tamb+273))*(((Ts+273)^2) + ((Tamb+273)^2));

e = 0.79;

et = 5.67E-08;

Rad = h_rad*2*3.142*R_out*L;

#Radiation from gas to walls

h_rad_w = e*et*((T_airout+273) + (Ts+273))*(((T_airout+273)^2) + ((Ts+273)^2));

Rad_w = h_rad_w*2*3.142*R_out*L;

# Inside convection

R_in    = 1.90;

D_in    = R_in*2;

Re_in = (v_g*D_in*rho_g)/mu_g;

hinside =( k_air/D_in)*0.027*(Re_in^0.8)*(Pr^(1/3))*((mu_g/mu_s)^0.14);

conv_in = (hinside*2*3.142*r_in*L);

#Outside convection

g = 9.81;

B = 1/(t_airin+273);

alpha = 5.776E-11*((ts+273)^2) + 1.345E-07*(ts+273) - 2.466E-05;

v  =7.451E-11*((ts+273)^2) + 5.671E-08*(ts+273) - 8.152E-06;

Ra = (g*B*(Ts-Tamb)*(D_out^3))/(v*alpha);

R_out = 1.95;

D_out = R_out*2;
```

K_airo= -1.249E-08*(Ts^2) + 6.699E-05*(Ts) + 2.541E-02;

hout = (k_airo/D_out)*((0.60+((0.387*(Ra^(1/6)))/((1+((0.559/Pr)^(9/16)))^(8/27))))^2);

conv_out = hout*2*3.142*R_out*L;

#Conduction

cond = (LOG(R_out/r_in))/(k_s*2*3.142*L);

k_s = 54-3.33E-02*Ts;

Total resistance

R = (1/(conv_in + rad_w)) + cond + (1/(conv_out+ rad));

Heat loss

Q = lo*((T_airout - Tamb)/R);

Active phase

PARAMETER

Cp_w	AS REAL	#Specific heat capacity of water
Cp_z	AS REAL	# specific heat capacity of zinc
landa	AS REAL	#heat of vaporisation
Cp_air	AS REAL	# specific heat of air
P	AS REAL	# Pressure within the dryer
rho_p	AS REAL	# Particle density of zinc

VARIABLE

m_a	AS mass	# Active Mass
F_a	AS mass_flowrate	# Mass Flow from Passive Phase
F_r	AS mass_flowrate	# Mass Flow to Passive Phase
F_x	AS mass_flowrate	# Axial Mass Flow
T_a	AS mass_fraction	# Moisture Content in Active Phase
T_in	AS mass_fraction	# Moisture Content in Flow from Passive
c1	AS no_unit	# Geometric Solids Advance w/o Drag
ft	AS no_unit	# falling time
x_a	AS mass_fraction	# Moisture Content in Active Phase
x_in	AS mass_fraction	# Moisture Content in Flow from Passive
ta	AS temperature	# Moisture Content in Active Phase
tin	AS temperature	# Moisture Content in Flow from Passive
Rw	AS mass_flowrate	# Evaporation rate
Area	AS no_unit	# Area in contact with gas

```
v_g             AS no_unit          # Velocity of air
dp              AS no_unit          # Particle size diameter
conv_a          AS no_unit          # Convective heat transfer
T_airout        AS temperature      # Gas temperature
A_o             AS mass_flowrate    # Air mass flow rate
H_out           AS mass_fraction    # Gas humidity
hm              AS no_unit          # Mass transfer coefficient
Pw_s            AS no_unit          # Partial pressure of solid
Pw_air          AS no_unit          # vapour partial pressure
St              AS no_unit          # Stanton number
h               AS no_unit          # Area correction factor
Sc              AS no_unit          #Schmitt number
Pr              AS no_unit          #Prandtl number
da              AS no_unit          # diffusivity
mu_g            AS no_unit          # viscosity of gas
rho_g           AS no_unit          # density of gas
rad_solid       AS no_unit
STREAM
Axial           :F_x,T_a,x_a,ta         AS SOLIDFLOW
Return          :F_r,T_a,x_a,ta         AS SOLIDFLOW
Active          :F_a,T_in,x_in,tin      AS SOLIDFLOW
Data            :ft,c1                  AS DATAA
Convection      :conv_a                 AS CONVECTION
```

```
Air                 :A_o,H_out,T_airout      AS AIRFLOW
Evaporation         :Rw,area, ta             AS EVAPORATION
masstransfer        :mu_g,rho_g,st           AS masstransfer
Radiation           : rad_solid              AS RADIATION
EQUATION
# Mass & Energy balance
$m_a = F_a -F_r - F_x;
$(m_a*T_a) = (F_a*T_in) - (F_r + F_x)*T_a;
$(m_a*x_a) = (F_a*x_in) - (F_r + F_x)*x_a - Rw;
F_r + F_x = m_a / ft;
F_x = c1*m_a/ft;
$((m_a*(1-x_a)* Cp_z*ta) + (m_a*x_a*Cp_w*ta)) =
F_a*(((1-x_in)*Cp_z*tin) + (x_in*Cp_w*tin))- (F_r + F_x)*(((1-x_a)*Cp_z*ta) +
(x_a*Cp_w*ta))-Rw*(landa + (Cp_w*Ta)) + conv_a + rad_solid ;
# Gas velocity
v_g = A_o/(rho_g*3.142*(1.95^2));
# Area in contact with gas
area =h*m_a*(( 2*3.142*((0.5*dp)^2))/(4/3*3.142*((0.5*dp)^3)*rho_p));
# Evaporation rate
Rw= hm*(area)*(Pw_s-Pw_air);
Pw_s = exp(23.56143-(4030.182/(Ta+ 235)));
Pw_air= H_out*P*(26/18);
Sc = mu_g/(rho_g*da);
```

```
hm = (rho_g/Pw_air)*st*v_g*((Pr/Sc)^(2/3));

da = 2.65E-05;

Pr = 0.7;
```

Passive phase

PARAMETER

Cp_w	AS REAL	# specific heat capacity of water
Cp_z	AS REAL	# specific heat capacity of zinc

VARIABLE

m_p	AS mass	# Passive Mass
m_load	AS mass	# Loading Mass
k_2	AS no_unit	# Passive to Active Transport Coefficient
k_4	AS no_unit	# Kilning Transport Coefficient
F_x	AS mass_flowrate	# Axial flow rate into Passive Phase
F_a	AS mass_flowrate	# Passive to Active Mass Flow
F_r	AS mass_flowrate	# Active to Passive Mass Flow
F_k_in	AS mass_flowrate	# Kilning Mass Flow into Passive
F_k_out	AS mass_flowrate	# Kilning Mass Flow out of Passive
T_x	AS mass_fraction	# Tracer Content in Axial Flow
T_p	AS mass_fraction	# Tracer Content in Passive Cell
T_r	AS mass_fraction	# Tracer Content in Return Flow
T_k_in	AS mass_fraction	# Tracer Content of incoming Kilning Flow
x_x	AS mass_fraction	# Moisture Content in Axial Flow
x_p	AS mass_fraction	# Moisture Content in Passive Cell
x_r	AS mass_fraction	# Moisture Content in Return Flow
x_k_in	AS mass_fraction	# Moisture content of kilning flow
tx	AS temperature	# Temperature of Axial Flow

```
tp                  AS temperature      #Temperature of Passive Cell
tr                  AS temperature      # Temperature of Return Flow
tkin                AS temperature      # Temperature of kilning flow
STREAM
Axial               :F_x,T_x,x_x,tx                 AS SOLIDFLOW
Active              :F_a,T_p,x_p,tp                 AS SOLIDFLOW
Return              :F_r,T_r,x_r,tr                 AS SOLIDFLOW
Kiln_in             :F_k_in,T_k_in,x_k_in,tkin      AS SOLIDFLOW
Kiln_out            :F_k_out,T_p,x_p,tp             AS SOLIDFLOW
DataOut             :m_p                            AS DATAF
DataIn              :k_2,m_load                     AS DATAP
EQUATION
# Mass and Energy balance
IF m_p < m_load THEN
  $m_p = F_x + F_k_in + F_r - F_a - F_k_out;
  $(m_p*T_p) = (F_x*T_x) + (F_k_in*T_k_in) + (F_r*T_r) - (F_a*T_p) - (F_k_out*T_p);
  $(m_p*x_p) = (F_x*x_x) + (F_k_in*x_k_in) + (F_r*x_r) - (F_a*x_p) - (F_k_out*x_p);
  F_k_out = k_4*m_p;
  F_a = k_2 * m_p;
  $((m_p*(1-x_p)* Cp_z*tp) + (m_p*x_p*Cp_w*tp)) =
F_x*(((1-x_x)*Cp_z*tx)+(x_x*Cp_w*tx)) + F_k_in*(((1-x_k_in)*Cp_z*tkin) + (x_k_in*
Cp_w*tkin)) + F_r*(((1-x_r)*Cp_z*tr) + (x_r*Cp_w*tr))- F_a*(((1-x_p)*Cp_z*tp) +
(x_p*Cp_w*tp)) - F_k_out*(((1-x_p)*Cp_z*tp) + (x_p*Cp_w*tp))  ;
```

```
ELSE
    $m_p = F_x + F_k_in + F_r - F_a - F_k_out;
    $(m_p*T_p) = (F_x*T_x) + (F_k_in*T_k_in) + (F_r*T_r) - (F_a*T_p) - (F_k_out*T_p);
    $(m_p*x_p) = (F_x*x_x) + (F_k_in*x_k_in) + (F_r*x_r) - (F_a*x_p) - (F_k_out*x_p);
    F_k_out = k_4 * m_p;
    F_a =  k_2 * m_load;
    $((m_p*(1-x_p)* Cp_z*tp) + (m_p*x_p*Cp_w*tp)) =
    F_x*(((1-x_x)*Cp_z*tx)+(x_x*Cp_w*tx)) + F_k_in*(((1-x_k_in)*Cp_z*tkin) + (x_k_in*
    Cp_w*tkin)) + F_r*(((1-x_r)*Cp_z*tr) + (x_r*Cp_w*tr))- F_a*(((1-x_p)*Cp_z*tp) +
    (x_p*Cp_w*tp)) - F_k_out*(((1-x_p)*Cp_z*tp) + (x_p*Cp_w*tp));
END
```

Kilning cell for section A

```
PARAMETER
L1          AS REAL          # Length of plug flow section
Cp_w        AS REAL          #  Specific heat capacity of water
Cp_z        AS REAL          # Specific heat capacity of zinc
rho_p       AS REAL          # particle density of zinc
landa       AS REAL          # Heat of vaporisation
Cp_air      AS REAL          # specific heat capacity of air
DISTRIBUTION_DOMAIN
sl  AS [0:L1]
VARIABLE
# Solid phase
r                   AS DISTRIBUTION(sl) OF density   # mass distribution along reactor
rhob                AS DISTRIBUTION(sl) OF  no_unit          # Bulk solid density
T                   AS DISTRIBUTION(sl) OF mass_fraction     # Tracer fraction
Ts                  AS DISTRIBUTION(sl) OF temperature    # Temperature fraction
me                  AS DISTRIBUTION(sl) OF mass_fraction     # moisture content
Rw                  AS  DISTRIBUTION(sl) OF mass_flowrate       # Evaporation
Pw_s                AS DISTRIBUTION(sl) OF no_unit           # Partial pressure of solid
Pw_a                AS DISTRIBUTION(sl) OF no_unit           # Vapour partial pressure
Cpw_v           AS DISTRIBUTION(sl) OF no_unit   #specific heat capacity of  water vapour
T_k_in              AS mass_fraction                # Tracer conc. in inflow
T_out               AS mass_fraction                # Tracer conc. in outflow
```

```
F_k_in          AS mass_flowrate          # Solid inlet mass flow rate(kg/s
F_k_out         AS mass_flowrate          # Solid outlet mass flow rate(kg/s
the             AS mass_flowrate                # kilning angle
u               AS no_unit              # velocity of material in       # m s^-1
k               AS no_unit              # dispersion coefficient      # m^2 s^-1
M_active        AS mass                 # mass in contact with gas       # kg
x_out           AS mass_fraction  # Moisture content of solid leaving the plug flow
x_in            AS mass_fraction # Moisture content of solid entering the plug flow
tink            AS temperature          # Solid inlet temperature
Tout            AS temperature          #  Solid temperature at the plug flow outlet
da              AS no_unit              # Diffusivity
e_s             AS no_unit              # Solid surface emissivity
f               AS no_unit              #  area correction factor
dp              AS no_unit              # particle size
L               AS no_unit              # Length of chord based on kilning mass
A               AS no_unit              # Area in contact with gas
# Gas phase
Air             AS DISTRIBUTION(sl) OF mass          # mass of air
v_g             AS DISTRIBUTION(sl) OF  no_unit          # Velocity of gas
tair            AS DISTRIBUTION(sl) OF temperature     # temperate of air
H_out           AS DISTRIBUTION(sl) OF mass_fraction       # Gas humidity
F_ain           AS mass_flowrate          # Ga inlet mass flow rate
H_ain           AS mass_fraction          # Gas inlet humidity
```

T_airin AS temperature # Gas inlet temperature

A_o AS mass_flowrate # Mass of gas @ outlet

H_o AS mass_fraction # Gas humidity @ outlet

T_o AS temperature # Gas temperature @ outlet

rho_g AS DISTRIBUTION(sl) OF no_unit # Density of gas

k_air AS DISTRIBUTION(sl) OF no_unit #Thermal conductivity of air

hc AS DISTRIBUTION(sl) OF no_unit # Convective heat transfer

mu_g AS DISTRIBUTION(sl) OF no_unit # Viscosity of air

Sc AS DISTRIBUTION(sl) OF no_unit # Schmidit

St AS DISTRIBUTION(sl) OF no_unit # Staton number

hm AS DISTRIBUTION(sl) OF no_unit # Mass transfer coefficient

Re AS DISTRIBUTION(sl) OF no_unit # Mass transfer coefficient

Qlos AS DISTRIBUTION(sl) OF no_unit # Heat loss

rad_solid AS DISTRIBUTION(sl) OF no_unit # Radiation from gas to solid

h_rad_w AS DISTRIBUTION(sl) OF no_unit # Radiative heat transfer coefficient

rad_w AS DISTRIBUTION(sl) OF no_unit # Radiation from gas to wall

Res AS DISTRIBUTION(sl) OF no_unit # Resistance

conv_in AS DISTRIBUTION(sl) OF no_unit # Inside Convective heat transfer coefficient (from the gas to the wall)

hinside AS DISTRIBUTION(sl) OF no_unit #convective heat transfer

Re_in AS DISTRIBUTION (sl) OF no_unit # Inside Reynolds number

conv_out AS no_unit # Outside convective heat transfer coefficient

```
hout            AS no_unit      # outside convection
Ra              AS no_unit              # Rayleigh number
Pr              AS no_unit          # Prandtl
cond            AS no_unit          # Conduction
Rad             AS no_unit          # Radiation
g               AS no_unit          # acceleration due to gravity
B               AS no_unit          # expansion coefficient
Tamb            AS no_unit          # Ambient temperature
v               AS no_unit          # Kinematic viscosity
alpha           AS no_unit          #Thermal expansion
h_rad           AS no_unit      # Radiation heat transfer coefficient
e               AS no_unit      # emissivity
et              AS no_unit      # Stefan-Boltzmann
lo              AS no_unit              # Heat loss factor
heatloss        AS no_unit      # Total heat lost
K_airo          AS no_unit  # thermal conductivity of air based on shell temperature
#Geometry
D_out           AS no_unit          # Outside diameter
D_in            AS no_unit          # Inside diameter
R_out           AS no_unit          # Inside radius #m
R_in            AS no_unit          # Outside radius
d               AS no_unit      # Discretised cell length
#Shell properties
```

```
Tsd                 AS temperature      # Dryer shell temperature
mu_s                AS no_unit          # viscosity of gas @ shell temperature
k_s                 AS no_unit          # thermal conductivity of steel material
STREAM
Kiln_in             :F_k_in,T_k_in,x_in,tink        AS SOLIDFLOW
Kiln_out            :F_k_out,T_out, x_out,tout      AS SOLIDFLOW
Air_out             :A_o,H_o,T_o                    AS AIRFLOW
BOUNDARY
# Solid phase
r(0) = F_k_in/u;
T(0) = T_k_in;
me(0) = x_in;
Ts(0) = tink;
k*PARTIAL((Cp_w*Ts(L1)*r(L1)*me(L1)+ Cp_z*Ts(L1)*r(L1)*(1-me(L1))),sl,sl) = 0;
(k*(PARTIAL(r(L1),sl,sl))) = 0;
(k*(PARTIAL((r(L1)*T(L1)),sl,sl))) = 0;
(k*(PARTIAL((r(L1)*me(L1)),sl,sl))) = 0;
rhob(0) = (-3095.24*me(0))+ 2043.81;
rhob(L1) = (-3095.24*me(L1))+ 2043.81;
#Evaporation rate
Rw(0) = hm(0)*A*(Pw_s(0) - Pw_a(0));
Rw(L1) = hm(L1)*A*(Pw_s(L1) - Pw_a(L1));
hm(0) =  (rho_g(0)/Pw_a(0))*st(0)*v_g(0)*((Pr/Sc(0))^(2/3));
```

```
hm(L1) =  (rho_g(L1)/Pw_a(L1))*st(L1)*v_g(L1)*((Pr/Sc(L1))^(2/3));

Pw_s(0) = exp(23.56143-(4030.182/(Ts(0)+ 235)));

Pw_s(L1) = exp(23.56143-(4030.182/(Ts(L1)+ 235)));

Pw_a(0)= H_out(0)*101325*(26/18);

Pw_a(L1)= H_out(L1)*101325*(26/18);

# Gas phase

Tair(0) = T_airin;

PARTIAL((Air(L1)*(1-H_out(L1))*v_g(L1)*Cp_air*100 +

Air(L1)*H_out(L1)*Cp_w*v_g(L1)*100 + Air(L1)*(1-H_out(L1))*v_g(L1)*Cp_air*(tair(L1)-

100) + Air(L1)*H_out(L1)*Cpw_v(L1)*v_g(L1)*(tair(L1)-100)+

Air(L1)*H_out(L1)*v_g(L1)*landa) ,sl)= 0

H_out(0) = H_ain;

(PARTIAL((Air(L1)*H_out(L1)*v_g(L1)),sl)) = 0;

Air(0) = (F_ain/3600)/v_g(0);

(PARTIAL(Air(L1)*v_g(L1),sl)) = 0;

#Gas properties

rho_g(0) = 6.417E-13*(tair(0)^4) - 2.673E-09*(tair(0)^3) + 4.129E-06*(tair(0)^2) - 3.037E-

03*tair(0) + 1.225E+00;

k_air(0) =  -1.249E-08*(tair(0)^2) + 6.699E-05*(tair(0)) + 2.541E-02;

mu_g(0) =   -7.479E-12*(tair(0)^2) + 3.746E-08*(tair(0)) + 1.824E-05;

rho_g(L1) = 6.417E-13*(tair(L1)^4) - 2.673E-09*(tair(L1)^3) + 4.129E-06*(tair(L1)^2) -

3.037E-03*tair(L1) + 1.225E+00;

k_air(L1) =  -1.249E-08*(tair(L1)^2) + 6.699E-05*(tair(L1)) + 2.541E-02;
```

```
mu_g(L1) =   -7.479E-12*(tair(L1)^2) + 3.746E-08*(tair(L1)) + 1.824E-05;

St(0) = hc(0)/(Cp_air*rho_g(0)*v_g(0));

Sc(0) = mu_g(0)/(rho_g(0)*da);

St(L1) = hc(L1)/(Cp_air*rho_g(L1)*v_g(L1));

Sc(L1) = mu_g(L1)/(rho_g(L1)*da);

hc(0) = (0.33*(((v_g(0)*rho_g(0)*dp)/mu_g(0))^0.6)*(k_air(0)/dp));

hc(L1) = (0.33*(((v_g(L1)*rho_g(L1)*dp)/mu_g(L1))^0.6)*(k_air(L1)/dp));

Re(0) = (v_g(0)*dp*rho_g(0))/mu_g(0);

Re(L1) = (v_g(L1)*dp*rho_g(L1))/mu_g(L1);

v_g(0) = (F_ain/3600)/(rho_g(0)*3.142*(1.95^2));

v_g(L1) = (F_ain/3600)/(rho_g(L1)*3.142*(1.95^2));

Cpw_v(0) =-0.00000000031759*(tair(0)+273)^3 + 0.00000091451537*(tair(0)+273)^2 -

0.00014971847134*(tair(0)+273) + 1.84044937134494;

Cpw_v(L1) =-0.00000000031759*(tair(L1)+273)^3 + 0.00000091451537*(tair(L1)+273)^2 -

0.00014971847134*(tair(L1)+273) + 1.84044937134494;

#heat loss

Qlos(0) = lo*((tair(0) - Tamb)/Res(0));

Qlos(L1) = lo*((tair(L1) - Tamb)/Res(L1));

Res(0) = (1/(conv_in(0) + rad_w(0))) + cond +(1/(conv_out + rad));

Res(L1) = (1/(conv_in(L1) + rad_w(L1))) + cond +(1/(conv_out + rad));

rad_solid(0) = e_s*et*A*(((Tair(0)+273)^4)-((Ts(0)+273)^4));

rad_solid(L1) = e_s*et*A*(((Tair(L1)+273)^4)-((Ts(L1)+273)^4));

h_rad_w(0) = e*et*((Tair(0)+273) + (Tsd+273))*(((Tair(0)+273)^2) + ((Tsd+273)^2));
```

```
h_rad_w(L1) = e*et*((Tair(L1)+273) + (Tsd+273))*(((Tair(L1)+273)^2) + ((Tsd+273)^2));

Rad_w(0) = h_rad_w(0)*2*3.142*R_out;

Rad_w(L1) = h_rad_w(L1)*2*3.142*R_out;

Re_in(0) = (v_g(0)*D_in*rho_g(0))/mu_g(0);

hinside(0) =( k_air(0)/D_in)*0.027*(Re_in(0)^0.8)*(Pr^(1/3))*((mu_g(0)/mu_s)^0.14);

conv_in(0) = (hinside(0)*2*3.142*r_in);

Re_in(L1) = (v_g(L1)*D_in*rho_g(L1))/mu_g(L1);

hinside(L1) =( k_air(L1)/D_in)*0.027*(Re_in(L1)^0.8)*(Pr^(1/3))*((mu_g(L1)/mu_s)^0.14);

conv_in(L1) = (hinside(L1)*2*3.142*r_in);

EQUATION

# Area in contact with the gas

r(L1) =((1.95^2)/2)*rhob(0)*(the -Sin(the));

L   = 2*1.95*Sin(the/2);

M_active = ((L*dp)/(((1.95^2)/2)*(the-Sin(the))))*r(L1)*d;

A =f*M_active*(( 2*3.142*((0.5*dp)^2))/(4/3*3.142*((0.5*dp)^3)*rho_p));

d =L1/60;

dp  = 0.02;

da = 2.65E-05;

Pr = 0.7;

e_s = 0.9;

# Heat loss calculation

Tsd = 145;

# Radiation
```

```
h_rad = e*et*((Tsd+273) + (Tamb+273))*(((Tsd+273)^2) + ((Tamb+273)^2));

e = 0.79;

et = 5.67E-08;

Rad = h_rad*2*3.142*R_out;

# Inside convection

mu_s    = 2.3650E-05;

R_in    = 1.90;

D_in    = R_in*2;

# Outside convection

g = 9.81;

B = 1.3E-03;

alpha =4.16531E-05;

v  =2.8571E-05;

Ra = (g*B*(Tsd-Tamb)*(D_out^3))/(v*alpha);

R_out = 1.95;

D_out = R_out*2;

k_airo = 0.0348756;

hout = (k_airo/D_out)*((0.60+((0.387*(Ra^(1/6)))/((1+((0.559/Pr)^(9/16)))^(8/27))))^2);#W
m^-2 C^-1

conv_out = hout*2*3.142*R_out;              #W m^-1 C^-1

# Conduction

k_s = 54-3.33E-02*Tsd;      # W m^2 C^-1

#k_s =0.0348756;
```

```
cond = (LOG(R_out/r_in))/(k_s*2*3.142);

# Mass and Energy balance

FOR i:=0|+ TO L1|- DO

# Solid phase

$r(i) = (k*(PARTIAL(r(i),sl,sl)))-(u*(PARTIAL(r(i),sl)));       # Solid mass   (kg s^-1 m^-1)

# Tracer concentration

$(T(i)*r(i)) = (k*(PARTIAL((r(i)*T(i)),sl,sl)))-(u*(PARTIAL((r(i)*T(i)),sl)));

 # Solid moisture content (kg s^-1 m^-1)

$(me(i)*r(i)) = (k*(PARTIAL((r(i)*me(i)),sl,sl)))-(u*(PARTIAL((r(i)*me(i)),sl)))-Rw(i)/d; #

Solid moisture content(kg s^-1 m^-1)

rhob(i) = (-3095.24*me(i))+ 2043.81;   # Solid bulk denisty # kg m^3

# Solid temperature (J s^-1 m^-1)

$((Ts(i)*r(i)*Cp_w*me(i)) + (Ts(i)*r(i)*Cp_z*(1-me(i)))) =

k*PARTIAL((Cp_w*Ts(i)*r(i)*me(i)+ Cp_z*Ts(i)*r(i)*(1-me(i))),sl,sl)-

u*(PARTIAL((Cp_w*me(i)*Ts(i)*r(i)+ Cp_z*(1-me(i))*Ts(i)*r(i)),sl))- (Rw(i)/d)*(landa +

Cp_w*Ts(i)) + hc(i)*(A/d)*(tair(i)-Ts(i))+ (rad_solid(i)/d);

# Evaporation rate

Rw(i) =  hm(i)*(A)*(Pw_s(i) - Pw_a(i));

 hm(i) =  (rho_g(i)/Pw_a(i))*st(i)*v_g(i)*((Pr/Sc(i))^(2/3));

Pw_s(i) = exp(23.56143-(4030.182/(Ts(i)+ 235)));

Pw_a(i)= H_out(i)*101325*(26/18);

# Air phase

$Air(i) = -PARTIAL((Air(i)*v_g(i)),sl) + Rw(i)/d;
```

```
$(Air(i)*H_out(i))= -PARTIAL((Air(i)*H_out(i)*v_g(i)),sl)+ Rw(i)/d;

#Gas temperature (J s^-1 m^-1)

$(Air(i)*(1-H_out(i))*v_g(i)*Cp_air*100 + Air(i)*H_out(i)*Cp_w*v_g(i)*100 + Air(i)*(1-
H_out(i))*v_g(i)*Cp_air*(tair(i)-100) + Air(i)*H_out(i)*Cpw_v(i)*v_g(i)*(tair(i)-100)+
Air(i)*H_out(i)*landa-(8.314*(Tair(i)+273)*(10^3)*(Air(i)*H_out(i)/18))-
(8.314*(10^3)*(Tair(i)+273)*(Air(i)*(1-H_out(i))/29))) = -PARTIAL((Air(i)*(1-
H_out(i))*v_g(i)*Cp_air*100 + Air(i)*H_out(i)*Cp_w*v_g(i)*100 + Air(i)*(1-
H_out(i))*v_g(i)*Cp_air*(tair(i)-100) + Air(i)*H_out(i)*Cpw_v(i)*v_g(i)*(tair(i)-100)+
Air(i)*H_out(i)*v_g(i)*landa) ,sl) + (Rw(i)/d)*(landa + Cp_w*Ts(i))-hc(i)*(A/d)*(tair(i)-Ts(i))-
(rad_solid(i)/d)- Qlos(i) ;

#Gas properties

v_g(i) = (F_ain/3600)/(rho_g(i)*3.142*(1.95^2));

rho_g(i) = 6.417E-13*(tair(i)^4) - 2.673E-09*(tair(i)^3) + 4.129E-06*(tair(i)^2) - 3.037E-
03*tair(i) + 1.225E+00;

k_air(i) =  -1.249E-08*(tair(i)^2) + 6.699E-05*(tair(i)) + 2.541E-02;

mu_g(i) =   -7.479E-12*(tair(i)^2) + 3.746E-08*(tair(i)) + 1.824E-05;

St(i) = hc(i)/(Cp_air*rho_g(i)*v_g(i));

Sc(i) = mu_g(i)/(rho_g(i)*da);

hc(i) = (0.33*(((v_g(i)*rho_g(i)*dp)/mu_g(i))^0.6)*(k_air(i)/dp));

Re(i) = (v_g(i)*dp*rho_g(i))/mu_g(i);

# specific heat capacity of water vapour

Cpw_v(i) =-0.00000000031759*(tair(i)+273)^3 + 0.00000091451537*(tair(i)+273)^2 -
0.00014971847134*(tair(i)+273) + 1.84044937134494;
```

```
# Heat loss
Qlos(i) = lo*((tair(i) - Tamb)/Res(i));
# radiation from gas to solid
rad_solid(i) = e_s*et*A*(((Tair(i)+273)^4)-((Ts(i)+273)^4));
 # radiation from gas to the wall
h_rad_w(i) = e*et*((Tair(i)+273) + (Tsd+273))*(((Tair(i)+273)^2) + ((Tsd+273)^2));
Rad_w(i) = h_rad_w(i)*2*3.142*R_out;
#Inside convective heat transfer (from gas to wall)
Re_in(i) = (v_g(i)*D_in*rho_g(i))/mu_g(i);
hinside(i) =( k_air(i)/D_in)*0.027*(Re_in(i)^0.8)*(Pr^(1/3))*((mu_g(i)/mu_s)^0.14);
conv_in(i) = (hinside(i)*2*3.142*r_in);
Res(i) = (1/(conv_in(i) + rad_w(i))) + cond +(1/(conv_out + rad));
END
#Total heat loss from the section
heatloss = INTEGRAL(i := 0:L1; Qlos(i));
# Variables linking the next section
r(L1) = F_k_out/u;
T(L1) = T_out;
me(L1) = x_out;
Ts(L1) = Tout;
Air(L1) = A_o/v_g(L1);
Tair(L1) = T_o;
H_out(L1) = H_o;
```

Kilning cell for section E

```
PARAMETER
L5                  AS REAL          # Length of plug flow section
Cp_w                AS REAL          # Specific heat capacity of water
Cp_z                AS REAL          # Specific heat capacity of zinc
landa               AS REAL        # Heat of vaporisation
Cp_air              AS REAL         # specific heat capacity of air
P                   AS REAL          # Pressure within the dryer
rho_p               AS REAL          # Particle density of zinc
DISTRIBUTION_DOMAIN
sl  AS [0:L5]
VARIABLE
# Solid phase
r                   AS DISTRIBUTION(sl) OF density   # mass distribution along reactor
T                   AS DISTRIBUTION (sl) OF mass_fraction     # Tracer fraction
Ts                  AS DISTRIBUTION (sl) OF temperature    # Temperature
me                  AS DISTRIBUTION(sl) OF mass_fraction     # moisture content
Rw                  AS  DISTRIBUTION(sl) OF mass_flowrate       # Evaporation
Pw_s                AS DISTRIBUTION(sl) OF no_unit            # Partial pressure of solid
Pw_a                AS DISTRIBUTION(sl) OF no_unit            # Vapour partial pressure
rhob                AS DISTRIBUTION(sl) OF  no_unit              # Density of solid
Cpw_v           AS DISTRIBUTION(sl) OF no_unit   #specific heat capacity of  water vapour
```

```
F_t             AS mass_flowrate          # mass flow rate into the section
T_t             AS mass_fraction      # tracer fraction entering the section
x_t             AS mass_fraction      # moisture content entering the section
tt              AS temperature        # Solid temperature(inlet)
da              AS no_unit                                  # Diffusivity
Tout            AS temperature          # Solid temperature at the plug flow outlet
T_out           AS mass_fraction              # Tracer conc. in outflow
F_k_out         AS mass_flowrate               # Mass flow out
the             AS mass_flowrate                # kilning angle
u               AS no_unit                # solid velocity
k               AS no_unit                  # dispersion coefficient
M_active        AS mass                 # mass in contact with gas
x_out           AS mass_fraction      # Moisture content of solid leaving plug flow
dp              AS no_unit            # particle size
e_s             AS no_unit            # Solid surface emissivity
L               AS no_unit            # Length of chord
A               AS no_unit            # Area in contact with gas
n               AS no_unit            # Area correction factor
# Gas Phase
Air             AS DISTRIBUTION(sl) OF mass          # mass of air
v_g             AS  DISTRIBUTION(sl) OF  no_unit
Qlos            AS DISTRIBUTION(sl) OF no_unit       # Heat loss
```

tair AS DISTRIBUTION(sl) OF temperature # temperate of air

rho_g AS DISTRIBUTION(sl) OF no_unit #density of gas

k_air AS DISTRIBUTION(sl) OF no_unit # thermal conductivity of air

hc AS DISTRIBUTION(sl) OF no_unit #Convective heat transfer coefficient(from gas to solids)

mu_g AS DISTRIBUTION(sl) OF no_unit # Viscosity of air

Sc AS DISTRIBUTION(sl) OF no_unit # Schmidt

St AS DISTRIBUTION (sl) OF no_unit # Stanton number

hm AS DISTRIBUTION(sl) OF no_unit # Mass transfer coefficient

H_out AS DISTRIBUTION (sl) OF mass_fraction # Gas humidity

rad_solid AS DISTRIBUTION(sl) OF no_unit # Mass transfer coefficient

h_rad_w AS DISTRIBUTION(sl) OF no_unit # Heat loss

rad_w AS DISTRIBUTION(sl) OF no_unit # Heat loss

Res AS DISTRIBUTION(sl) OF no_unit # Heat loss

Re_in AS DISTRIBUTION(sl) OF no_unit # Inside Reynolds number

hinside AS DISTRIBUTION(sl) OF no_unit # Inside convection transfer coefficient(from gas to walls)

conv_in AS DISTRIBUTION(sl) OF no_unit # inside convective heat transfer(from gas to walls)

A_o AS mass_flowrate # Gas mass flow rate at outlet

H_o AS mass_fraction # Gas humidity at outlet

T_o AS temperature # Gas temperature at outlet

Pr AS no_unit # Prandtl number

```
hout            AS no_unit          # outside convection
Ra              AS no_unit                  # Rayleigh number
conv_out        AS no_unit          # Outside convective heat transfer coefficient
Cond            AS no_unit          # Conduction
Rad             AS no_unit          # Radiation
g               AS no_unit          # acceleration due to gravity
B               AS no_unit          # expansion coefficient
Tamb            AS no_unit          # Ambient temperature
v               AS no_unit          # Kinematic viscosity
alpha           AS no_unit
h_rad           AS no_unit          # Radiation heat transfer coefficient
e               AS no_unit          # emissivity
et              AS no_unit          # Stefan-Boltzmann
A_air           AS mass_flowrate    # Gas mass flow rate
H_t             AS mass_fraction    # Gas humidity at inlet
T_air           AS temperature      # Gas temperature at inlet
lo              AS no_unit          # heat loss correction factor
heatloss        AS no_unit          # Total heat loss
#Shell properties
mu_s            AS no_unit          # viscosity of gas @ shell temperature
K_airo          AS no_unit  # Therrmal conductivity of air based on shell temperature
k_s             AS no_unit  # Thermal conductivity of shell
Tsd             AS temperature      # Dryer shell temperature
```

#Geometry

D_out AS no_unit # Outside diameter

D_in AS no_unit # Inside diameter

R_out AS no_unit # Inside radius

R_in AS no_unit # Outside radius

d AS no_unit # Discertized cell length

STREAM

Kiln_in :F_t, T_t, x_t, tt AS SOLIDFLOW

Kiln_out :F_k_out,T_out,x_out,tout AS SOLIDFLOW

Air_in :A_air,H_t,T_air AS AIRFLOW

Air_out : A_o, H_o, T_o AS AIRFLOW

BOUNDARY

r(0) = (F_t)/u;

T(0) = T_t ;

Ts(0) = tt ;

me(0) = x_t ;

(k*(PARTIAL(r(L5),sl,sl))) = 0;

(k*(PARTIAL((r(L5)*T(L5)),sl,sl))) = 0;

(k*(PARTIAL((r(L5)*me(L5)),sl,sl))) = 0;

(k*(PARTIAL((Cp_w*Ts(L5)*r(L5)*me(L5)+ Cp_z*Ts(L5)*r(L5)*(1-me(L5))),sl,sl))) = 0;

Air(0) = A_air/v_g(0);

(PARTIAL(Air(L5)*v_g(L5),sl)) = 0;

Tair(0) = T_air;

PARTIAL((Air(L5)*(1-H_out(L5))*v_g(L5)*Cp_air*100 +

Air(L5)*H_out(L5)*Cp_w*v_g(L5)*100 + Air(L5)*(1-H_out(L5))*v_g(L5)*Cp_air*(tair(L5)-

100) + Air(L5)*H_out(L5)*Cpw_v(L5)*v_g(L5)*(tair(L5)-100)+

Air(L5)*H_out(L5)*v_g(L5)*landa) ,sl)= 0;

H_out(0) = H_t;

(PARTIAL((Air(L5)*H_out(L5)*v_g(L5)),sl)) = 0;

Rw(0) = hm(0)*A*(Pw_s(0) - Pw_a(0));

Rw(L5) = hm(L5)*A*(Pw_s(L5) - Pw_a(L5));

Pw_s(0) = exp(23.56143-(4030.182/(Ts(0)+ 235)));

Pw_s(L5) = exp(23.56143-(4030.182/(Ts(L5)+ 235)));

Pw_a(0)= H_out(0)*P*(26/18);

Pw_a(L5)= H_out(L5)*P*(26/18);

Qlos(0) = lo*((tair(0) - Tamb)/Res(0));

Qlos(L5) =lo*((tair(L5) - Tamb)/Res(L5));

rho_g(0) = 6.417E-13*(tair(0)^4) - 2.673E-09*(tair(0)^3) + 4.129E-06*(tair(0)^2) - 3.037E-

03*tair(0) + 1.225E+00;

rho_g(L5) = 6.417E-13*(tair(L5)^4) - 2.673E-09*(tair(L5)^3) + 4.129E-06*(tair(L5)^2) -

3.037E-03*tair(L5) + 1.225E+00;

k_air(0) = -1.249E-08*(tair(0)^2) + 6.699E-05*(tair(0)) + 2.541E-02;

k_air(L5) = -1.249E-08*(tair(L5)^2) + 6.699E-05*(tair(L5)) + 2.541E-02;

mu_g(0) =   -7.479E-12*(tair(0)^2) + 3.746E-08*(tair(0)) + 1.824E-05;

mu_g(L5) =   -7.479E-12*(tair(L5)^2) + 3.746E-08*(tair(L5)) + 1.824E-05;

```
Cpw_v(0) =-0.00000000031759*(tair(0)+273)^3 + 0.00000091451537*(tair(0)+273)^2 -
0.00014971847134*(tair(0)+273) + 1.84044937134494;
Cpw_v(L5) =-0.00000000031759*(tair(L5)+273)^3 + 0.00000091451537*(tair(L5)+273)^2 -
0.00014971847134*(tair(L5)+273) + 1.84044937134494;
St(0) = hc(0)/(Cp_air*rho_g(0)*v_g(0));
St(L5) = hc(L5)/(Cp_air*rho_g(L5)*v_g(L5));
Sc(0) = mu_g(0)/(rho_g(0)*da);
Sc(L5) = mu_g(L5)/(rho_g(L5)*da);
hm(0) =  (rho_g(0)/Pw_a(0))*st(0)*v_g(0)*((Pr/Sc(0))^(2/3));
hm(L5) =  (rho_g(L5)/Pw_a(L5))*st(L5)*v_g(l5)*((Pr/Sc(L5))^(2/3));
hc(0) = (0.33*(((v_g(0)*rho_g(0)*dp)/mu_g(0))^0.6)*(k_air(0)/dp));
hc(L5) = (0.33*(((v_g(L5)*rho_g(L5)*dp)/mu_g(L5))^0.6)*(k_air(L5)/dp));
rhob(0) = (-3095.24*me(0))+ 2043.81;   # Angle of repose
rhob(L5) = (-3095.24*me(L5))+ 2043.81;   # Angle of repose
rad_solid(0) = e_s*et*A*(((Tair(0)+273)^4)-((Ts(0)+273)^4));
rad_solid(L5) = e_s*et*A*(((Tair(L5)+273)^4)-((Ts(L5)+273)^4));
h_rad_w(0) = e*et*((Tair(0)+273) + (Tsd+273))*(((Tair(0)+273)^2) + ((Tsd+273)^2));
h_rad_w(L5) = e*et*((Tair(L5)+273) + (Tsd+273))*(((Tair(L5)+273)^2) + ((Tsd+273)^2));
Res(0) = (1/(conv_in(0) + rad_w(0))) + cond +(1/(conv_out + rad));
Res(L5) = (1/(conv_in(L5) + rad_w(L5))) + cond +(1/(conv_out + rad));
Rad_w(0) = h_rad_w(0)*2*3.142*R_out;
Rad_w(L5) = h_rad_w(L5)*2*3.142*R_out;
Re_in(0) = (v_g(0)*D_in*rho_g(0))/mu_g(0);
```

```
Re_in(L5) = (v_g(L5)*D_in*rho_g(L5))/mu_g(L5);

hinside(0) =( k_air(0)/D_in)*0.027*(Re_in(0)^0.8)*(Pr^(1/3))*((mu_g(0)/mu_s)^0.14);

hinside(L5) =( k_air(L5)/D_in)*0.027*(Re_in(L5)^0.8)*(Pr^(1/3))*((mu_g(L5)/mu_s)^0.14);

conv_in(0) = (hinside(0)*2*3.142*r_in);

conv_in(L5) = (hinside(L5)*2*3.142*r_in);

v_g(0) = A_air/(rho_g(0)*3.142*(1.95^2));

v_g(L5) = A_air/(rho_g(L5)*3.142*(1.95^2));

EQUATION

# Area in contact with the gas

r(L5) =((1.95^2)/2)*rhob(0)*(the -Sin(the));        # Area of kilning

L   = 2*1.95*Sin(the/2);                          # length of chord

M_active = ((L*dp)/(((1.95^2)/2)*(the-Sin(the))))*r(L5)*d;

A =n*M_active*(( 2*3.142*((0.5*dp)^2))/(4/3*3.142*((0.5*dp)^3)*rho_p));

d =L5/100;

dp = 0.007;

da = 2.65E-05;

Pr = 0.7;

e_s = 0.9;

#Heat loss calculation

Tsd = 65;

# Radiation heat transfer to the environment

h_rad = e*et*((Tsd+273) + (Tamb+273))*(((Tsd+273)^2) + ((Tamb+273)^2));

e = 0.79;
```

```
et = 5.67E-08;

Rad = h_rad*2*3.142*R_out;

# Inside convection heat transfer from gas to walls

R_in    = 1.90;

D_in    = R_in*2;

mu_s    = 2.3E-05;

# Outside convection heat transfer from walls to environment

R_out = 1.95;

D_out = R_out*2;

g = 9.81;          # acceleration

B = 1/(tair(0)+273);

alpha = 2.7399E-05;

v  =2.0366E-05;

Ra = (g*B*(Tsd-Tamb)*(D_out^3))/(v*alpha);

k_airo = 0.029668371;

hout = (k_airo/D_out)*((0.60+((0.387*(Ra^(1/6)))/((1+((0.559/Pr)^(9/16)))^(8/27))))^2);

conv_out = hout*2*3.142*R_out;

# Conduction

k_s = 54-3.33E-02*Tsd;

cond = (LOG(R_out/r_in))/(k_s*2*3.142);

# Mass and energy balance

FOR i: =0|+ TO L5|- DO

# Solid phase
```

```
$r(i) = (k*(PARTIAL(r(i),sl,sl)))-(u*(PARTIAL(r(i),sl)));

$(T(i)*r(i)) = (k*(PARTIAL((r(i)*T(i)),sl,sl)))-(u*(PARTIAL((r(i)*T(i)),sl)));

$(me(i)*r(i)) = (k*(PARTIAL((r(i)*me(i)),sl,sl)))-(u*(PARTIAL((r(i)*me(i)),sl)))-Rw(i)/d;

$((Ts(i)*r(i)*Cp_w*me(i)) + (Ts(i)*r(i)*Cp_z*(1-me(i)))) =

k*PARTIAL((Cp_w*Ts(i)*r(i)*me(i)+ Cp_z*Ts(i)*r(i)*(1-me(i))),sl,sl)-

u*(PARTIAL((Cp_w*me(i)*Ts(i)*r(i)+ Cp_z*(1-me(i))*Ts(i)*r(i)),sl))- (Rw(i)/d)*(landa +

Cp_w*Ts(i)) + hc(i)*(A/d)*(tair(i)-Ts(i)) + (rad_solid(i)/d);

rhob(i) = (-3095.24*me(i))+ 2043.81;

Rw(i) =  hm(i)*(A)*(Pw_s(i) - Pw_a(i));

Pw_s(i) = exp(23.56143-(4030.182/(Ts(i)+ 235)));

Pw_a(i)= H_out(i)*P*(26/18);

# Air phase

$(Air(i)*(1-H_out(i))*v_g(i)*Cp_air*100 + Air(i)*H_out(i)*Cp_w*v_g(i)*100 + Air(i)*(1-

H_out(i))*v_g(i)*Cp_air*(tair(i)-100) + Air(i)*H_out(i)*Cpw_v(i)*v_g(i)*(tair(i)-100)+

Air(i)*H_out(i)*landa-(8.314*(Tair(i)+273)*(10^3)*(Air(i)*H_out(i)/18))-

(8.314*(10^3)*(Tair(i)+273)*(Air(i)*(1-H_out(i))/29))) = -PARTIAL((Air(i)*(1-

H_out(i))*v_g(i)*Cp_air*100 + Air(i)*H_out(i)*Cp_w*v_g(i)*100 + Air(i)*(1-

H_out(i))*v_g(i)*Cp_air*(tair(i)-100) + Air(i)*H_out(i)*Cpw_v(i)*v_g(i)*(tair(i)-100)+

Air(i)*H_out(i)*v_g(i)*landa) ,sl) + (Rw(i)/d)*(landa + Cp_w*Ts(i))-hc(i)*(A/d)*(tair(i)-Ts(i))-

(rad_solid(i)/d)- Qlos(i) ;

v_g(i) = A_air/(rho_g(i)*3.142*(1.95^2));

Qlos(i) = lo*((tair(i) - Tamb)/Res(i)); # Heat loss
```

```
rho_g(i) = 6.417E-13*(tair(i)^4) - 2.673E-09*(tair(i)^3) + 4.129E-06*(tair(i)^2) - 3.037E-
03*tair(i) + 1.225E+00;
k_air(i) =  -1.249E-08*(tair(i)^2) + 6.699E-05*(tair(i)) + 2.541E-02;
mu_g(i) =   -7.479E-12*(tair(i)^2) + 3.746E-08*(tair(i)) + 1.824E-05;
St(i) = hc(i)/(Cp_air*rho_g(i)*v_g(i));
Sc(i) = mu_g(i)/(rho_g(i)*da);
hm(i) =  (rho_g(i)/Pw_a(i))*st(i)*v_g(i)*((Pr/Sc(i))^(2/3));
hc(i) = (0.33*(((v_g(i)*rho_g(i)*dp)/mu_g(i))^0.6)*(k_air(i)/dp));
rad_solid(i) = e_s*et*A*(((Tair(i)+273)^4)-((Ts(i)+273)^4));
h_rad_w(i) = e*et*((Tair(i)+273) + (Tsd+273))*(((Tair(i)+273)^2) + ((Tsd+273)^2));
Rad_w(i) = h_rad_w(i)*2*3.142*R_out;
Re_in(i) = (v_g(i)*D_in*rho_g(i))/mu_g(i);
hinside(i) =( k_air(i)/D_in)*0.027*(Re_in(i)^0.8)*(Pr^(1/3))*((mu_g(i)/mu_s)^0.14);
conv_in(i) = (hinside(i)*2*3.142*r_in);
Res(i) = (1/(conv_in(i) + rad_w(i))) + cond +(1/(conv_out + rad));
# specific heat capacity of water vapour
Cpw_v(i) =-0.00000000031759*(tair(i)+273)^3 + 0.00000091451537*(tair(i)+273)^2 -
0.00014971847134*(tair(i)+273) + 1.84044937134494;
END
#Total heat loss from this section
heatloss = INTEGRAL(i := 0:L5; Qlos(i));
# Outlet variables
r(L5) = F_k_out/u;
```

```
T(L5) = T_out;

me(L5) = x_out;

Ts(L5) = Tout;

Air(L5) = A_o/v_g(L5);

Tair(L5) = T_o;

H_out(L5) = H_o;
```

Geometric modelling for section B

PARAMETER

L2 AS REAL # Drum Length (m)

R AS REAL # Drum Radius (m)

theta AS REAL # Inclination of Drum (degrees)

Nf_2 AS INTEGER # No. Flights

s1_2 AS REAL # Flight Length 1

s2_2 AS REAL # Flight Length 2

alpha1_2 AS REAL # Flight Angle 1 (deg)

alpha2_2 AS REAL # Flight Angle 2 (deg)

N2 AS INTEGER # Number of Cells

VARIABLE

omega AS no_unit # Angular Velocity of Drum (RPM)

m_p AS mass # Passive Mass from Passive Phase

m_load AS mass # Calculated Loging Mass for Passive Phase

load AS no_unit # Loading Level of Flight

U AS no_unit # Unloading Level of Flight

phi AS no_unit # Angle of Repose of Solids in Flights

a1 AS no_unit # alpha1 in radians

a2 AS no_unit # alpha2 in radians

Rf AS length # Radius of flight tip

psi_ft AS no_unit # Angle between flight tip and flight base from centre of dryer

```
c1                  AS no_unit          # Geometricaly Calculated Axial Advance
k_2                 AS no_unit
maft                AS no_unit          # Mass averaged fall time of solids
mafh                AS length           # Mass averaged fall height of solids
tpas                AS no_unit          # Average passive cycle time
dl                  AS length           # Length of cell
pi                  AS no_unit          # Pi
#sf                 AS no_unit          # Scaling factor
m_bak               AS mass             # Design load
m_des               AS mass             # modified design load
rhob                AS no_unit    # Density of Solids
STREAM
Data_In             :m_p                AS DATAF
Data_A              :maft,c1            AS DATAA
Data_P              :k_2,m_load         AS DATAP
EQUATION
pi = 3.141592654;
dl = L2/N2;             # Length of Slice
a1 = alpha1_2*pi/180;      # Convert alpha1 to radians
a2 = alpha2_2*pi/180;      # Convert alpha2 to radians
# Basic Dryer Geometry Calculations
# Calculation of flight tip radius
Rf = sqrt(((R-s1_2)^2) + (s2_2^2) - 2*s2_2*(R-s1_2)*cos((3/2)*pi-a1-a2));
```

```
# Calculation of angle between flight tip and flight base from centre of dryer
psi_ft = asin(s2_2*sin(pi-a2)/Rf);
# Calculating Theoretical Loading Mass using Porter's Assumption

m_bak = rhob*dl*(-8.44885457098519+ 1.20811962158233*phi -0.0696338151338383*(phi^2)
+ 0.00212647019010012*(phi^3) -3.60759970976406E-05*(phi^4) + 3.22758303782236E-
07*(phi^5)-1.18976131428293E-09*(phi^6));
m_des = (1.24*m_bak);
m_load = m_des;
# Calculating Loading Level, using theoretical loading holdup and actual passive holdup
#       If dryer is overloaded, load is set to 1.
IF m_p < m_load THEN
   load = m_p/m_load;
ELSE
   load = 1;
END
U = 1 - load;
# Calculation of mass averaged fall time and height
IF load > 0 THEN
maft =  0.535877216576409 + 0.0045785629077670 4*phi -0.000129598737028669*(phi^2) +
1.07883836331524E-06*(phi^3) + 0.117473908470856*U -0.0744009282461775*(U^2) +
0.0810434707665877*(U^3) + 0.0128083149957092*phi*U -
```

```
0.00875061991473558*phi*(U^2)-0.000108364812479778*(phi^2)*U + 4.74471791775954E-
05*(phi^2)*(U^2);
   mafh = 0.5*9.81*(maft^2);
   tpas = acos(1-((mafh*cos(theta*pi/180))^2)/(2*(R^2)))/(omega*2*pi/60);
   k_2 = 1/tpas;
ELSE

   maft = 0;
   mafh = 0;
   tpas = 0;
   k_2 = 0;
END
c1 = mafh*sin (theta*pi/180)/(L2/N2);    # Geometric axial advance of solids w/o drag
```

Geometric modelling for section C

PARAMETER

L3 AS REAL # Drum Length (m)

R AS REAL # Drum Radius (m)

theta AS REAL # Inclination of Drum (degrees)

Nf_3 AS INTEGER # No. Flights

s1_3 AS REAL # Flight Length 1

s2_3 AS REAL # Flight Length 2

alpha1_3 AS REAL # Flight Angle 1 (deg)

alpha2_3 AS REAL # Flight Angle 2 (deg)

N3 AS INTEGER # Number of Cells

VARIABLE

omega AS no_unit # Angular Velocity of Drum (RPM)

m_p AS mass # Passive Mass from Passive Phase

m_load AS mass # Calculated Loging Mass for Passive Phase

load AS no_unit # Loading Level of Flight

U AS no_unit # Unloading Level of Flight

phi AS no_unit # Angle of Repose of Solids in Flights

a1 AS no_unit # alpha1 in radians

a2 AS no_unit # alpha2 in radians

Rf AS length # Radius of flight tip

psi_ft AS no_unit # Angle between flight tip and flight base from centre of dryer

```
c1                  AS no_unit          # Geometricaly Calculated Axial Advance
k_2                 AS no_unit
maft                AS no_unit          # Mass averaged fall time of solids
mafh                AS length          # Mass averaged fall height of solids
tpas                AS no_unit          # Average passive cycle time
dl                  AS length          # Length of cell
pi                  AS no_unit          # Pi
#sf                 AS no_unit          # Scaling factor
m_bak               AS mass
m_des               AS mass
rhob                AS no_unit     # Density of Solids
STREAM
Data_In             :m_p                        AS DATAF
Data_A              :maft,c1                    AS DATAA
Data_P              :k_2,m_load                 AS DATAP
EQUATION
pi = 3.141592654;
dl = L3/N3;             # Length of Slice
a1 = alpha1_3*pi/180;       # Convert alpha1 to radians
a2 = alpha2_3*pi/180;       # Convert alpha2 to radians
# Basic Dryer Geometry Calculations
# Calculation of flight tip radius
Rf = sqrt(((R-s1_3)^2) + (s2_3^2) - 2*s2_3*(R-s1_3)*cos((3/2)*pi-a1-a2));
```

```
# Calculation of angle between flight tip and flight base from centre of dryer
psi_ft = asin(s2_3*sin(pi-a2)/Rf);
# Design load calculation
m_bak = rhob*dl*(-4.6584030831466 + 0.646205724290255*phi-0.0358998918593869*(phi^2)
+ 0.00106187909781541*(phi^3) -1.74218037964184E-05*(phi^4) + 1.50728281484852E-
07*(phi^5)  -5.36928902950201E-10*(phi^6));
m_des = (1.24*m_bak);
m_load = m_des;
# Calculating Loading Level, using theoretical loading holdup and actual passive holdup
#       If dryer is overloaded, load is set to 1.
IF m_p < m_load THEN
   load = m_p/m_load;
ELSE
   load = 1;
END
U = 1 - load;
# Calculation of mass averaged fall time and height
IF load > 0 THEN
maft = 0.455364714961433 + 0.00500606517559277*phi -0.000135762841787734*(phi^2) +
1.2918647217012E-06*(phi^3) + 0.0104733203115757*U + 0.0148187169761513*(U^2) +
0.0522743789468905*(U^3) + 0.0160364376692996*phi*U -0.00896672863768799*phi*(U^2)
-0.000151022103693776*(phi^2)*U + 6.46798505794521E-05*(phi^2)*(U^2);
   mafh = 0.5*9.81*(maft^2);
```

```
    tpas = acos(1-((mafh*cos(theta*pi/180))^2)/(2*(R^2)))/(omega*2*pi/60);
    k_2 = 1/tpas;
ELSE
    maft = 0;
    mafh = 0;
    tpas = 0;
    k_2 = 0;
END
c1 = mafh*sin(theta*pi/180)/(L3/N3);    # Geometric axial advance of solids w/o drag
```

Geometric modelling for section D

PARAMETER

L4 AS REAL # Drum Length (m)

R AS REAL # Drum Radius (m)

theta AS REAL # Inclination of Drum (degrees)

Nf_4 AS INTEGER # No. Flights

s1_4 AS REAL # Flight Length 1

s2_4 AS REAL # Flight Length 2

alpha1_4 AS REAL # Flight Angle 1 (deg)

alpha2_4 AS REAL # Flight Angle 2 (deg)

N4 AS INTEGER # Number of Cells

VARIABLE

omega AS no_unit # Angular Velocity of Drum (RPM)

m_p AS mass # Passive Mass from Passive Phase

m_load AS mass # Calculated Loging Mass for Passive Phase

load AS no_unit # Loading Level of Flight

U AS no_unit # Unloading Level of Flight

phi AS no_unit # Angle of Repose of Solids in Flights

a1 AS no_unit # alpha1 in radians

a2 AS no_unit # alpha2 in radians

Rf AS length # Radius of flight tip

psi_ft AS no_unit # Angle between flight tip and flight base from centre of dryer

c1 AS no_unit # Geometricaly Calculated Axial Advance

```
k_2             AS no_unit
maft            AS no_unit          # Mass averaged fall time of solids
mafh            AS length           # Mass averaged fall height of solids
tpas            AS no_unit          # Average passive cycle time
dl              AS length           # Length of cell
pi              AS no_unit          # Pi
#sf             AS no_unit          # Scaling factor
m_bak           AS mass               #design load
m_des           AS mass               # modified design load
rhob            AS no_unit    # Density of Solids
STREAM
Data_In         :m_p                        AS DATAF
Data_A          :maft,c1                    AS DATAA
Data_P          :k_2,m_load                 AS DATAP
EQUATION
pi = 3.141592654;
dl = L4/N4;             # Length of Slice
a1 = alpha1_4*pi/180;       # Convert alpha1 to radians
a2 = alpha2_4*pi/180;       # Convert alpha2 to radians
# Basic Dryer Geometry Calculations
# Calculation of flight tip radius
Rf = sqrt(((R-s1_4)^2) + (s2_4^2) - 2*s2_4*(R-s1_4)*cos((3/2)*pi-a1-a2));
# Calculation of angle between flight tip and flight base from centre of dryer
```

```
psi_ft = asin(s2_4*sin(pi-a2)/Rf);
# Calculating THeoretical Loading Mass using Porter's Assumption
#m_load = mf_max * Nf_4/2;
m_bak = rhob*dl*(5.91313117986886 -0.796114307860833*phi +
0.0456776806338413*(phi^2) -0.00137025615939124*(phi^3) + 2.28826870054856E-
05*(phi^4) -2.01534907281941E-07*(phi^5) + 7.31905932620977E-10*(phi^6));
m_des = (1.24*m_bak);
m_load = m_des;
# Calculating Loading Level, using theoretical loading holdup and actual passive holdup
#       If dryer is overloaded, load is set to 1.
IF m_p < m_load THEN
   load = m_p/m_load;
ELSE
   load = 1;
END
U = 1 - load;
# Calculation of mass averaged fall time and height
IF load > 0 THEN
maft = 0.563922134596396 + 0.0041998168595969*phi -0.000122322728935087*(phi^2) +
9.82402884711769E-07*(phi^3) + 0.155664820234961*U -0.124796430711285*(U^2) +
0.101432837793894*(U^3) + 0.0117097541137809*phi*U -0.00852018863838566*phi*(U^2)
-9.63187980449476E-05*(phi^2)*U + 4.14518306346423E-05*(phi^2)*(U^2);
   mafh = 0.5*9.81*(maft^2);
```

```
    tpas = acos(1-((mafh*cos(theta*pi/180))^2)/(2*(R^2)))/(omega*2*pi/60);
    k_2 = 1/tpas;
ELSE
    maft = 0;
    mafh = 0;
    tpas = 0;
    k_2 = 0;
END
c1 = mafh*sin(theta*pi/180)/(L4/N4);    # Geometric axial advance of solids w/o drag
```

Mixing cell

{The mixing cell combines the output from the last passive and active cells in Section D. this #serves as input data into last unflighted section}

PARAMETER

Cp_w AS REAL # Specific heat capacity of water

Cp_z AS REAL # specifice heat capacity of zinc

VARIABLE

F_p AS Mass_flowrate # Flowrate from the passive cell

F_x AS Mass_flowrate # Flowrate from the active cell(axial)

T_p AS mass_Fraction # Tracer conc

F_t AS mass_flowrate # Total flow into the plug section (agglomeration)

T_x AS mass_Fraction # Tracer conc.(from the active phase(axial)

T_t AS mass_Fraction # Total tracer conc. into the last plug section

x_x AS mass_Fraction # Moisture content.(from the active phase(axial)

x_t AS mass_Fraction #Total moisture content into the last plug section

x_p AS mass_Fraction #Moisture content from the passive cell

tt AS temperature #temperature into the plug section(agglomeration)

tp AS temperature #temperature of the passive phase

tx AS temperature #temperature of the active phase(axial

STREAM

Passive :F_p,T_p,x_p,tp AS SOLIDFLOW

Axial :F_x,T_x, x_x,tx AS SOLIDFLOW

Out :F_t,T_t, x_t,tt AS SOLIDFLOW

EQUATION

$$F_t = F_p + F_x;$$

$$(T_t * F_t) = (F_p * T_p) + (F_x*T_x);$$

$$(x_t * F_t) = (F_p * x_p) + (F_x*x_x);$$

$$F_t*(((1-x_t)* Cp_z*tt)+ (x_t*Cp_w*tt)) = F_p*(((1-x_p)* Cp_z*tp)+ (x_p*Cp_w*tp)) +$$

$$F_x*(((1-x_x)* Cp_z*tx)+ (x_p*Cp_w*tx));$$

```
UNIT
A            AS Active_Phase
G            AS Geometry1
P            AS Passive_Phase
AIR          AS Air_phase
EQUATION
P.Active IS A.Active;
P.Return IS A.Return;
P.DataOut IS G.Data_In;
P.DataIn IS G.Data_P;
A.Data IS G.Data_A;
AIR.Evaporation IS A.Evaporation;
A.Air  IS AIR.Air_out;
A.Convection IS AIR.Convection;
A.masstransfer  IS AIR.masstransfer;
A.Radiation IS AIR.radiation;
```

Parameter estimation

ESTIMATE

D.C1.u

0.015 0.01 0.017

ESTIMATE

D.y

0.0001 0 0.01

MEASURE

D.O.T_ppm

CONSTANT_RELATIVE_VARIANCE

(0.05:0.01:100)

RUNS

Clean

Experimental entity

INTERVALS

3

1500.0

60.0

2500.0

PIECEWISE_CONSTANT

D.C1.T_k_in

0.0

1.255E-4

0.0

MEASURE

D.O.T_ppm

2190.0 1.24

2220.0 1.09

2250.0 3.26

2280.0 7.38

2310.0 13.5

2340.0 31.5

2370.0 28.4

2400.0 38.4

2430.0 51.7

2460.0 40.7

2490.0	13.6
2520.0	10.4
2550.0	5.09
2580.0	3.49
2610.0	1.55
2640.0	1.9
2670.0	1.24
2700.0	0.869
2760.0	0.839
2880.0	0.813
3000.0	0.81
3300.0	0.677
3600.0	0.613
3900.0	0.603
4200.0	0.511